OBSERVATIONAL STUDIES OF HYDROGEN-DEFICIENT STARS FOR INVESTIGATING THEIR EVOLUTIONARY CONNECTIONS

A thesis

submitted for the degree of

Doctor of Philosophy

In

Department of Physics,

School of Physical, Chemical and Applied Sciences

Pondicherry University

By

HEMA B. P.

Indian Institute of Astrophysics, Bangalore-34

April 2014

Declaration of Authorship

I hereby declare that the material presented in this thesis is the result of investigations carried out by me at the Indian Institute of Astrophysics, Bangalore under the supervision of Prof. Gajendra Pandey. This thesis has not been submitted for the award of any degree, diploma, associateship, fellowship, etc. in any university or institute.

Hema B. P.
(Candidate)

Bangalore-560034
April 2014

Certificate

This is to certify that the thesis entitled **"Observational Studies of Hydrogen-Deficient Stars for Investigating their Evolutionary Connections"** submitted to the Pondicherry University by Ms. Hema B. P. for the award of the degree of Doctor of Philosophy in the faculty of Science, is the result of investigations carried out by her under my supervision and guidance, at the Indian Institute of Astrophysics. This thesis has not been submitted for the award of any degree, diploma, associateship, fellowship, etc. in any university or institute.

Prof. Gajendra Pandey
(Supervisor)

Indian Institute of Astrophysics
Bangalore - 560034, India

Dedicated to
my beloved parents and my brother

Acknowledgements

I am indebted to my supervisor Prof. Gajendra Pandey for the guidance, constant support, and encouragement, without whose help the completion of this thesis wouldn't have been possible.

I express my heartfelt gratitude to Prof. David Lambert for the guidance and comments during the course of my research, which laid the foundation for my basic understanding of stellar spectroscopy. I am indebted to you Sir. I also take this opportunity to thank Prof. N. Kameswara Rao for fruitful discussions. I thank Dr. Kjell Eriksson and Dr. Anibal García-Hernández for providing the hydrogen-deficient models of the cool stars, particularly Kjell Eriksson for providing these models in our required format. I also thank Nils Ryde for making available a C_2 line list sample.

I am grateful to the former and the current directors of Indian Institute of Astrophysics, Prof. S. S. Hassan and Prof. P. Sreekumar, for providing all the required facilities and support for my thesis work. My sincere thanks to my doctoral committee members, Prof. Aruna Goswami, Prof. Govindaraj, and Prof. A. V. Ravindran for the comments and suggestions. My sincere thanks to Prof. H. C. Bhatt for the fruitful discussions and comments. I thank Prof. Eswar Reddy, Prof. Sunetra Giridhar, Prof. R. K. Chaudhuri, and Dr. Sivarani Thirupathi for their help and fruitful discussions. My sincere thanks to Prof. Aruna Goswami and Prof. Muthumariappan, and Dr. S. Ramya for reading the manuscript of my thesis and for their valuable comments. I thank Dr. B. A. Varghese for all the support provided in the software related issues, and for helping in handling the model atmospheres. I thank the Chair, VTAC for providing ample time on the Vainu Bappu Telescope, Kavalur, which enabled me to acquire the sufficient data.

I thank the former and the current HOD, Dept. of Physics, Pondicherry University, Prof. G. Govindaraj and Prof. G. Chandrasekaran, for all their help starting from processing of the registration till the submission of my thesis at Pondicherry University. I thank Prof. Annapurni Subramaniam for helping with all the registration related matters with Pondicherry University.

I thank all the observing staff of Vainu Bappu Observatory (VBO), Kavalur, for their help during my observations. And I also thank the staff of the electronics, electrical, computers and mechanical sections of VBO.
I am thankful to IIA library staff, and the Librarian Ms. Christina Birdie for making available all the required material for my research work. I thank the support staff of IIA for helping in computer related issues. I thank all the staff members of IIA Bangalore, VBO and Crest, for all their help and support during my stay.

I am very grateful to Prof. Kagali, Dept. of Physics, Bangalore University, for his support and encouragement and for being an inspiration for pursuing research in astronomy. I thank all my teachers of JNV Tumkur, Sri Siddaganga College for Women, Tumkur, and Dept. of Physics, Bangalore University, for their encouragement, guidance, support and their blessings throughout my student life. I thank all the scientists at Indian Institute of Astrophysics, Bangalore who have helped me directly or indirectly.

I am very thankful to Dr. Bharat Kumar Yerra and Dr. L. S. Anusha who were always there for me during my learning process. I thank A. B. Sudhakar Reddy for helping in learning synthesis with MOOG, Avijeet Pasad and Prashanth Mohan for helping with Mathematica, Manpreet Singh for helping with xmgrace plotting tool and other software tools. I thank Sandra Rajiva, Vineeth, Avijeet, Prashanth, and Krishna Prasad for reading the manuscript of this thesis and for their corrections and suggestions. I thank all my friends for their love and support. I thank all my batchmates, seniors, and juniors at IIA, who made my stay a memorable one.

I am falling short of words to express my gratitude to my parents, B. R. Prakash and Anusuya Prakash, and my brother B. P. Pavan Kumar, whose love and support was the constant source of inspiration to me without which, the successful completion of my thesis wouldn't have been possible.

Abstract

The group of hydrogen-deficient (H-deficient) and carbon rich supergiants spanning a range in their effective temperatures are: hydrogen deficient carbon (HdC) stars, R Coronae Borealis (RCB) stars, and extreme helium (EHe) stars, in the order of their increasing effective temperature. The origin and evolution of these stars is not yet clear. There are two proposed scenarios for their origin. In one dubbed the double degenerate (DD) scenario, a helium white dwarf merges with a carbon–oxygen (C–O) white dwarf. A merger of these two white dwarfs, both having a very thin outer H-rich layer, makes the resulting star H-deficient. An alternative scenario dubbed the final flash (FF) scenario involves a single post-asymptotic giant branch (AGB) star experiencing a final helium shell flash which causes the H-rich envelope to be ingested by the He shell. The result is that the star becomes a H-deficient supergiant for a brief period and is sometimes referred in this condition as a 'born-again' AGB star. In this thesis, the origins and evolution of H-deficient supergiants are investigated: First, by conducting a survey for identifying H-deficient stars in the Galactic globular cluster ω Centauri, and to pin-point their positions on the HR-diagram, and second, by deriving the Galactic RCB/HdC stars C-abundances and the $^{12}C/^{13}C$ ratios that are potential clues to their origin.

The distances are not accurately known to any of the Galactic H-deficient stars. The position of a star on the HR-diagram, gives us an idea about its evolution and possibly its origin. To place the H-deficient stars on the HR-diagram, one of the best ways would be to search for these stars in the globular clusters of the Galaxy. Hence, a survey was conducted to identify new H-deficient stars in the largest and brightest globular cluster of the Galaxy: ω Centauri. Our survey is based on the Strömgren photometric studies of red giant stars in ω Cen by Calamida et al. (2009). From the photometric and the spectroscopic studies of the red giant stars of ω Cen, it is clear that they show a large spread in their

metallicity: $-2.5 < [\mathrm{Fe/H}] < +0.5$. This spread in metallicity, not as expected for the globular cluster, is taken as a clue for the presence of H-deficient stars in ω Cen. By applying the photometric and the spectroscopic characteristics of the RCB/HdC stars, the program stars were selected. For these program stars, the low-resolution spectra were obtained from the Vainu Bappu Observatory (VBO), Kavalur, India. The analyses were carried out based on the strengths of the (0,0) MgH band extending from 5330 to 4950Å, with the band head at 5211Å, and the Mg *b* lines at 5167.32Å, 5172.68Å and 5183.60Å. Based on the strengths of these features, the three groups were identified in our sample: (i) the metal rich giants with strong Mg *b* lines and the MgH band, (ii) the metal poor giants with weak Mg *b* lines and no MgH band, and (iii) the metal rich giants with strong Mg *b* lines, but no MgH band. By comparing the observed MgH bands among the stars of (i) and (iii) group, with similar stellar parameters, four stars were identified having weaker or absent MgH band. Two stars: 178243 and 73170 are from the first group showing the strong Mg *b* lines, but weaker MgH band than expected for their stellar parameters. The other two stars: 262788 and 193804 are from the third group showing strong Mg *b* lines, but absent MgH band not as expected for their stellar parameters. The MgH band strengths in the observed spectra of these four stars along with all the first and third group stars, were further analyzed by synthesis. The Mg abundances derived for these four stars are much lower than that expected for the red giants of ω Cen as given by Norris & Da Costa (1995) for their metallicities. The weak/absent MgH band in the observed spectra of these four giants inspite of the presence of strong Mg *b* lines, may not be due to the stellar parameters or a lower Mg abundance. The only plausible reason is a relatively lower abundance of hydrogen in their atmosphere. Hence, from our survey, we report the discovery of four giants with relatively lower abundance of hydrogen in their atmospheres. In this survey we have not found any H-deficient star of RCB-type. This result is in agreement with our prediction for the number of H-deficient stars formed by the DD and FF scenario in the globular cluster,

ω Cen.

To explore the origin of the Galactic RCB stars, the carbon abundances and the $^{12}C/^{13}C$ ratios of RCB and HdC stars were determined by synthesizing the (0, 0), (1, 0) and (0, 1) C_2 Swan bands, and matching them with the observed spectrum. High-resolution optical spectra of RCB/HdC stars at maximum light were obtained from the W. J. McDonald Observatory, USA, and the Vainu Bappu Observatory, India. The carbon abundances determined from the C I lines are a factor of four lower than that adopted for the model atmosphere, and is dubbed as the 'carbon problem' (Asplund et al. 2000). This discrepancy persists with the change in the input carbon abundance of the adopted model atmosphere. Whereas, the carbon abundance derived from the C_2 Swan bands is about the same for the adopted models constructed with different carbon abundances over the range 8.5 (C/He = 0.1%) to 10.5 (C/He = 10%). The $^{12}C/^{13}C$ ratios determined for the majority RCBs and all the HdCs are much higher than the CN-cycle equilibrium value of 3.4. These high values are consistent with that predicted for the cold merger of a He white dwarf with a CO white dwarf. The two minority RCB stars (stars which are metal poor and having high [Si/Fe] and [S/Fe] ratios, relative to the majority RCB stars) are having low values of $^{12}C/^{13}C$ ratios, that are close to the CN-cycle equilibrium value. These low values of $^{12}C/^{13}C$ ratios remain unaccounted due to their distinctive pattern of elemental abundances. The carbon abundance and the $^{12}C/^{13}C$ ratio were also determined for the final flash object, V4334 Sgr. The carbon abundance of V4334 Sgr is about 10-100 times higher than the RCB/HdC stars, and the $^{12}C/^{13}C$ ratio is about 3.4, the CN-cycle equilibrium value. These values are as expected for the final flash object.

Publications

Refereed publications

1. **The Galactic R Coronae Borealis Stars: The C_2 Swan Bands, The Carbon Problem, and the $^{12}C/^{13}C$ Ratio**
   B. P. Hema, Gajendra Pandey & David L. Lambert, 2012, The Astrophysical Journal, 747, 102

2. **The Galactic R Coronae Borealis Stars and the Final Helium-Shell Flash Object V4334 Sgr (Sakurais Object): A Comparison**
   B. P. Hema, Gajendra Pandey, & David L. Lambert, 2012, Proceedings of NIC XII, 195H

3. **Discovery of relatively hydrogen-poor giants in the Galactic globular cluster ω Centauri**
   B. P. Hema & Gajendra Pandey, 2014, ApJL, 792, L28

4. **High-resolution optical spectroscopy of the R Coronae Borealis star V532 Ophiuchi at maximum light**
   N. Kameswara Rao, David L. Lambert, Vincent M. Woolf, & B. P. Hema, 2014, PASP, 126, 813

Conference proceedings

1. **Clues to the origin of R Coronae Borealis Stars**
   B. P. Hema & Gajendra Pandey, 2011, Proceedings of 29th Meeting of the Astronomical Society of India, Vol. 3, p. 128, Ed. Pushpa Khare & C. H. Ishwara-Chandra

2. **Spectroscopic survey for identifying the hydrogen-deficient stars in globular cluster: ω Centauri**
   B. P. Hema & Gajendra Pandey, 2013, Proceedings of 31st Meeting of the Astronomical Society of India, Vol. 9, p. 113, Ed. Pushpa Khare & C. H. Ishwara-Chandra

Contents

List of Figures

List of Tables

Chapter 1

Introduction

Hydrogen is the most common element in the universe. All the stars are made up of about 71.5% of hydrogen and 27.0% of helium by mass, and all the other elements are in small quantities called the trace elements. The stars start their life by burning hydrogen in the core and evolve by burning hydrogen in the shell. Hydrogen is the main source of energy in stars from their birth through their evolved stages. Can there be a star whose surface is devoid of hydrogen, the far most abundant element, in the course of its evolution? There exists an enigmatic group of stars which have tens of thousands to tens of millions of times less hydrogen than in the normal stars. These are known as hydrogen-deficient (H-deficient) stars. These stars have very weak or absent H-Balmer lines in their spectra than that expected for the normal stars, with similar effective temperatures, indicating that these are H-poor.

The existence of H-deficient stars came to light by the discovery of R Coronae Borealis (R CrB) in 1797 by Pigott & Englefield (1797). R CrB is a variable star in the constellation of 'Corona Borealis' (Northern Crown). The observations carried out by Pigott & Englefield (1797) from 1783 through 1785 revealed that the star is a peculiar variable in its optical light, by undergoing sudden declines upto several magnitudes and recovering slowly to its maximum light after an interval of weeks,

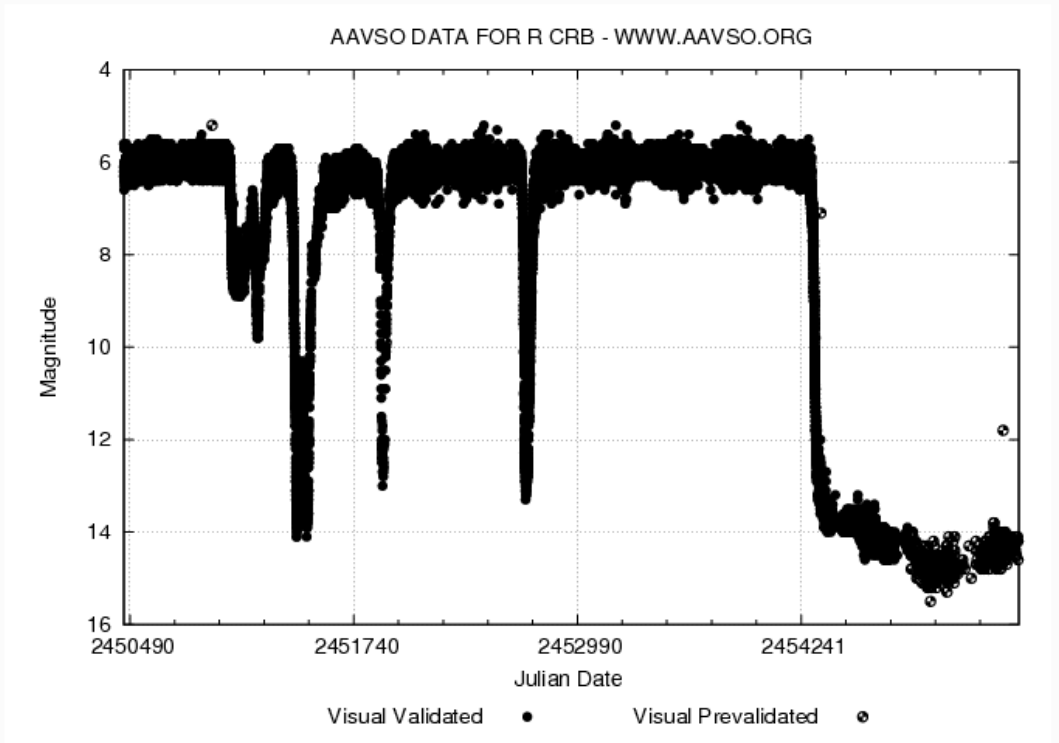

FIGURE 1.1: The light curve for R CrB is shown in figure. The variability upto several magnitudes and at irregular times can be noticed. Courtesy: AAVSO

months, or even years. The star stays for longer time at its maximum light than at minimum light (see Figure 1.1).

The H-deficiency of R CrB was discovered by Cannon & Pickering (1912) by identifying the weak CH-band in its spectrum, and was confirmed by Berman (1935) by analyzing the weak H-Balmer lines in its spectrum.

The group of stars that share the properties of R CrB, i.e., the peculiar optical light variability, and the H-deficiency, are known as the R Coronae Borealis stars or RCB stars, named after their prototype R CrB.

There are two groups of stars that are related to RCBs: the hydrogen deficient carbon (HdC) stars and the extreme helium (EHe) stars, which are cooler and warmer than the RCB effective temperatures, respectively. The HdCs and EHes do not show the light variability, characteristic to the RCB stars.

These H-deficient supergiants (RCB/HdC/EHes) with a large span in their effective temperature: 3500-35000 K, show strong neutral carbon lines in their observed optical spectra. With relatively cooler effective temperatures, the RCB and the HdC stars show strong C_2 Swan bands. The EHe stars, with relatively warmer effective temperatures, show the neutral helium lines and the singly ionized carbon lines in their observed optical spectra. The presence of strong carbon features in the spectra of these stars indicates that RCBs/HdCs/EHes are carbon rich.

1.1 Distribution of H-deficient stars in the Galaxy, and in the Magellanic Clouds

Starting from the discovery of R CrB star in 1797, about 100 H-deficient stars have been discovered till date, in our Galaxy and in the Magellanic Clouds. There are 77 RCBs (Clayton 1996; Clayton et al. 2002, 2009; Hesselbach et al. 2003; Miller et al. 2012; Tisserand et al. 2013, 2008; Zaniewski et al. 2005), 21 EHes (Jeffery et al. 1996), and 6 HdCs (Bidelman 1953; Goswami et al. 2010; Warner 1967) known in the Galaxy. About 23 RCBs are also known in Large Magellanic Cloud (LMC) (Alcock et al. 2001; Clayton 1996; Jeffery et al. 1996; Tisserand et al. 2009). About 6 RCB candidates are also identified in Small Magellanic Cloud (SMC) (Kraemer et al. 2005; Morgan et al. 2003; Tisserand et al. 2004). All these RCBs/HdCs/EHes are listed with their coordinates (RA and Dec) and the apparent visual magnitudes (maximum light) in Appendix A.

Most of the known H-deficient stars are the bulge population, located towards the center of the Galaxy (Drilling 1996). Since the known RCB, HdC and EHes are located in almost the same region of the Galaxy, Drilling (1996) infer that they belong to the same population (Galactic bulge population) and they are related objects. However, the RCB stars of the LMC are located in the bar (Tisserand et al. 2008). The distances are known for none of the Galactic H-deficient stars. By knowing the distance to LMC, the absolute magnitudes are estimated for LMC RCB stars, which span the range: $-5 \leq M_v \leq -3.5$. This range of absolute magnitudes is assumed for the Galactic RCB stars.

Hydrogen is the most abundant element in stars. All the stars evolve by burning hydrogen in their core, and then in the shell in their later stages. But, at what stages of their evolution, the stars may become H-deficient, by loosing the substantial amount of hydrogen from their surface? Before discussing the formation of H-deficient stars, we discuss the evolution of normal stars. The position of the known H-deficient stars on the log g – $T_{\rm eff}$ plane suggests that these are low and intermediate mass stars. Hence, in the following section we discuss the evolution of 'normal' low and intermediate mass stars.

1.2 Origin and evolution of low and intermediate mass stars

The stars with the initial masses in the range: 0.8 to 2.3$M_\odot$, are classified as the low mass stars, and the stars with the initial masses in the range: 2.3 to 8$M_\odot$, are the intermediate mass stars (Iben & Renzini 1983).

The sites of star formation are the giant molecular clouds of hydrogen, located mostly in the disk of the Galaxy. Due to the gravitational pull, the cloud starts collapsing under its own gravity. When the core temperature reaches a few million kelvin, the nuclear fusion reaction begins. The hydrogen is converted into helium either through the PP-chain or through the CNO-cycle. The stars with the initial mass $<1.3M_\odot$ having relatively lower central temperatures, convert hydrogen into helium through the PP-chain. And, the stars with the initial mass $>1.3M_\odot$ having relatively high central temperatures, convert hydrogen into helium through the CNO-cycle (Iben 1967). The CNO nuclei act as 'catalysts' in the conversion of hydrogen into helium. When the CNO-cycle reaches the equilibrium, the value of $^{12}C/^{13}C$ ratio is driven to the equilibrium value of 3.4, and the abundance of ^{14}N increases (Böhm-Vitense 1992). The nuclear fusion reactions involved in the PP-chain and the CNO-cycle are given below,

PP-chain:

$$ {}^1_1H + {}^1_1H \rightarrow {}^2_1H + e^+ + \nu_e $$

$$ {}^2_1H + {}^1_1H \rightarrow {}^3_2He + \gamma $$

$$ \swarrow \searrow $$

$$ {}^3_2He + {}^3_2He \rightarrow {}^4_2He + 2{}^1_1H \qquad {}^3_2He + {}^4_2He \rightarrow {}^7_4Be + \gamma $$

(PP I)

$$ \swarrow \searrow $$

$$ {}^7_4Be + e^- \rightarrow {}^7_3Li + \nu_e \qquad {}^7_4Be + {}^1_1H \rightarrow {}^8_5B + \gamma $$

$$ {}^7_3Li + {}^1_1H \rightarrow 2\,{}^4_2He \qquad {}^8_5B \rightarrow {}^8_4Be + e^+ + \nu_e $$

(PP II)

$$ {}^8_4Be \rightarrow 2{}^4_2He $$

(PP III)

CNO-cycle:

a. $$ {}^{12}_6C + {}^1_1H \rightarrow {}^{13}_7N + \gamma $$

$$ {}^{13}_7N \rightarrow {}^{13}_6C + e^+ + \nu_e $$

$$ {}^{13}_6C + {}^1_1H \rightarrow {}^{14}_7N + \gamma $$

$$ {}^{14}_7N + {}^1_1H \rightarrow {}^{15}_8O + \gamma $$

$$ {}^{15}_8O \rightarrow {}^{15}_7N + e^+ + \nu_e $$

$$ {}^{15}_7N + {}^1_1H \rightarrow {}^{12}_6C + {}^4_2He $$

b. $${}^{15}_{7}\mathrm{N} + {}^{1}_{1}\mathrm{H} \rightarrow {}^{16}_{8}\mathrm{O} + \gamma$$

$${}^{16}_{8}\mathrm{O} + {}^{1}_{1}\mathrm{H} \rightarrow {}^{17}_{9}\mathrm{F} + \gamma$$

$${}^{17}_{9}\mathrm{F} \rightarrow {}^{17}_{8}\mathrm{O} + e^{+} + \nu_e$$

$${}^{17}_{8}\mathrm{O} + {}^{1}_{1}\mathrm{H} \rightarrow {}^{14}_{7}\mathrm{N} + {}^{4}_{2}\mathrm{He}$$

The core hydrogen burning phase of evolution of stars is known as the *main sequence*. About 80% of the star's lifetime is spent in this phase. Once the hydrogen is exhausted in the core, the hydrogen burning starts in the shell. The hydrogen burning in the shell increases the mass of the helium core. As the mass of the core increases, the core contracts and the temperature in the surrounding layers increases, and in turn the rate of energy production in the hydrogen burning shell. The increased rate of energy production expands the envelope and increases the luminosity of the star, which makes the star to evolve nearly vertically upward on the HR-diagram. The HR-diagram: the Hertzsprung-Russell diagram represents the absolute magnitude versus the colour or effective temperature of stars (see Figure 1.2). The path along which the star climbs up along the HR-diagram with increasing luminosity is called the *red giant branch* (RGB) (Iben 1974), see Figure 1.3, showing the evolution of a two solar mass ($2M_{\odot}$) star (Herwig 2005).

Due to the expansion of the outer layers, the effective surface temperature of the star decreases and the opacity increases. Hence, the convection becomes the dominant mechanism for the energy transport. The convection zone extends inwards and reaches the layers, where the hydrogen burning has taken place. The convection brings the products of H-burning from the deeper layers and mixes with the surface. This process is termed as the *first dredge-up* (FDU). The FDU increases the abundance of ^{14}N and ^{13}C, and decreases the abundance of ^{12}C. As a result, decreasing the ^{12}C/^{14}N and the ^{12}C/^{13}C ratios in the envelope (Iben 1974).

During the ascent of the RGB, the core continues to contract. At the tip of the red giant branch, when the central temperature reaches about 10^{8}K, the helium is

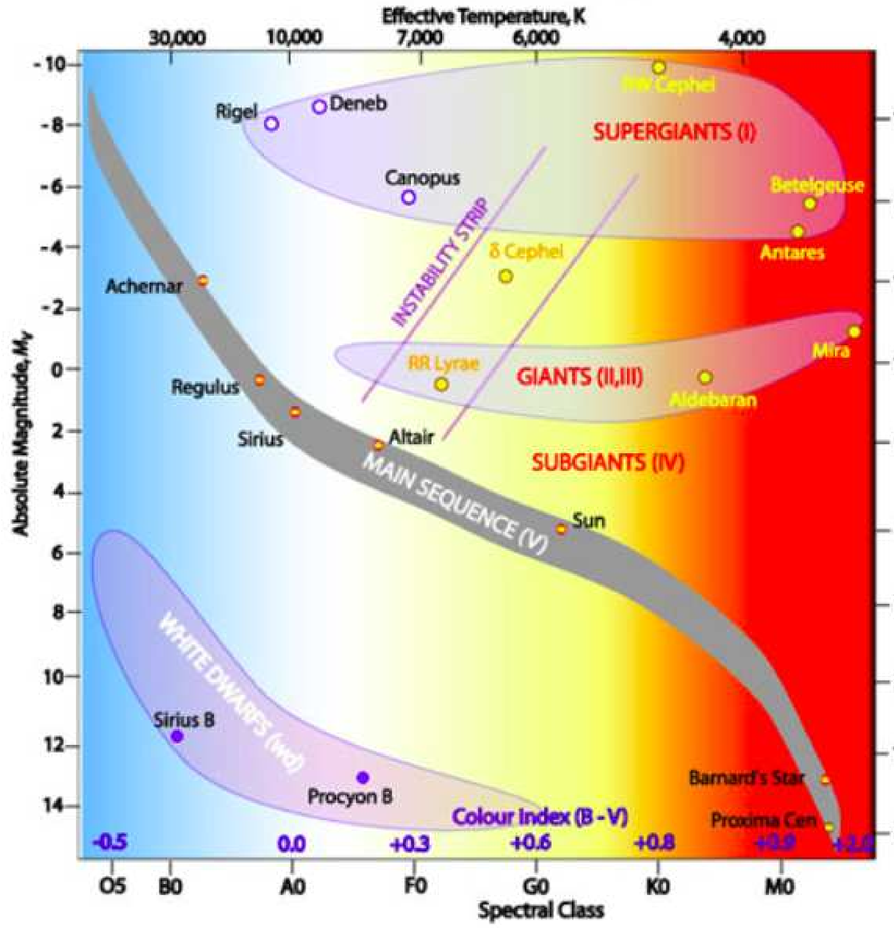

FIGURE 1.2: Figure showing the positions of stars on the the HR-diagram. stellar evolutionary stages with well known bright stars in that stage are also shown. Courtesy: CSIRO (www.csiro.au)

ignited in the core. The helium is converted into carbon, and further into oxygen via $triple - \alpha$ process.

Triple-α process

$$ {}^{4}_{2}\mathrm{He} + {}^{4}_{2}\mathrm{He} \rightarrow {}^{8}_{4}\mathrm{Be} $$
$$ {}^{8}_{4}\mathrm{Be} + {}^{4}_{2}\mathrm{He} \rightarrow {}^{12}_{6}\mathrm{C} + \gamma $$

The helium in the core is ignited in a flash under degenerate conditions in the low mass stars, and the helium fusion in the core starts smoothly in the intermediate

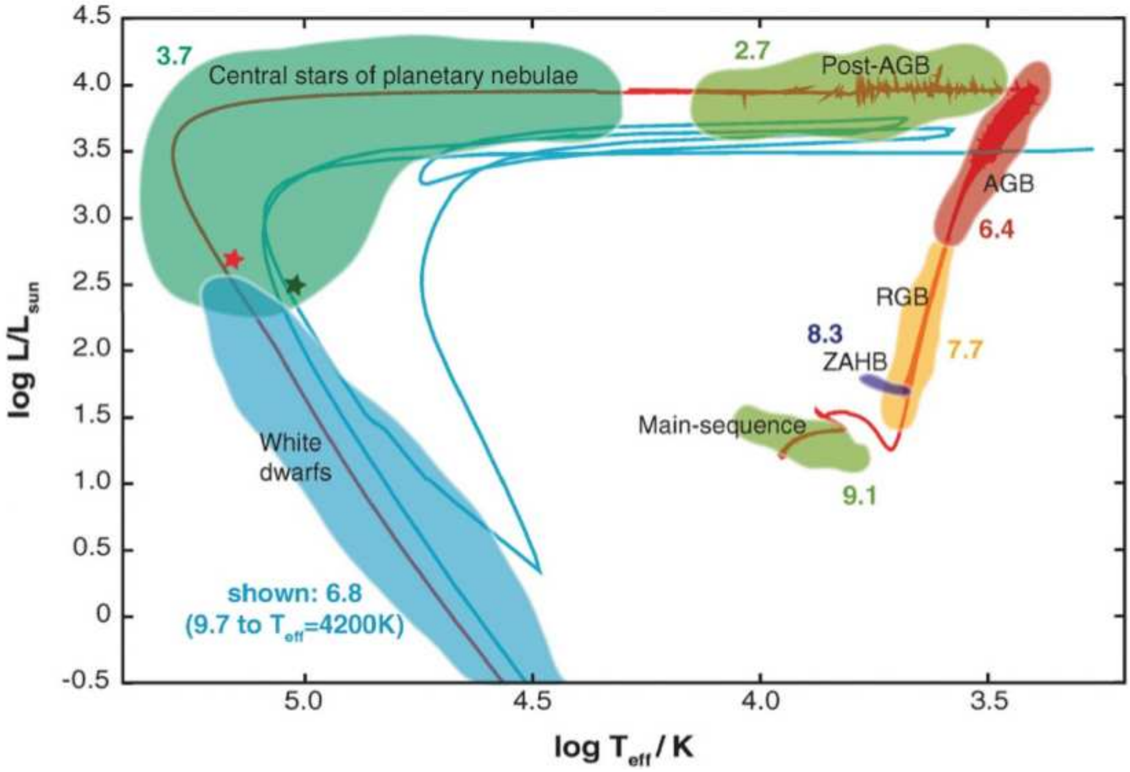

FIGURE 1.3: The evolution of a $2M_{\odot}$ star is shown. The different phases are shown in different colours as labeled. The numbers indicate the log of the approximate duration of that phase for a $2M_{\odot}$ star. The blue line shows the path of evolution of a born-again AGB star by experiencing a final He-shell flash (see section 1.3). Courtesy: Herwig (2005).

mass stars. This phase of evolution is known as the *horizontal branch*. Once the helium in the core is exhausted, the core begins to collapse, with no radiation pressure to support it. The temperature becomes high enough to ignite the helium in the shell. The energy released by the helium shell burning expands the surrounding material, making the envelope to expand and cool. This makes the hydrogen burning in the outer shell stop temporarily. Due to the core contraction, and the energy released by the helium burning in the shell, the luminosity of the star increases and the effective temperature decreases. Now, the star is said to be in the *asymptotic giant branch* (AGB) phase of its evolution (Herwig 2005). It is also called as the *red supergiant phase*. Once the helium is exhausted in the shell, the above lying layers contract and the hydrogen burning begins in the outer shell surrounding the helium rich inter-shell. This phase is known as the *early-AGB phase*. The other phase of the AGB evolution is *thermally pulsating AGB* ($TP - AGB$) (Herwig 2005). The TP-AGB phase is that the helium and hydrogen burn in two thin shells, separated by the helium rich inter-shell, alternatively. That is, the hydrogen burning in the thin shell around the He-inter-shell dumps the freshly synthesized helium on to the He-rich layer. When the helium rich layer reaches a critical mass, it re-ignites the He in the shell, and burns in a flash. This is called as the helium shell flash. The energy produced by the He burning causes the expansion of the above lying layers. Due to the expansion, the temperature decreases and ceases the hydrogen burning in the shell, and the strong convection zone develops between the two shells. The energy production by the He-shell flash lasts only for few years. Now, the above lying layers contract. The temperature increases due to the contraction and re-ignites the H-shell, and the cycle begins again. After each thermal pulse, the convection zone between the two shells brings up newly synthesized elements, both from the H- and He-shell burning, to the surface, such as the $triple - \alpha$ processed carbon, the $s - process$ elements, and also sometimes the material from the core, to the outer layers. This is referred to as the *third dredge-up* (TDU). The thermal pulses are also responsible for the the mass loss on the AGB phase. The star ends the AGB phase by a huge mass loss, 10^{-7}-10^{-4} $M_{\odot}$ yr^{-1}, loosing most of the H-rich material in the envelope. The star evolves on a faster timescale to higher temperatures with constant luminosity. When the temperature of the star is high enough, that is about 30000 K, it ionizes the expanded circumstellar material. And, the star becomes a *planetary nebula* (PN). The hot central star (thin He and H shells around the degenerate CO-core) starts cooling without having any nuclear energy source. The luminosity of the star decreases. The hot central star cools by radiating heat, and finally becomes a white dwarf. When all the heat content is lost, the star fades away. All the stars with initial masses less than $8M_{\odot}$ end their life as white dwarfs.

Until the end phases of their life, the stars remain H-rich. Only in the TP-AGB phase star looses its outer envelope to some extent, through mass loss events. A scenario that can get rid of the thin hydrogen rich outer shell of the star on the white dwarf cooling track, with a degenerate CO-core surrounded by a thin He- and H-shells, may possibly make the star H-deficient. It is also important that the scenario should explain the high abundances of carbon besides the H-deficiency. To explain the formation of H-deficient supergiants, there are two proposed scenarios, which are discussed in detail in the following section.

1.3 Origin and evolution of H-deficient supergiants

There are two proposed scenarios for the formation of H-deficient supergiants: RCBs/HdCs/EHes. One is the double degenerate (DD) scenario, that involves the merger of two white dwarfs, and the other is the final flash (FF) scenario, that involves a single post-AGB star experiencing the final helium shell flash.

DD scenario

The DD scenario was proposed by Webbink (1984). In this scenario, a helium white dwarf merges with a carbon–oxygen (CO) white dwarf (Iben & Tutukov 1985; Iben et al. 1996; Webbink 1984). The close white dwarf binary results from mass exchange and mass loss of a binary system as it evolves from a pair of main-sequence stars. The final step to the merger is driven by loss of angular momentum by gravitational waves (Renzini 1979). A merger of these two white dwarfs, having a very thin H-rich layer, makes the resulting star H-deficient (see Figure 1.4). A merger of two helium white dwarfs is also proposed for the origin of the RCB stars (Zhang & Jeffery 2012), and the relatively C-poor EHe stars with high surface gravity (Jeffery & Saio 2002).

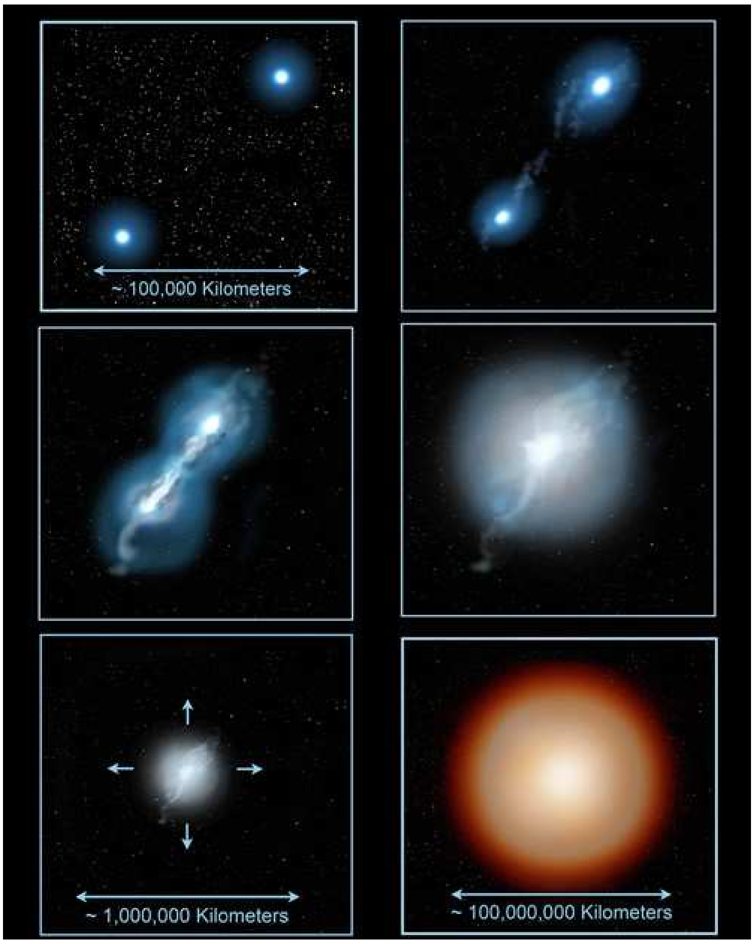

FIGURE 1.4: The two main sequence stars evolving in a binary system, and finally transforming into a H-deficient supergiant by merging in their white dwarf phases, is illustrated in the figure. Courtesy: www.gemini.edu.

For the formation of an RCB star, mass of the merged star should not be $> 1.4M_{\odot}$. Iben et al. (1996) have determined that the merger product of a $0.6\mathrm{M}_{\odot}$ CO white dwarf with a $0.3\mathrm{M}_{\odot}$ helium white dwarf immediately becomes a red supergiant in the RCB domain.

FF scenario

The FF scenario was proposed by Renzini (1979). This scenario involves a single post-AGB star, on the white dwarf cooling track, experiencing a final helium shell flash. The helium flash causes the H-rich envelope to be ingested by the He shell.

The result is that the star becomes a H-deficient supergiant for a brief period. The energy released by the He-flash inflates the star to supergiant dimensions, resulting in reducing its effective surface temperature. This makes the star to move to the right on the HR-diagram and becomes an AGB star for the second time in its evolution. Hence, these stars are also known as 'born-again AGB stars' (Renzini 1990), (see Figure 1.3). Examples of the 'born-again AGBs' are Sakurai's Object (Asplund et al. 1997b; Pavlenko et al. 2004), V605 Aql (Clayton & De Marco 1997; Lundmark 1921), and FG Sge (Gonzalez et al. 1998).

1.4 Investigating the Origin of H-deficient supergiants

The key to reveal the origin of the H-deficient supergiants (RCB/HdC/EHe) is to study their surface chemical composition using high-resolution spectra. The high-resolution spectroscopic studies of these H-deficient supergiants are being carried out since the discovery of R CrB. The comprehensive studies of RCB/HdC/EHe stars by: Asplund et al. (2000); Berman (1935); Clayton (1996); Cottrell & Lambert (1982); Feast (1975); Heber (1986); Jeffery (1996); Lambert & Rao (1994); Pandey (2006); Pandey et al. (2001); Schoenberner (1975); Warner (1967) and others, have played a significant role in understanding their chemical composition, and hence, their origin and evolution.

As discussed above, in these stars carbon is the most abundant element next to helium. The continuous opacity in the optical spectra of RCB stars is predicted to arise from the photoionization of neutral carbon from highly excited states (Asplund et al. 2000). Hence, the strengths of the C I lines from these excitations are predicted to be insensitive in the spectra of the RCB stars. This prediction is also supported by the observations: similar strengths of the C I lines are observed in the optical spectra of the RCB stars with different stellar parameters, while the strengths of the other metal lines varies from star to star, as shown in the Figure 1 of Rao & Lambert (1996). However, the predicted strengths of the C I lines are much stronger than their observed strengths. The correction of a factor of four or about 0.6 dex, is required to match the predicted line strength with that of the observed. This discrepancy was identified by Asplund et al. (2000), and they dubbed this as the 'carbon problem'. A similar carbon problem was also shown by the [C I] lines in RCB stars (Pandey et al. 2004). However, the carbon abundances for the EHe stars are known by the direct measurement, as the chief continuum opacity source at the EHe effective temperatures is helium. Since RCB/HdC and EHes are thought to be related objects, the carbon abundances derived from EHe stars were adopted for the RCB/HdC stars. Note that, the carbon abundances from C I lines for RCB/HdC stars are dependent on the adopted model's carbon abundance input, and are not yet known. Knowledge of carbon abundances in RCB stars will be a potential clue to their origin.

The other potential clue would be the determination of $^{12}C/^{13}C$ ratios. For the merger scenario, high values of the $^{12}C/^{13}C$ ratios are expected as the carbon is mostly coming from the He-shell of the CO white dwarf that is produced by the *triple*-α process. Nevertheless, low $^{12}C/^{13}C$ ratios are expected for the FF-objects. In the FF scenario, due to the ingestion of H-rich layer by the He-shell, ^{13}C is freshly produced by the operation of the CNO-cycle. Hence, the $^{12}C/^{13}C$ ratio reaches the equilibrium value of 3.4 in the He-shell after ingesting the H-rich layer.

The clues to the origin of these stars were provided by the discoveries of high abundances of ^{18}O relative to ^{16}O (or the low value of $^{16}O/^{18}O$ ratio) and the high abundances of fluorine. The high abundance ratios of ^{18}O relative to ^{16}O are determined for the cool RCBs and HdCs by the analyses of CO bands in their infrared spectra (Clayton et al. 2007, 2005; García-Hernández et al. 2009, 2010). The low values of $^{16}O/^{18}O$ determined for these stars are several magnitudes lower than that measured in the solar neighborhood. The value of $^{16}O/^{18}O$ in the solar neighborhood is about 500 (Scott et al. 2006). These high ^{18}O abundances relative to ^{16}O are expected to be produced only at high temperatures of about 1-2 $\times$ 10^8 K, such as the base of the accreted envelope of the merged product (Clayton et al. 2007). The abundances of fluorine in the RCB (Pandey et al. 2008) and EHe stars (Pandey 2006) were determined using the F I lines. The fluorine abundances in RCB and EHe stars are about 800-8000 times higher than that expected for their metallicities (Pandey 2006; Pandey et al. 2008). These high abundances of fluorine in RCB/EHe stars are as expected for the merger scenario or DD scenario (Menon et al. 2013). Hence, the derived chemical composition of RCB/HdC/EHe stars suggest DD scenario for their origin.

Knowing the position of a star on the HR-diagram gives us an idea about its evolution and possibly its origin. As discussed in section 1.1, the distances are not known for any of the Galactic H-deficient stars. To place the H-deficient stars on the HR-diagram, the best way would be to search for these stars in the Galactic globular clusters that have well represented HR-diagram. Note that, apriori knowledge of the distance to the cluster is not an issue as the cluster's stars are at the same distance from us. Discovery of even a single RCB/HdC star in a globular cluster would be of great help in understanding their evolution and origin. Hence, a survey is needed to identify new H-deficient stars in the Galactic globular clusters. For conducting the survey of this kind, the obvious choice would be the brightest globular cluster ω Cen as the potential target.

1.5 Globular Cluster ω Centauri

The globular cluster ω Centauri is one of the most massive and the brightest globular clusters in the Galaxy. The physical and structural parameters of ω Cen are given in Table 1.1.

Table 1.1: The physical and structural parameters ω Cen

Parameters		Reference[a]
Coordinates($J2000$)	RA:13 26 47.24, Dec:−47 28 46.5	(1)
Galactic longitude and latitude (in degrees)	l:309.10, b:14.97	(1)
Apparent magnitude (v)[b]	3.68	(1)
Absolute visual magnitude	-10.26	(1)
Distance from Sun(kpc)	4.8	(2)
Distance from Galactic center (kpc)	6.4	(1)
Mass ($M_\odot$)	2.5×10^6	(2)
Number of stars	10^6	(2)
Age (years)	12×10^9	(3)
Radial velocity (km s^{-1})	+232	(1)
Core radius (arcmin)	2.37	(1)
Mean Metallicity	−1.73	(3)

Notes.
[a] References: (1) Harris (1996), (2) van de Ven et al. (2006), (3) Calamida et al. (2009)
[b] Integrated v magnitude of the cluster

In general, the globular cluster stars are expected to be of uniform metallicity. The assumption is that the stars in a globular cluster are formed from the same material and at about the same time . However, some globular clusters show a range in their metallicity, for example globular cluster ω Cen. The wide spread in the metallicity of ω Cen red giants was discovered by Dickens & Woolley (1967) by their photometric studies. This spread in metallicity in the ω Cen red giants is also confirmed by the photometric studies of Calamida et al. (2009); Lee et al. (1999); Pancino et al. (2000); Rey et al. (2004); Sollima et al. (2005) and the spectroscopic studies of Freeman & Rodgers (1975); Norris & Da Costa (1995); Norris et al. (1996); Smith et al. (2000); Suntzeff & Kraft (1996). The range in the observed metallicity of the ω Cen red giants is: $-2.5 < [Fe/H] < +0.5$, with a mean metallicity of $[Fe/H] = -1.7$. Within this metallicity range, by Calamida et al. (2009), about four distinct subpopulations are identified: $[Fe/H] \leq -1.5$ (metal poor), $-1.49 < [Fe/H] < -0.9$ (metal-intermediate), $-0.95 < [Fe/H] < -0.15$ (metal-rich), and $[Fe/H] \sim 0$ (solar metallicity). A similar spread in metallicity is also observed in the subgiant branch (SGB) and the main sequence turn-off (MSTO) stars of ω Cen (Hilker et al. 2004; Sollima et al. 2005; Stanford et al. 2006). The giants with a large range in the metallicities also show an enhancement in the α-elements, [α/Fe] $\sim +0.3 - +0.5$. and this [α/Fe] is flat as a function of [Fe/H] in the range: [Fe/H]$=-2.0$ to -0.7 (Norris & Da Costa 1995). It is observed that the abundances of *s*-process elements in the giants of ω Cen increase with increasing metallicity (Norris & Da Costa 1995; Smith et al. 1995). There exists a set of red giants with strong CO-band in their observed spectra. The dichotomous distribution of CO band strengths: the weak and the strong, in the giants of ω Cen is in strong contrast to the other clusters (Norris & Da Costa 1995).

About 16%−17% of the main sequence (MS) and main sequence turn-off (MSTO) stars are enhanced in carbon and nitrogen (Stanford et al. 2007). There are two observed main sequences in ω Cen: the blue main sequence (bMS) and the red main sequence (rMS). These were discovered by Anderson (1997), and were further confirmed by Bedin et al. (2004); Norris (2004). They also hypothesized that, the stars in the bMS may be enriched in helium abundance. From the studies of Norris (2004); Piotto et al. (2005), it was confirmed that the bMS stars were enriched in helium upto Y $\sim$ 0.38, with the range: ($0.35 < Y < 0.4$). Piotto et al. (2005) also found that the bMS stars are less metal poor than the rMS stars, which is not as expected. Dupree & Avrett (2013); Dupree et al. (2011) have discovered the helium enriched red giants in ω Cen by analyzing the He I line at 1.08μm in the stars' infrared spectra. These are some of the abundance anomalies observed in ω Cen, that needs to be addressed.

The presence of the helium enhanced main sequence stars, bMS, and the helium enhanced red giants in ω Cen strengthens our suspicion of the presence of H-deficient stars in ω Cen. In addition to this, the discovery of a H-deficient hot post-AGB star ZNG 1 in the globular cluster M5 also supports our suspicion (Dixon et al. 2004). Some of the proposed scenarios for the origin of the observed abundance anomalies in ω Cen are discussed below.

There are three scenarios in contention for the origin of observed abundance anomalies in ω Cen: (a) the abundance anomalies could be due to the accretion of the material from the AGB stars through stellar winds, or from the ejecta of supernova Ia and II (Norris & Da Costa 1995), (b) the material with which these stars are formed might have been polluted by the material from the AGB stars and supernova Ia and II (Piotto et al. 2005), and (c) ω Cen may possibly be the remnant core of a tidally disrupted dwarf galaxy, that was captured by Milky Way (Freeman 1993; Ideta & Makino 2004; Zinnecker et al. 1988). The tidal stripping scenario is found to account for many of the observed abundance anomalies in ω Cen than the other two scenarios (Johnson & Pilachowski 2010; Norris 2004; Norris & Da Costa 1995; Piotto et al. 2005). Hence, the tidal stripping scenario is the most favored over the others.

1.6 Aim of the thesis

Our aim is to investigate the origin and evolution of the H-deficient supergiants. Knowing the position of a star on the HR-diagram is a potential clue to understand its evolution and possibly its origin. The HR-diagram is well studied for the stars in globular clusters. Hence, to locate the H-deficient supergiants on the HR-diagram, a spectroscopic survey needs to be conducted for a sample of red giants in the globular cluster, ω Cen. The H-deficient giants in ω Cen will be identified by analyzing the (0, 0) MgH band and the Mg *b* lines in the observed spectra of the sample. The results of our spectroscopic survey will be compared with our predictions of the number of H-deficient stars, formed by the DD and FF scenario, in ω Cen.

The origin and evolution of the H-deficient stars, the Galactic RCB/HdC will be investigated by determining the carbon abundances and the $^{12}C/^{13}C$ ratios from the C_2 Swan bands using their high-resolution spectra. The carbon abundances and the $^{12}C/^{13}C$ ratios are potential clues to the origin of these stars, and are not available. The carbon abundance and the $^{12}C/^{13}C$ ratio will be derived for the FF-object, V4334 Sgr, for comparison with the Galactic RCB/HdC stars.

The outline of the thesis is given below:

A brief introduction on H-deficient stars and the globular cluster ω Cen is presented in this Chapter.

Chapter 2 deals with the sample selection and the methodology adopted for the survey to identify H-deficient stars in ω Cen.

The analyses of the program stars' observed spectra selected for our survey are described in Chapter 3.

Chapter 4 describes our predictions of the number of H-deficient stars formed by the DD and FF scenario in the globular cluster ω Cen, and also in the Galaxy for comparison.

In Chapter 5, the analyses of C_2 Swan bands in the spectra of Galactic RCB/HdC stars, and the FF-object, V4334 Sgr (Sakurai's Object), for determining the carbon abundances and the $^{12}C/^{13}C$ ratios, are discussed.

The conclusions, and the scope for future works are discussed in Chapter 6.

Chapter 2

Sample Selection, Methodology and Observations

Our survey for identifying the hydrogen-deficient (H-deficient) stars in the globular cluster ω Centauri was based on the Strömgren photometric studies of Calamida et al. (2009) of the red giant stars in ω Cen. The characteristics of the known H-deficient stars, such as the metal rich appearance of their spectra, and the distinct (J_0-H_0) and (H_0-K_0) colours, were applied to select the potential H-deficient candidates from the sample of red giants in ω Cen. The methodology, the sample selection, the observations and the data reduction procedures are discussed in detail in the following sections.

2.1 Sample Selection

Using the narrow band photometric technique also known as the Strömgren photometry (discussed in 2.1.1), Calamida et al. (2009) have determined the metallicities for the red giant stars in ω Cen. They provide the metallicity estimates for the largest sample of about 4000 red giants in ω Cen. Our spectroscopic survey for identifying H-deficient stars in the largest and the brightest globular cluster ω Cen is based on the dispersion in metallicity of its red giants.

The stars in a globular cluster are formed at the same time and by the same cloud of gas. Hence, these are expected to be of same metallicity ([Fe/H]). There are a few Galactic globular clusters which show a large dispersion in their metallicities. One being the globular cluster ω Cen. The photometric (Calamida et al. 2009; Dickens & Woolley 1967; Lee et al. 1999; Pancino et al. 2000; Rey et al. 2004; Sollima et al. 2005) and the spectroscopic (Freeman & Rodgers 1975; Johnson & Pilachowski 2010; Norris & Da Costa 1995; Norris et al. 1996; Smith et al. 2000; Suntzeff & Kraft 1996) studies of ω Cen red giants have confirmed a large spread in their metallicity: $-2.5 <$ [Fe/H] $< +0.5$. This spread in metallicity, which is not as expected for a globular cluster, is taken as a clue for the presence of H-deficient stars in ω Cen. Note that the spectra of H-deficient supergiants: the RCB and the HdC stars, due to the less continuum absorption by carbon than by hydrogen in normal stars, appear metal rich than they actually are. Hence, our suspicion was that the metal rich giants of ω Cen may possibly be H-deficient. In this survey the priority was given to the giants in the metallicity range: $-0.5 >$ [Fe/H] $<$ $+0.5$. However, for the sake of the completeness of the survey, irrespective of the metallicity, all the giants, brighter than 14.5 y magnitude (Strömgren visual) were considered for our study.

The other criterion that was applied to increase the probability of finding H-deficient stars in our sample was the (J_0-H_0) and (H_0-K_0) (IR-colours) colours. The RCB and the HdC stars' distribution in the IR colour-colour plot is distinct from the normal dwarfs and giants (see Figure 2.1). This is mainly attributed to the infrared-excess (IR-excess) observed in RCB stars, due to the circumstellar dust formation. But, the HdC stars have little or no IR-excess, as they do not form the circumstellar dust and undergo optical declines. Hence, it is assumed that the HdC stars' IR-colours are intrinsic colours of the stars unaffected by the circumstellar emission (or absorption). The intrinsic stellar IR-colours of hydrogen-poor stars

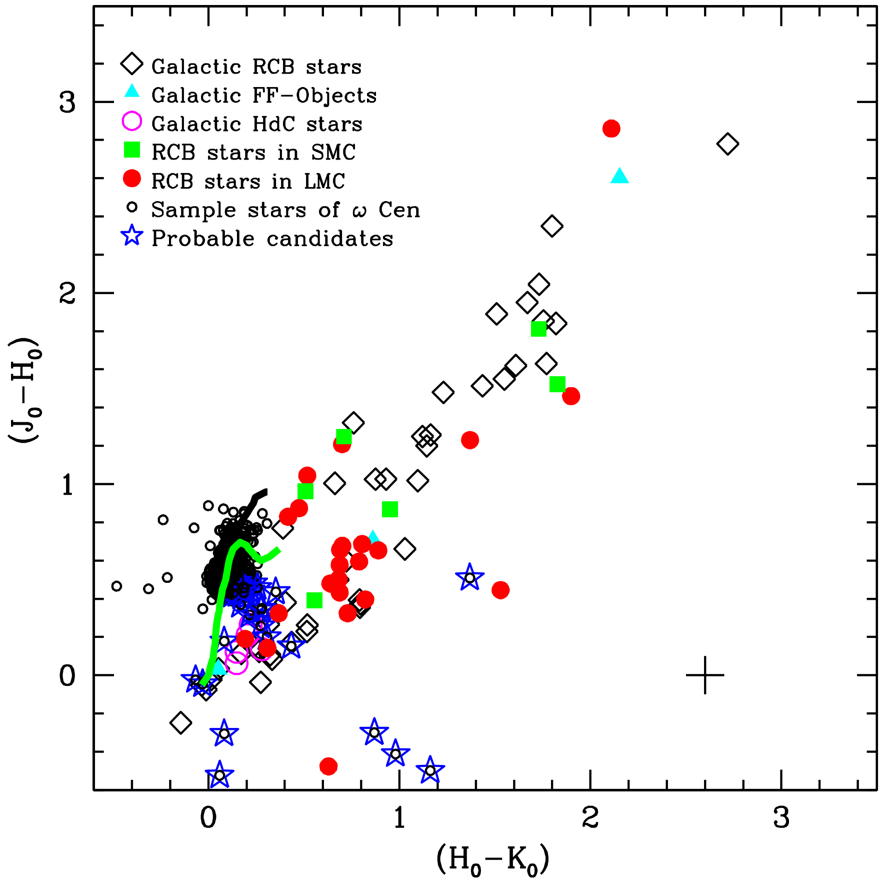

FIGURE 2.1: The (J_0-H_0) versus (H_0-K_0) colour diagram. The program stars along with the known RCB/HdC stars are represented. The program stars (belonging to all the metallicities and brighter than the y magnitude 14.5) are shown as black open circles. The most probable candidates which are having IR-colours similar to known RCB/HdC stars are shown as blue open stars. The black open diamonds are the Galactic RCB stars (Clayton 1996; Clayton et al. 2002, 2009; Hesselbach et al. 2003; Miller et al. 2012; Tisserand et al. 2013, 2008; Zaniewski et al. 2005), the red dots are the RCB stars in Large Magellanic Cloud (LMC) (Alcock et al. 2001; Clayton 1996; Jeffery et al. 1996; Tisserand et al. 2009), green filled squares are the RCB stars in Small Magellanic Cloud (SMC) (Kraemer et al. 2005; Morgan et al. 2003; Tisserand et al. 2004), magenta open circles are the Galactic HdC stars (Bidelman 1953; Goswami et al. 2010; Warner 1967), and the three filled cyan triangles are the final flash (FF) objects (Schönberner 2008). The expected position of the normal dwarfs and giants stars (Bessell & Brett 1988) are shown in green and black curve respectively.

are therefore near the blackbody line rather than to the left of it, as they are for normal hydrogen-rich stars. This is consistent with the fact that the colours of the normal stars fit models that have H^- as a major opacity source (Catchpole & Glass 1974; Feast 1997). In his detailed IR-photometric studies on the Galactic RCB stars, Feast (1997) has clearly explained that the position of a star on the (J_0-H_0) and (H_0-K_0) plot depends on the amount of the circumstellar dust formed around the star. The low or moderate infrared excess is observed in the stars which exhibit relatively low deep obscuration minima, hence the star appears relatively blue in the (J_0-H_0) and (H_0-K_0) plot, for example RCB stars of LMC.

Hence, we constrained the sample by selecting all the stars, irrespective of their metallicity, having RCB IR-colours.

2.1.1 Narrow Band Photometry

The photometry with a band width less than 90Å is referred to as the narrow band photometry or the Strömgren photometry. The u, v, b and y are the Strömgren magnitudes with the mean wavelengths at 3500, 4110, 4670 and 5470Å respectively. The intensity measured in these bands are used to derive the three indices, namely, the colour index, $b-y$, the Balmer discontinuity index, c_1, and the metal-line index, m_1 (Strömgren 1966). The c_1 and the m_1 indices are defined by,

$$c_1 = (u - v) - (v - b)$$
$$m_1 = (v - b) - (b - y)$$

These indices are affected by interstellar reddening. By applying the extinction corrections from Whitford (1958),

$$E(c_1) = 0.20\ E(b - y)$$
$$E(m_1) = -0.18\ E(b - y)$$

The reddening corrected colour and metallicity indices are defined as,

$$[c_1] = c_1 - 0.20(b - y)$$
$$[m_1] = m_1 + 0.18(b - y)$$

2.2 Data collection and Observations

For identifying the red giants of ω Cen, Calamida et al. (2009) have adopted the data set that includes the stars mostly in the periphery of the cluster. However, their data sets also include the stars from the cluster center. They have applied several criteria to exclude the field stars from the cluster stars. Their confirmed red giant sample of ω Cen includes only the giants with the membership probabilities higher than 65%, obtained from proper motion studies. We have adopted their confirmed red giant sample of ω Cen, excluding the giants in the core of the cluster, to avoid confusion in identifying the giants in this crowded field, for our study. For the sample stars, we have adopted the identifications given by Calamida et al. (2009) in their study. From their studies, the y magnitude, XY-offsets of the stars from the center of the cluster, $(b - y)$, m_1 index and [Fe/H] derived by their calibrations were provided (private communication). For our observations, the XY-offsets of the stars were converted into Right Ascensions (RA) and Declinations (Dec) using the standard conversion tool given by NASA/IPAC Extra Galactic Database (NED)[1].

The giants brighter than 14.5 y magnitude in the metallicity range: +0.5 > [Fe/H] > −2.5, are about 1221. To further constrain the sample, the most probable candidates were selected by their (J_0-H_0) and (H_0-K_0) colours. The J, H and K magnitudes are from the Two Micron All Sky Survey (2MASS) Catalogue[2]. A search for the J, H, and K magnitudes for the program star's given co-ordinates

[1] http://ned.ipac.caltech.edu/
[2] http://irsa.ipac.caltech.edu/Missions/2mass.html

(RA and Dec), the 2MASS Catalogue returns the values for all the nearby stars within a radius of 10 arcseconds to the program star. To identify the J, H, K values corresponding to the program star's coordinates, the ALADIN interactive sky atlas[3] (Bonnarel et al. 2000) was used to obtain the sky map for the required star's field. By comparing our calculated star's coordinates with the coordinates given in the 2MASS Catalogue, the program star was identified in the ALADIN interactive sky map within an accuracy of RA=±0.3 seconds, and Dec=±3.0 arcseconds, and hence, confirmed. The corresponding J, H and K values from the 2MASS Catalogue were adopted for the identified and confirmed program star. For each of the program star the Galactic dust reddening and the extinctions in the line of sight were retrieved from NASA/IPAC Infrared Science Archive[4]. Applying the extinction corrections to J, H and K magnitudes, the IR colours, (J_0-H_0), (H_0-K_0) and (J_0-K_0) were calculated. Similarly, the J, H and K magnitudes and the extinction corrections were also obtained for the known Galactic RCB stars. All the program stars that are brighter than y magnitude of 14.5 were plotted on the (J_0-H_0) and (H_0-K_0) plane along with the known RCB and HdC stars. Figure 2.1 shows the plot of (J_0-H_0) versus (H_0-K_0) for the ω Cen giants along with the known Galactic RCB and HdC stars, and the RCB stars in Large Magellanic Cloud (LMC) and in Small Magellanic Cloud (SMC). Also plotted are the final flash (FF) objects. The ω Cen giants are shown as black open circles. The ω Cen giants that share the RCB/HdC IR-colours are shown as 'blue stars'. These 'blue stars' are the probable H-deficient candidates. The position of the normal dwarfs and the normal giants are represented by a thick green and a black line, respectively.

Note that, for observations, we selected all the metal rich giants ($+0.5 >$ [Fe/H] $>$ -0.5), irrespective of their (J_0-H_0) and (H_0-K_0) colours – these are about 130 in number. However, the metal poor giants ($-0.5 >$ [Fe/H] > -2.5), selected for observations have (J_0-H_0) and (H_0-K_0) colours like RCB stars – these are about 40 in number. Though, the sample of red giants from the core of ω Cen were

[3]http://aladin.u-strasbg.fr/

[4]http://irsa.ipac.caltech.edu/applications/DUST/

not included in our sample, many of the giants in the periphery were double or multiple objects. The giants which were not clearly resolved were excluded from our observations. Hence, only about 34 of the 130 metal rich stars and about 11 of the 40 metal poor stars were selected for observations, which are well resolved. The y magnitude, [Fe/H], and the coordinates (RA and Dec) of these giants selected for observations are given in Table 2.1.

Low-resolution optical spectra for these selected red giants of ω Cen were obtained from Vainu Bappu Observatory, Kavalur. The spectra were obtained using the 2.34 m Vainu Bappu Telescope (VBT) equipped with the Optomechanics Research (OMR) Spectrograph (Prabhu et al. 1998) and 1K $\times$ 1K CCD. The spectra were obtained using the 600 l/mm grating centered near Hα line at 6563Å. The 600 l/mm grating covers about 2500Å with a resolution of about 8Å. The wavelength span of our observed spectra is 4900 – 7500Å. The log of the observations is given in Table 2.2.

TABLE 2.1: The selected stars for observations.

Star	**y**	**[Fe/H]**	**RA**	**Dec**
107712	14.2	0.720	13 26 19.448	-47 23 34.871
112777	14.5	-0.097	13 26 21.518	-47 23 16.253
113294	12.5	-0.398	13 26 21.680	-47 30 20.521
113435	13.0	-0.219	13 26 21.770	-47 26 16.114
114047	14.2	0.807	13 26 22.023	-47 26 08.970
131105	12.7	-0.281	13 26 29.384	-47 32 25.875
135901	13.4	0.165	13 26 31.811	-47 32 04.871
140641	14.0	-0.143	13 26 34.248	-47 32 38.523
148292	14.5	0.108	13 26 38.226	-47 23 08.584
153402	13.2	0.882	13 26 40.767	-47 36 43.598
166240	12.9	0.421	13 26 47.244	-47 34 12.336
170311	12.7	0.155	13 26 49.302	-47 33 51.011

Table 2.1 – continued from previous page

Star	y	[Fe/H]	RA	Dec
172980	12.6	-0.310	13 26 50.707	-47 37 01.083
178243	12.4	-0.324	13 26 53.351	-47 36 34.922
178691	12.0	-0.334	13 26 53.550	-47 31 58.332
193804	12.7	-0.360	13 27 00.792	-47 25 17.620
197946	14.2	-0.331	13 27 02.810	-47 24 02.138
205105	14.0	-0.332	13 27 06.343	-47 25 01.430
214247	13.3	-0.448	13 27 11.034	-47 26 21.219
216815	13.4	0.347	13 27 12.378	-47 29 04.029
219549	12.6	0.198	13 27 13.861	-47 34 17.988
221120	13.6	-0.232	13 27 14.584	-47 23 51.293
233832	14.3	0.592	13 27 21.513	-47 25 55.332
243759	14.5	-0.119	13 27 27.033	-47 30 21.544
244157	13.6	0.079	13 27 27.296	-47 30 52.948
250000	13.2	0.241	13 27 31.356	-47 24 15.584
251701	13.3	0.069	13 27 33.198	-47 23 47.959
262788	13.0	0.012	13 27 53.714	-47 24 43.309
269309	13.0	-0.062	13 28 19.644	-47 24 57.866
270931	12.4	0.104	13 28 33.801	-47 27 22.113
271054	13.4	-0.329	13 28 35.599	-47 26 01.506
40867	13.4	0.073	13 25 42.187	-47 33 44.749
5001638	12.8	0.324	13 27 01.308	-47 39 47.142
73170	12.8	-0.217	13 26 03.935	-47 26 54.105
205399	14.3	-0.981	13 27 06.552	-47 35 38.565
5004102	14.0	-0.558	13 27 46.501	-47 31 38.248
46903	14.4	-1.643	13 25 46.825	-47 27 41.204
265450	14.0	-0.987	13 28 02.021	-47 29 56.240
77368	13.7	-1.339	13 26 06.341	-47 31 55.750

Table 2.1 – continued from previous page

Star	y	[Fe/H]	RA	Dec
109390	14.3	-1.799	13 26 20.052	-47 33 52.940
14943	12.8	-1.691	13 25 18.003	-47 33 27.609
250303	14.4	-0.949	13 27 31.697	-47 25 34.578
168636	13.5	-2.076	13 26 48.428	-47 24 05.318
264349	14.4	-0.844	13 27 58.238	-47 27 22.351
261069	13.8	-0.547	13 27 49.647	-47 28 36.584

Notes– Program star coordinates (J2000): Units of right ascension are hours, minutes, and seconds, and the units of declination are degrees, arcminutes, and arcseconds.

Table 2.2: The log of observations for the program stars.

Star	Date of Observation	y	Exp. Time (in minutes)	S/N
107712	2011 April 12	14.2	20	15
112777	2011 April 13	14.5	30	15
113294	2011 April 08	12.5	15	25
113435	2011 March 11	13.0	20	30
114047	2011 May 07	14.2	20	20
131105	2011 March 11	12.7	20	80
135901	2011 April 07	13.4	20	30
140641	2011 May 07	14.0	20	10
148292	2011 April 13	14.5	25	20
153402	2011 April 08	13.2	20	20
166240	2011 March 11	12.9	20	60
170311	2011 March 11	12.7	20	10
172980	2011 March 07	12.6	15×2	110
178243	2011 April 08	12.4	15	100

Table 2.2 – continued from previous page

Star	Date of Observation	y	Exp. Time (in minutes)	S/N
178691	2011 March 11	12.0	40	110
193804	2011 April 08	12.7	20	80
197946	2011 April 10	14.2	20	30
205105	2011 April 12	14.0	20	10
214247	2011 April 06	13.3	30	60
216815	2011 April 06	13.4	30	80
219549	2011 April 08	12.6	20	20
221120	2011 April 09	13.6	15	20
233832	2011 May 07	14.3	20	25
243759	2011 April 13	14.5	20	15
244157	2011 May 07	13.6	15	20
250000	2011 March 11	13.2	30	90
251701	2011 March 10	13.3	30	100
262788	2011 March 08	13.0	40	110
269309	2012 January 25	13.0	30	70
270931	2012 January 25	12.4	30	100
271054	2011 March 08	13.4	30	100
40867	2011 March 09/2012 January 25	13.4	40/30	110
5001638	2011 March 10	12.8	30	150
73170	2011 April 08	12.8	20	100
205399	2013 March 13	14.3	40	40
5004102	2013 March 12	14.0	40	40
46903	2013 April 11	14.4	40	50
265450	2013 April 12	14.0	40	40
77368	2013 March 11/2013 April 12	13.7	30/40	50
109390	2013 March 11	14.3	40	60

Table 2.2 – continued from previous page

Star	Date of Observation	y	Exp. Time (in minutes)	S/N
14943	2012 February 19	12.8	20	100
250303	2013 March 13	14.4	50	30
168636	2013 March 12	13.5	40	30
264349	2013 March 14	14.4	40	40
261069	2013 April 12	13.8	40	40

Table 2.3: The log of observations for the reference stars.

Star	Date of Observation	Exp. Time (in minutes)	S/N
Arcturus	2013 April 14	200msec	400
GU Sgr	2011 May 10	15	300
HD 137613	2011 May 08	05	150
HD 182040	2011 May 28	03	200
RS Tel	2011 May 10	15	150
RT Nor	2011 May 08	15	200
RY Sgr	2011 May 29	01	200
UX Ant	2012 January 25	30	150
V1783 Sgr	2011 May 06	10	150
V3795 Sgr	2011 May 29	40	150
V517 Oph	2011 May 09	10	150
V854 Cen	2012 January 25	0.50	250
V CrA	2011 May 10	07	150
VZ Sgr	2011 May 29	15	150
XX Cam	2011 February 19	05	150
Z UMi	2011 May 07	10	130

The spectra for known Galactic RCB and HdC stars, and the Galactic field giants, for example Arcturus, were also obtained for reference (see Table 2.3 for the log of observations).

Depending on the brightness of the stars, the program stars were observed with exposure times of about 15 to 50 minutes (see Table 2.2). Multiple exposures were obtained for some of the stars to improve the signal-to-noise of their spectra. The ALADIN interactive sky atlas was used to identify the program star in the field of the cluster, before the star was centered on the slit for observations. Also obtained were the bias/dark frames, and the flat-field frames to remove the bias/dark counts and the pixel-to-pixel variations of the CCD image, respectively. The FeNe lamp spectra were also obtained after or just before the exposures of the program stars to provide the wavelength calibration.

The data reduction procedures, spectrum extraction, and wavelength calibrations are discussed in the following sections.

2.3 Data Reduction

The data reduction is a process of extracting the one-dimensional spectrum from the raw spectrum image (object frame), recorded on the CCD produced by the spectrometer. The data reductions were carried out using the IRAF[5] (Image Reduction and Analysis Facility) software package. The data reduction involves: bias/dark subtraction, flat-fielding, spectrum extraction and wavelength calibration that is discussed below in detail.

[5]The IRAF software is distributed by the National Optical Astronomy Observatories under contract with the National Science Foundation.

2.3.1 Bias subtraction

Bias frames were obtained with a zero exposure time with the CCD camera shutter closed. The bias-level refers to the number of counts recorded in each pixel of the camera with zero exposure time and with camera shutter closed. These counts can be attributed to the DC voltage maintained in the camera electronics to bias the semiconductor and ensure that the analogue-to-digital converter always receives the positive signal. The bias frames were subtracted from the object frames (pixel by pixel) to remove the CCD detector's zero exposure counts. The dark frames were obtained with an exposure time equivalent to the exposure time of the program stars with the CCD camera shutter closed. In our observations, the dark frame counts were same as the bias frame counts, hence, no dark correction was applied.

Multiple bias frames were obtained on each observing night, and were averaged using the IRAF task *zerocombine* to obtain the master bias frame. The master bias frame is subtracted from all the object, the flat-field and the comparison lamp frames using the task *ccdproc*.

2.3.2 Flat-fielding

The quantum efficiency or the sensitivity of the CCD detector varies from pixel to pixel. To make the sensitivity uniform across the pixels, object frames were divided by a normalized flat-field frame. The flat field frames were obtained by observing the uniform light or the uniformly illuminated white screen. In our case dome flats were taken by observing the white screen that was illuminated uniformly by a Tungsten-Halogen Quartz lamp.

The flat-field frames were averaged using the task *flatcombine*, to obtain the master flat. The bias subtracted master flat-field frame was normalized using the task *response* or *apnorm*. All the bias subtracted object frames were then divided (pixel by pixel) by the normalized flat-field frame using the task *ccdproc*.

2.3.3 Spectrum Extraction

The spectrum extraction is an interactive process that involves, finding the aperture of the object, editing the aperture (centering and resizing), background subtraction, tracing the aperture along the dispersion axis, fitting the traced points using a polynomial function, and extraction of the one-dimensional spectrum from the spectrum image by adding the signal within the aperture of the target. The spectrum extraction process was carried out using the IRAF task *apall*.

2.3.4 Wavelength Calibration

For extracting the one-dimensional spectrum of the comparison obtained using FeNe lamp, we use the same procedure as described in section 2.3.3, however, same aperture tracing of the star's spectrum is adopted for tracing the recorded comparison spectrum. Using the task *identify*, the emission lines in the extracted comparison lamp spectrum were identified. For this purpose, we have used a chart of FeNe lamp spectra with lines identified. A dispersion relation was found by fitting a polynomial function i.e., the pixel numbers along the dispersion axis were converted into a spectrum wavelength calibrated. This dispersion relation determined from the comparison spectrum was then applied to the stellar spectrum, using the tasks *refspec* and *dispcor*, to provide us with wavelength calibrated spectrum. These wavelength calibrated program stars' spectra were then used for further analyses.

Chapter 3

The Spectrum Analysis and Results

3.1 Observed sample of ω Cen red giants

The observed optical spectra of the program stars, with the signal-to-noise ratio greater than 50 were analyzed. To carry out the analysis, the observed spectra of all the program stars were continuum normalized. The region of the spectrum (having maximum flux) free of absorption lines is treated as the continuum point, and a smooth curve passing through these points is defined as the continuum. The well defined continuum in the spectrum of the sample metal poor giant, and in the spectrum of Arcturus with very high signal-to-noise (S/N), is used as a reference for judging the continuum for the sample metal rich stars in the wavelength window 4900 - 5400Å including the Mg b triplet and the complete MgH band. Using the task *continuum* in the *specred* IRAF package, and using the polynomial function *spline*3 with order 5 to 8, the spectra of the program stars were normalized.

The prominent spectral features in the observed spectra of program stars, such as Hα: 6563Å, Na D lines: ∼5893Å, Mg b triplet: 5167.32Å, 5172.68Å, and 5183.60Å, (0, 0) MgH band: 5330 – 4950Å (Spinrad & Wood 1965; Whitford & Rich 1983), Fe I lines at 5265Å, 5300Å, 5325Å, 5370Å, Mg I lines at 5528Å, 5711Å, and 6313Å and several other metal lines were identified. Note that, the wavelength span of our observed spectra: 4900 – 7500Å, do not cover the CH-band or the G-band with the band head at about 4300Å. The preliminary analyses of the spectra were to examine the strength of the key features such as Hα line, C_2 Swan bands and neutral carbon lines. Note that, our observed spectra did not show any of the carbon features typical to RCB/HdC stars. Nevertheless, these observed spectra exhibit the characteristics of the typical red giants. We do notice the presence of strong Mg b lines and (0, 0) MgH band at about 5165Å in the metal rich ω Cen giants.

Based on the strengths of the Mg b lines and the MgH band in the observed spectra, three groups were identified in our sample:

1. The metal rich giants with strong Mg b lines and the strong MgH band (see Figure 3.1),

2. The metal poor giants with weak Mg b lines and no MgH band (see Figure 3.2), and

3. The metal rich giants with strong Mg b lines but no MgH band (see Figure 3.3).

These groups are discussed in detail in the following sections.

3.2 Determination of stellar parameters

Literature survey was done for the high-resolution spectroscopic studies of the program stars. Many of the program stars were found in Johnson & Pilachowski (2010), one of the largest high resolution spectroscopic studies of red giants stars of ω Cen. The stellar parameters: effective temperature ($T_{\rm eff}$), surface gravity

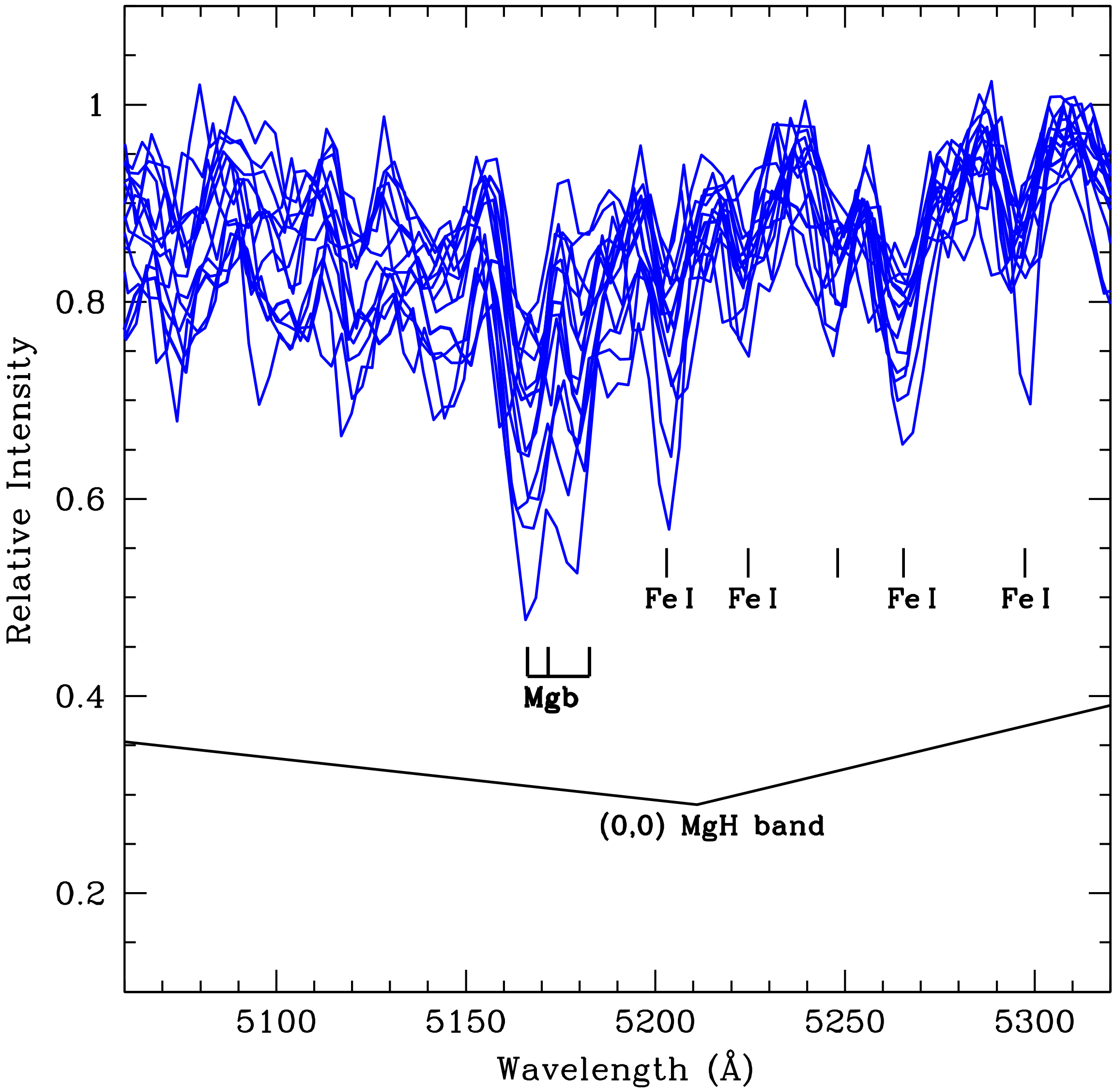

FIGURE 3.1: The spectra of stars, with strong Mg *b* lines and MgH band, belonging to the 1st group with the metallicity range: $-0.5 > [Fe/H] > -1.2$ (Johnson & Pilachowski 2010), are superposed. The key lines are marked. The vertical line marked is a blend of many atomic lines.

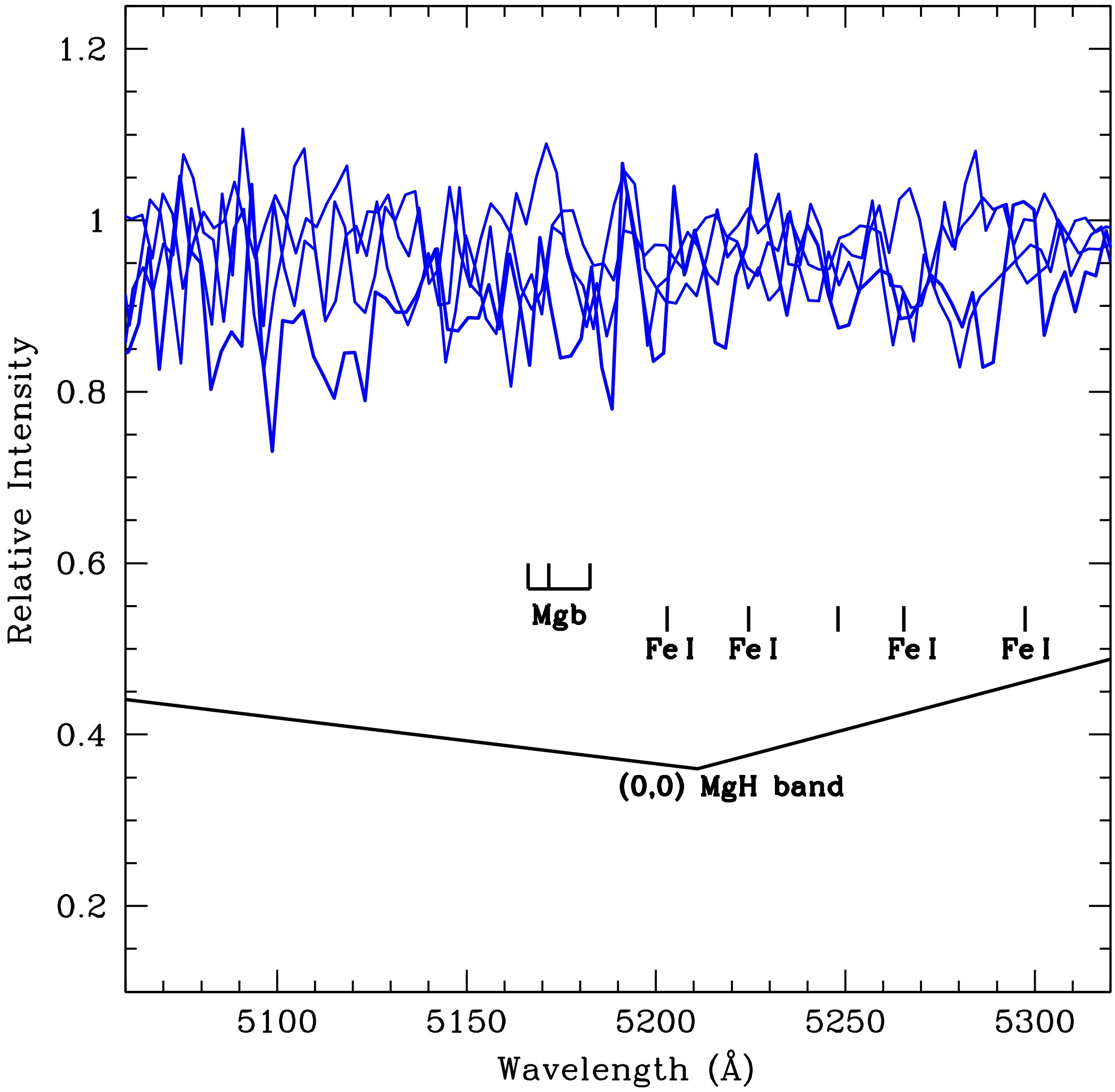

FIGURE 3.2: The spectra of stars, with weak Mg *b* lines and no MgH band, belonging to the 2^{nd} group with the metallicities: [Fe/H] < -1.7 (Johnson & Pilachowski 2010), are superposed. The key lines are marked. The vertical line marked is a blend of many atomic lines.

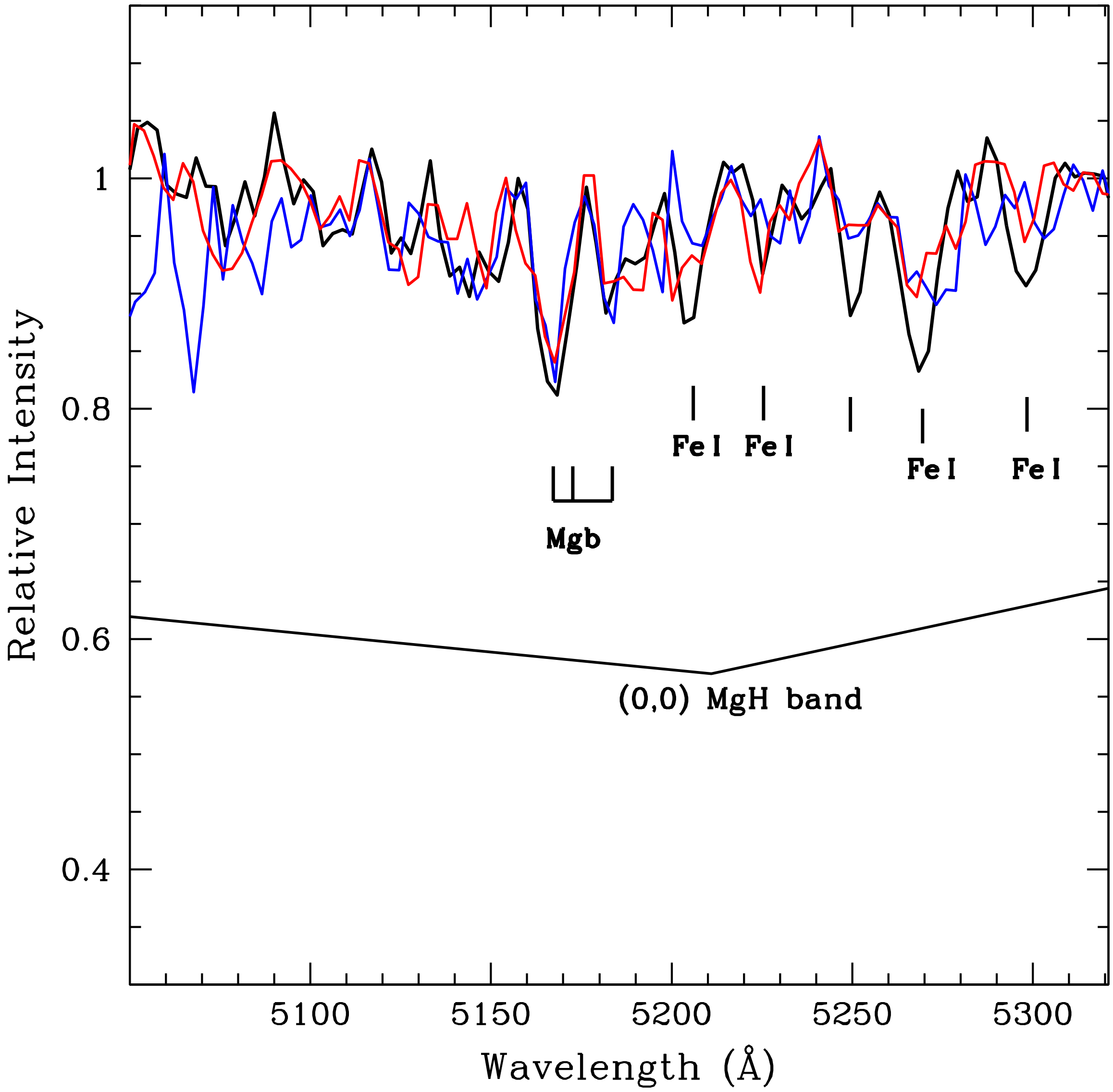

FIGURE 3.3: The spectra of the 3^{rd} group stars: 262788 (shown in black), 214247 (shown in blue), and 193804 (shown in red), with strong Mg *b* lines and no MgH band, are superposed. The metallicity of 262788 and 193804 is [Fe/H]=−1.0, and metallicity of 214247 is [Fe/H]=−1.5 (Johnson & Pilachowski 2010). The key lines are marked. The vertical line marked is a blend of many atomic lines.

($\log g$), and metallicity ([Fe/H]) for the program stars were adopted from Johnson & Pilachowski (2010). Note that, the metallicities determined by Calamida et al. (2009) for the stars in the metal rich regime are about 0.5 – 1.4 dex[1] higher than those determined by Johnson & Pilachowski (2010). However, the metallicity determinations for the metal poor stars from these two studies are matching.

The $T_{\rm eff}$ and $\log g$ for the program stars were also determined using their photometric colours: $(J_0 - H_0)$, $(J_0 - K_0)$, and $(b - y)$. The procedures followed to determine the $T_{\rm eff}$ and $\log g$ are discussed below.

3.2.1 Determination of effective temperature ($T_{\rm eff}$)

Using the empirical calibrations of $T_{\rm eff}$ versus colours and [Fe/H] by Alonso et al. (1999), the effective temperatures for the program stars were determined. For deriving these empirical relations, Alonso et al. (1999) have used a large sample of Galactic and globular cluster giants belonging to the spectral class of F0 to K0 with accurate photometric data. Alonso et al. (1999) have provided the calibrations for different colours and for a large metallicity range: $(+0.2 \geq [\rm Fe/H] > -3.0)$.

Using their calibrations, the $T_{\rm eff}$ for the program stars were determined:

$$\theta_{\rm eff} = a_0 + a_1 X + a_2 X^2 + a_3 X[\rm Fe/H] + a_4[\rm Fe/H] + a_5[\rm Fe/H]^2 \quad (1)$$

Where, X is the photometric colour, and in our study the three colours are $(J_0 - H_0)$, $(J_0 - K_0)$ and $(b - y)$. [Fe/H] is the star's Strömgren photometric metallicity derived by Calamida et al. (2009), and the a_0, a_1, a_2, a_3, a_4, and a_5 are the coefficients provided by Alonso et al. (1999) (see their Table 2). The $T_{\rm eff}$ i.e., $5040/\theta_{\rm eff}$, determined using these three colors are in agreement within ±200K.

[1] x dex=10^x

The photometric colours with y magnitudes and metallicities are given in Table 3.1. The temperatures determined from these colours are given in Table 3.2.

The IR-colors are less affected by reddening, marginally affected by line blanketing, and show less dependence on star's surface gravity (Alonso et al. 1999). Hence, the effective temperature determined by $(J_0 - K_0)$ colours with large wavelength difference compared to $(J_0 - H_0)$ and $(b - y)$ were given the preference. The $T_{\rm eff}$ for the program stars range from 3500 – 5000 K. The typical errors on $T_{\rm eff}$ of the red giant stars from the spectroscopic studies are about ±100K, as given by Johnson & Pilachowski (2010); Norris & Da Costa (1995); Reddy & Lambert (2005). These errors were adopted in our analyses by spectrum syntheses.

3.2.2 Determination of surface gravity (log g)

The log g is determined using the standard relation (Johnson et al. 2009),

$$\log(\mathrm{g}_*) = 0.40(M_{\rm bol.} - M_{{\rm bol},\odot}) + \log(\mathrm{g}_\odot) + 4(\log(T/T_\odot)) + \log(M/M_\odot)$$
— (2)

The bolometric correction to $M_{\rm v}$ was applied using the relation given by Alonso et al. (1999) and the distance modulus for ω Cen, $(m - M)_{\rm v} = 13.7$ (Johnson & Pilachowski 2010) is used. The mass of ω Cen red giants are assumed to be 0.8$\mathrm{M}_\odot$ (Johnson & Pilachowski 2010).

The surface gravities for the program stars were calculated for all the three temperatures determined from $(J_0 - H_0)$, $(J_0 - K_0)$ and (b−y) colours. These log g values determined are in agreement within ±0.2 (cgs units) (see Table 3.2). The log g of the program stars are in the range 0.5 - 2.3 (cgs units). In Figure 3.4, the program stars are shown on the $T_{\rm eff}$ and log g plane.

TABLE 3.1: The y magnitude, metallicity and colours for the program stars.

Star	**y**	**[Fe/H]**	$\mathbf{J_0\text{-}H_0}$	$\mathbf{J_0\text{-}K_0}$	**(b-y)**
107712	14.2	0.720	0.547	0.674	0.724
112777	14.5	-0.097	0.470	0.544	0.572
113294	12.5	-0.398	0.624	0.781	0.860
113435	13.0	-0.219	0.600	0.727	0.769
114047	14.2	0.807	0.578	0.722	0.729
131105	12.7	-0.281	0.689	0.826	0.877
135901	13.4	0.165	0.456	0.639	0.718
140641	14.0	-0.143	0.563	0.626	0.677
148292	14.5	0.108	0.500	0.582	0.623
153402	13.2	0.882	0.714	0.829	0.842
166240	12.9	0.421	0.627	0.779	0.805
170311	12.7	0.155	0.675	0.841	0.857
172980	12.6	-0.310	0.733	0.901	0.979
178243	12.4	-0.324	0.769	0.956	0.993
178691	12.0	-0.334	0.701	0.909	0.976
193804	12.7	-0.360	0.693	0.805	0.841
197946	14.2	-0.331	0.527	0.662	0.678
205105	14.0	-0.332	0.582	0.706	0.696
214247	13.3	-0.448	0.433	0.618	0.725
216815	13.4	0.347	0.459	0.648	0.670
219549	12.6	0.198	0.706	0.847	0.871
221120	13.6	-0.232	0.647	0.816	0.864
233832	14.3	0.592	0.569	0.702	0.716
243759	14.5	-0.119	0.459	0.549	0.613
244157	13.6	0.079	0.547	0.672	0.690
250000	13.2	0.241	0.658	0.781	0.814
251701	13.3	0.069	0.641	0.773	0.774

Table 3.1 – continued from previous page

Star	**y**	**[Fe/H]**	**J_0-H_0**	**J_0-K_0**	**(b-y)**
262788	13.0	0.012	0.632	0.716	0.806
269309	13.0	-0.062	0.760	0.985	0.976
270931	12.4	0.104	0.562	0.686	0.769
271054	13.4	-0.329	0.639	0.811	0.804
40867	13.4	0.073	0.712	0.843	0.889
5001638	12.8	0.324	0.497	0.624	0.718
73170	12.8	-0.217	0.727	0.920	0.951
205399	14.3	-0.981	0.487	0.589	0.623
5004102	14.0	-0.558	0.200	0.507	0.569
46903	14.4	-1.643	0.412	0.568	0.603
265450	14.0	-0.987	0.478	0.590	0.619
77368	13.7	-1.339	0.341	0.616	0.629
109390	14.3	-1.799	0.316	0.532	0.598
14943	12.8	-1.691	0.550	0.608	0.692
250303	14.4	-0.949	0.464	0.585	0.602
168636	13.5	-2.076	0.481	0.716	0.658
264349	14.4	-0.844	0.449	0.553	0.591
261069	13.8	-0.547	0.422	0.546	0.584

TABLE 3.2: The T_{eff} and $\log g$ for the program stars

Star	$\mathbf{T_{eff}(J_0\text{-}H_0)}$	$\mathbf{T_{eff}(J_0\text{-}K_0)}$	$\mathbf{T_{eff}(b\text{-}y)}$	$\mathbf{\log g(J_0\text{-}H_0)}$	$\mathbf{\log g(J_0\text{-}K_0)}$	$\mathbf{\log g(b\text{-}y)}$
107712	4400.872	4453.557	4630.903	1.981	2.017	2.133
112777	4800.609	4865.870	4936.046	2.313	2.347	2.382
113294	4258.411	4175.822	4102.612	1.187	1.125	1.064
113435	4325.308	4309.994	4313.325	1.441	1.428	1.433
114047	4284.442	4323.013	4640.952	1.864	1.893	2.108
131105	4054.841	4072.346	4079.067	1.097	1.113	1.120
135901	4828.548	4555.554	4510.395	1.920	1.765	1.735
140641	4446.204	4595.016	4570.263	1.910	2.002	1.988
148292	4655.851	4735.414	4801.490	2.252	2.296	2.332
153402	3881.928	4065.697	4334.876	1.099	1.289	1.510
166240	4180.004	4180.590	4327.843	1.292	1.293	1.406
170311	4063.935	4039.404	4164.331	1.124	1.100	1.211
172980	3934.781	3914.774	3907.473	0.971	0.951	0.942
178243	3842.037	3809.727	3886.536	0.772	0.729	0.824
178691	4023.659	3898.973	3910.987	0.793	0.665	0.677
193804	4047.647	4119.744	4142.210	1.092	1.156	1.173

Table 3.2 – continued from previous page

Star	$T_{eff}(J_0\text{-}H_0)$	$T_{eff}(J_0\text{-}K_0)$	T_{eff}(b-y)	$\log g(J_0\text{-}H_0)$	$\log g(J_0\text{-}K_0)$	$\log g$(b-y)
197946	4593.378	4487.850	4535.562	2.087	2.021	2.053
205105	4394.052	4365.390	4484.959	1.891	1.871	1.950
214247	4996.860	4619.744	4393.624	1.937	1.740	1.597
216815	4790.386	4528.745	4702.864	1.884	1.732	1.836
219549	3973.635	4026.435	4140.799	0.974	1.026	1.127
221120	4176.255	4094.727	4107.673	1.559	1.490	1.504
233832	4344.487	4376.158	4619.778	1.958	1.980	2.143
243759	4849.773	4848.184	4780.835	2.352	2.352	2.316
244157	4482.474	4459.225	4575.071	1.771	1.754	1.827
250000	4105.543	4175.822	4273.482	1.332	1.393	1.469
251701	4171.935	4194.984	4342.479	1.440	1.461	1.571
262788	4204.475	4338.775	4257.273	1.343	1.442	1.383
269309	3850.724	3757.561	3925.253	1.016	0.889	1.098
270931	4426.690	4419.946	4360.862	1.260	1.254	1.216
271054	4206.990	4106.046	4221.619	1.526	1.442	1.535
40867	3967.300	4035.068	4089.323	1.287	1.356	1.405
5001638	4640.431	4601.165	4545.270	1.583	1.559	1.525

Table 3.2 – continued from previous page

Star	**T$_{\mathrm{eff}}$(J$_0$-H$_0$)**	**T$_{\mathrm{eff}}$(J$_0$-K$_0$)**	**T$_{\mathrm{eff}}$(b-y)**	**log g(J$_0$-H$_0$)**	**log g(J$_0$-K$_0$)**	**log g(b-y)**
73170	3945.909	3877.542	3955.236	1.053	0.982	1.063
205399	4786.372	4712.342	4614.857	2.247	2.207	2.152
5004102	6427.350	5001.977	4843.415	2.738	2.218	2.140
46903	4838.552	4782.435	4642.320	4.766	2.288	2.213
265450	4824.728	4709.069	4625.956	2.138	2.078	2.031
77368	5510.818	4625.980	4576.568	2.336	1.932	1.905
109390	5645.091	4908.987	4657.643	2.616	2.316	2.186
14943	4529.115	4651.143	4422.189	1.493	1.565	1.428
250303	4884.540	4725.491	4680.315	2.343	2.259	2.235
168636	4782.488	4338.775	4521.017	1.922	1.662	1.776
264349	4947.888	4834.152	4725.528	2.360	2.303	2.246
261069	5056.033	4858.776	4794.664	2.195	2.100	2.066

The $T_{\rm eff}$ and $\log g$ estimated were compared with those determined by Johnson & Pilachowski (2010). These determinations of $T_{\rm eff}$ and $\log g$ are in agreement within ±200K and ±0.2 (cgs units), respectively. The correlation between these two determinations of $T_{\rm eff}$ are shown in Figure 3.5. Hence, we have used our estimates of the $T_{\rm eff}$ and $\log g$ for the stars not available in Johnson & Pilachowski (2010).

3.3 Analyses of the observed spectra of the 1^{st} and 3^{rd} group stars

The observed spectra of the program stars of the 1^{st} and 3^{rd} groups are shown in the order of their increasing $T_{\rm eff}$ from bottom to top (See Figures 3.6 to 3.8) to analyze the strengths of the MgH bands in their spectra. Figure 3.6 shows the spectra of the relatively cooler giants of the 1^{st} group. It is to be noted that, the strength of the MgH bands decrease as the effective temperature of the giants increase, from bottom to top, as expected. But, the two stars, 73170 and 178243, for their stellar parameters, are showing the weaker MgH bands, as seen through out the extent of the (0, 0) MgH band: 5330 – 4950 Å, in their observed spectra (see Figure 3.6). Note the extent of the weak MgH band, in these two stars, to the red and blue of the strong Mg *b* lines when compared with the spectra of 172980, with similar $T_{\rm eff}$ and log g but, relatively lower [Fe/H] than these two stars (see Sections 3.5 and 3.7, for further discussions). Similarly, it is to be noted that the 3^{rd} group stars, 262788 and 193804 and the 1^{st} group star 251701, have similar stellar parameters. The observed spectrum of the 1^{st} group star 251701 (see Figure 3.7) shows the clear presence of the MgH band with Mg *b* lines. However, the observed spectra of the 3^{rd} group stars, 262788 and 193804 (see Figures 3.7 and 3.8) show clearly the Mg *b* lines but no MgH bands (see Sections 3.6 and 3.7,

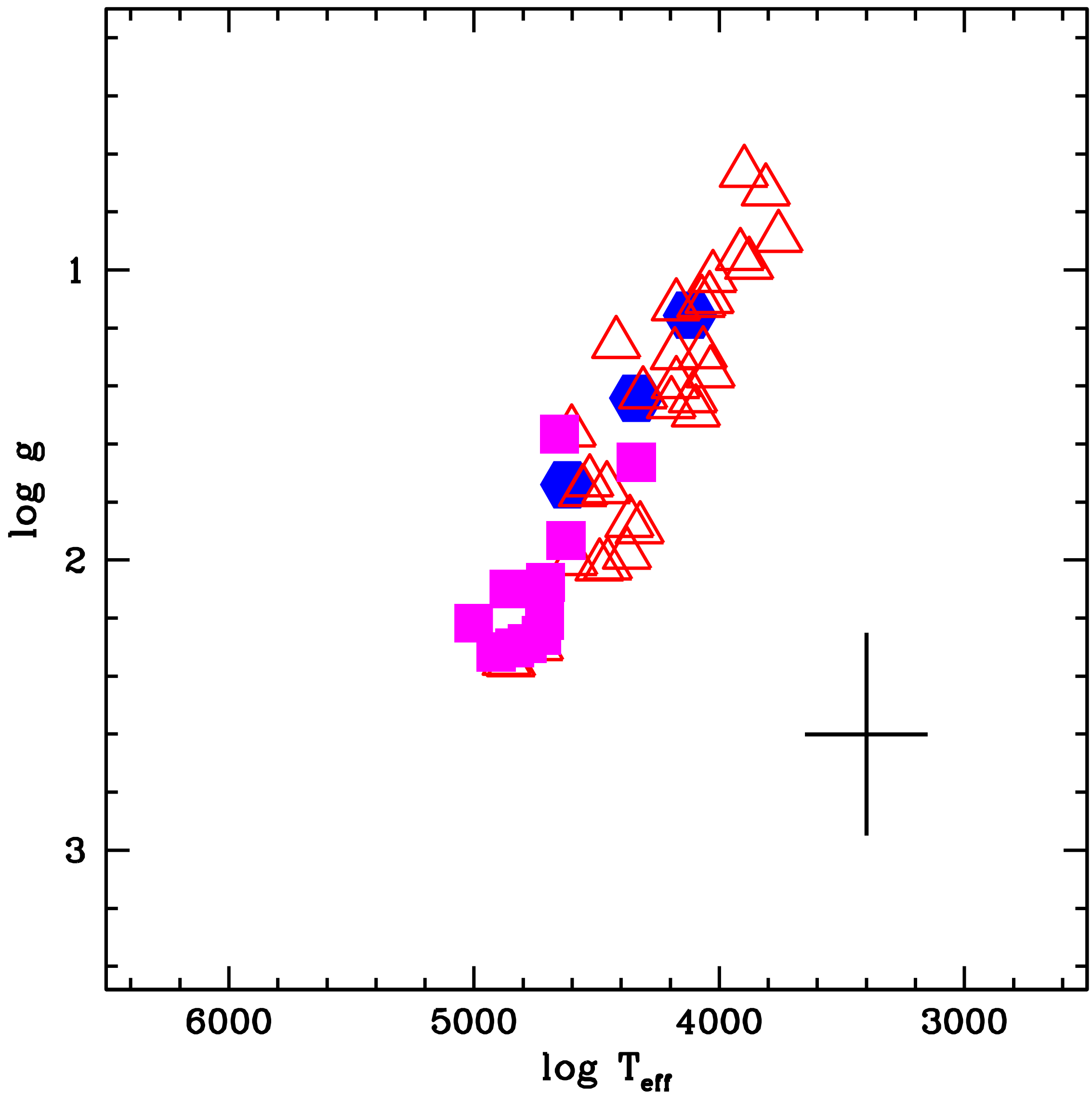

FIGURE 3.4: The program stars on the $T_{\rm eff}$ vs. $\log g$ plane. The open red triangles show the program stars of 1^{st} group (metal rich stars with strong Mg b lines and MgH band), the filled magenta squares are the program stars of 2^{nd} group (metal poor stars with weak or no Mg b lines and absent MgH band) and the filled blue hexagons are the program stars of 3^{rd} group (metal rich stars with strong Mg b lines and no MgH band). The cross in the bottom right indicate the errors on the $T_{\rm eff}$ and $\log g$, estimated by the uncertainties on the $(J_0 - K_0)$ colour.

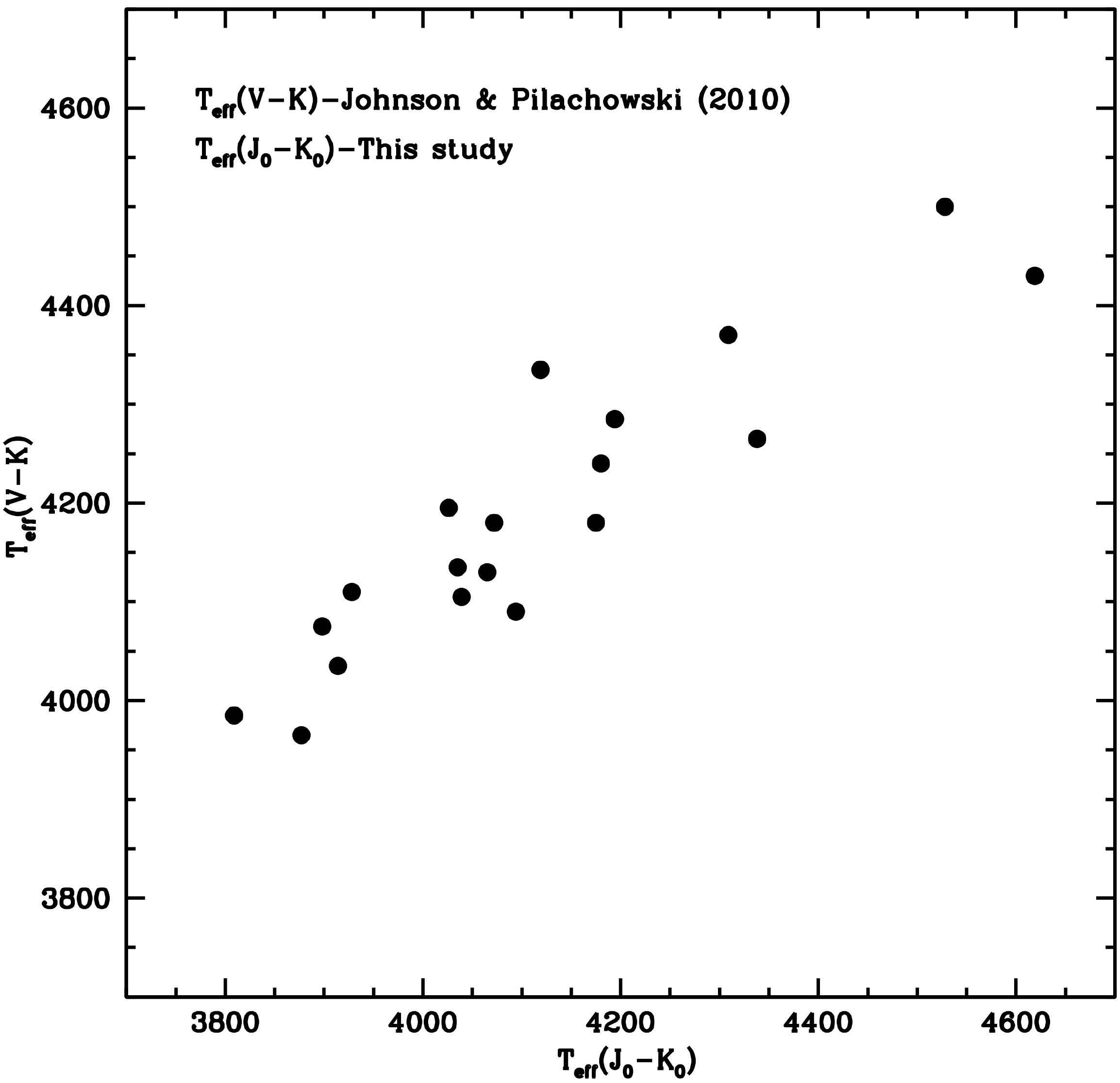

FIGURE 3.5: The T_{eff} determined from (V_0-K_0) colour by Johnson & Pilachowski (2010) versus the T_{eff} determined from (J_0-K_0) colour in our study are shown for common stars.

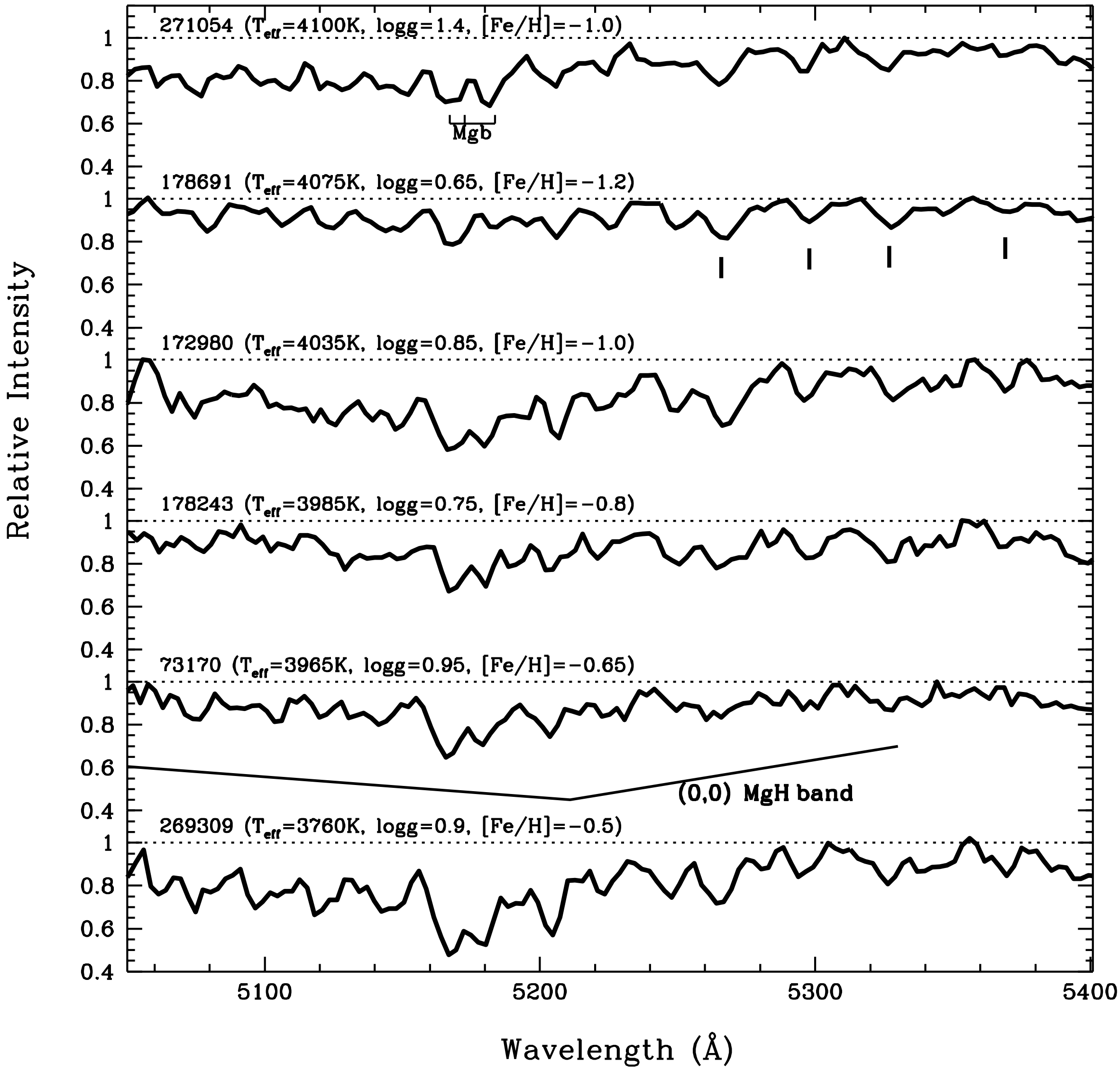

FIGURE 3.6: The spectra of the 1^{st} and 3^{rd} group stars are shown in the order of their increasing $T_{\rm eff}$ from bottom to top. The strong Mg *b* lines and the (0, 0) MgH band are marked. The vertical lines marked to the red of the Mg *b* lines are Fe I lines.

for further discussions). These four stars (73170, 178243 of 1^{st} group and 262788 and 193804 of 3^{rd} group) discussed above, are plausible H-deficient candidates.

The strengths of the MgH bands are further analyzed by synthesizing the spectra

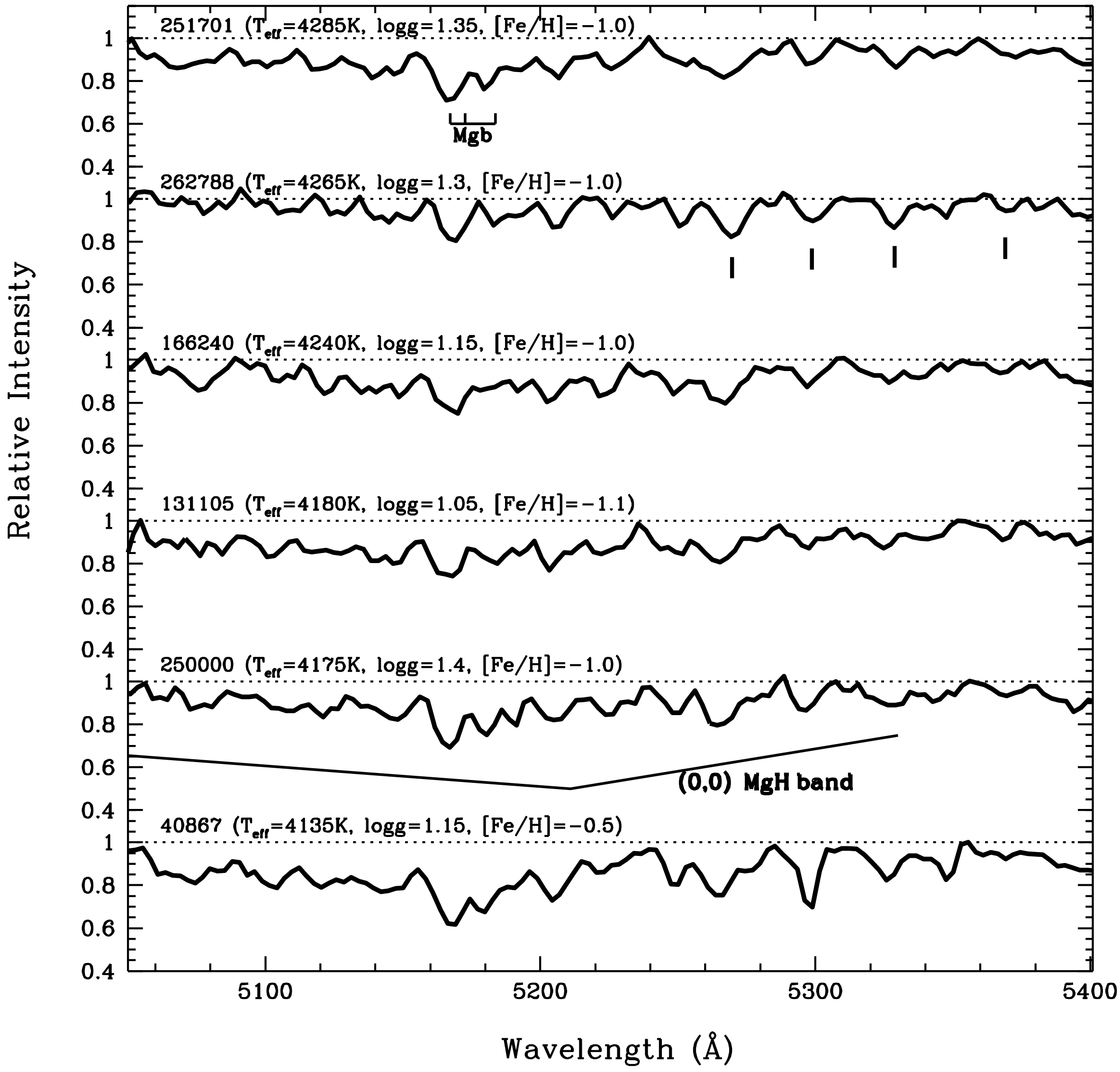

FIGURE 3.7: The spectra of the 1^{st} and 3^{rd} group stars are shown in the order of their increasing $T_{\rm eff}$ from bottom to top. The strong Mg b lines and the (0, 0) MgH band are marked. The vertical lines marked to the red of the Mg b lines are Fe I lines.

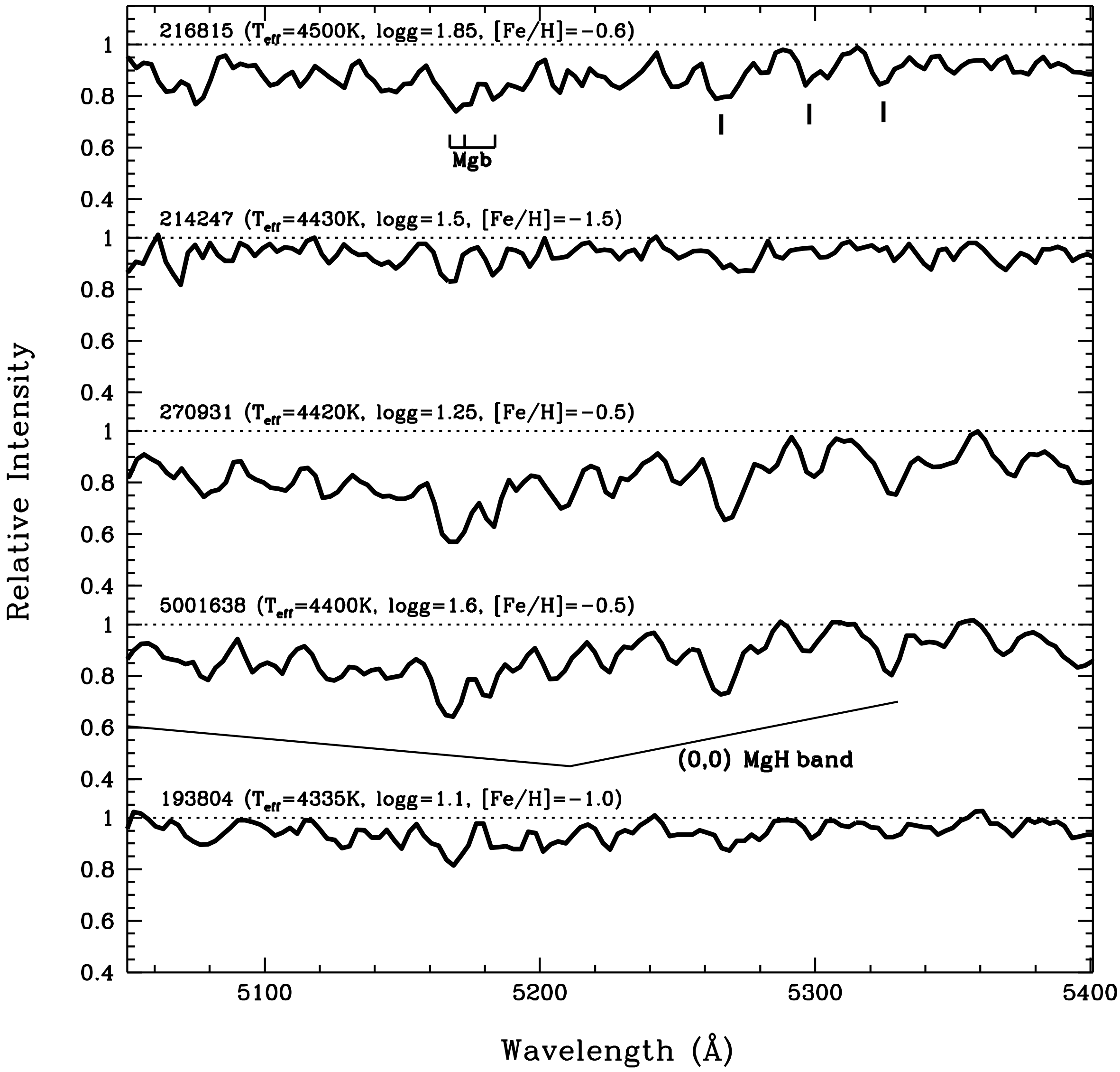

FIGURE 3.8: The spectra of the 1^{st} and 3^{rd} group stars are shown in the order of their increasing $T_{\rm eff}$ from bottom to top. The strong Mg b lines and the (0, 0) MgH band are marked. The vertical lines marked to the red of the Mg b lines are Fe I lines.

for all the program stars of 1^{st} and 3^{rd} groups for their adopted stellar parameters. These synthesized spectra are then compared with their observed spectra. The syntheses and analyses of the program stars' spectra are discussed below.

3.4 Spectrum syntheses and analyses

The spectra were synthesized in the 5165Å region that includes the Mg b lines and the (0, 0) MgH band. For synthesizing the spectra, the atomic lines for the synthesis were compiled from Kurucz database[2], VALD database[3], and NIST database[4]. The (0, 0) MgH molecular line list was adopted from Hinkle et al. (2013). Synthetic spectra were generated by combining the LTE spectral line analysis/spectrum synthesis code MOOG (Sneden 1973), and the ATLAS9 (Kurucz 1998) plane parallel, line-blanketed LTE model atmospheres with convective overshoot.

As a test case, using these line list, spectrum of Arcturus, a typical red giant, was synthesized to validate the gf-values of the atomic lines. All the atomic lines that are identified by Hinkle et al. (2000) in the observed Arcturus spectrum were included along with the MgH line list by Hinkle et al. (2013). The Mg isotopic ratios are taken from McWilliam & Lambert (1988). Using the spectrum synthesis code, *synth* in MOOG, the high resolution optical spectrum of Arcturus was synthesized for the stellar parameters and the abundances given by Ramírez & Allende Prieto (2011). Note that, Ramírez & Allende Prieto (2011)'s estimates are in good agreement with Peterson et al. (1993). The synthesized spectrum was convolved with a Gaussian profile with a width that represents the broadening due to macroturbulence and the instrumental profile. Minimal adjustments were made to the abundances of the atomic lines to obtain the best fit to the observed high-resolution optical spectrum of Arcturus (Hinkle et al. 2000). A reasonably

[2]http://kurucz.harvard.edu
[3]http://www.astro.uu.se
[4]http://www.nist.gov

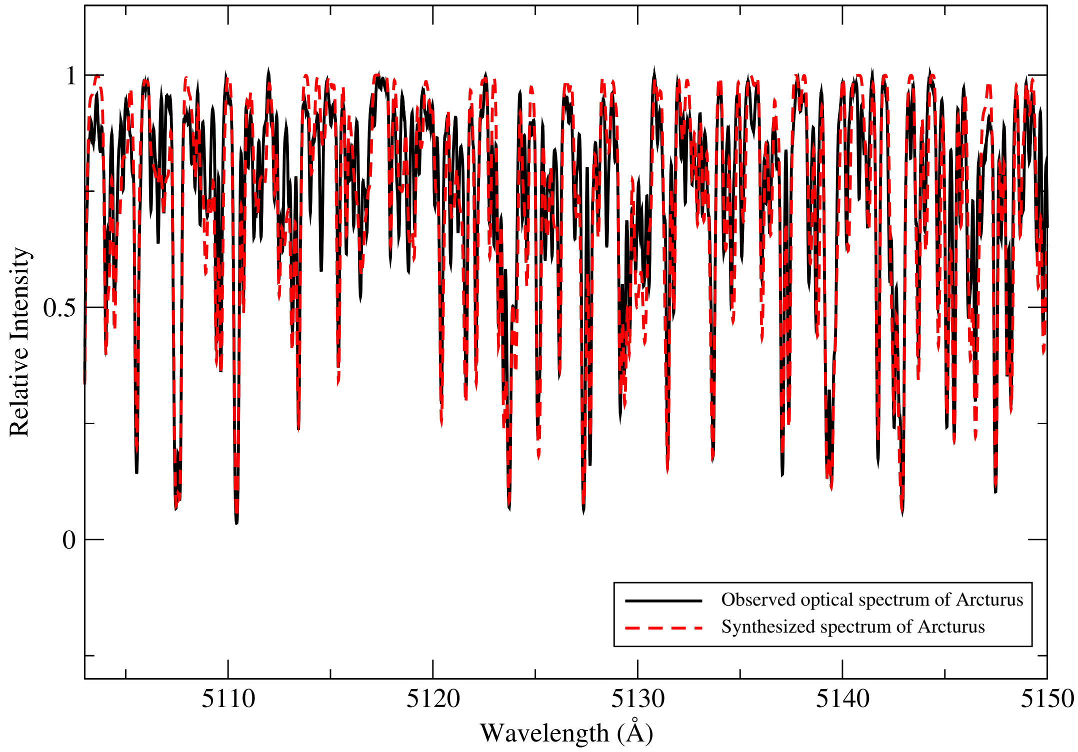

FIGURE 3.9: The figure shows the observed and the synthesized spectra for Arcturus in the window 5105–5150 Å. The observed spectrum is shown in black solid line and the synthesized spectrum is shown in the red dashed line.

good fit was obtained to the MgH molecular lines for the adopted isotopic values from McWilliam & Lambert (1988) (see Figures 3.9 and 3.10).

The synthesized high-resolution spectrum was further convolved by a Gaussian profile of width of about 8Å, to match with the observed low-resolution Arcturus spectrum obtained from VBT (see Figure 3.11).

A good match of the synthesized Arcturus spectrum to the observed, both high- and low-resolution spectra, validates the adopted line list for the adopted stellar parameters of Arcturus. These checks on published analysis of Arcturus, a typical red giant, are taken as evidence that our implementation of the code MOOG, the LTE models, and the adopted line list was successful for the syntheses of the red giants' spectra. Hence, the spectra of the program stars were synthesized following

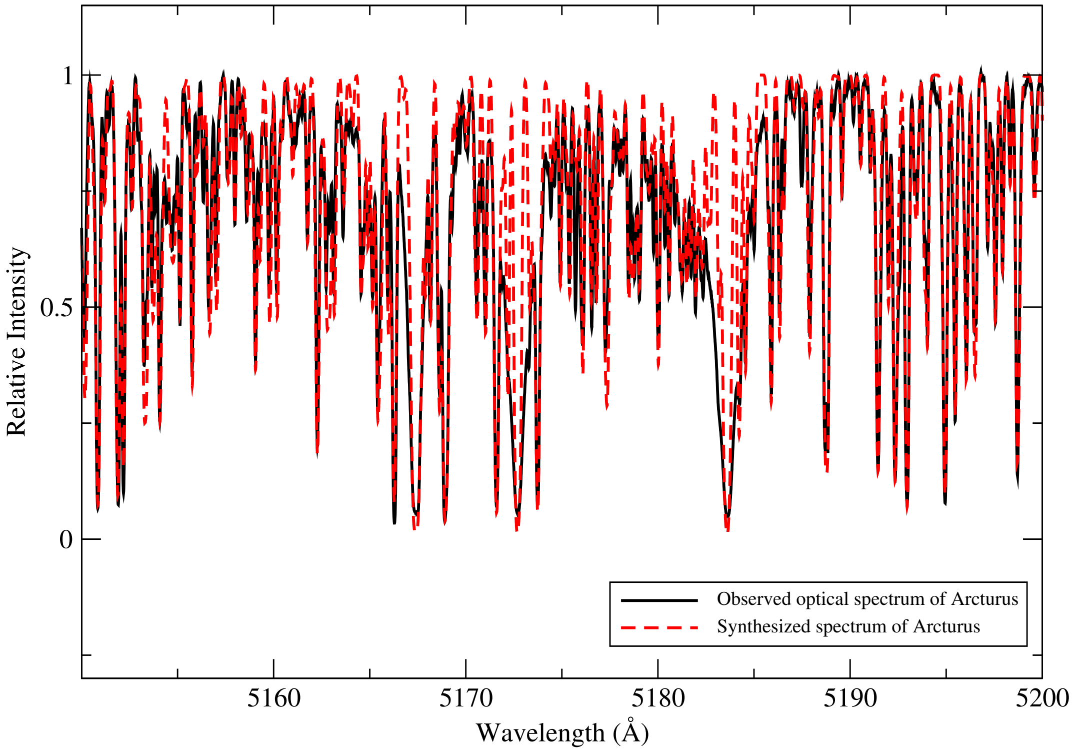

FIGURE 3.10: The figure shows the observed and the synthesized spectra for Arcturus in the window 5150–5200 Å. The observed spectrum is shown in black solid line and the synthesized spectrum is shown in the red dashed line.

the above procedure. The synthesized spectra for their adopted stellar parameters and abundances were then compared with the observed spectra.

3.5 Spectrum Syntheses and Analyses of the 1^{st} group stars

To investigate the MgH band strengths in these program stars for their stellar parameters, the spectra were synthesized and compared with their observed spectra. The stellar parameters for most of the program stars were adopted from the study of Johnson & Pilachowski (2010). The program stars for which the stellar parameters were not available in the study of Johnson & Pilachowski (2010), the

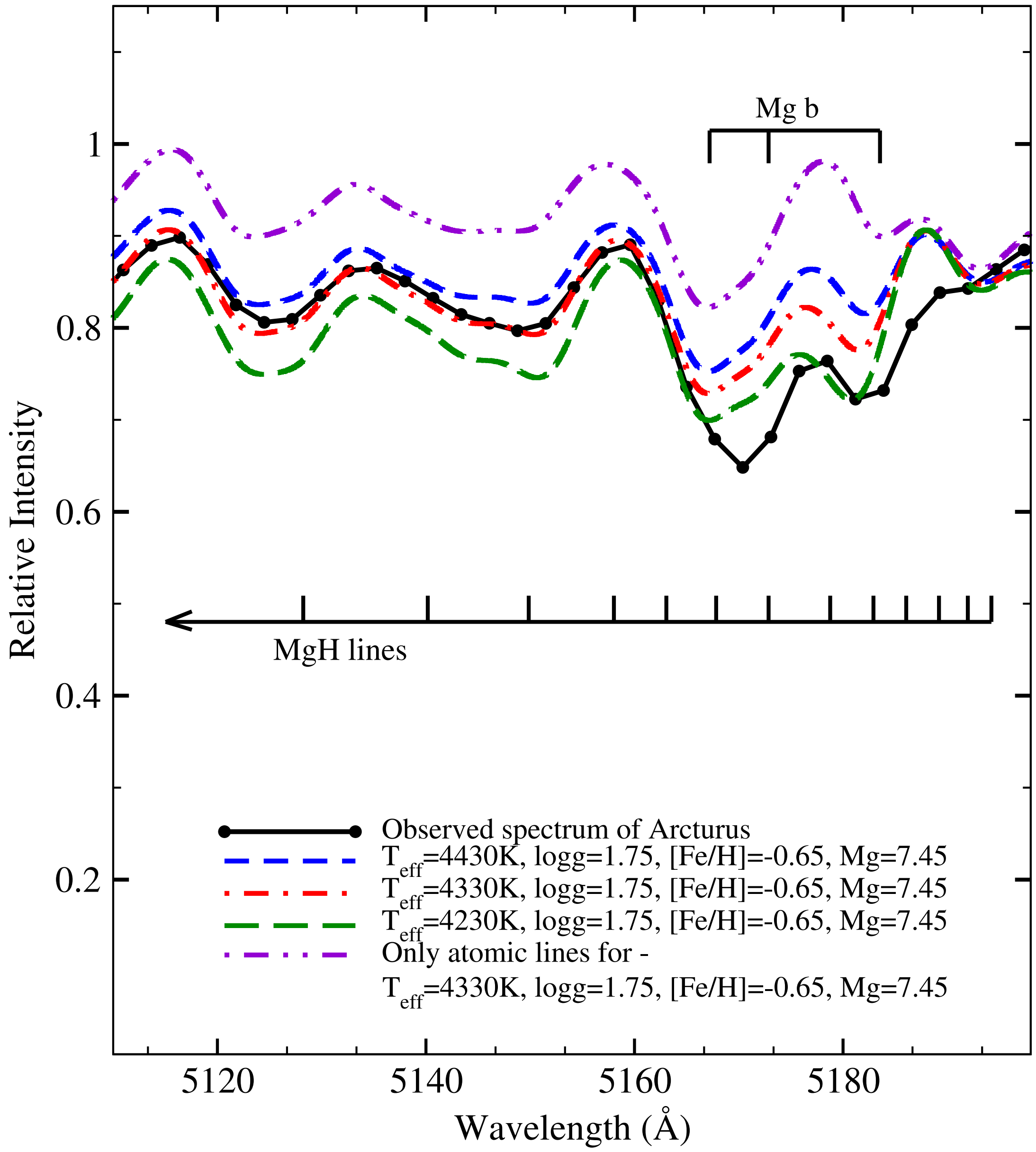

FIGURE 3.11: The figure shows the observed and the synthesized spectra for Arcturus. The synthesis for the best fit value for the Mg abundance of about 7.45, is shown in the red dash dotted line, along with upper (blue short dashed line) and lower (green long dashed line) limit of the $T_{\rm eff}$. The synthesis for the pure atomic lines are also shown in violet dash double dotted line.

$T_{\rm eff}$ and log g were adopted from our estimates. For these stars, the metallicities were estimated by comparing their spectra with the spectra of stars having similar $T_{\rm eff}$ and log g from Johnson & Pilachowski (2010). From the studies of Norris & Da Costa (1995), the average [Mg/Fe][5] for the red giants of ω Cen is about +0.4 dex over a metallicity range of [Fe/H]=−2.0 to −0.7. Hence, in our synthesis the [Mg/Fe]=+0.4 dex was adopted initially. Since the subordinate lines of MgH band at about 5167Å are blended with the saturated Mg b lines, the subordinate lines of MgH band in the wavelength window 5120–5160Å were given more weight in our synthesis. The best fit of the spectrum synthesized for the adopted stellar parameters to the observed was obtained by adjusting the Mg abundance, and therefore estimating the Mg abundance[6] for the program star. Note that, the derived Mg abundances is in excellent agreement with the common stars in Norris & Da Costa (1995) study. The adopted stellar parameters, the metallicities and the derived Mg abundances for the program stars are given in Table 3.3. The program stars are discussed below in the order of their increasing effective temperature:

269309: The spectrum was synthesized in the wavelength window: 5110–5200 Å, that includes Mg b lines and the MgH band, for the estimated value of star's $T_{\rm eff}$ = 3760K, log g=0.9, and [Fe/H]=−0.5. By adjusting the Mg abundance, as discussed above, the best fit to the observed subordinate MgH lines was obtained. The Mg abundance derived was about 7.1, or [Mg/Fe]=0.0. The [Mg/Fe] value is as expected for the star's metallicity. The Mg b lines are too strong and saturated in the observed spectra to estimate the Mg abundance. However, the best fit was judged by the subordinate MgH lines to the blue of the Mg b lines. The spectrum was also synthesized for the upper and the lower limit of the $T_{\rm eff}$. The synthesized spectra are shown in Figure 3.12.

73170: The spectrum was synthesized in the wavelength window as discussed above for the star's $T_{\rm eff}$ = 3965K, log g=0.95 and [Fe/H]=-0.65, as given by Johnson

[5] $[\mathrm{Mg/Fe}] = (\mathrm{Mg/Fe})_* - (\mathrm{Mg/Fe})_\odot$

[6] $\log\,\epsilon(Mg) = \log\,(Mg/H) + 12.0$, this convention is used throughout this study.

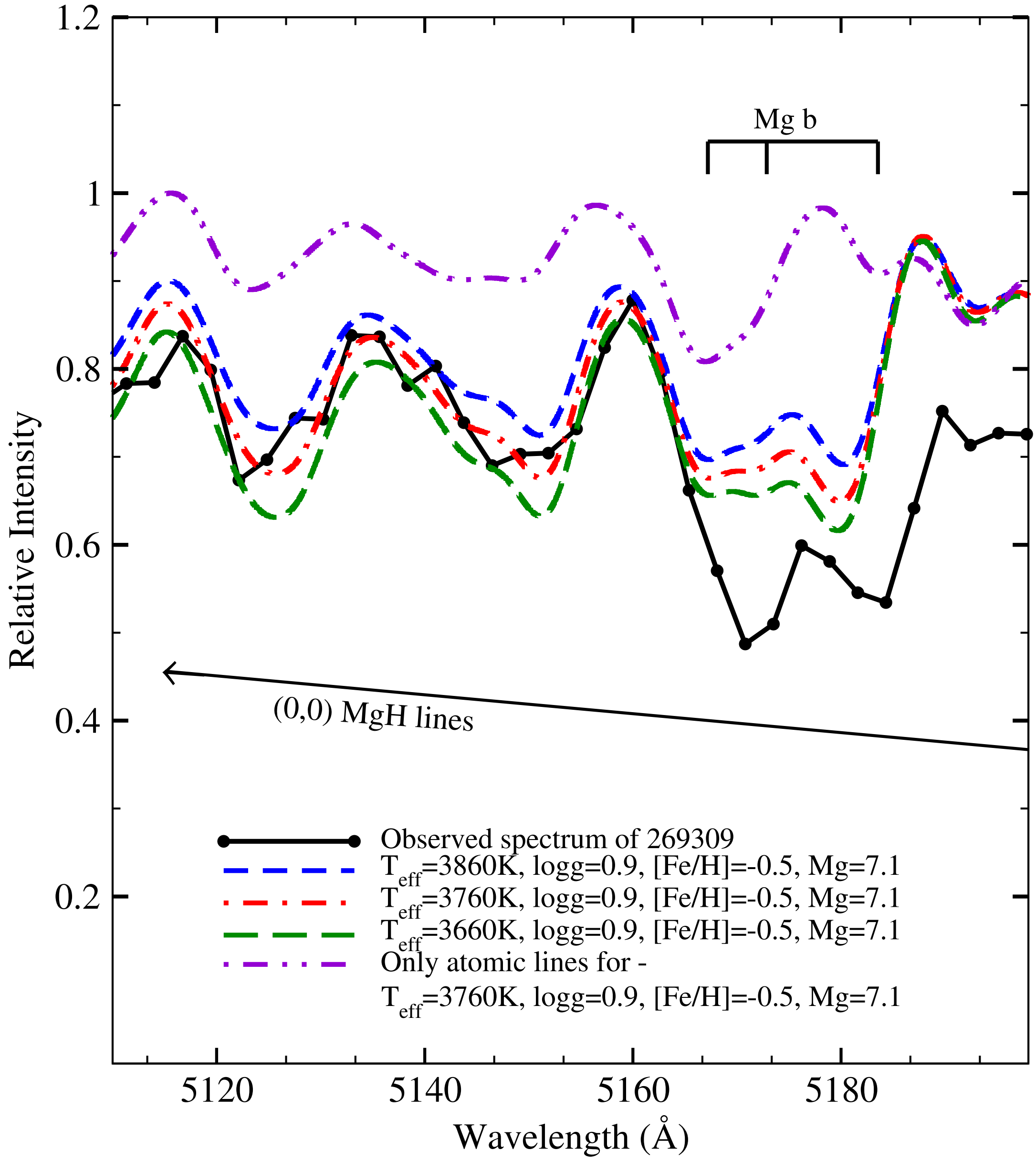

FIGURE 3.12: The figure shows the observed spectrum and the synthesized spectra for the star 269309. The synthesis for the best fit value of the Mg abundance of 7.1, is shown in the red dash dotted line, along with upper (blue short dashed) and lower (green long dashed) limit of the $T_{\rm eff}$. The synthesis for the pure atomic lines is also shown in violet dash double dotted line. See Figure 3.11 for the identifications of the subordinate lines of MgH band.

& Pilachowski (2010). By adjusting the Mg abundance, as discussed above, the best fit to the observed subordinate MgH lines was obtained. The derived Mg abundance was about 6.75, or [Mg/Fe]= -0.2 (see Figure 3.13). The [Mg/Fe] as determined by Norris & Da Costa (1995) for the red giant stars of ω Cen at this metallicity, i.e.[Fe/H]=-0.65, is not less than +0.2 dex. In comparison to this value, the derived [Mg/Fe] is about 0.4 dex less than the expected. The derived low value of [Mg/Fe] that is not as expected, is further discussed in the section 3.7. Figure 3.13 shows the synthesis for the derived Mg abundance and synthesis for the average value of the Mg abundance for the red giants of ω Cen. Spectra were also synthesized for the upper and the lower limit of the star's $T_{\rm eff}$, for the average [Mg/Fe] value of ω Cen giants. Note that, the spectrum synthesized for the upper limit of the $T_{\rm eff}$ with the average Mg abundance of the ω Cen giants do not provide the fit to the observed spectrum. The synthesis for the pure atomic lines is also shown in Figure 3.13. Hence, from the syntheses it is clear that the change in the stellar parameters cannot account for the observed spectrum of 73170.

178243: The star is one of the coolest in this sample with $T_{\rm eff}$ = 3985K, $\log g$=0.75, and [Fe/H]=-0.8, as given by Johnson & Pilachowski (2010). The spectrum was synthesized for these stellar parameters in the wavelength window as discussed above. By adjusting the Mg abundance, the best fit to the observed subordinate MgH lines was obtained. The Mg abundance derived was about 6.4, or [Mg/Fe]=-0.4 (see Figure 3.14). The [Mg/Fe] is about +0.8 dex lower than the average value of the [Mg/Fe], and about +0.6 dex lower than the lowest [Mg/Fe] value reported for the red giants of ω Cen, at the star's metallicity (Norris & Da Costa 1995). The synthesis for the average value of [Mg/Fe]=+0.4 is also shown in Figure 3.14, and is stronger than the observed subordinate MgH lines. Spectra were also synthesized for the upper and the lower limit of the star's $T_{\rm eff}$=3985K (see Figure 3.14). Note that, the spectrum synthesized for the upper limit of the $T_{\rm eff}$ with the average Mg abundance of the ω Cen giants do not provide the fit to the observed spectrum. The synthesis for the pure atomic lines is also shown in

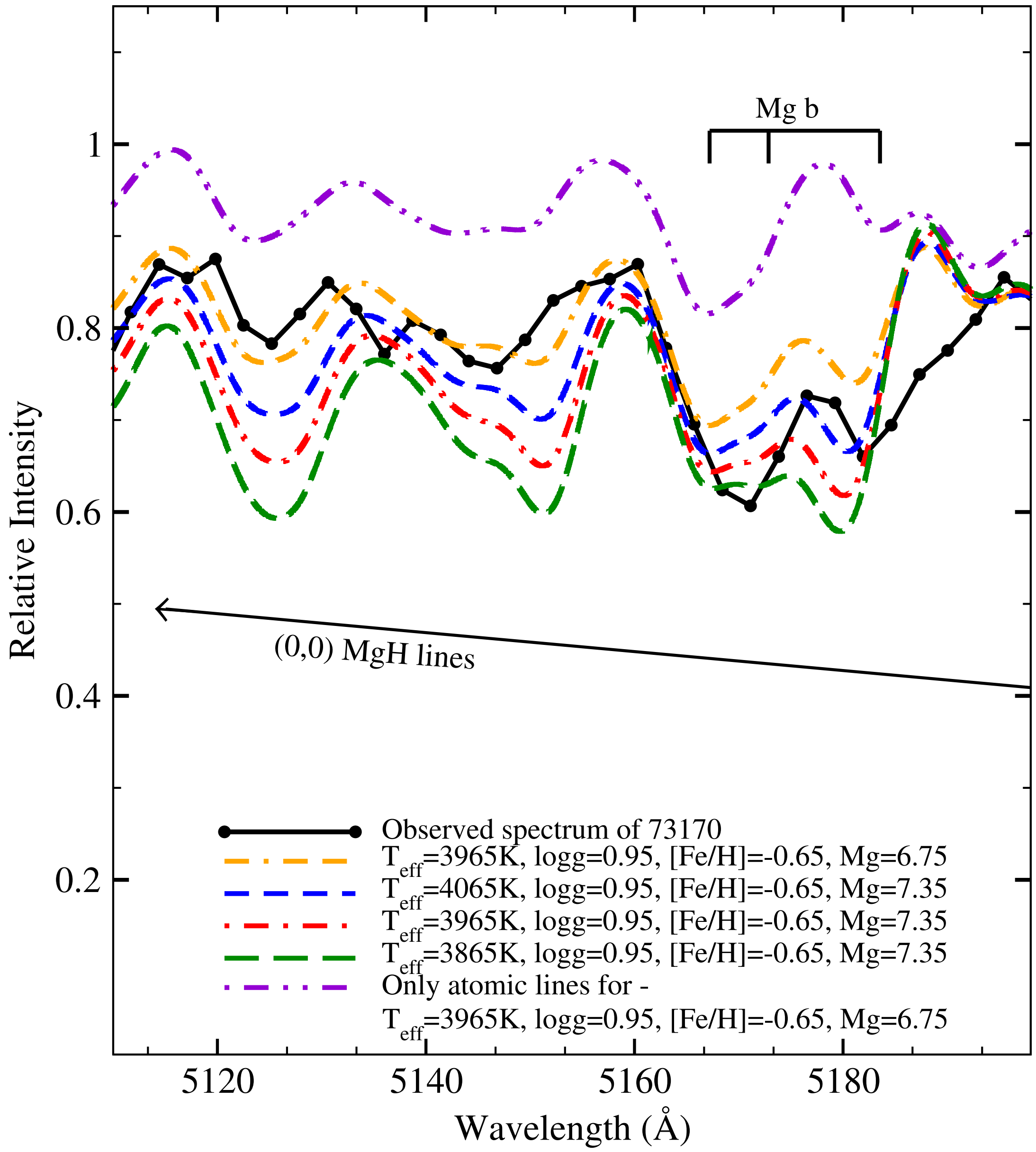

FIGURE 3.13: The figure shows the observed spectrum and the synthesized spectra for the star 73170. The best fit to the observed spectrum is shown in orange dot double dashed line, synthesized for the Mg abundance of about 6.75. The syntheses for the expected Mg abundance for the ω Cen giants i.e. [Mg/Fe]=+0.4, is shown in red dash dotted line, along with the upper (blue short dashed line) and the lower (green long dashed line) limit of the $T_{\rm eff}$. Note that, the synthesis for the upper limit of the $T_{\rm eff}$ do not provide a fit to the observed spectrum. The synthesis for the pure atomic lines, for the derived Mg abundance, is also shown in violet dash double dotted line. See Figure 3.11 for the identifications of the subordinate lines of MgH band.

Table 3.3: The stellar parameters, the metallicities and the Mg abundances for the program stars in the order of their increasing effective temperature.

Star	Star(LEID)	S/N	$T_{\rm eff}$	$\log g$	[Fe/H]	Group	$\log \epsilon$(Mg)	[Mg/Fe]
269309	-	70	3760	0.90	−0.5	First	7.1±0.2	0.0
73170[a]	39048	100	3965	0.95	−0.65	First	6.75±0.2	−0.2
178243[a]	60073	100	3985	0.75	−0.8	First	6.4±0.2	−0.4
172980[a,b]	61067	110	4035	0.85	−1.0	First	7.0±0.2	+0.4
178691	50193	110	4075	0.65	−1.2	First	6.6±0.2	+0.2
271054	-	100	4100	1.40	−1.0	First	6.7±0.2	+0.1
40867	54022	110	4135	1.15	−0.5	First	7.2±0.2	+0.1
250000	-	90	4175	1.40	−1.0	First	6.9±0.2	+0.3
131105	51074	80	4180	1.05	−1.1	First	6.9±0.2	+0.4
166240[b]	55101	60	4240	1.15	−1.0	First	6.8±0.2	+0.2
262788[c]	34225	110	4265	1.30	−1.0	Third	6.0±0.2	< −0.6
251701[c]	32169	100	4285	1.35	−1.0	First	7.0±0.2	+0.4
193804[c]	35201	80	4335	1.10	−1.0	Third	6.5±0.2	< −0.1
5001638	-	150	4400	1.6	−0.5	First	7.3±0.2	+0.2
270931	-	100	4420	1.25	−0.5	First	7.2±0.2	+0.1
214247	37275	60	4430	1.45	−1.5	Third	6.5±0.2	+0.4
216815	43475	80	4500	1.85	−0.6	First	7.3±0.2	+0.3
14943	53012	100	4605	1.35	−1.8	Second	<6.7±0.2	< +0.9

[a] The stars in boldface are the newly discovered H-deficient stars of first group, and one without boldface is their comparator.
[b] The stars those are found in the sample of Norris & Da Costa (1995).
[c] The stars in boldface are the newly discovered H-deficient stars of third group, and one without boldface is their comparator.

Figure 3.14. Hence, from the syntheses it is clear that the change in the stellar parameters, cannot account for the observed spectrum of 178243. The results are further discussed in the section 3.7.

172980: The spectrum was synthesized in the wavelength window: 5110-5200 Å as discussed above, for the star's $T_{\rm eff}$=4035K, $\log g$=0.85, and [Fe/H]=-1.0, as given by Johnson & Pilachowski (2010). The spectrum synthesized for these parameters provided the best fit to the observed spectrum for the Mg abundance of about 7.0 or [Mg/Fe]=+0.4. The derived [Mg/Fe] value for the star is as expected. This star was also found in the sample of Norris & Da Costa (1995), for which they

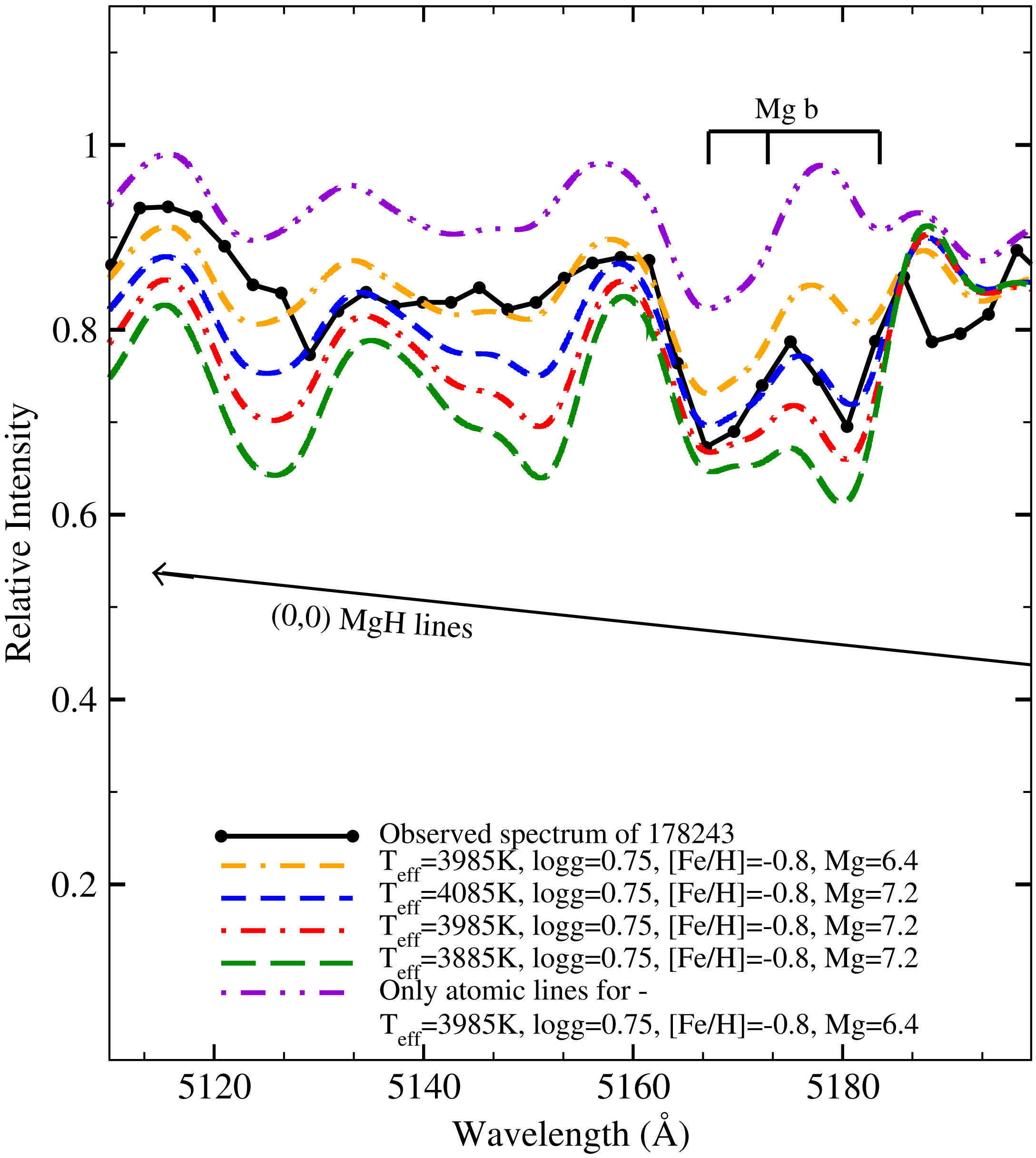

FIGURE 3.14: The figure shows the observed spectrum and the synthesized spectra for the star 178243. The best fit to the observed spectrum is shown in orange dot double dashed line, synthesized for the Mg abundance of 6.4. The syntheses for the expected Mg abundance for the ω Cen giants i.e. [Mg/Fe]=+0.4, is shown in red dash dotted line, along with the upper (blue short dashed line) and the lower (green long dashed line) limit of the $T_{\rm eff}$. Note that, the synthesis for the upper limit of the $T_{\rm eff}$ do not provide a fit to the observed spectrum. The synthesis for the pure atomic lines, for the derived Mg abundance, is shown in violet dash double dotted line. See Figure 3.11 for the identifications of the subordinate lines of MgH band.

have determined the Mg abundance using a high resolution spectrum. The stellar parameters from their studies are in good agreement with the values given by Johnson & Pilachowski (2010). The [Mg/Fe]=+0.53, determined by Norris & Da Costa (1995) is in good agreement with our estimates. Figure 3.15 shows the syntheses for Mg=7.0, the best fit value, and also shown are the syntheses for the upper and lower limit of the $T_{\rm eff}$.

178691: The spectrum was synthesized in the wavelength window as discussed above, for the star's $T_{\rm eff}$=4075K, $\log g$=0.65, and [Fe/H]=−1.2, as given by Johnson & Pilachowski (2010). With these stellar parameters, the Mg abundance required for the synthesized spectrum to match the observed spectrum was about 6.6 or [Mg/Fe]=+0.2. The [Mg/Fe] derived is as expected for the red giants of ω Cen, at the star's metallicity. The spectra were also synthesized for the upper and the lower limits of the $T_{\rm eff}$, and are shown in Figure 3.16.

271054: The spectrum was synthesized in the wavelength window: 5110–5200Å for the star's $T_{\rm eff}$=4100K, $\log g$=1.4, and [Fe/H]=−1.0, as given by Johnson & Pilachowski (2010). The Mg abundance was adjusted for the synthesis to match the observed subordinate MgH lines in the spectrum. The Mg abundance derived was about 6.7, or the [Mg/Fe]=+0.1, which is as expected for the red giants of ω Cen. The spectrum was also synthesized for the upper and the lower limits of the $T_{\rm eff}$ (see Figure 3.17).

40867: The spectrum was synthesized in the wavelength window as discussed above, for the star's $T_{\rm eff}$=4135K, $\log g$=1.15, and the [Fe/H]=−0.5, as given by Johnson & Pilachowski (2010). The Mg abundance was adjusted as discussed above, to obtain the best fit to the observed subordinate MgH lines. The Mg abundance derived was about 7.2, or [Mg/Fe]=+0.1, which is as expected for the giants of ω Cen, at the star's metallicity. The synthesized spectra are shown in Figure 3.18. The spectra were also synthesized for the upper and the lower limit of the star's $T_{\rm eff}$. (see Figure 3.18).

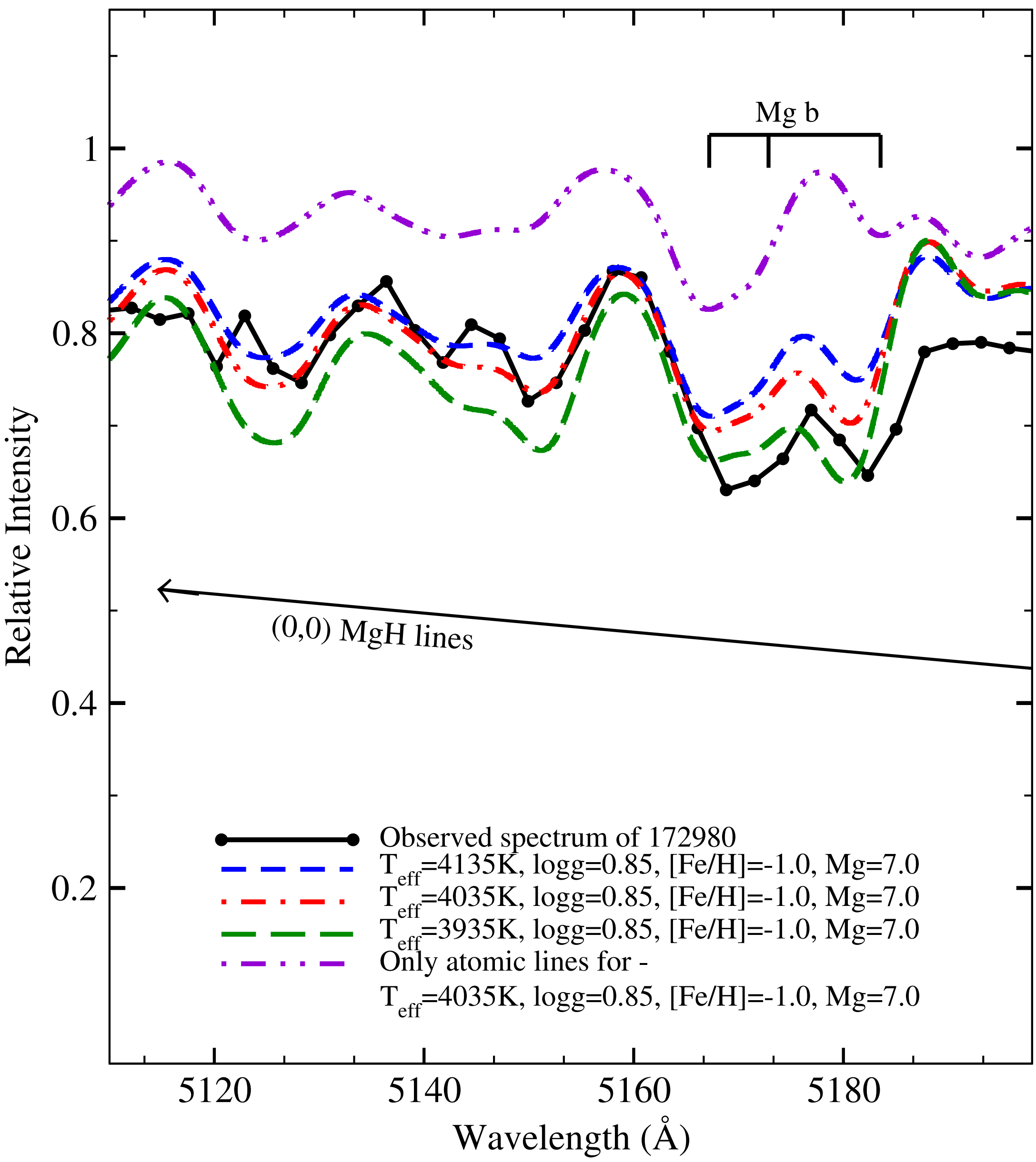

Figure 3.15: The figure shows the observed spectrum and the synthesized spectra for the star 172980. The best fit obtained for the Mg abundance of about 7.0 is shown in red dash dotted line. The upper (blue short dashed line) and the lower (green long dashed line) limit of the $T_{\rm eff}$ are also shown.The synthesis for the pure atomic lines is also shown in violet dash double dotted line. See Figure 3.11 for the identifications of the subordinate lines of MgH band.

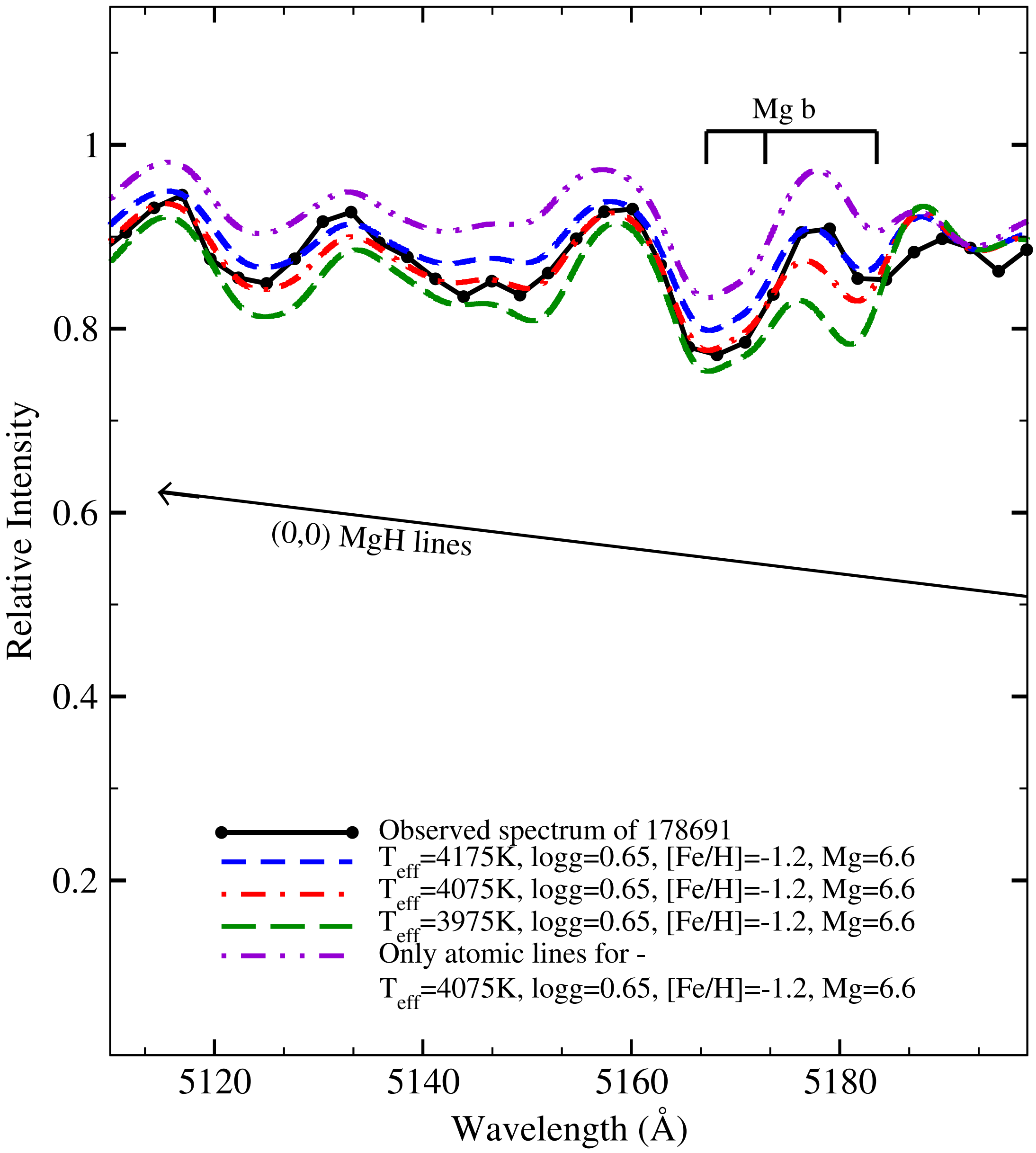

FIGURE 3.16: The figure shows the observed spectrum and the synthesized spectra for the star 178691. The best fit obtained for the Mg abundance of about 6.6 is shown in red dash dotted line. The upper (blue short dashed line) and the lower (green long dashed line) limit of the $T_{\rm eff}$ are also shown.The synthesis for the pure atomic lines is also shown in violet dash double dotted line. See Figure 3.11 for the identifications of the subordinate lines of MgH band.

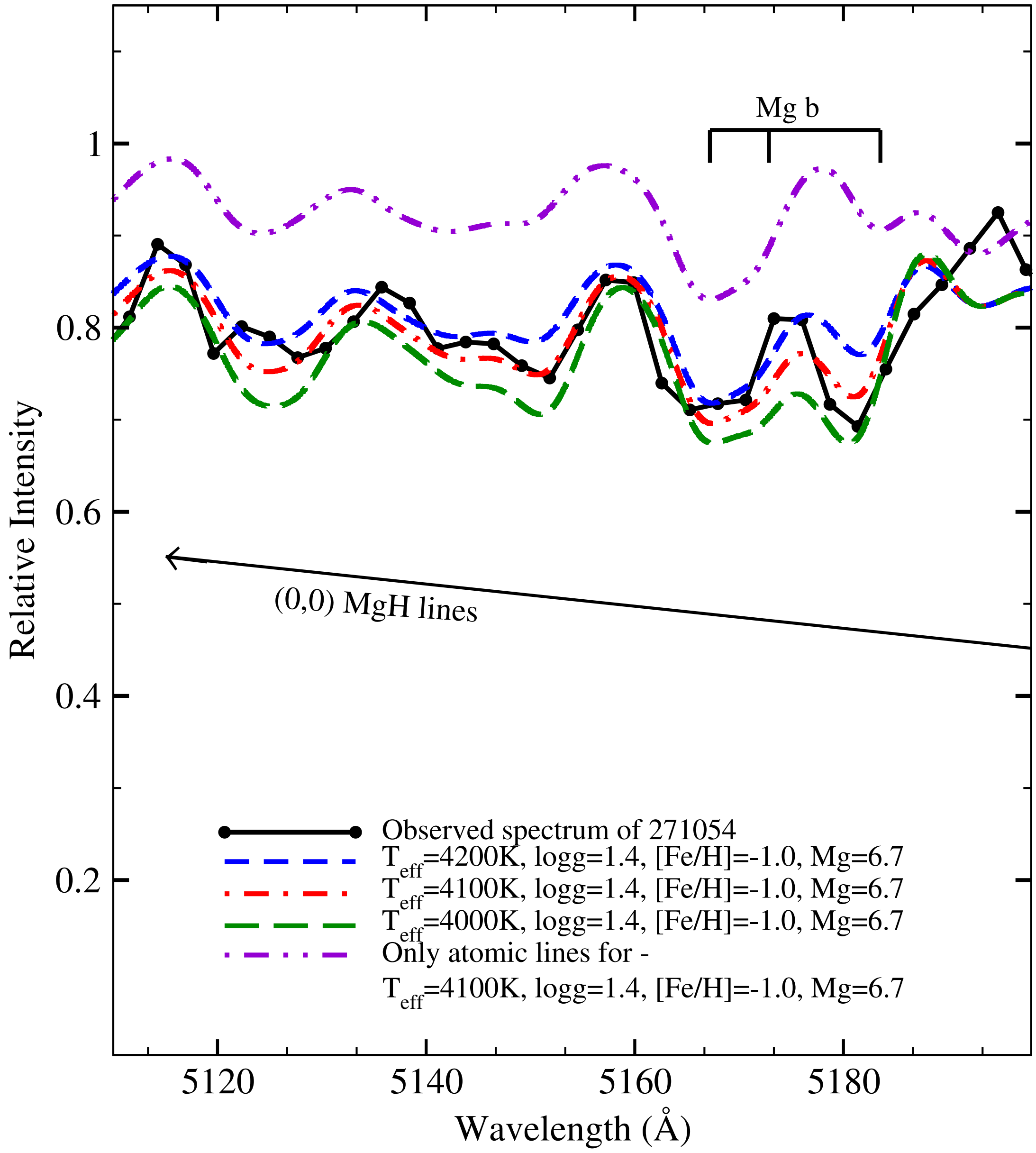

FIGURE 3.17: The figure shows the observed spectrum and the synthesized spectra for the star 271054. The best fit obtained for the Mg abundance of about 6.7 is shown in red dash dotted line. The syntheses for the upper (blue short dashed line) and the lower (green long dashed line) limit of the $T_{\rm eff}$ are also shown.The synthesis for the pure atomic lines is shown in violet dash double dotted line. See Figure 3.11 for the identifications of the subordinate lines of MgH band.

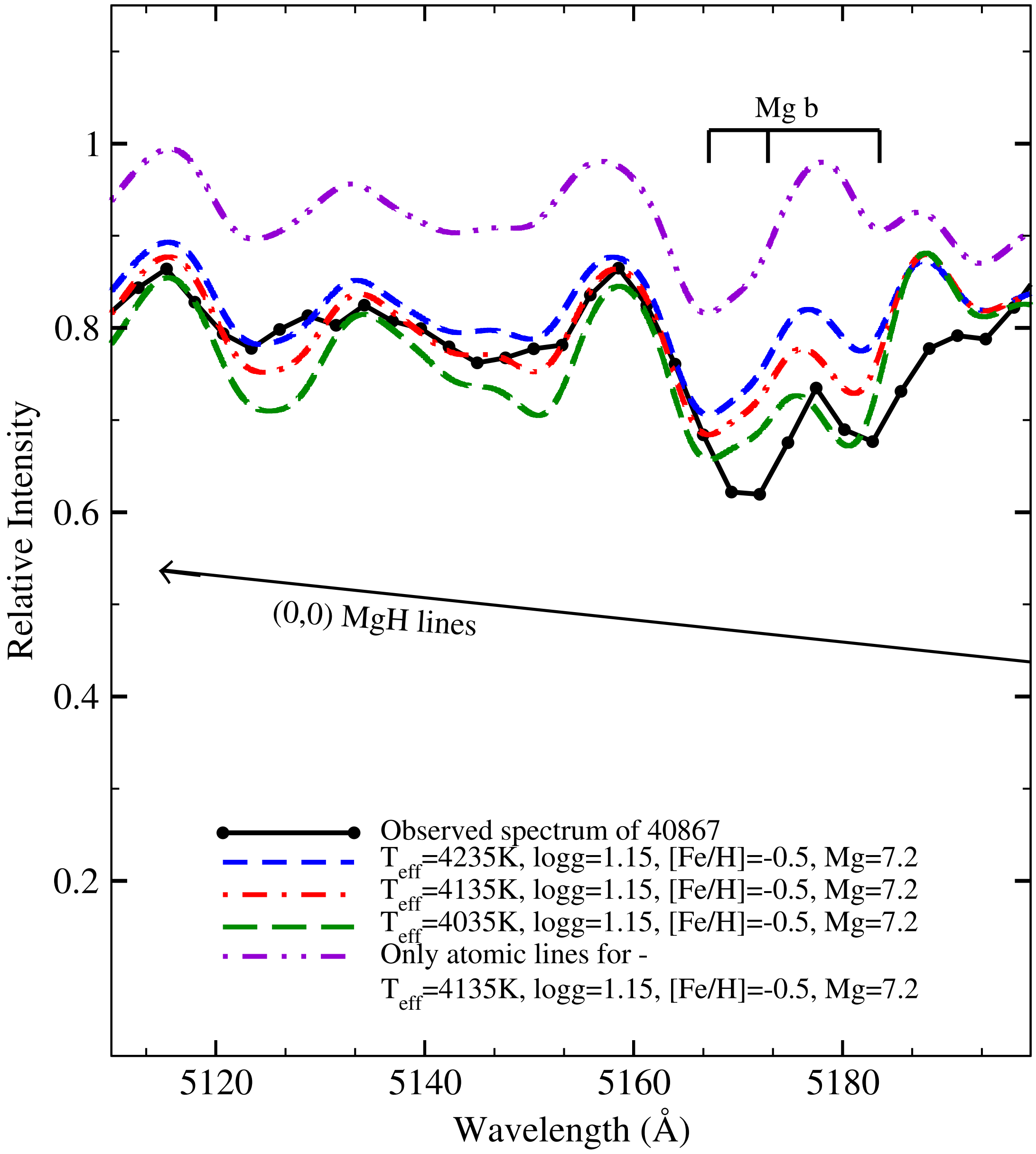

Figure 3.18: The figure shows the observed spectrum and the synthesized spectra for the star 40867. The best fit obtained for the Mg abundance of about 7.2 is shown in red dash dotted line. The syntheses for the upper (blue short dashed line) and the lower (green long dashed line) limit of the $T_{\rm eff}$ are also shown.The synthesis for the pure atomic lines is shown in violet dash double dotted line. See Figure 3.11 for the identifications of the subordinate lines of MgH band.

250000: The spectrum was synthesized in the wavelength window as discussed above, for the star's $T_{\rm eff}$=4175K, $\log g$=1.4 and [Fe/H]=−1.0, as estimated in this study. The Mg abundance was adjusted, as discussed above, to obtain the best fit to the observed subordinate MgH lines. The Mg abundance derived was about 6.9, or [Mg/Fe]=+0.3. The [Mg/Fe] is as expected. The syntheses for the best fit Mg abundance is shown in Figure 3.19, along with the syntheses for the upper and the lower limits of the star's $T_{\rm eff}$.

131105: The spectrum was synthesized in the wavelength window as discussed above for the star's $T_{\rm eff}$=4180K, $\log g$=1.05 and [Fe/H]=−1.1, as given by Johnson & Pilachowski (2010). By adjusting the Mg abundance, as discussed, the best fit to the observed subordinate MgH lines was obtained. The derived Mg abundance was about 6.9, or [Mg/Fe]=+0.4, that is as expected for the red giants of ω Cen. The synthesized spectra are shown in Figure 3.20. The spectra were also synthesized for the upper and the lower limit of the $T_{\rm eff}$ (see Figure 3.20).

166240: The spectrum was synthesized in the wavelength window: 5110–5200Å, as discussed above, for the star's $T_{\rm eff}$=4240K, $\log g$ = 1.15, and [Fe/H]=−1.0, as given by Johnson & Pilachowski (2010). By adjusting the Mg abundance the best fit to the observed subordinate lines of MgH band was obtained. The Mg abundance derived was about 6.8, or [Mg/Fe]=+0.2. For this star, Norris & Da Costa (1995) have derived the Mg abundance from the high resolution spectrum. The Mg abundance given by them is about, [Mg/Fe]=+0.27, which is in good agreement with our estimates. The synthesized spectra are shown in Figure 3.21. The spectra were also synthesized for the upper and the lower limits of the $T_{\rm eff}$, and are shown in Figure 3.21.

251701: The spectrum was synthesized in the wavelength window as discussed above, for star's $T_{\rm eff}$=4285K, $\log g$=1.35, and [Fe/H]=−1.0, as given by Johnson & Pilachowski (2010). The Mg abundance was adjusted for the synthesis to match the observed subordinate MgH lines. The Mg abundance derived was about 7.0, or

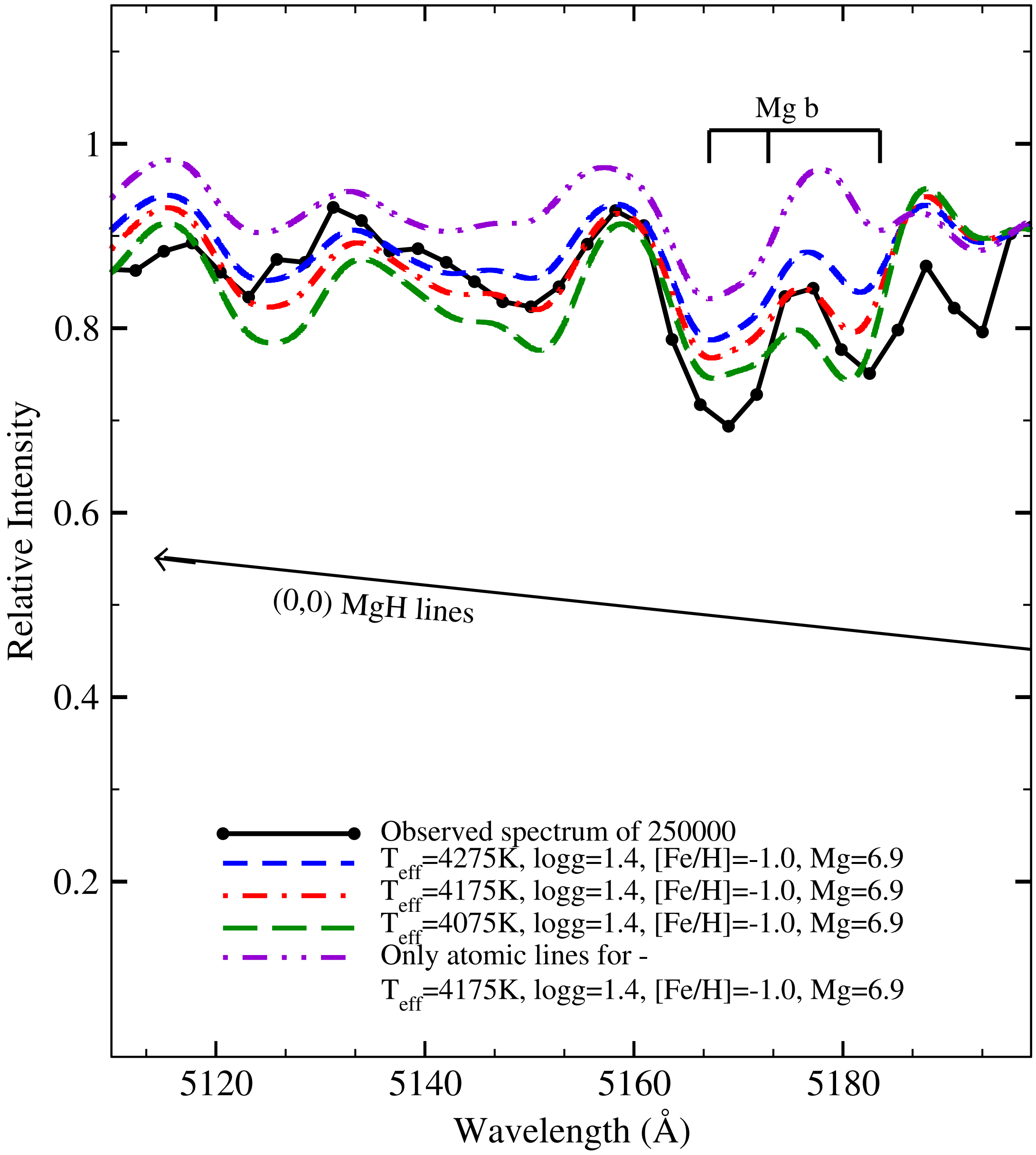

FIGURE 3.19: The figure shows the observed spectrum and the synthesized spectra for the star 250000. The best fit obtained for the Mg abundance of about 6.9, is shown in red dash dotted line. The syntheses for the upper (blue short dashed line) and the lower (green long dashed line) limit of the $T_{\rm eff}$ are also shown.The synthesis for the pure atomic lines is shown in violet dash double dotted line. See Figure 3.11 for the identifications of the subordinate lines of MgH band.

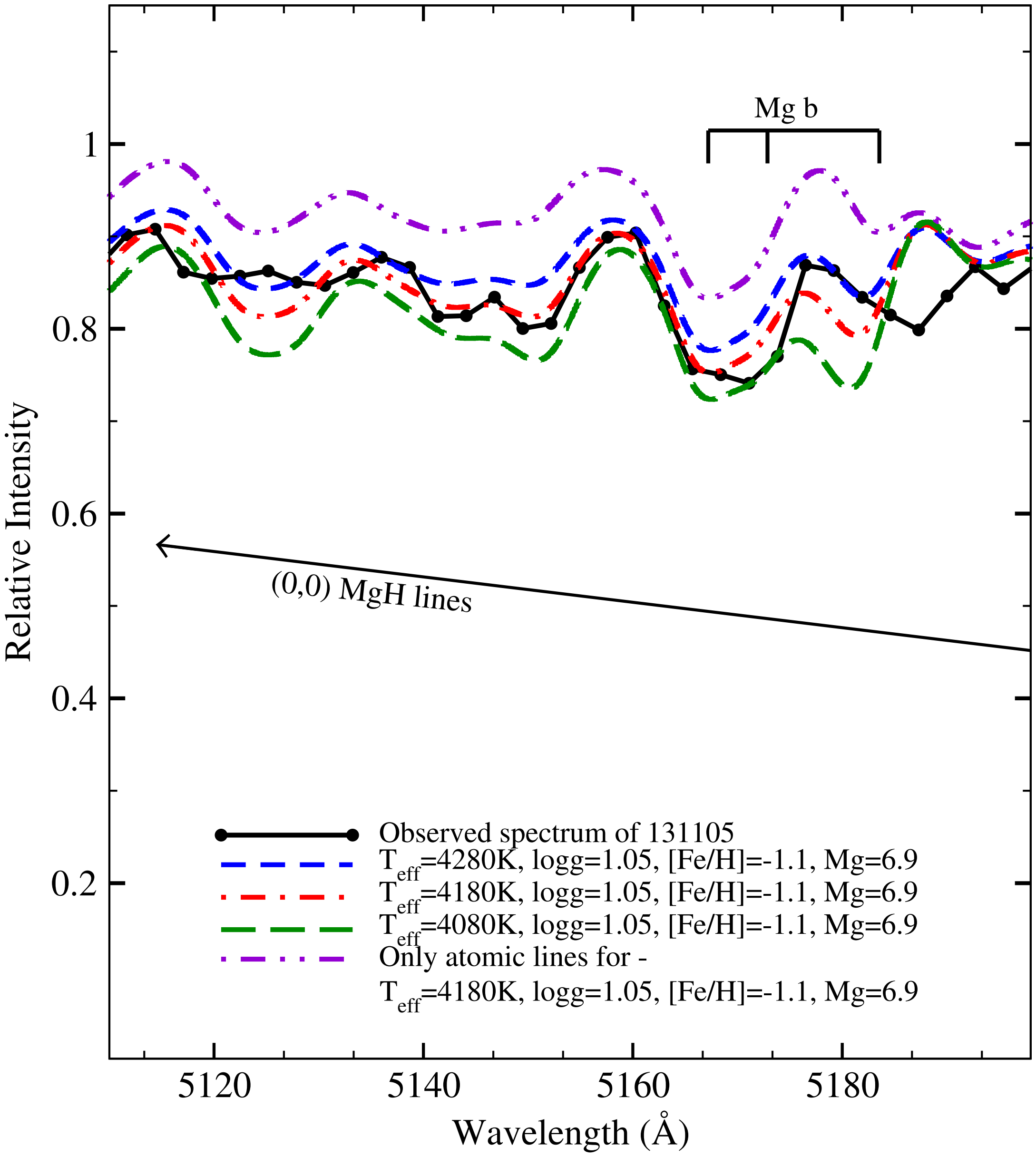

Figure 3.20: The figure shows the observed spectrum and the synthesized spectra for the star 131105. The best fit obtained for the Mg abundance of about 6.9, is shown in red dash dotted line. The syntheses for the upper (blue short dashed line) and the lower (green long dashed line) limit of the $T_{\rm eff}$ are also shown.The synthesis for the pure atomic lines is shown in violet dash double dotted line. See Figure 3.11 for the identifications of the subordinate lines of MgH band.

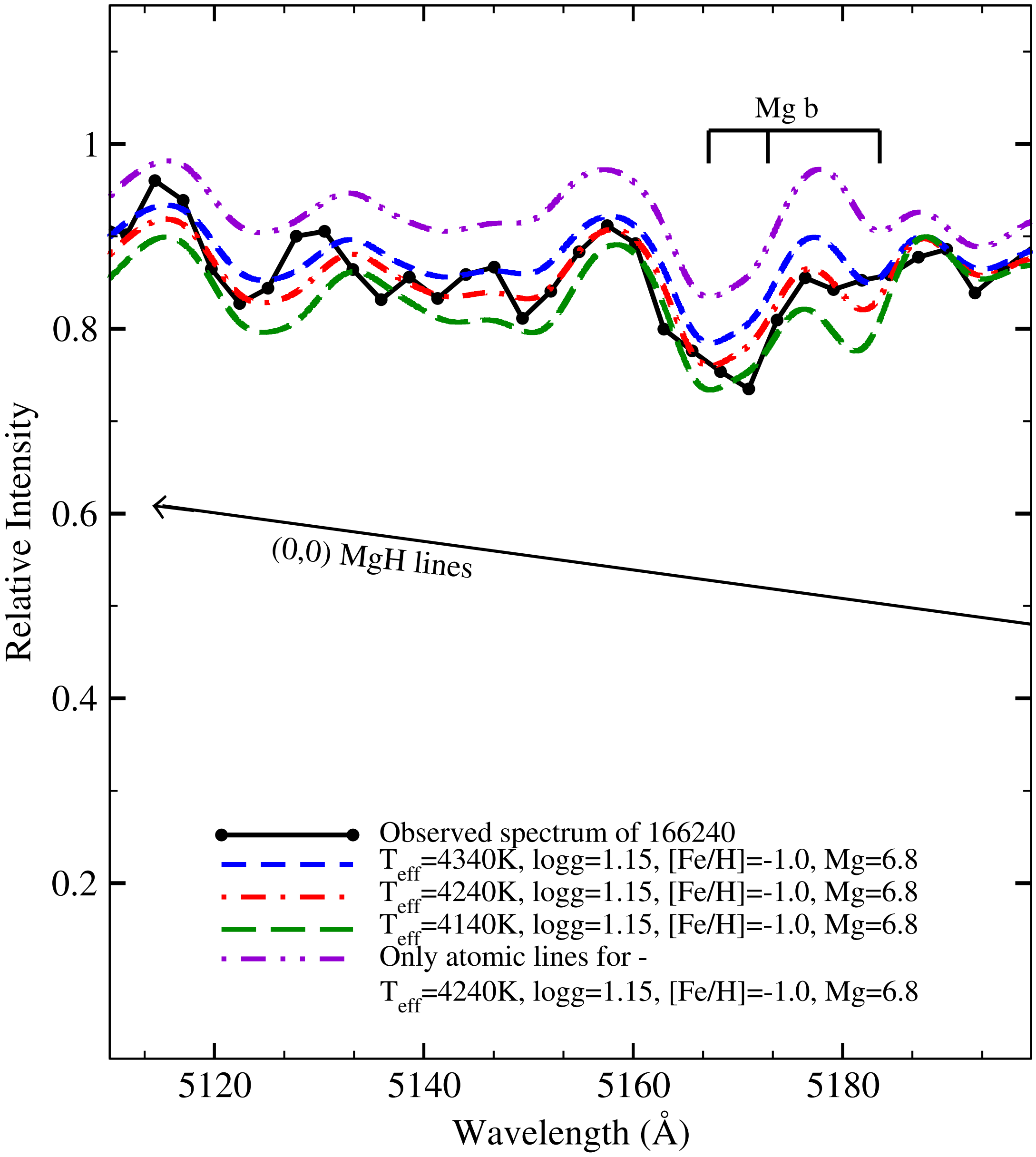

FIGURE 3.21: The figure shows the observed spectrum and the synthesized spectra for the star 166240. The best fit obtained for the Mg abundance of about 6.8 is shown in red dash dotted line. The syntheses for the upper (blue short dashed line) and the lower (green long dashed line) limit of the $T_{\rm eff}$ are also shown.The synthesis for the pure atomic lines is shown in violet dash double dotted line. See Figure 3.11 for the identifications of the subordinate lines of MgH band.

[Mg/Fe]=+0.4, which is as expected for red giants of ω Cen. The spectra were also synthesized for the upper and the lower limits of the star's $T_{\rm eff}$, and the syntheses are shown in Figure 3.22.

5001638: The spectrum was synthesized in the wavelength window as discussed above, for the star's $T_{\rm eff}$=4400K, $\log g$=1.60, and [Fe/H]=-0.5, as estimated in this study. By adjusting the Mg abundance, the best fit was obtained to the observed subordinate MgH lines. The Mg abundance derived was about 7.3, or [Mg/Fe]=+0.2, which is as expected. The spectrum was also synthesized for the upper and the lower limit of the $T_{\rm eff}$, and are shown in Figure 3.23.

270931: The spectrum was synthesized in the wavelength window as discussed above, for the star's stellar parameters, $T_{\rm eff}$=4420K, $\log g = 1.25$, and [Fe/H]=−0.5, as estimated in this study. By adjusting the Mg abundance, the best fit to the observed subordinate MgH lines was obtained. The Mg abundance derived was about 7.2, or [Mg/Fe]=+0.1. The [Mg/Fe] is as expected for the giants of ω Cen. The syntheses for the best fit and for the upper and the lower limits of $T_{\rm eff}$ are shown in Figure 3.24.

216815: The spectrum was synthesized in the wavelength window as discussed above, for the star's $T_{\rm eff}$=4500K, $\log g = 1.85$, and [Fe/H]=−0.6, as given by Johnson & Pilachowski (2010). By adjusting the Mg abundance, the best fit was obtained to the observed subordinate MgH lines. The Mg abundance derived was about 7.3, or [Mg/Fe] = +0.3. The [Mg/Fe] value is as expected for the ω Cen red giants. The syntheses are shown in Figure 3.25. The spectra were also synthesized for the upper and the lower limit of the $T_{\rm eff}$ and are shown in the Figure 3.25.

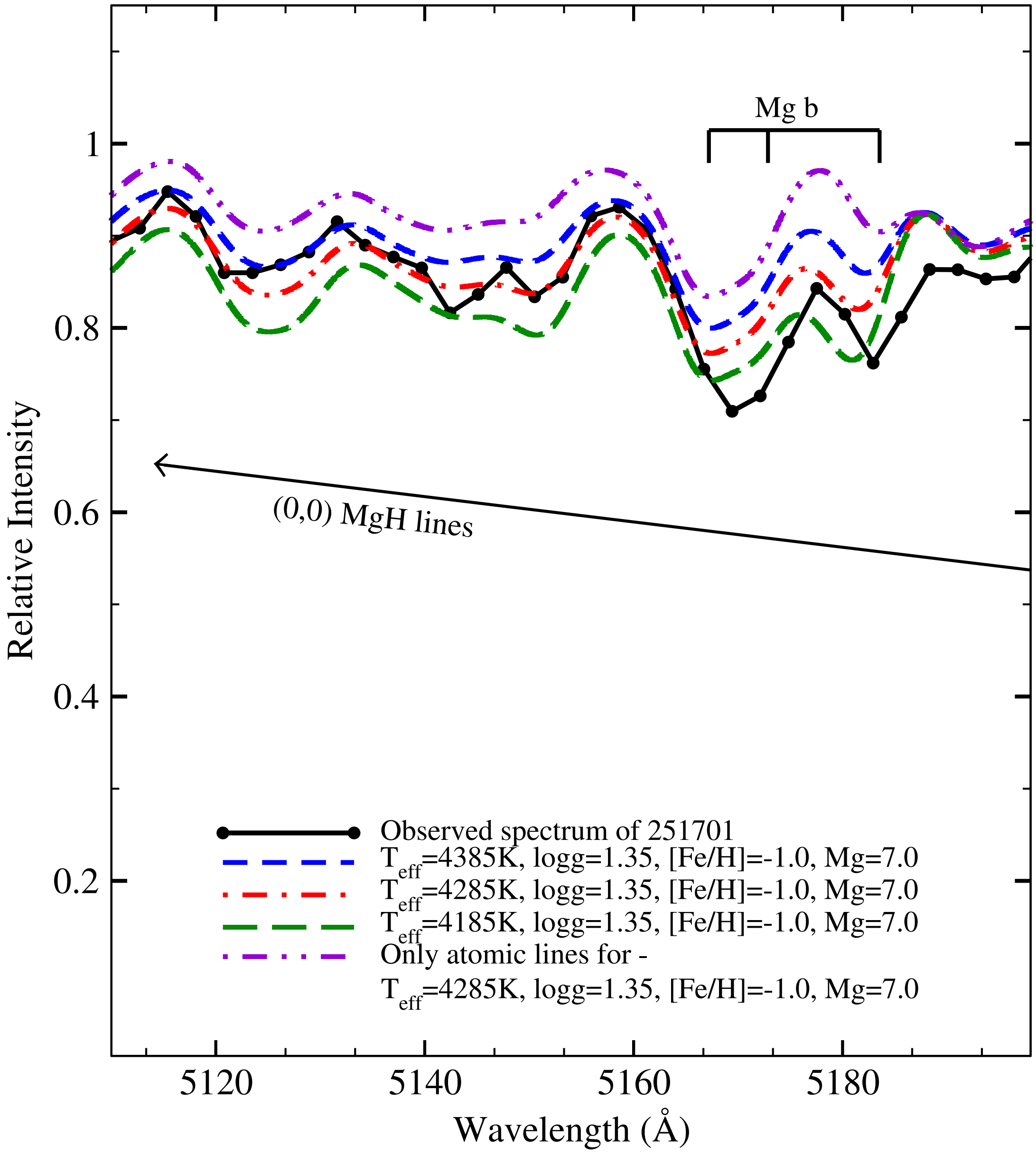

FIGURE 3.22: The figure shows the observed spectrum and the synthesized spectra for the star 251701. The best fit obtained for the Mg abundance of about 7.0 is shown in red dash dotted line. The syntheses for the upper (blue short dashed line) and the lower (green long dashed line) limit of the $T_{\rm eff}$ are also shown.The synthesis for the pure atomic lines is shown in violet dash double dotted line. See Figure 3.11 for the identifications of the subordinate lines of MgH band.

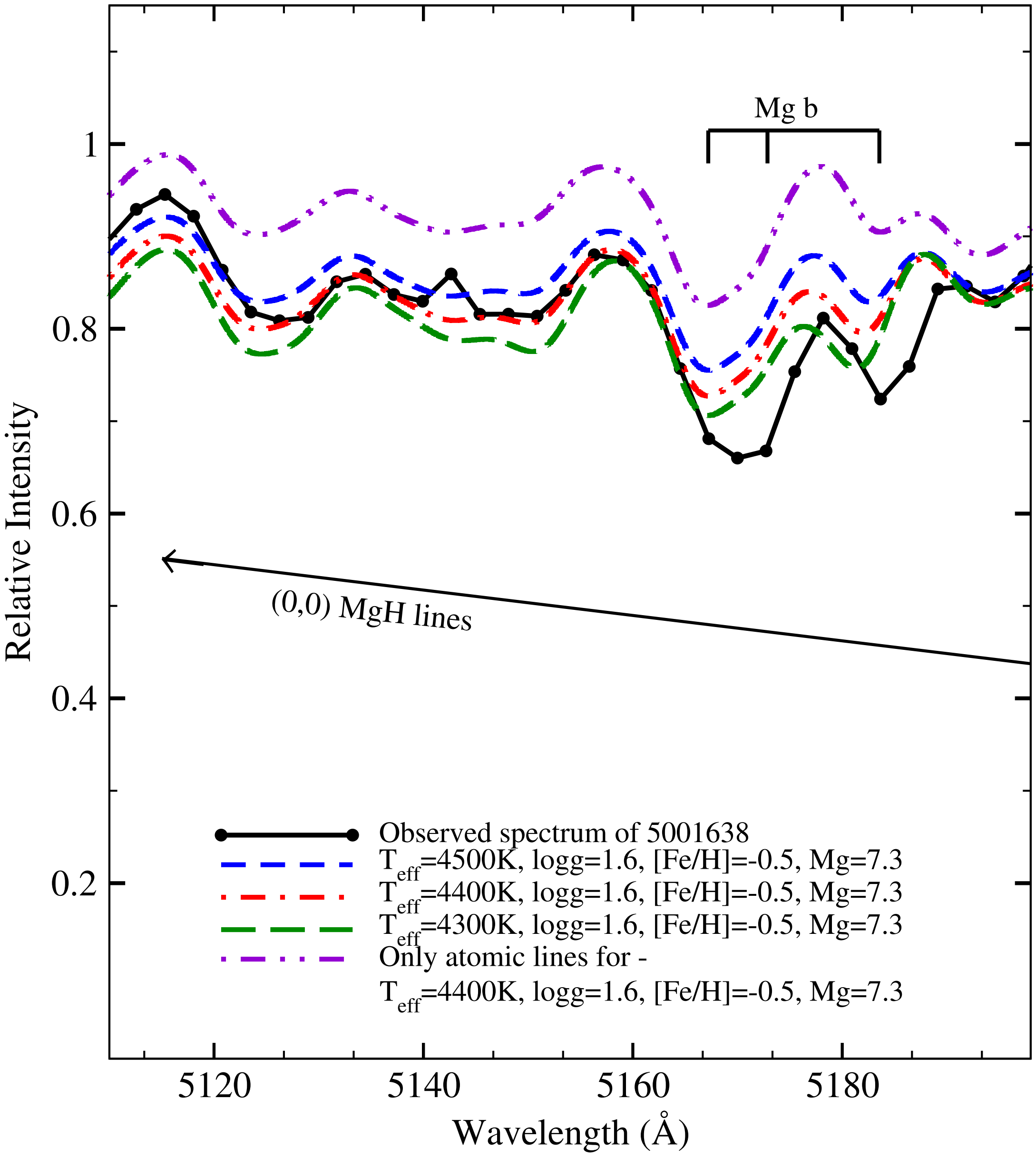

FIGURE 3.23: The figure shows the observed spectrum and the synthesized spectra for the star 5001638. The best fit obtained for the Mg abundance of about 7.3 is shown in red dash dotted line. The syntheses for the upper (blue short dashed line) and the lower (green long dashed line) limit of the $T_{\rm eff}$ are also shown.The synthesis for the pure atomic lines is shown in violet dash double dotted line. See Figure 3.11 for the identifications of the subordinate lines of MgH band.

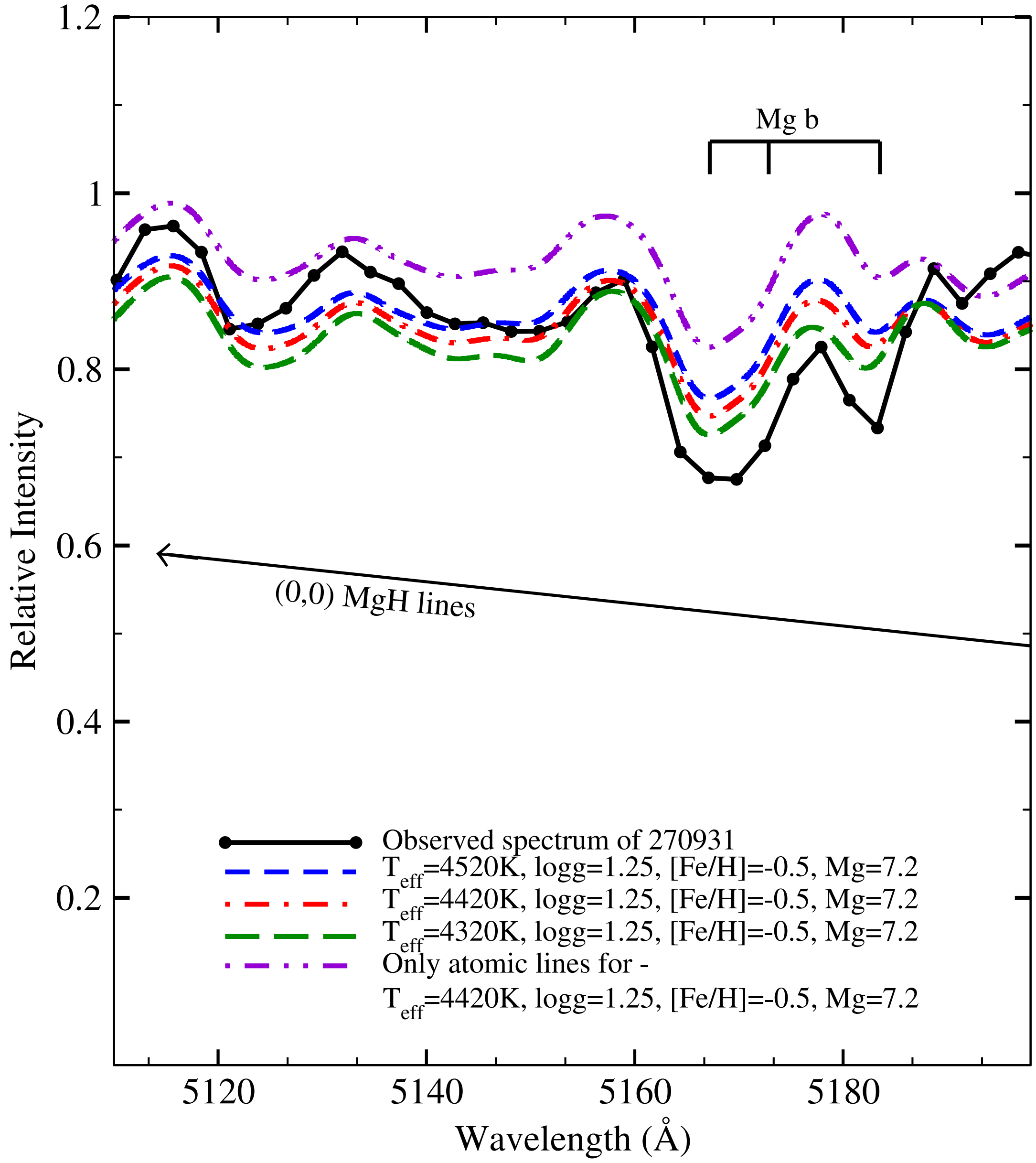

FIGURE 3.24: The figure shows the observed spectrum and the synthesized spectra for the star 270931. The best fit obtained for the Mg abundance of about 7.2 is shown in red dash dotted line. The syntheses for the upper (blue short dashed line) and the lower (green long dashed line) limit of the $T_{\rm eff}$ are also shown.The synthesis for the pure atomic lines is shown in violet dash double dotted line. See Figure 3.11 for the identifications of the subordinate lines of MgH band.

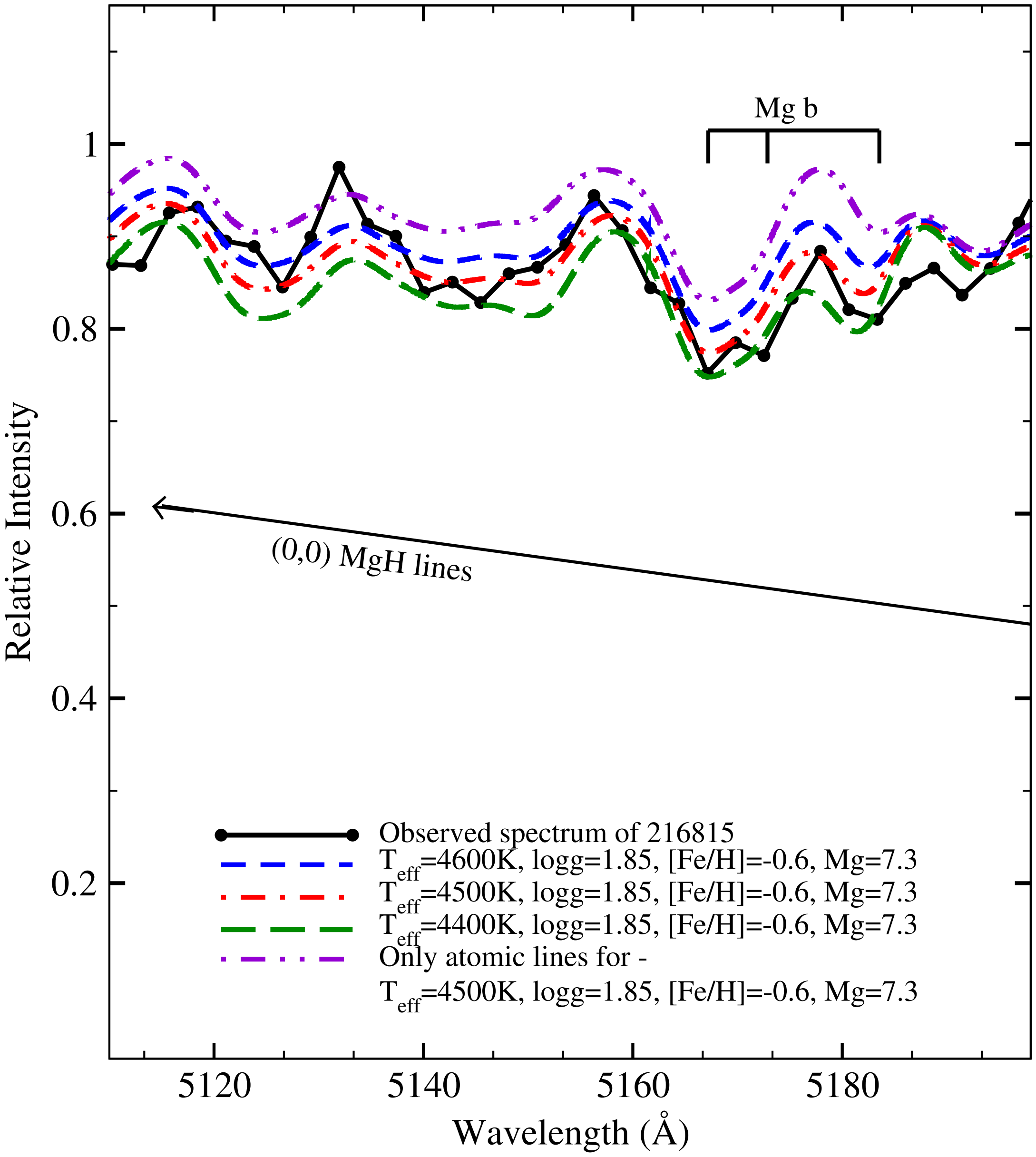

FIGURE 3.25: The figure shows the observed spectrum and the synthesized spectra for the star 216815. The best fit obtained for the Mg abundance of about 7.3 is shown in red dash dotted line. The syntheses for the upper (blue short dashed line) and the lower (green long dashed line) limit of the $T_{\rm eff}$ are also shown.The synthesis for the pure atomic lines is shown in violet dash double dotted line. See Figure 3.11 for the identifications of the subordinate lines of MgH band.

3.6 Spectrum Syntheses and Analyses of the 3^{rd} group stars

The 3^{rd} group comprises stars having strong Mg b lines and no MgH band in their observed spectra.

To investigate the reason for the absence of the MgH band in the observed spectra of the 3^{rd} group stars, the metal rich/poor stars (1^{st} and 2^{nd} group) with similar stellar parameters as the 3^{rd} group were selected. Figure 3.26 shows the plot of y magnitude (Strömgren visual) versus (J_0-K_0) colour for the three groups identified. The stars encircled are of similar y and (J_0-K_0) values, hence, representing similar effective temperatures and surface gravities. The error bar at the bottom right represents the error in (J_0-K_0), and the error in y is less than the size of the symbols (see Figure 3.26).

The spectra of these encircled stars including the 3^{rd} group are then compared with each other. For similar (J_0-K_0) colours and y magnitudes, the observed spectra of metal rich stars, the 1^{st} group, show clearly the presence of the MgH band, which is absent in the observed spectra of the 3^{rd} group (see Figure 3.27 for example). In the following sections, the observed spectra of the 3^{rd} group are analysed in detail.

262788: The observed spectrum of the 3^{rd} group star 262788 was compared with the observed spectrum of the 1^{st} group star 251701. Note that, these two stars have similar y magnitude and the (J_0-K_0) colour. Similar stellar parameters are also reported by Johnson & Pilachowski (2010) for these stars. In the wavelength region that includes Mg b lines and the MgH band, the observed spectra of 262788, the 3^{rd} group star, 251701, the 1^{st} group star, and 14943, the 2^{nd} group star, were compared (see Figure 3.27).

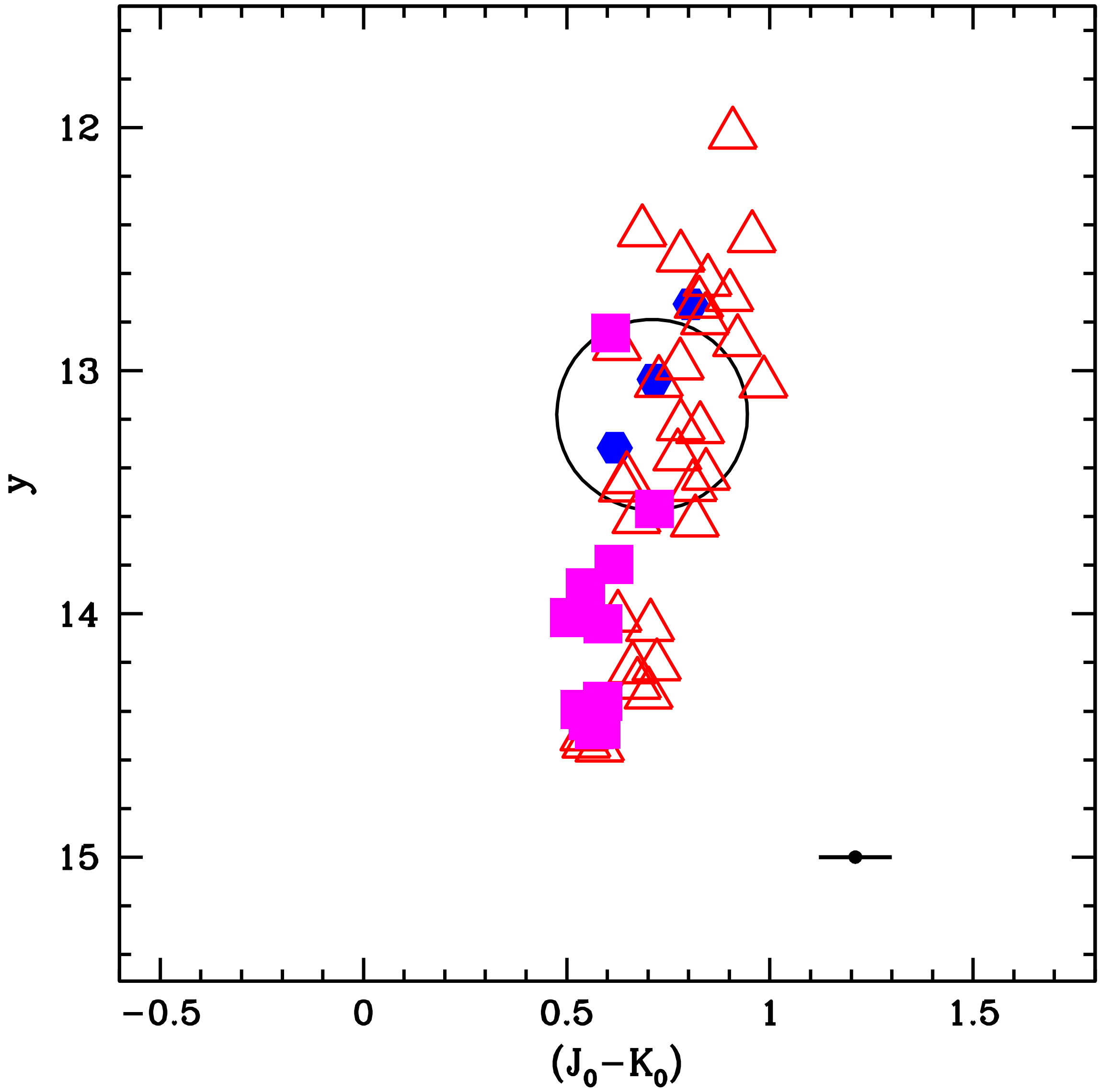

FIGURE 3.26: Figure shows the plot of y magnitude (Strömgren visual) vs. (J_0-K_0). The open red triangles are the metal rich stars, the filled magenta squares are metal poor stars and the filled blue hexagons are the stars of 3^{rd} group. The circle represent the stars with similar (J_0-K_0) and y magnitude. The error bar at the bottom right represents the error in (J_0-K_0), and the error in y is not significant.

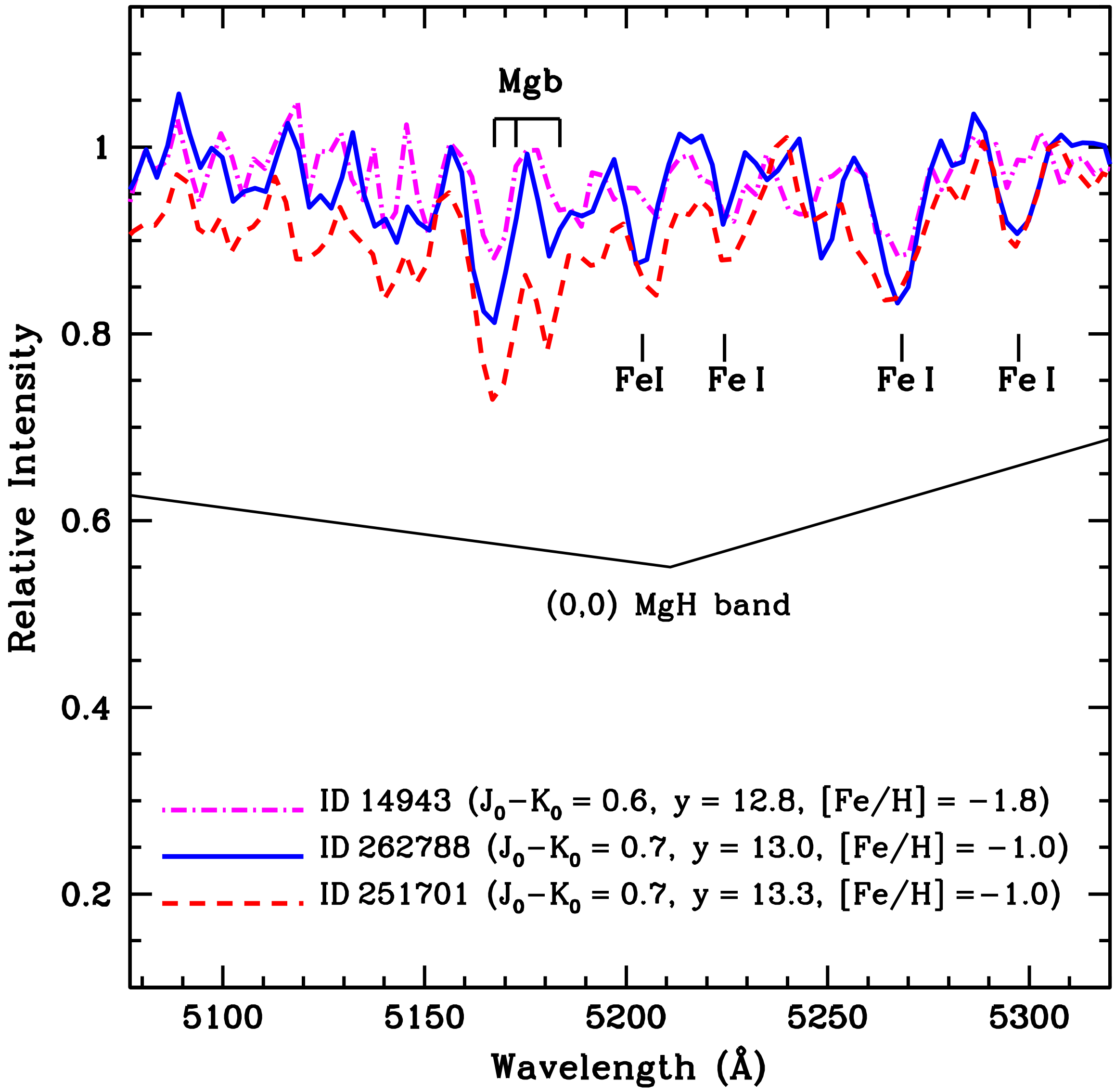

FIGURE 3.27: Figure shows the observed spectrum of 262788, the 3^{rd} group star (in thick blue line) compared with the observed spectrum of 251701, the 1^{st} group star (in red dashed line). These two stars have similar colours (J_0-K_0) and y magnitudes. Also shown is the spectra of 2^{nd} group star with similar (J_0-K_0) and y magnitude (in magenta dash dotted line). The key features such as Mg *b* lines, the MgH band and the Fe I lines are marked. The [Fe/H] values are from Johnson & Pilachowski (2010).

Since the stars 251701 (1^{st} group) and 262788 (3^{rd} group) are of similar $T_{\rm eff}$, $\log g$ and [Fe/H] (see Table 3.3), they are expected to show the MgH band of similar strength. Note the clear presence of the MgH band in the observed spectrum of 251701, 1^{st} group, when compared with 262788, the 3^{rd} group. The 3^{rd} group star, 262788 does not show the MgH band in the observed spectrum (see Figure 3.27). Nevertheless, the observed spectrum of the 3^{rd} group star, 262788 shows strong Mg b lines than the observed spectrum of the 2^{nd} group star 14943, as expected for their respective metallicities. This suggests that the 3^{rd} group star, 262788, is not poor in Mg for its metallicity. Note that, the Fe I lines are of similar strengths in the spectrum of 262788 and 251701, indicating similar metallicities for these two stars (see the Figure 3.27). The observed spectra of these two stars were also compared in the observed wavelength range: 5300 – 6650 Å (see Figure 3.28 for example). The observed spectra of 262788 and 251701, exactly match with one another (note the vertical lines marked in the Figure 3.28).

This comparison clearly shows that, the absence of the MgH band in the 3^{rd} group star, 262788, is not due to the effective temperature, surface gravity and the star's metallicity. Hence, the other reasons for the absence of MgH band would be a relatively lower abundance of magnesium or hydrogen in its atmosphere. The strength of the MgH band in the observed spectrum of 262788 was further analysed by synthesis.

The spectrum was synthesized in the wavelength window: 5110–5200 Å for the star's $T_{\rm eff}$=4265K, $\log g$=1.3, and the [Fe/H]=−1.0, as given by Johnson & Pilachowski (2010). To compare with the observed MgH band strength, the spectrum was synthesized for the Mg abundance of 7.0, or [Mg/Fe]=+0.4, an average value of the [Mg/Fe] for the red giant stars of ω Cen (Norris & Da Costa 1995). The synthesized spectrum for [Mg/Fe]=+0.4 resulted in stronger MgH band strength than the observed (see Figure 3.29). The Mg abundance was then adjusted to match the synthesized spectrum with the observed MgH band strength. The Mg abundance required to obtain the best fit to the observed MgH band strength in

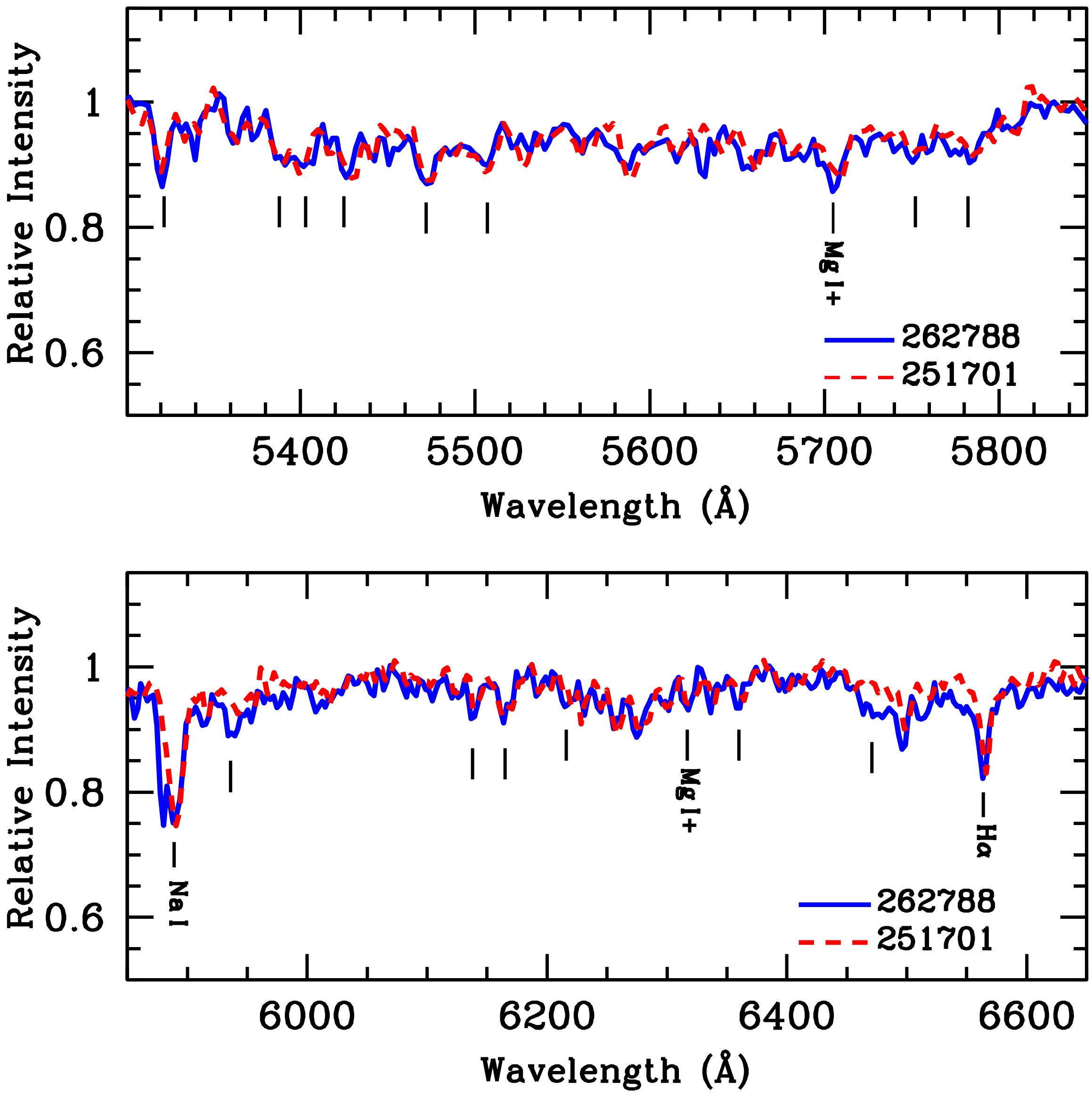

FIGURE 3.28: The Figure shows the comparison of the observed spectrum of 262788, the 3rd group star, with the observed spectrum of 251701, 1st group star. The vertical lines represent the blending metal lines. The Mg I+ represents the blending metal lines including the Mg I lines.

the window 5110–5200Å was about 6.0 or [Mg/Fe]=−0.6. Our derived [Mg/Fe] is about +0.8 dex less than the lowest value ([Mg/Fe]=+0.2) that is reported by Norris & Da Costa (1995) for the red giants of ω Cen at this metallicity. Hence, going by the observed strengths of the Mg b lines, and the reported Mg abundance for the star's metallicity, our derived low Mg abundance for this star is unacceptable.

The observed spectra and the synthesized spectra are shown in Figure 3.29. Spectra were also synthesized for the upper and the lower limit of the $T_{\rm eff}$. Note that, the spectrum synthesized for the upper limit of the $T_{\rm eff}$ with the average Mg abundance of the ω Cen giants do not provide the fit to the observed spectrum. The synthesis for the pure atomic lines is also shown in Figure 3.29. Hence, from the syntheses it is clear that the change in the stellar parameters, cannot account for the observed spectrum of 262788. The results are further discussed in the section 3.7.

193804: The star is identified with the 3^{rd} group. This star has very similar stellar parameters when compared to the other 3^{rd} group star, 262788, as given by Johnson & Pilachowski (2010). The observed spectra of these two 3^{rd} group stars are very similar (see Figure 3.3). Hence, we conclude this star is a twin of 262788.

The spectrum of the star was synthesized in the wavelength window: 5110–5200Å for its stellar parameters, $T_{\rm eff}$=4335K, $\log g$=1.1, and [Fe/H]=−1.0, as given by Johnson & Pilachowski (2010). The spectrum was synthesized by adjusting the Mg abundance to match with the observed spectrum. The best fit of the synthesized spectrum to the observed spectrum was obtained for the Mg abundance less than 6.5, or [Mg/Fe]<−0.1. However, the derived Mg abundance is the upper limit for the star, and is lower than that expected for the star's metallicity, similar to that of 262788, the twin. Note that, these two stars, with similar stellar parameters, have Mg b lines of the same strength in their observed spectra. As judged by the Mg b lines strengths, the derived Mg abundances from MgH band are much lower than expected for the stars' metallicities. Nevertheless, absence of MgH band in

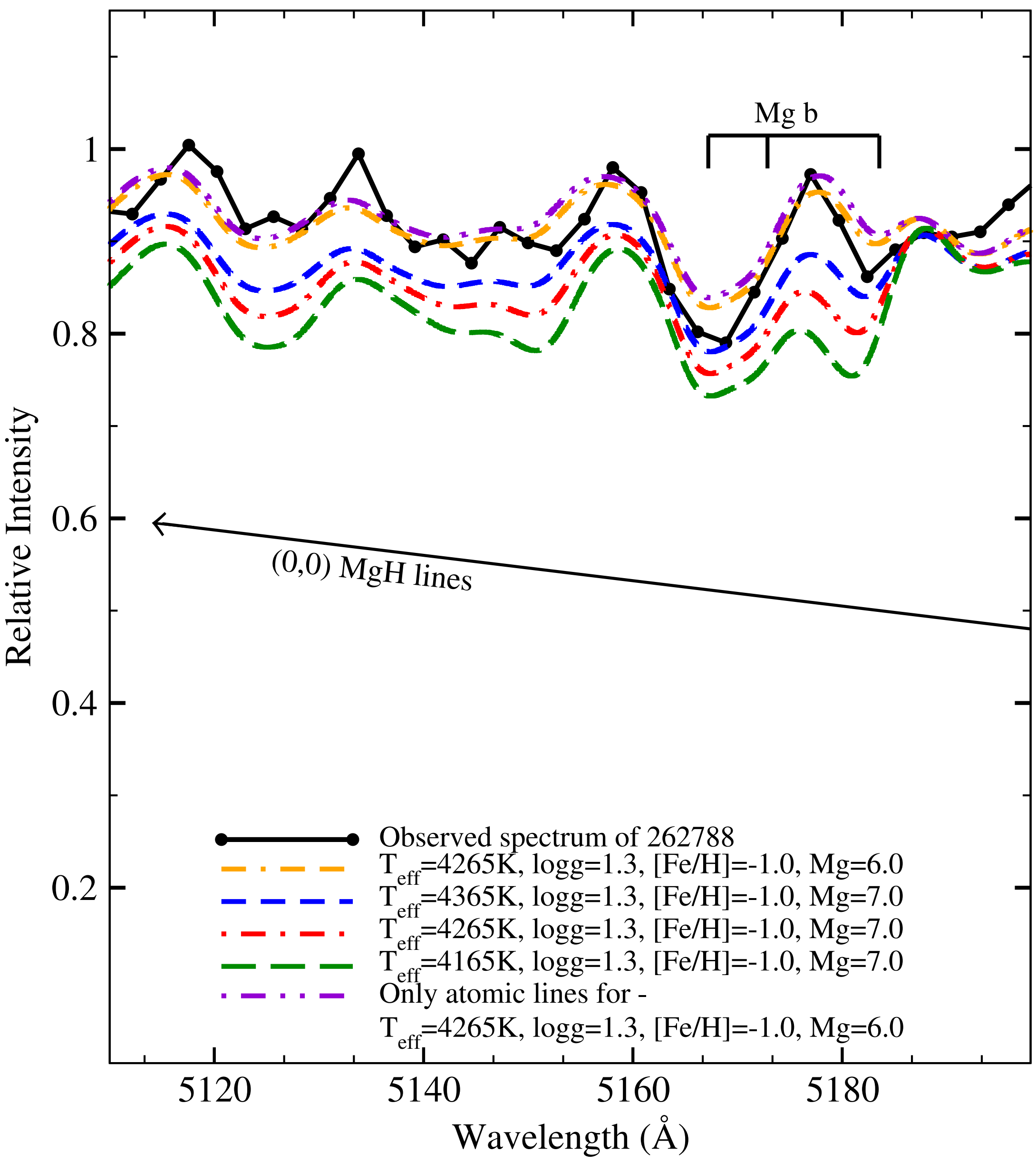

FIGURE 3.29: The figure shows the observed spectrum and the synthesized spectra for the star 262788. The best fit to the observed spectrum is shown in orange dot double dashed line, synthesized for the Mg=6.0. The syntheses for the expected Mg abundance for the ω Cen giants i.e. [Mg/Fe]=+0.4, is shown in red dash dotted line, along with the upper (blue short dashed line) and the lower (green long dashed line) limit of the $T_{\rm eff}$. Note that, the synthesis for the upper limit of the $T_{\rm eff}$ is not providing the better fit to the observed spectrum. The synthesis for the pure atomic lines, for the derived Mg abundance, is also shown in violet dash double dotted line. See Figure 3.11 for the identifications of the subordinate lines of MgH band.

the observed spectrum can be explained by relatively lower hydrogen in the stars' atmosphere. The syntheses for the upper and the lower limit of the star's $T_{\rm eff}$ are also shown in Figure 3.30, along with the pure atomic lines.

214247: This is one of the three stars identified in the 3^{rd} group. As given by Johnson & Pilachowski (2010) the stellar parameters for 214247 are $T_{\rm eff}$=4430K, $\log g$=1.45, and [Fe/H]=−1.5. The star is hotter and metal poor than the other two stars of the 3^{rd} group, namely, 262788 and 193804.

The observed strength of the MgH band was analyzed by synthesis. The spectrum was synthesized in the wavelength window: 5110–5200 Å, for the above mentioned stellar parameters as given by Johnson & Pilachowski (2010). The best fit of the synthesized spectrum to the observed spectrum was obtained by adjusting the Mg abundance. The best fit to the observed spectrum was obtained for the Mg abundance of about 6.5, or [Mg/Fe]=+0.4, which is as expected for star's metallicity (see Figure 3.31). The syntheses are also shown for the upper and the lower limit of the $T_{\rm eff}$, along with the synthesis for the pure atomic lines. The synthesis shows that the absence of the MgH band in the observed spectrum of 214247 is due to a relatively higher effective temperature and the lower metallicity, for the expected/normal Mg and H abundance.

3.7 Discussion

The observed spectra of the red giant stars of ω Cen were analyzed by comparative studies, and also by synthesizing the spectra for their adopted stellar parameters. Spectra of 17 stars, having good signal-to-noise were analysed. Based on the strengths of the Mg b lines and the (0, 0) MgH band in their observed spectra, these program stars were classified into three groups. The first group stars are metal rich having strong Mg b lines and the MgH band in their observed spectra. The second group stars are metal poor with weak Mg b lines and no MgH band in

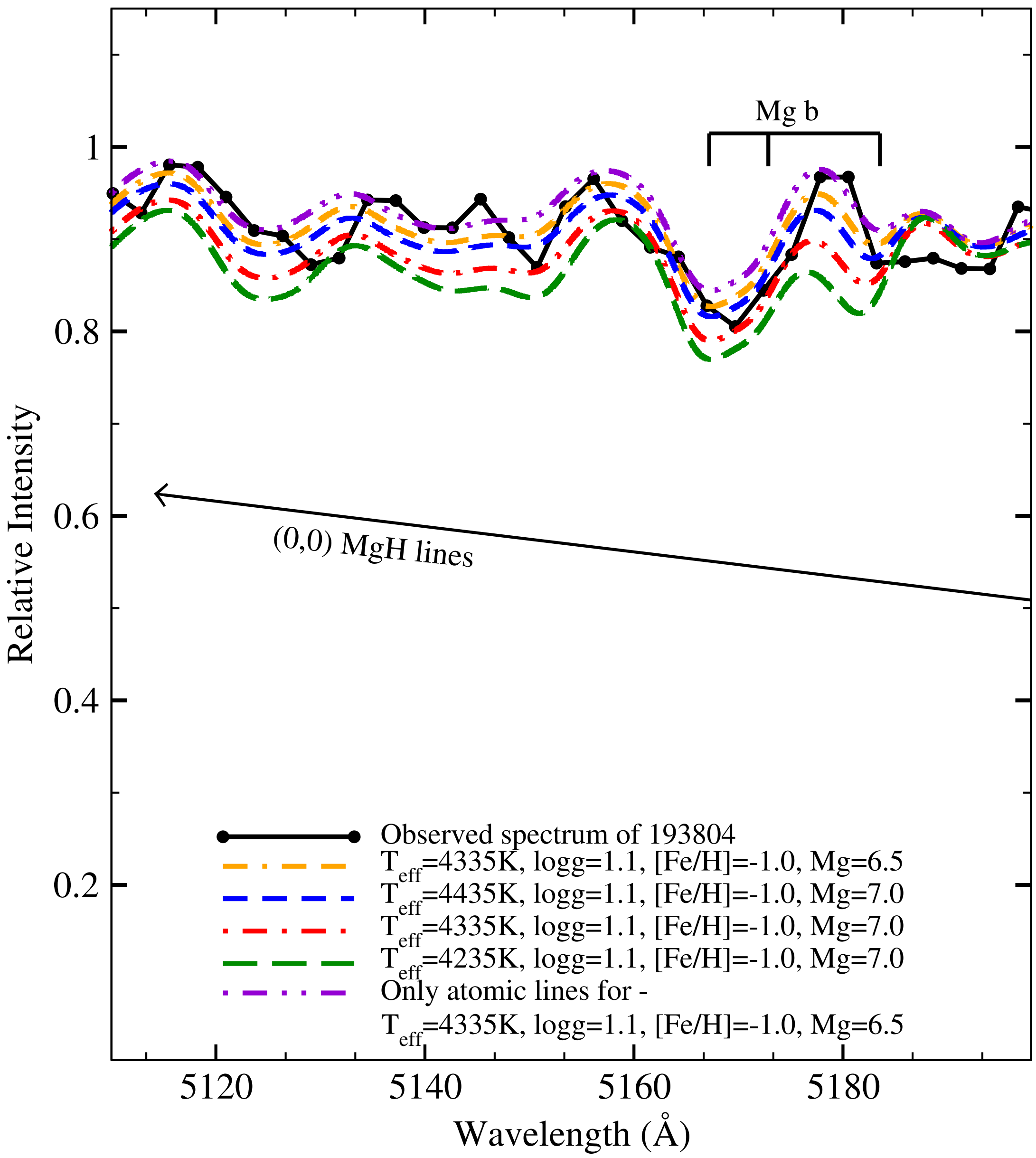

FIGURE 3.30: The figure shows the observed spectrum and the synthesized spectra for the star 193804. The best fit to the observed spectrum is shown in orange dot double dashed line, synthesized for the Mg=6.5. The syntheses for the expected Mg abundance for the ω Cen giants i.e. [Mg/Fe]=+0.4, is shown in red dash dotted line, along with the upper (blue short dashed line) and the lower (green long dashed line) limit of the $T_{\rm eff}$. The synthesis for the pure atomic lines, for the derived Mg abundance, is also shown in violet dash double dotted line. See Figure 3.11 for the identifications of the subordinate lines of MgH band.

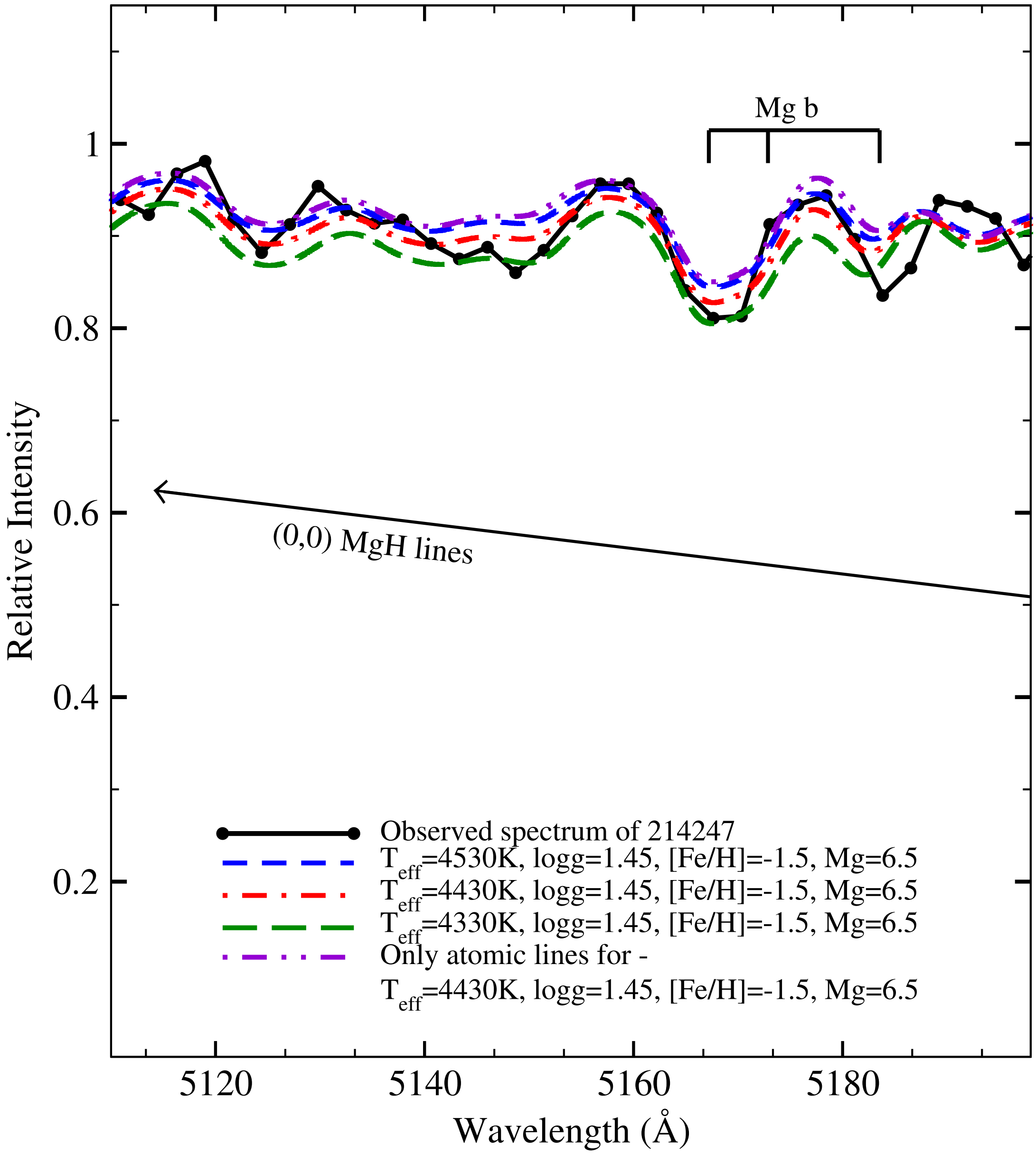

FIGURE 3.31: The figure shows the observed spectrum and the synthesized spectrum for the star 214247. The best fit obtained for the Mg abundance of about 6.5 is shown in red dash dotted line. The syntheses for the upper (blue short dashed line) and the lower (green long dashed line) limit of the T_{eff} are also shown.The synthesis for the pure atomic lines is shown in violet dash double dotted line. See Figure 3.11 for the identifications of the subordinate lines of MgH band.

their observed spectra. The third group stars are metal rich having strong Mg b lines but no MgH band in their observed spectra. The Mg abundances for these stars were estimated from the observed MgH band strengths.

The Mg b lines and the MgH band in the observed spectra of the 1^{st} group stars with similar stellar parameters ($T_{\rm eff}$, log g and [Fe/H]) were compared with each other. In almost all the stars of the 1^{st} group, the strengths of the Mg b lines and the MgH bands were as expected for their adopted stellar parameters but for two. The two stars of the 1^{st} group with strong Mg b lines and weaker MgH band are 73170 and 178243. The blue degraded (0, 0) MgH band extends from 5330Å–4950Å, with the band head at 5211Å. The MgH subordinate lines to the redward and the blueward of the Mg b lines are clearly weaker in the observed spectra of 73170 and 178243, when compared with the spectra of stars with similar stellar parameters (see Figure 3.6, showing the stars in the order of their increasing $T_{\rm eff}$ from bottom to top). This comparison clearly shows that the weaker MgH band in the spectra of these two stars are not as expected for their adopted stellar parameters. If the weaker MgH band is not due to the star's $T_{\rm eff}$, log g and [Fe/H], the reason would be a lower Mg abundance. Since, these stars are metal rich with strong Mg b lines in their observed spectra, indicate that the Mg abundance in their atmospheres is as expected for their metallicities. Hence, neither the stellar parameters nor the Mg abundances are the possible reasons for the weaker MgH bands in these stars. The only possible reason for the weaker MgH bands would be the lower abundance of hydrogen in these stars.

Further, the Mg abundances for the 1^{st} group stars were estimated from the observed MgH band strengths by syntheses. Our estimated Mg abundances were compared with those determined by Norris & Da Costa (1995) for the two common stars in our sample. And, our determinations are in very good agreement with those determined by them. For all the 1^{st} group stars, our derived Mg abundances for the adopted stellar parameters are as expected for the red giants of ω Cen, as given by Norris & Da Costa (1995), with just two exceptions, 73170 and 178243

Table 3.4: The abundances of α elements from Johnson & Pilachowski (2010) for the program stars. The newly identified hydrogen deficient stars are given in boldface.

Star	Star(LEID)	Group	[Si/Fe]	[Ca/Fe]	[Mg/Fe]
73170	39048	First	+0.62	+0.29	···
178243	60073	First	+0.48	+0.34	···
172980	61067	First	+0.74	+0.46	···
178691	50193	First	+0.40	+0.10	···
40867	54022	First	+0.42	+0.21	···
131105	51074	First	+0.48	+0.29	···
166240	55101	First	+0.39	+0.34	···
262788	34225	Third	+0.36	+0.30	···
251701	32169	First	+0.42	+0.35	···
193804	35201	Third	+0.06	+0.11	···
214247	37275	Third	+0.45	+0.41	···
216815	43475	First	+0.20	+0.05	···
14943	53012	Second	+0.31	+0.25	···

(see Figure 3.32). For the derived Mg abundance of 73170, the [Mg/Fe] is about −0.2. This value is about +0.6 dex lower than the average value of the Mg abundance, and about +0.4 dex lower than the minimum Mg abundance, derived for the ω Cen giants at the star's metallicity of [Fe/H]=−0.65, as reported by Norris & Da Costa (1995). For the derived Mg abundance of 178243, the [Mg/Fe] is about −0.4. This value is about +0.8 dex lower than the average Mg abundance, and about +0.6 dex lower than the minimum Mg abundance, derived for the red giants of ω Cen at the star's metallicity of [Fe/H]=−0.8 (Norris & Da Costa 1995). Nevertheless, going by the observed strengths of the Mg b lines and the reported Mg abundance for the stars' metallicity, our derived low Mg abundances for these two stars are unacceptable. Hence, this confirms that the weaker MgH bands in these two stars are not due to the stellar parameters and the Mg abundances, but most probably due to a relatively lower abundance of hydrogen in their atmospheres.

The two 3^{rd} group stars, 262788 and 193804, have similar stellar parameters, as given by Johnson & Pilachowski (2010), and their observed spectra are identical

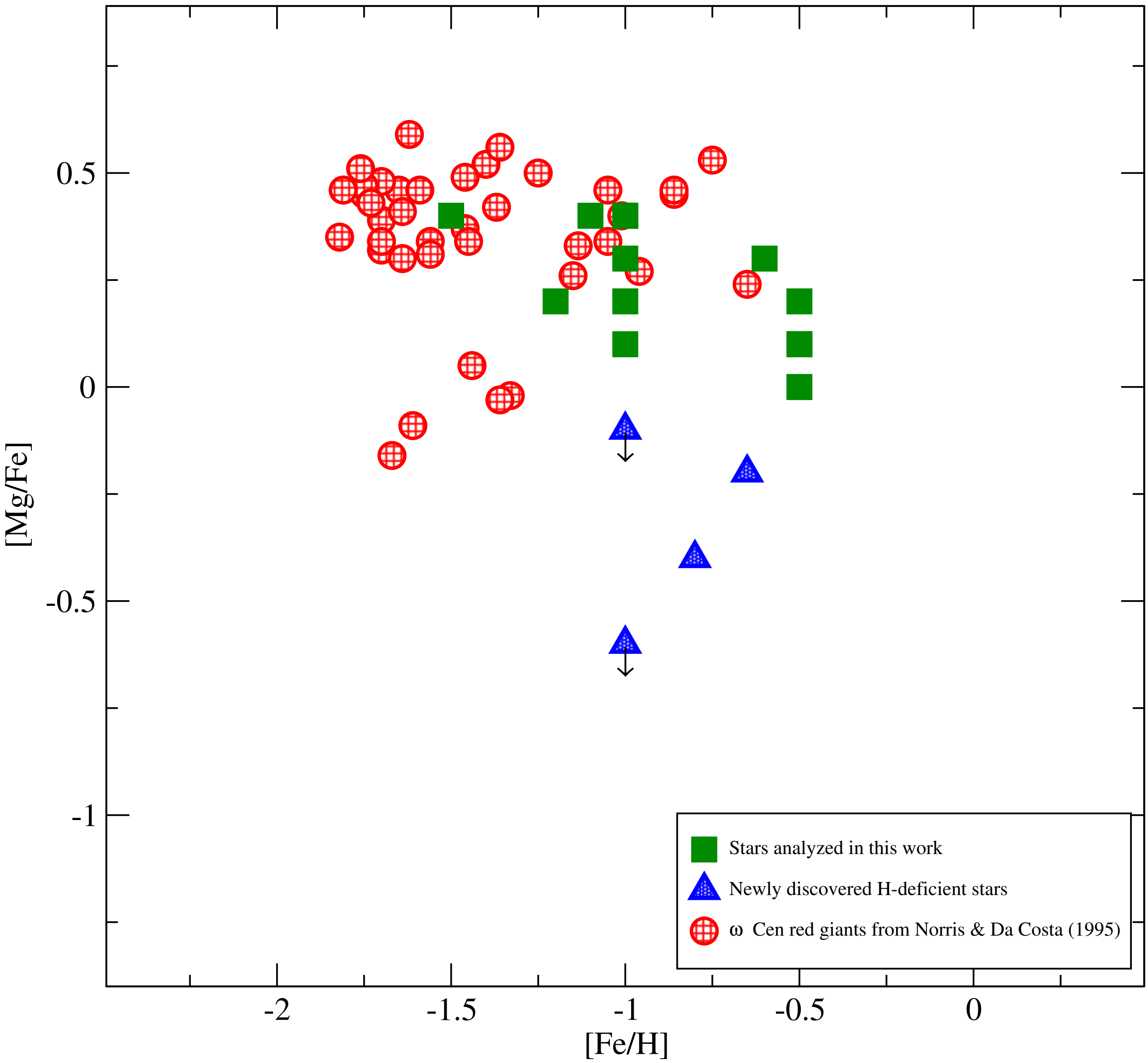

FIGURE 3.32: The figure shows the plot of [Mg/Fe] vs. [Fe/H] for the red giants of ω Cen. The red filled circles are from Norris & Da Costa (1995), the 40 red giants from their study. The green filled squares are the stars analysed in this work. The blue filled triangles are the four newly discovered H-deficient stars, from our sample. The [Mg/Fe] for the two H-deficient stars with downward arrow represent the upper limits.

(see Figure 3.3). Hence, these two stars are treated as twins. The observed spectra of these two 3^{rd} group stars were compared with the observed spectra of the 1^{st} group stars of similar stellar parameters (see Figure 3.28 for example). The 1^{st} group stars with similar stellar parameters as the twins of the 3^{rd} group, show a clear presence of the MgH band in their observed spectra, but note the absence of MgH bands in the observed spectra of the twins. The reason for the absence of the MgH band in the spectra of these twins would be a lower Mg abundance in their atmospheres. However, the Mg *b* lines in their observed spectra are strong, as expected for their metallicity and similar in strengths to those of the 1^{st} group stars. The Mg *b* lines in the spectra of these twins, belonging to the 3^{rd} group, are fairly stronger than the spectra of the 2^{nd} group stars. Note that, the 2^{nd} group stars are metal poor and have weak or no Mg *b* lines. The strong Mg *b* lines in the spectra of the 3^{rd} group stars, 262788 and 193804, clearly indicate that the Mg abundance is normal or as expected for the stars' metallicity. Hence, the stellar parameters and the lower Mg abundances are ruled out as the possible reasons for the absence of the MgH band in the spectra of these stars. The only possibility could be a relatively lower abundance of hydrogen in their atmospheres.

Further, the Mg abundances were estimated for the three stars of the 3^{rd} group by spectrum syntheses (see Figure 3.32). The Mg abundance for the relatively warmer star, 214247, of the 3^{rd} group is as expected for the star's metallicity. The observed weak/absent MgH band in 214247 is as expected for the star's warmer $T_{\rm eff}$ and metallicity. For 262788, the derived [Mg/Fe]≤-0.6. This is about $+1.0$ dex lower than the average [Mg/Fe] value, or about $+0.8$ dex lower than the minimum [Mg/Fe] value, derived for the red giants of ω Cen (Norris & Da Costa 1995), for the star's metallicity, [Fe/H]$=-1.0$. For 193804, the derived [Mg/Fe]<-0.1. This value is about $+0.5$ dex lower than the average [Mg/Fe] value, or about $+0.3$ dex lower than the minimum [Mg/Fe] value, as reported for the red giants of ω Cen by Norris & Da Costa (1995), for the star's metallicity [Fe/H]$=-1.0$. Hence, going by the observed strengths of the Mg *b* lines, and the reported Mg abundance for the stars' metallicity, our derived low Mg abundances for these two stars are unacceptable. This rules out the effect of stellar parameters and the lower Mg abundances, as the possible reasons for the absence of the MgH band in the observed spectra of 262788 and 193804, the 3^{rd} group stars. The only possible reason for the absence of MgH band, can be a relatively lower abundance of hydrogen in their atmospheres.

As seen in Figure 3.32, there are five ω Cen giants in the sample of Norris & Da Costa (1995) which are underabundant in Mg compared to the other stars of their sample. The common property of this group of five stars is that it contains only CN-strong objects, and all but one of them is clearly oxygen-depleted. However, these are metal poor stars unlike our metal rich program stars.

From the analyses of the observed spectra of these four stars, two from the 1^{st} group and two from the 3^{rd} group, by comparative studies and by spectrum syntheses, we conclude that these stars are hydrogen-deficient.

Johnson & Pilachowski (2010) have reported the abundances of α-elements, Si and Ca, for these four H-deficient stars. These stars show a clear enhancement in the α-elements (see Table 3.4). Hence, the enhancement in these α-elements also imply an enhancement in the Mg abundances. This suggests that these four stars are not expected to be Mg-poor.

From the studies of ω Cen, it is confirmed that there exists a double main sequence. The double main sequence in ω Cen was discovered by Anderson (1997). And, Bedin et al. (2004) confirmed the existence of the double main sequence: the blue main sequence (bMS), and the red main sequence (rMS). Bedin et al. (2004); Norris (2004) hypothesized that, the bMS stars might have a strong He enhancement. By fitting the isochrones for the metallicities determined for rMS and bMS, Norris (2004); Piotto et al. (2005) have confirmed that, the ridge line of the bMS can only be best fitted by an isochrone calculated for Y=0.38, with a range ($0.35 < Y < 0.45$), and the models with the standard He content cannot fit the bMS (see

Figure 7 of Piotto et al. 2005). Piotto et al. (2005) have also determined that the bMS stars are less metal poor than the rMS stars. But, from the canonical stellar models with canonical chemical composition, the bMS should be more metal-poor than rMS.

Dupree & Avrett (2013); Dupree et al. (2011) have provided the direct measure of the helium abundance from the near-infrared transition of He I at 1.08μm for the red giant stars of ω Cen. The helium abundance for the red giants from the spectroscopic studies of Dupree & Avrett (2013); Dupree et al. (2011) is about Y=0.39-0.44. This value is in good agreement with the helium abundance inferred from the stellar structure models for the bMS stars by Norris (2004); Piotto et al. (2005). Dupree et al. (2011) also suggests that the progenitors of the helium enriched red giants may belong to the bMS. The source of helium enrichment in ω Cen stars is not yet clear.

Hence, the four H-deficient stars discovered from our study may belong to the helium enriched red giant population of ω Cen. None of these newly discovered hydrogen deficient stars, show the carbon features as seen in the spectra of RCB stars. Hence, these are not the hydrogen deficient stars of RCB type. To confirm their H-deficiency or the helium enrichment, it is essential to study all these stars by obtaining their high resolution spectra. Hence, we plan to obtain the high resolution spectra of all these stars in the optical/near-infrared wavelengths, for future studies.

Chapter 4

Number of hydrogen-deficient stars in ω Cen and the Galaxy: A prediction

The Extreme Helium (EHe) stars, R Coronae Borealis (RCB) stars, and hydrogen deficient carbon (HdC) stars, in the order of their decreasing effective temperatures, are hydrogen deficient (H-deficient) and carbon rich supergiants. There are only about 104 H-deficient supergiants known in the Galaxy (see Chapter 1, section 1.4). Due to their sparsity and chemical peculiarity, the origin and evolution of these stars is not yet clear. There are two scenarios in contention for their origin. One is the double degenerate (DD) scenario in which a He white dwarf (WD) merges with a CO-WD (Iben & Tutukov 1985; Webbink 1984). The close WD binary results from mass exchange and mass loss of a binary system as it evolves from a pair of main-sequence stars. The final step to the merger is driven by loss of angular momentum by gravitational waves (Renzini 1979). A merger of these two WDs, having a very thin H-rich outer layer, makes the resulting star H-deficient. A merger of two He-WDs is also proposed for the origin of RCBs

(Zhang & Jeffery 2012) and relatively C-poor EHes with high surface gravity (Jeffery & Saio 2002). And, the other is the final flash (FF) scenario, which involves a post-asymptotic giant branch (AGB) star on the WD cooling track, experiencing a final helium shell flash. Ingestion of the H-rich layer into the helium shell makes the star H-deficient (Renzini 1990).

The spectroscopic studies of the H-deficient stars support the DD-scenario for their origin (Asplund et al. 2000; Clayton et al. 2007, 2005; García-Hernández et al. 2009, 2010; Hema et al. 2012; Pandey 2006; Pandey et al. 2001; Saio & Jeffery 2002). The position of a star on the HR-Diagram gives us an idea about its evolution and possibly its origin. Since, the HR-diagram is best studied for the globular clusters, a survey was conducted for identifying the H-deficient stars in the globular clusters. The globular cluster, ω Centauri is the brightest and the largest globular cluster which is well studied in our Galaxy (see Johnson & Pilachowski (2010) and the references therein). Hence, the survey for identifying H-deficient stars was conducted among the red giant stars of globular cluster ω Centauri, spectroscopically. To compare the results of our spectroscopic survey, the number of H-deficient stars, formed by the above discussed scenarios, in the Galaxy and in the globular cluster ω Centauri are estimated.

4.1 Number of H-deficient stars formed by the DD scenario in ω Cen and in the Galaxy

In this section, we discuss the number of H-deficient stars, formed by the DD-scenario in the Galaxy, and in the globular cluster ω Centauri.

For calculating the number of H-deficient stars in the Galaxy formed by DD-scenario, the binary WD fractions are adopted from Nelemans et al. (2001). Nelemans et al. (2001) have studied the double WD systems of the Galaxy theoretically and observationally. The initial binary fraction in the Galaxy was assumed to be 50% (the current binary fraction is assumed to be same as that of the initial binary fraction). For our calculations, we have considered their Model-A, see Table 2 of Nelemans et al. (2001), which assumes an exponential star formation rate and the total population of close binary WDs in the Galactic disk of 2.5×10^8 with 50% binary fraction. Out of this total population, 53%, 25%, and 20% of the double WD systems have two He WDs, two CO WDs, and CO-He WDs, respectively. The remaining 1% of the double WD systems have ONeMg WD.

As given by Nelemans et al. (2001), the current merger rate of WD binaries of all types (mentioned above) is about 2.2×10^{-2} yr^{-1}. Of which, the current merger rate for CO-He WD systems that can form RCB stars is about 4.4×10^{-3} yr^{-1}. Since the fraction of CO+He WD pairs which can form SN Ia, with the combined mass $M_{\rm total} > 1.44 M_\odot$ is negligible, we assume that all the CO+He WD pairs would form H-deficient EHe/RCB/HdC type of stars.

Using the merger rate of 4.4×10^{-3} yr^{-1} for CO-He WDs that form RCB/HdC stars, and their evolutionary time-scales of 10^5 yrs (Saio & Jeffery 2002), the number of RCB/HdC stars in the Galactic field is predicted to be about 440. Recent studies suggest the merger rate for CO+He WD of about 3.8×10^{-3} yr^{-1} (Toonen et al. (2013), private communication). This is in fair agreement with the merger rate estimated by Nelemans et al. (2001).

In globular clusters of the Galaxy, the observed binary fraction of the stars is very low due to the dynamical interactions (binary-single and binary-binary) that leads to a rapid depletion of the binary population in the cluster core and to a lesser extent in the cluster field (Ivanova et al. 2005). Ivanova et al. (2005) study the evolution of binary stars in globular clusters using the population synthesis code and dynamical interactions in the cluster cores with an assumed initial binary fraction of 100%, the current close-binary fraction in the cores of the globular clusters is about 5% – 10%. Milone et al. (2012) from their observational studies, and Ji &

Bregman (2013) from their observational and theoretical studies, have shown that the binary fraction decreases outwards from the center of the globular cluster. Ji & Bregman (2013) have determined the binary fraction for main-sequence stars in 35 globular clusters in the Galaxy, and are in good agreement with their theoretical models. They have also studied the radial distribution of binary fraction in globular clusters. Their observations suggest a decreasing trend towards the periphery which is also consistent with their theoretical predictions. Milone et al. (2012) have investigated the distribution of main-sequence binaries in the core and beyond for 59 globular clusters. According to their analysis, the binary fraction decreases by a factor of 2 at two core radii with respect to the core binary fraction. But, in the cluster envelope, the binary fraction trend with radius tends to flatten, see Figure 36 of Milone et al. (2012).

As determined by Ivanova et al. (2005), the binary fraction for WDs in globular cluster core is about 8% for their model 1. Their model 1 assumes the initial binary fraction of 100%, the number density of stars of about 10^5 pc^{-3}, in the core of the cluster and the cluster age of 14 Gyrs (see Table 2 of their paper). An assumption was made that in globular clusters the observed trend for the distribution of binary fraction for main-sequence stars (Milone et al. 2012) also holds for the distribution of the WD binaries. Hence, in the envelop of the globular cluster, white dwarf binary fraction of 4% was adopted, which is a factor of two lower than that in the core of the cluster. Note that, the WD binary fraction as estimated by Hurley & Shara (2003) and Ivanova et al. (2005) in the globular clusters is about 9% and 8%, respectively. Since the binary fraction calculations by Hurley & Shara (2003) are for the globular cluster age of 4 Gyrs, and by assuming the initial binary fraction of 40%, their estimates were thought to be inappropriate for our calculations. Hence, we have adopted the binary fraction from Ivanova et al. (2005), and the correction is applied to estimate the binary fraction in the periphery of the globular cluster. Since our survey for identifying H-deficient stars was conducted in the periphery of the globular cluster ω Centauri, we predict the number of H-deficient stars in the periphery of the cluster.

The total stellar population of the globular cluster ω Centauri is about 2.5×10^6 (van de Ven et al. 2006). From the studies of Ivanova et al. (2005), the cluster core contains only about 1% of the total population of the cluster. The remaining 99% of the stars are located outside the cluster core. Hence, in the case of ω Centauri, the stellar population outside the cluster core is about 2.475×10^6. Taking 4% (the WD binary fraction outside the cluster core) of the total population in the periphery of the cluster, the total number of white dwarf pairs in the periphery of the cluster ω Centauri is about 10^5. Assuming that all these WD pairs are close enough to merge in the Hubble time, the merger rate for all types of WDs was calculated using the age of 12 Gyrs for the globular cluster ω Centauri (Forbes & Bridges 2010). Hence, the merger rate for all types of white dwarf pairs in the globular cluster ω Centauri is about 8.33×10^{-6} yr^{-1}. From the theoretical calculations of Nelemans et al. (2001), about 20% of the double white dwarf systems are the pairs of CO+He white dwarfs. Hence, the merger rate for the CO+He WD pairs in ω Centauri is 1.66×10^{-6} yr^{-1} i.e., 20% of the merger rate for all types of WD pairs. For H-deficient stars cooler than 10,000 K (RCB and HdC stars), the evolutionary time-scales are about 10^5 yrs (Saio & Jeffery 2002). Combining the merger rate and the evolutionary time-scales, the number of RCB/HdC stars (formed by the merger of CO+He WD) in ω Centauri is predicted to be about 0.2. The evolutionary time-scales for EHe stars are as low as 3000 - 300 yr (Saio & Jeffery 2002). With these evolutionary time-scales, no EHe stars (formed by the merger of CO+He WDs) are prdicted in the globular clusters.

The studies of Zhang & Jeffery (2012) show that RCB/HdC and EHe stars can also be formed by the merger of two He WD systems having the merged total mass, $M_{\rm total} \geq 0.8 M_{\odot}$; the total mass less than this value would form sdB and sdO stars (Iben et al. 1996). The merger rate for the double He WD systems in the Galaxy is estimated to be about $0.0057\,{\rm yr}^{-1}$ (Han 1998) and $0.029\,{\rm yr}^{-1}$ (Iben et al.

1997). The number of double He WD systems in the Galaxy peaks around the total mass of 0.6$M_\odot$. About 2.3% of all the He+He WD systems have a merged total mass $\geq$0.8$M_\odot$, the minimum mass required to form H-deficient stars (Han 1998). Hence, the merger rate for double He WDs in the Galaxy resulting in RCB/HdC/EHe stars is about (1.3 - 6.67) $\times$ 10^{-4} yr^{-1}.

From Nelemans et al. (2001), about 53% of all the WD pairs are the pairs of double He WDs. About 2.3% of these He WD pairs are having the M_{total} $\geq$0.8$M_\odot$, and can form RCB/HdC stars. Hence, the merger rate for He WD pairs of all mass range in ω Cen, is about 4.41 $\times$ 10^{-6} i.e., 53% of the merger rate for all types of WDs in ω Centauri, which is about 8.33 $\times$ 10^{-6} yr^{-1}. Hence, the merger rate for the He WD pairs that can form RCB/HdC stars in ω Cen is about 1.00 $\times$ 10^{-7} (which is 2.3% of the merger rate of the double helium white dwarfs of all mass ranges, as discussed above).

From their numerical simulations, Zhang & Jeffery (2012) have calculated the evolutionary time-scales of different stages of a He+He WD merger, with a combined mass of 0.8$M_\odot$, that can form an RCB/HdC/EHe star. The total time taken by a He+He WD merger to evolve into a H-deficient star in the temperatures regime, $3.7 < \log T_{\rm eff} < 3.9$, i.e., RCB/HdC stars, is about 8.1 $\times$ 10^4 yr (see their Figure 1). Using this time-scale with the estimated merger rates for He+He WD binaries in globular cluster ω Centauri, the number of RCB/HdC stars estimated in ω Cen is just about 0.01. Note that, Zhang & Jeffery (2012) predict about 11 - 54 stars in the Galaxy. Similarly, the total evolutionary time-scale required for He-He WD mergers to form H-deficient stars in the temperature range, $4.3 < \log T_{\rm eff} < 4.5$, i.e., EHe stars, is about 16.6 $\times$ 10^4 yr. Combining the evolutionary time-scale with the merger rates for He+He WD binaries in ω Cen, the number of EHe stars estimated in different stages of evolution is about 0.02. The prediction of about 22 - 110 EHes in the Galaxy by Zhang & Jeffery (2012) is noted.

Table 4.1. The predicted number of H-deficient stars in ω Cen for the peripheral white dwarf binary fraction $f_{WD} = 4\%$, in comparison with the number of H-deficient stars in the Galaxy.

	Galaxy	ω Cen for $f_{WD} = 4\%$
Total population	2.5×10^{11}	$2.475\times 10^{6(a)}$
Age (years)	10×10^{9}	12×10^{9}
white dwarf binary population	2.5×10^{8}	$1.0 \times 10^{4(b)}$
Merger rate for all WD pairs (per year)	2.2×10^{-2}	8.33×10^{-6}
Merger rate for CO+He WD pairs (per year) [c]	4.4×10^{-3}	1.66×10^{-6}
Merger rate for He+He WD pairs (per year) [d]	1.16×10^{-2}	4.4×10^{-6}
Merger rate for He+He WD pairs (per year) with ($M_{total} \geq 0.8 M_\odot$)[e]	2.66×10^{-4}	1.00×10^{-7}
No. of RCB/HdCs by the merger of CO+He WD	440	0.17
No. of RCB/HdCs by the merger of He-He WD	27	0.008
No. of EHe stars by the merger of He-He WD	44	0.017

Note. — The evolutionary time-scale for CO+He WD merger for RCB/HdC stars is 10^5 yr. The evolutionary time-scale for He+He WD merger for RCB/HdC stars is 8.1×10^4 yr. The evolutionary time-scale for He+He WD merger for EHe stars is 16.6×10^4 yr.

[a]The population in the periphery of the cluster, that is 99% of the total population, 2.5×10^6.

[b]The white dwarf binary population in the periphery of the globular cluster, that is 4% of the total population in the periphery of the cluster.

[c]About 20% of all the white dwarf binary population are the pairs of CO+He white dwarf binaries.

[d]About 53% of all the white dwarf binary population are the pairs of He+He white dwarf binaries.

[e]Only about 2.3% of the He+He white dwarf binary population with $M_{total} \geq 0.8 M_\odot$ can form RCB-stars.

4.2 Number of FF-objects in ω Cen and in the Galaxy

The other channel that can produce RCB stars is the FF scenario. In this scenario, the asymptotic giant branch (AGB) stars which have evolved off their AGB phase (post-AGB) will experience a final helium shell flash, and enter the AGB phase for the second time in the course of their evolution. The final helium shell flash engulfs the H-rich envelope on top of the He-shell, hence, making the star H-deficient. The final He-shell flash may occur (a) immediately before the star leaves the AGB-phase, (b) in the constant luminosity phase, and (c) on the white dwarf cooling track of the post-AGB stars. The final helium flash that occurs just before the star leaves the AGB-phase, is called 'AGB final thermal pulse' (AFTP) (Blöcker 2003; Herwig et al. 1999; Schönberner 2008). The final flash that occurs on the constant luminosity phase is called the 'late thermal pulse' (LTP). FG Sge, for example, is one such star which is H-deficient, and has experienced LTP (Blöcker 2003; Herwig et al. 1999; Schönberner 2008). The final flash that occurs on the white dwarf cooling track (decreasing luminosity phase) of the post-AGB phase is called 'very late thermal pulse' (VLTP). V4334 Sgr (Sakurai's Object), which is H-deficient, is an example for VLTP (Herwig 2001; Herwig et al. 1999; Schönberner 2008). All these events make a star H-deficient. These events are fast evolving phases of the stellar evolution. For the LTP models, the time interval from the occurence of the LTP/VLTP to the return to the AGB is about 100-200 yr (Bloecker 1995; Herwig 2001; Schoenberner 1979). However, the observed evolutionary time-scale of this event in V4334 Sgr is only few years (Herwig 2001). Note that, just about 20-25% of the stars moving off the AGB are expected to become H-deficient (Iben 1984).

The number of FF-objects in ω Cen were predicted by estimating the total number of AGB stars in ω Cen. In a simple stellar population, such as globular cluster, in which all the stars are formed at the same time, that is with the single cluster age, the number of stars, n_j, in any individual post-main sequence (PMS) phase is directly proportinal to the total bolometric luminosity (L_T) of the population and the duration of that phase (t_j), and is given by the relation:

$n_j = B(t) L_T \, t_j$ — (1)

The proportionality constant $B(t)$ is the *specific evolutionary flux* of the population, which is the number of stars entering or leaving any PMS phase of evolution per year and per solar luminosity of the population (Renzini 1998; Renzini & Buzzoni 1986; Renzini & Fusi Pecci 1988). For the age of ω Cen of about 12 Gyr, $B(t)$ is estimated to be 2.2 × 10^{-11} stars $L_{\odot}^{-1}$ yr^{-1} by Renzini & Buzzoni (1986). The duration of the AGB phase is about 10^7 yrs (Herwig 2005) and the total luminosity of ω Cen of about 10^6 $L_{\odot}$ (Harris 1996). Hence, from Eq. (1), the number of AGB stars in ω Cen are about 220.

The number of stars moving off the AGB phase in ω Cen is estimated by using the total number of AGB stars and the duration of the AGB phase. We estimate about 2.2 × 10^{-5} stars moving off the AGB phase per year. As discussed above, about 20-25% of the stars moving off the AGB phase may experience the final helium shell flash and become H-deficient, i.e., about 4.4 × 10^{-6} to 5.5 × 10^{-6} stars yr^{-1}. Hence, for the post-AGB lifetime of about 10^5 yr, just about 0.44 to 0.55 FF-objects are predicted in ω Cen. For comparison, the predicted FF-objects in the Galaxy are also discussed.

Since the Galactic population is not of the same age, the above discussed method cannot be applied to estimate the number of AGB stars in the Galaxy. Jackson et al. (2002) have studied the distribution of AGB stars in the bulge and the disc of the Galaxy by determining the characteristic luminosity (L_{AGB}) for an AGB star. From their studies, they estimate total of about 2 × 10^5 AGB stars in the Galaxy. We have estimated the number of FF-objects in the Galaxy by adopting their estimated total number of AGB stars in the Galaxy. The number of AGB stars moving off the AGB phase in the Galaxy is calculated to be about 0.02 stars

yr^{-1}, (as discussed above). About 4×10^{-3} to 5×10^{-3} stars yr^{-1}, which is 20-25% of the total AGB stars moving off the AGB phase may experience the final helium shell flash. Hence, for the post-AGB lifetime of 10^5 yr, about 400 - 500 FF-objects are predicted in the Galaxy.

4.3 Conclusions

In the Galactic globular cluster ω Cen, less than a couple of H-deficient supergiants (RCB/HdC/EHe stars and FF-objects) are predicted. These are either formed through the CO+He and He+He WD mergers, or by experiencing the late thermal pulse. The estimated number of H-deficient stars in the Galaxy and in ω Cen, formed by the DD and the FF scenarios are summarized in Tables 4.1 and 4.2. The H-deficient stars predicted in globular cluster ω Cen is about 500 times lower than in the Galactic field.

Table 4.2. The predicted number of FF-objects in the globular cluster ω Centauri and in the Galaxy.

	Galaxy	ω Cen
Total number of AGB stars	2×10^5	220
No. of stars moving off the AGB phase per year	0.02	2.2×10^{-5}
No. of stars experiencing the final flash per year$^{(a)}$	$4 - 5 \times 10^{-3}$	$4.4 - 5.5 \times 10^{-6}$
The total predicted number of FF-objects	400 - 500	0.44 - 0.55

Note. — The duration of AGB phase and the post-AGB phase of 10^7 yr and 10^5 yr are adopted.

[a]About 20-25% of stars moving off the AGB phase are expected to experience the final helium shell flash.

Chapter 5

The Galactic R Coronae Borealis Stars and the Final Flash Object V4334 Sgr

5.1 Introduction

R Coronae Borealis (RCB) stars are a rare class of F- and G-type supergiants with remarkable photometric and spectroscopic peculiarities. The photometric peculiarity is that a RCB may fade rapidly in visual brightness by up to several magnitudes at unpredictable times and slowly return back to maximum light after an interval of weeks, months or even years. Most RCB stars stay for a longer time at maximum light than at minimum light. This fading is generally attributed to the formation of dust in the line of sight. Spectroscopic peculiarities are led by the very weak or undetectable hydrogen Balmer lines in their spectra. This indicates that they have a very H-poor atmosphere. This hydrogen deficiency but not the propensity to undergo optical declines is shared by other rare classes of stars : extreme helium (EHe) stars at the hotter end and hydrogen-deficient carbon (HdC) stars at the cooler end of the RCB temperature range.

Keys to understanding origins of RCB stars and their putative relatives have come from the determination and interpretation of the stars' surface chemical compositions. Two proposed scenarios remain in contention. In one dubbed the double degenerate (DD) scenario, a helium white dwarf merges with a carbon-oxygen (C-O) white dwarf (Iben & Tutukov 1985; Webbink 1984). The close white dwarf binary results from mass exchange and mass loss of a binary system as it evolves from a pair of main sequence stars. The final step to the merger is driven by loss of angular momentum by gravitational waves (Renzini 1979). The envelope of the merged star is inflated to supergiant dimensions for a brief period. An alternative scenario dubbed the final flash (FF) scenario involve a single post-AGB star experiencing a final helium shell flash which causes the H-rich envelope to be ingested by the He shell. The result is the star becomes a hydrogen-deficient supergiant for a brief period, and is sometimes referred in this condition as a born-again AGB star (Renzini 1990).

For the RCB stars, determination of chemical compositions by Lambert & Rao (1994) and Asplund et al. (2000) suggested that the DD rather than the FF scenario gave the superior accounting of the determined elemental abundances. This conclusion has since been supported by the determination from analysis of CO infrared bands of a high ^{18}O (relative to ^{16}O) in cool RCBs and HdC stars (Clayton et al. 2007, 2005; García-Hernández et al. 2009, 2010). Additional evidence comes from high fluorine abundances in EHe (Pandey 2006) and RCB stars (Pandey et al. 2008).

In the case of the RCB stars, there is an unease about the results for the elemental abundance on account of 'the carbon problem' identified and discussed by Asplund et al. (2000). Since the continuous opacity in the optical is predicted to arise from the photoionization of neutral carbon from highly excited states, the strength of an optical C I line, also from a highly excited state, is predicted to be quasi-independent of atmospheric parameters such as effective temperature, surface gravity and metal abundance. Indeed, a C I line has a nearly constant strength across the RCB sample even as (for example) a Fe I or Fe II line may vary widely in strength from one star to the next. However, the predicted strength of a C I line is much stronger than its observed strength: if one were to choose to resolve this discrepancy by adjusting the line's gf-value, it must be reduced by a factor of four or 0.6 dex on average. This discrepancy between predicted and observed C I line strengths is termed 'the carbon problem'. Adjustment of the gf-values of the C I lines is not the only potential or even the preferred way to address the carbon problem.

In this chapter, we present and discuss spectra showing the C_2 Swan bands in a sample of RCB and HdC stars. Our first goal is to compare predicted and observed strengths of C_2 Swan bands in RCB stars to see if they exhibit a carbon problem and if that problem differs from that shown by the C I lines. Our second goal is to look for $^{12}C^{13}C$ lines and determine the $^{12}C/^{13}C$ ratio. A high value of $^{12}C/^{13}C$ ratio is expected for the DD scenario, but a low ratio seems likely for the FF scenario. High ratios or high lower limits on the isotopic ratio have been set for HdC stars : HD 137613 (Fujita & Tsuji 1977), HD 182040 (Climenhaga 1960; Fujita & Tsuji 1977). A limit of greater than 40 was set for R CrB (Cottrell & Lambert 1982). But the RCB star V CrA is apparently an exception with a reported low value of $^{12}C/^{13}C$ ratio: Rao & Lambert (2008) estimated the ratio at 4 - 10 for V CrA.

As expected, a low value of $^{12}C/^{13}C$ ratio is shown by the final flash object V4334 Sgr (Sakurai's object), the ratio is 2 to 5 (Asplund et al. 1997b; Pavlenko et al. 2004). However, the other objects which are thought to be final flash objects, like, FG Sge (Gonzalez et al. 1998) and V605 Aql (Clayton & De Marco 1997; Lundmark 1921), do not show the presence of $^{12}C^{13}C$ bands in their spectrum.

TABLE 5.1: Log of the observations : the stars are listed in the decreasing order of their effective temperature from top to bottom.

Star	Date of Observation	V	Observatory	S/N Ratio
V3795 Sgr	26 July 1996	11.2	McDonald	110
XX Cam	17 November 2002	7.4	McDonald	200
VZ Sgr	22 May 2007	10.2	McDonald	200
UX Ant	5 May 2007	12.8	McDonald	120
RS Tel	28/29 May 2010	9.9	VBT	25
R CrB	5 May 2007	6.0	McDonald	200
V2552 Oph	22 May 2007	11.0	McDonald	128
V854 Cen	24-27 May 2010/10 February 1999	7.25	VBT/McDonald	250
V482 Cyg	23/24 May 2007	10.8	McDonald	152
SU Tau	15 Nov 2002	9.8	McDonald	196
V CrA	6 September 2003	9.5	McDonald	137
GU Sgr	23 May 2007	11.1	McDonald	135
FH Sct	24 May 2007	12.1	McDonald	87
U Aqr	23 July 1996	11.2	McDonald	125
HD 173409	27 May 2010	9.5	VBT	70
HD 182040	25 May 2010	7.0	VBT	110
HD 175893	25 May 2010	9.3	VBT	30
HD 137613	24 May 2010	7.5	VBT	90

5.2 Observations

High resolution optical spectra of RCB/HdC stars at maximum light were obtained from the W. J. McDonald Observatory and the Vainu Bappu Observatory. The dates of observations, the visual validated magnitudes (AAVSO[1]) and the signal-to-noise ratio per pixel of the spectra in the continuum near the 4737 Å $^{12}C_2$ bandhead are given in Table 5.1. In addition to the RCB stars, a spectrum of γ Cyg was obtained at the McDonald Observatory. This F5Ib star is of similar spectral type to the warm RCBs such as R CrB.

The spectra from the McDonald Observatory were obtained with the 2.7-m Harlan J. Smith Telescope and Tull coudé cross-dispersed echelle spectrograph (Tull et al. 1995) at a resolving power of $\lambda/d\lambda$ = 60,000. The spectra from the Vainu Bappu Observatory were obtained with the 2.34-m Vainu Bappu Telescope (VBT)

[1]http://www.aavso.org

equipped with the fiber-fed cross-dispersed echelle spectrometer (Rao et al. 2005) and a 4K × 4K CCD are at a resolving power of about 30,000.

5.3 Spectrum synthesis

Our analysis of the high-resolution spectra proceeds by fitting synthetic spectra to the observed spectra in several band passes providing lines of the C_2 Swan system. For the synthesis of the C_2 Swan bands, we use model atmospheres and as complete a line list as possible. In the following subsections we introduce the line lists for the C_2 Swan bands and the atomic lines blended with the C_2 bands and, finally, the procedure for computing the synthetic spectra.

5.3.1 The Swan bands

The C_2 Swan bands are detectable in all but the hottest RCB stars. They are not seen in either V3795 Sgr or XX Cam with effective temperatures of 8000 K and 7250 K, respectively. In our sample, they are first detectable in VZ Sgr at $T_{\rm eff}$ = 7000 K. The bands are very strong in the coolest RCB stars like U Aqr and the HdC stars. The leading bands of the three sequences: $\Delta\nu = +1$, 0, and -1 are each considered. All bands have blue-degraded bandheads. The (0,0) band of the $^{12}C_2$ molecule with its head at 5165 Å is the strongest band of the entire Swan system. The (1,0) and (0,1) bandheads are at 4737 Å and 5636 Å, respectively. All three bands are synthesized using detailed line lists including the blending atomic lines and appropriate model atmospheres. The (1,0), (0,0), and (0,1) $^{12}C_2$ bands are used to determine the C abundance and, hence, to assess the carbon problem. The (0,1) band is generally a superior indicator of the C abundance because it is less affected by blending atomic lines. However, the (1,0) band is the focus of efforts to determine the $^{12}C/^{13}C$ ratio because the $^{12}C^{13}C$ bandhead is shifted to 4745 Å

TABLE 5.2: Sample lines for (1, 0) C_2 swan band.

Wavelength (Å)	J''	χ **(eV)**	**log** gf
4692.348	28.0	0.342	-0.270
4692.485	28.0	0.342	-0.270
4692.548	27.0	0.342	-0.286
4692.679	26.0	0.342	-0.302
4692.794	61.0	0.940	0.064
4692.838	61.0	0.940	0.064
4692.848	62.0	0.940	0.071
4692.931	60.0	0.940	0.057
4693.077	60.0	0.940	0.057
4694.391	27.0	0.331	-0.286

Note – Table 5.2 is provided in its entirety in the Appendix B of this thesis.

and, thus, 8 Å clear of the blue-degraded $^{12}C_2$ band. For the (0,0) and (0,1) bands, the $^{12}C^{13}C$ lines are mixed among the stronger $^{12}C_2$ lines.

Data required for synthesis of Swan bands include: wavelengths of the transitions, excitation energies of the lower levels, gf-values of the lines and the C_2 molecule's dissociation energy. Accurate wavelengths for $^{12}C_2$ lines are taken from Phillips & Davis (1968). Excitation energies are computed from the molecular constants given by the latter reference. The wavelength shift between a $^{12}C^{13}C$ line and the corresponding $^{12}C_2$ line is calculated using standard formulae for the vibrational and rotational shifts (Herzberg & Phillips 1948; Russo et al. 2011; Stawikowski & Greenstein 1964). Predictions for the bandhead wavelength shifts were checked against the measurements by Pesic et al. (1983).

gf-values are calculated from the theoretical band oscillator strengths computed by Schmidt & Bacskay (2007): f(1,0) = 0.009414, f(0,0) = 0.03069, and f(0,1) = 0.01015. These theoretical computations predict radiative lifetimes for the upper state of the Swan system that are within a few per cent of the accurate measurements by laser-induced fluorescence reported by Naulin et al. (1988). The

C_2 dissociation energy is taken from an experiment involving multi-photon dissociation of acetylene: $D_0(C_2) = 6.297$ eV (Urdahl et al. 1991). Our molecular data for individual $^{12}C_2$ lines – gf-values and excitation energies – are in excellent agreement with values listed by Asplund et al. (2005) for their determination of the solar C abundance. Detailed molecular line lists used in our analyses of C_2 bands including the wavelengths, J-values of the lower level, the lower excitation potentials, and the log gf-values, are published in the electronic edition (see for SAMPLE Table 5.2, which gives some lines of (1,0) $^{12}C_2$ band).

5.3.2 Atomic lines

In order to ensure a satisfactory synthesis of a RCB spectrum, an accounting for the atomic lines at the wavelengths covered by the C_2 bands is necessary, most especially for the (1,0) $^{12}C^{13}C$ bandhead which is always weak and generally seriously blended. The region 4729-4748 Å was given especial attention. The procedure applied to the (1,0) band was followed for the (0,0) and (0,1) bands.

Prospective atomic lines were first compiled from the usual primary sources: the Kurucz database [2], the NIST database[3], the VALD database[4] and the comprehensive multiplet table for Fe I (Nave et al. 1994). Our next step was to identify the atomic lines in the spectrum of γ Cyg, Arcturus, and the Sun and to invert their equivalent widths to obtain the product of a line's gf-value and the element's abundance. For lines of a given species (e.g., Fe I), the assumption is that the relative gf-values obtained from these sources may be applied to a RCB spectrum synthesis but an adjustment may be needed to allow for an abundance difference between the source and the RCB. After the adjustment for abundance differences between the sources, the gf-values are in agreement within 0.1 dex (see Table 5.3 for the individual estimates of the gf-values as well as the adopted value). For

[2]http://kurucz.harvard.edu
[3]http://www.nist.gov
[4]http://vald.astro.univie.ac.at

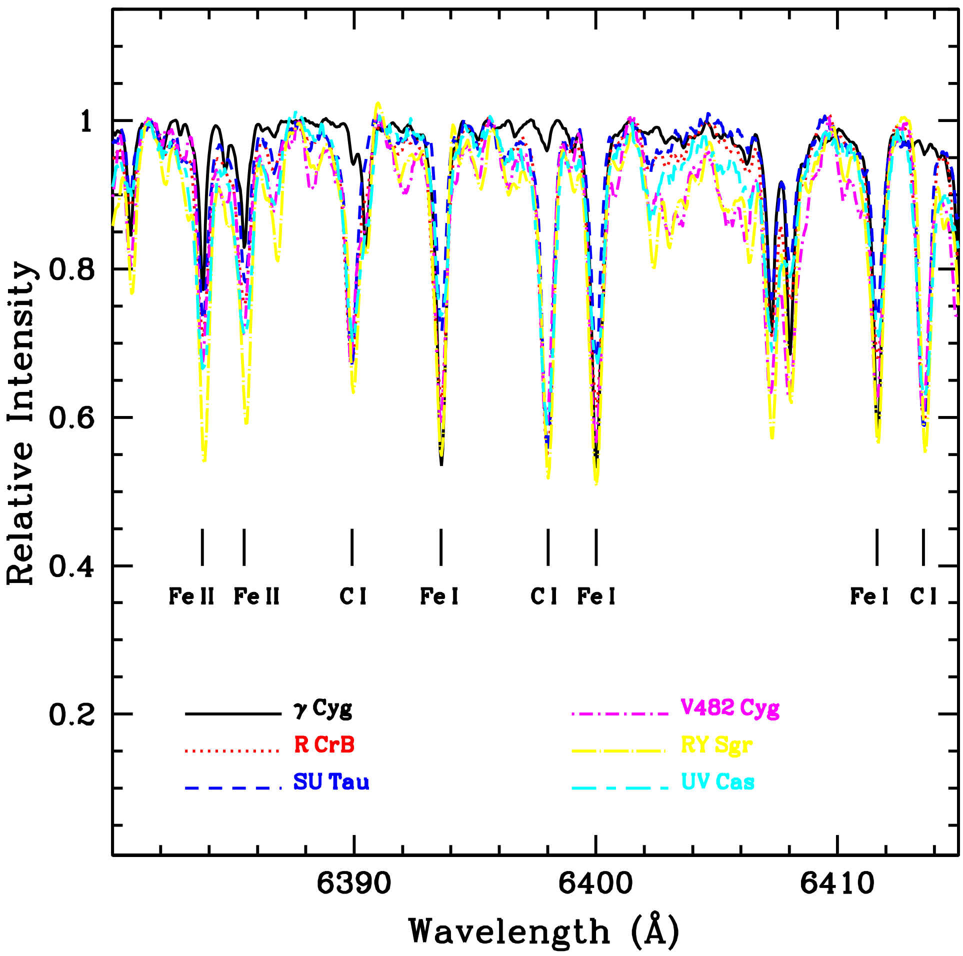

FIGURE 5.1: Spectra of the RCB stars of varying metallicity are superposed to illustrate the constancy of C I line strengths in these stars. The spectrum of the normal supergiant γ Cyg is also shown as a comparison. The positions of the key lines are marked.

most lines the gf-values adopted are those derived from γ Cyg spectrum. For the lines which are not resolved in γ Cyg spectrum, the gf-values are adopted from the solar spectrum.

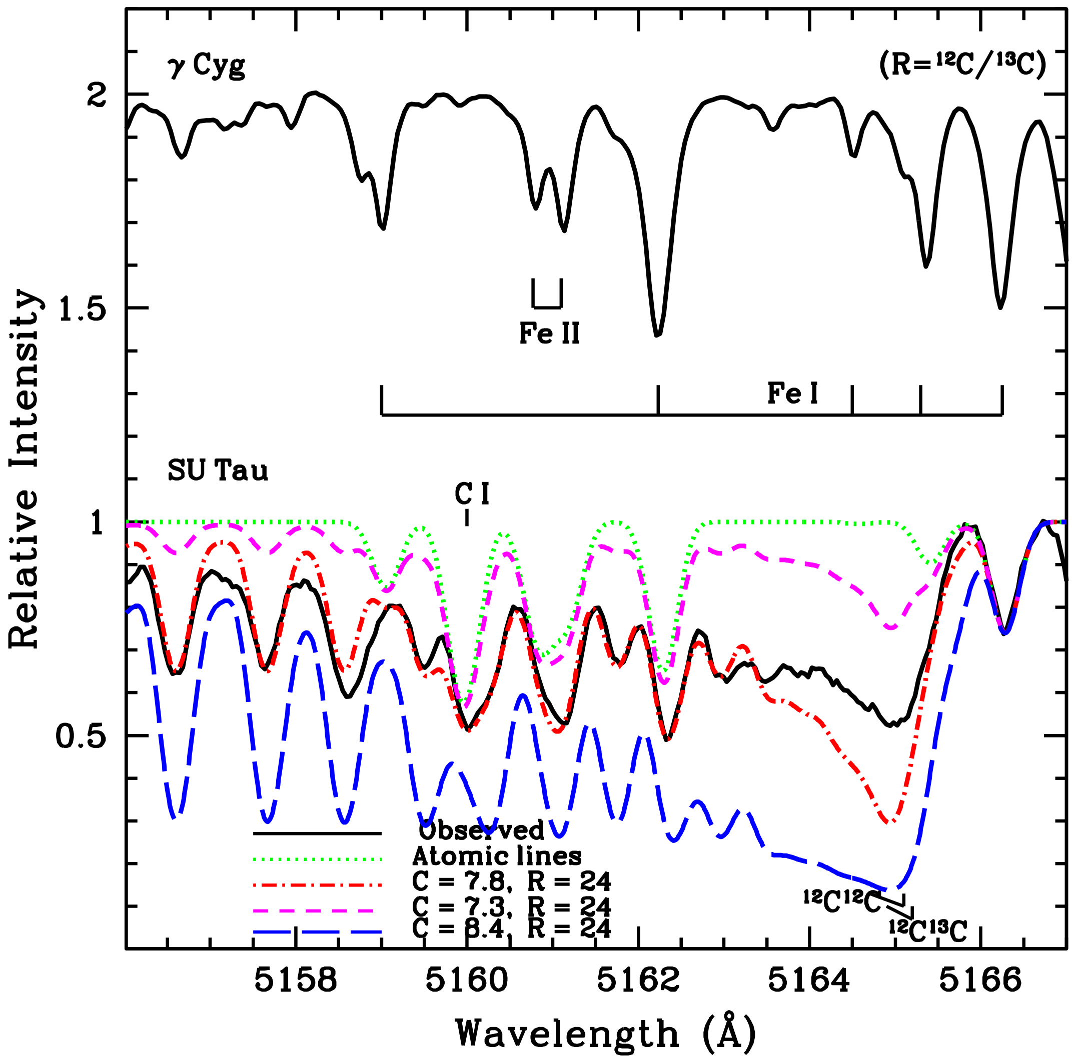

FIGURE 5.2: Observed and synthetic spectra of the (0, 0) C_2 band for SU Tau. Synthetic spectra are plotted for different values of the C abundance – see key on the figure. The spectrum of the γ Cyg is plotted with the positions of the key lines marked.

Table 5.3. The atomic line list used in the syntheses of the (1,0) C_2 swan band region with the individual estimates of the log gf-values from the γ Cyg, Sun, and Arcturus spectra and the adopted log gf-values.

Line	χ **(eV)**	**log** $gf_{\gamma\,\mathrm{Cyg}}$[a]	**log** gf_{Sun}[b]	**log** gf_{Arcturus}[c]	**log** gf_{Source}	Source	**log** gf_{adopted}
Fe I λ4729.018	4.07	-1.72	-1.60	-1.70	-1.61	NIST	-1.72
Ni I λ4729.280	4.10	-2.00	-1.20	···	-1.20	NIST	-2.00
Fe I λ4729.676	3.40	-2.36	-2.32	-2.50	-2.42	NIST	-2.36
Mg I λ4730.028	4.34	-2.49	-2.42	-2.49	-2.34	NIST	-2.49
Cr I λ4730.710	3.08	-0.48	-0.38	-0.38	-0.19	NIST	-0.48
Ti I λ4731.165	2.17	···	-0.51	-0.51	-0.41	Kurucz	-0.51
Ni I λ4731.798	3.83	···	-0.93	-1.10	-0.85	NIST	-0.93
Ni I λ4732.457	4.10	-0.59	-0.55	···	-0.55	NIST	-0.59
Ti I λ4733.421	2.16	···	-0.70	-0.65	-0.40	Kurucz	-0.70
Fe I λ4733.591	1.48	-3.17	-3.03	-3.03	-2.98	NIST	-3.17
Fe I λ4734.098	4.29	-1.60	-1.57	-1.43	-1.56	NIST	-1.60
C I λ4734.260	7.94	...	...	...	-2.36	NIST	···
Ti I λ4734.670	2.24	...	-0.87	-0.87	-0.86	Kurucz	-0.87
C I λ4734.917	7.94	...	...	...	-4.29	NIST	···
C I λ4735.163	7.94	...	...	...	-3.11	NIST	···
Fe I λ4735.843	4.07	-1.12	-1.22	-1.32	-1.22	Kurucz	-1.12
Fe I λ4736.773	3.21	-0.88	-0.75	-0.90	-0.75	NIST	-0.88

Table 5.3 (cont'd)

Line	χ **(eV)**	**log** $gf_{\gamma\,\mathrm{Cyg}}$ [a]	**log** gf_{Sun} [b]	**log** gf_{Arcturus} [c]	**log** gf_{Source}	Source	**log** gf_{adopted}
Cr I λ4737.355	3.09	0.00	-0.30	-0.30	-0.09	NIST	0.00
Fe I λ4737.635	3.26	-2.55	-2.50	-2.45	-2.24	Kurucz	-2.55
C I λ4738.213	7.94	...	...	...	-3.11	NIST	...
C I λ4738.460	7.94	...	...	...	-2.63	NIST	...
Mn I λ4739.110	2.94	-0.48	-0.62	-0.70	-0.49	NIST	-0.48
Zr I λ4739.480	0.65	-0.13	-0.13	-0.13	0.23	Kurucz	-0.13
Mg II λ4739.588	11.56	-0.20	...	...	-0.66	NIST	-0.20
Ni I λ4740.165	3.48	-1.33	-1.83	-1.85	-1.90	NIST	-1.33
Fe I λ4740.340	3.01	-1.90	-2.67	-2.75	-2.63	NIST	-1.90
Sc I λ4741.024	1.43	0.98	0.94	0.84	2.27	NIST	0.98
Fe I λ4741.067	3.33	-2.48	-2.45	-2.50	-2.76	Kurucz	-2.48
Fe I λ4741.530	2.83	-2.10	-2.10	-2.50	-1.76	NIST	-2.10
Ti I λ4742.106	2.15	-3.96	-3.96	-3.92	-0.67	Kurucz	-3.96
C I λ4742.561	7.94	...	...	...	-2.99	NIST	...
Ti I λ4742.800	2.24	-0.09	0.01	-0.09	0.21	NIST	-0.09
Fe I λ4742.932	4.19	-2.16	-2.36	-2.23	-2.36	Kurucz	-2.16
Fe I λ4744.387	4.50	-0.90	-1.00	-1.10	-1.18	ccp7	-0.90

Table 5.3 (cont'd)

Line	χ **(eV)**	**log** $gf_{\gamma\,\mathrm{Cyg}}$[a]	**log** gf_{Sun}[b]	**log** gf_{Arcturus}[c]	**log** gf_{Source}	Source	**log** gf_{adopted}
Fe I λ4744.942	3.26	-2.45	-2.42	-2.40	-2.38	Kurucz	-2.45
Fe I λ4745.128	2.22	-4.10	-4.05	-4.10	-4.08	NIST	-4.10
Fe I λ4745.799	3.65	-1.25	-1.30	-1.40	-1.27	NIST	-1.25
Fe I λ4749.947	4.55	-1.33	-1.33	-1.33	-1.33	NIST	-1.33
Fe I λ4765.480	1.60	-3.81	-3.81	-3.70	-4.01	Kurucz	-3.81
Fe I λ4786.806	3.01	-1.60	-1.60	-1.65	-1.60	NIST	-1.60
Fe I λ4787.826	2.99	-2.56	-2.56	-2.50	-2.60	NIST	-2.56
Fe I λ4788.756	3.23	-1.76	-1.76	-1.76	-1.76	NIST	-1.76
Fe I λ4789.650	3.54	-1.16	-1.16	-1.20	-0.96	NIST	-1.16
Fe I λ4799.405	3.63	-1.89	-1.89	-1.93	-2.19	NIST	-1.89
Fe I λ4802.879	3.64	-1.51	-1.51	-1.51	-1.51	NIST	-1.51
Fe I λ4808.148	3.25	-2.84	-2.84	-2.70	-2.74	NIST	-2.84
Fe I λ4809.938	3.57	-2.08	-2.10	-2.15	-2.60	NIST	-2.08

Note. —

[a]MARCS Model atmosphere with atmospheric parameters and abundances from Luck & Lambert (1981).

[b]MARCS Model atmosphere with atmospheric parameters and abundances from Asplund et al. (2009).

[c]MARCS Model atmosphere with atmospheric parameters and abundances from Peterson et al. (1993).

Lines of C I present in all RCB spectra are not present in the reference spectra of γ Cyg, Arcturus and the Sun (see Figure 5.1). The C I lines were identified using Moore's(1993) multiplet table with gf-values taken from the NIST database. A C I line is betrayed by the fact that a given C I line has a similar strength in all RCB spectra (see Figure 5.1). In this regard the feature coincident with the $^{12}C^{13}C$ $(1, 0)$ bandhead is unlikely to be a very weak unidentified C I line because its strength varies from star to star. Note, for example, the absence or near absence of this line in the spectra of V3795 Sgr and V854 Cen. Furthermore, this line is stronger in the spectrum of γ Cyg, where the C I lines are very weak.

Initially, elemental abundances for RCB stars were adopted from Asplund et al. (2000) and Rao & Lambert (2003). Then, equivalent widths were measured off our spectra and the abundances redetermined for RCB stars were found to be in good agreement with Asplund et al. (2000). In particular, we derived the Fe abundance from lines in the 4745-4810 Å window where C_2 contamination is minimal. The Fe abundances derived from these Fe I lines are in good agreement with the Fe abundances derived by Asplund et al. (2000) (see Table 5.4). These Fe abundances were adopted for deriving the $^{12}C/^{13}C$ ratios in RCB stars. The uncertainties on the Fe abundance is used to derive the upper and lower limits to $^{12}C/^{13}C$ ratios in RCB stars (including U Aqr). The metal abundances for the synthetic spectra are adopted from Asplund et al. (2000) for most of the stars. However, for V2552 Oph we adopt the abundances from Rao & Lambert (2003). We also assume the solar relative abundances with the correction of about +0.3 dex for the α-elements at these metallicities, if these abundances are not measured in these stars. Fe abundances are derived also for HdC stars and the cool RCB U Aqr.

5.3.3 Spectrum synthesis of the C_2 bands

For the spectrum synthesis, we used the line-blanketed H-deficient model atmospheres by Asplund et al. (1997a) and the UPPSALA spectrum synthesis BSYN-RUN program. For equivalent width analysis we used EQWRUN program. The appropriate model atmosphere for a given RCB star was chosen using the stellar parameters from Asplund et al. (2000): effective temperature $T_{\rm eff}$, surface gravity log g, and microturbulence $\xi_{\rm t}$.

The stellar parameters for the cool RCB star U Aqr and HdC stars are adopted from Asplund et al. (1997a) and García-Hernández et al. (2009, 2010) and used with the MARCS model atmospheres (Gustafsson et al. 2008) provided by Kjell Eriksson (private communication) used by García-Hernández et al. (2009, 2010). For the four HdC stars and the cool RCB star U Aqr, we have derived the microturbulence ($\xi_{\rm t}$) from Fe I lines in the region of 4750-4960 Å, since there are no significant molecular bands in this wavelength region (Warner 1967). The microturbulent velocity derived from Fe I lines for U Aqr is $\xi_{\rm t} = 5.0\pm2$ km s^{-1} and the Fe abundance is $\log\epsilon({\rm Fe}) = 6.7\pm0.3$, but adoption of a lower effective temperature, $T_{\rm eff}$ = 5400 K, suggested by García-Hernández et al. (2010) gives an Fe abundance of 6.5±0.3. For HdC stars, the derived microturbulent velocities and Fe abundances are: for HD 137613, $\xi_{\rm t} = 6.5\pm2$ km s^{-1} and $\log\epsilon({\rm Fe}) = 6.8\pm0.3$, for HD 182040, $\xi_{\rm t} = 6.5\pm2$ km s^{-1} and $\log\epsilon({\rm Fe}) = 6.6\pm0.3$, for HD 173409, $\xi_{\rm t} = 6.0\pm2$ km s^{-1} and $\log\epsilon({\rm Fe}) = 6.6\pm0.3$, and for HD 175893, $\xi_{\rm t} = 6.0\pm2$ km s^{-1} and $\log\epsilon({\rm Fe}) = 6.7\pm0.3$. The other stellar parameters like $T_{\rm eff}$ and log g, and the elemental abundances are judged from Warner (1967), Asplund et al. (1997a), and García-Hernández et al. (2009).

Stars with effective temperature less than or about 7000 K were selected for the analysis of their C_2 bands. The C_2 molecular bands were synthesized with the line lists discussed above. The synthesized spectrum was convolved with a Gaussian profile with a width that represents the combined effect of stellar macroturbulence

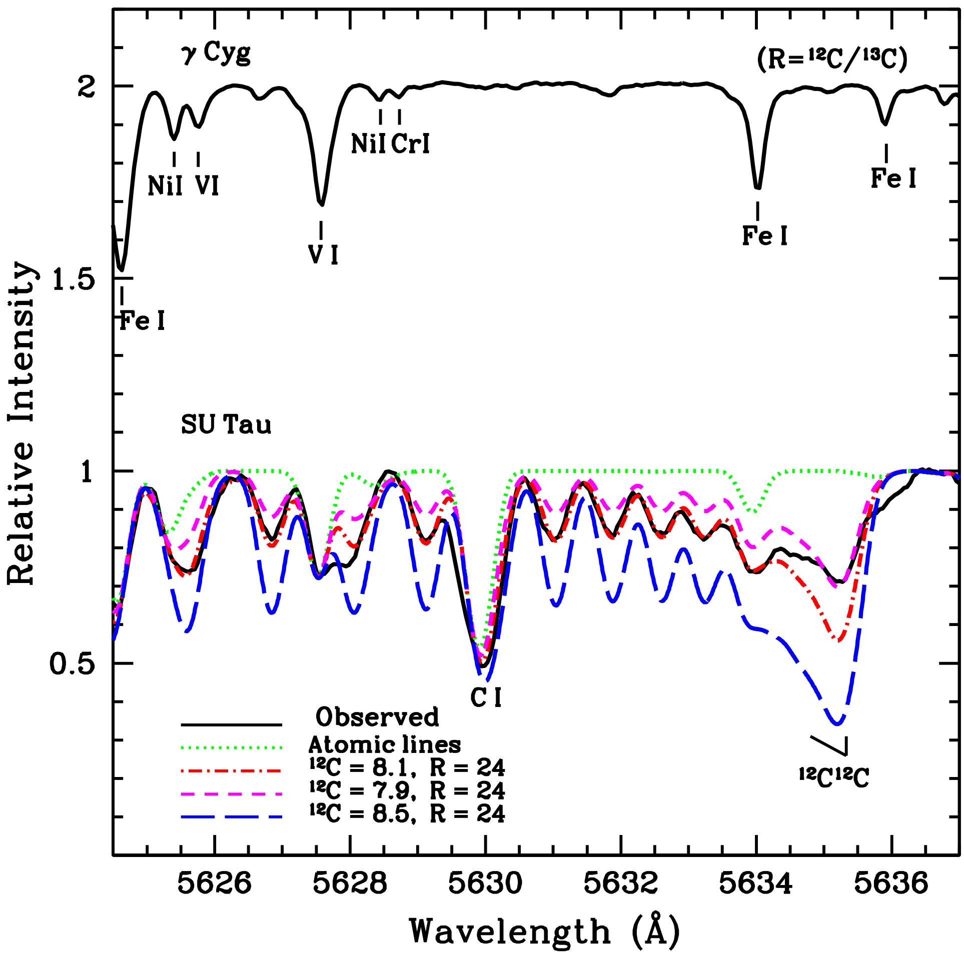

FIGURE 5.3: Observed and synthetic spectra of the $(0, 1)$ C_2 band for SU Tau. Synthetic spectra are plotted for different values of the C abundance – see key on the figure. The spectrum of the γ Cyg is plotted with the positions of the key lines marked.

and the instrumental profile. The synthesized spectrum is then matched to the observed spectrum by adjustment of the appropriate abundances.

5.4 The carbon abundance

If there were no carbon problem for C_2 the ^{12}C abundance derived by fitting each $^{12}C_2$ band would equal the input C abundance of the adopted model atmosphere

Table 5.4. The Fe abundances for RCB and HdC stars.

Star	logϵ(Fe)[a]	logϵ(Fe)[b]	logϵ(Fe)[c]
V3795 Sgr	5.7(0.3)(3)	5.6	<6.0
XX Cam	6.8(0.3)(5)	6.8	6.8
VZ Sgr	6.1(0.3)(4)	5.8	7.2
UX Ant	6.2(0.15)(5)	6.2	7.0
RS Tel	6.5(0.2)(3)	6.4	6.9
R CrB	6.6(0.2)(5)	6.5	7.0
V2552 Oph	6.6(0.2)(4)	6.4	6.9
V854 Cen	5.0(0.3)(3)	5.0	6.5
V482 Cyg	6.7(0.15)(5)	6.7	6.9
SU Tau	6.1(0.3)(4)	6.1	6.5
V CrA	5.5(0.1)(3)	5.5	6.6
GU Sgr	6.5(0.25)(6)	6.3	6.8
FH Sct	6.4(0.15)(5)	6.3	6.8
U Aqr	6.5(0.30)(8)	···	7.3
HD 173409	6.6(0.3)(10)	6.8	6.6
HD 182040	6.6(0.25)(9)	6.9	6.4
HD 175893	6.7(0.2)(5)	6.8	6.7
HD 137613	6.8(0.20)(9)	6.6	6.7

Note. —

[a]From 4700 Å region, the values in parentheses are the standard deviation and the number of lines used, respectively.

[b]From Asplund et al. (2000) for RCB stars and from Warner (1967) for HdC stars.

[c]From 4744.4 Å line, assuming it to be entirely Fe I.

to within the margin implied by the uncertainties arising from the errors assigned to the model atmosphere parameters. (The changes in spectrum syntheses arising from uncertainties in the basic data for the Swan bands and in the carbon isotopic ratio are negligible.)

In Tables 5.5, 5.6 and 5.7, the derived C abundances from C_2 bands for the RCB stars are summarized for the three bands and for models with C/He = 0.3, 1.0 and 3.0%. Table 5.8 gives the mean of the carbon abundance derived from (0,1), (0,0) and (1,0) C_2 bands for RCB stars. Table 5.9 similarly gives C abundances for the four HdC stars and the cool RCB star U Aqr. In Tables 5.5 to 5.9, we also give the C abundance from the C I lines but only for C/He=1% models. For a given model, the three bands give the same C abundance to within 0.2 dex, a quantity comparable to the fitting uncertainty. Along the sequence of models from C/He = 0.3 to 3.0%, the derived C abundance decreases by about 0.2 dex for the warmest stars to 0.1 dex for the coolest stars or equivalently the carbon problem increases from the warmest stars to the coolest stars. A carbon problem exists for all models with C/He in the range from 0.3 to 3.0%. Extrapolation of the C abundances in Tables 5.5, 5.6, 5.7, and 5.8, to lower input C/He ratio suggests that elimination of the C problem requires models with values of C/He across the range 0.3% (VZ Sgr, R CrB) to 0.03% (V2552 Oph, SU Tau). Table 5.9 suggests that C/He $\simeq$ 0.3% may account for the HdC stars and cool RCB U Aqr. Adoption of $T_{\rm eff}$ = 6000K for U Aqr suggests C/He of 10%, and not in line with that of HdC stars. Hence, the $T_{\rm eff}$ = 5400K is adopted for U Aqr over the $T_{\rm eff}$ = 6000K. Discussion of this C/He range is postponed to Section 5.6.

By way of illustrating the fits of the synthetic spectra to observed spectra for the warm RCB stars, we show synthetic and observed spectra for SU Tau in Figures 5.2, and 5.3 for the (0,0) and (0,1) C_2 bands, respectively. A corresponding figure for the (1,0) C_2 band for all stars is shown later. The (0,1), (0,0) and (1,0) bands each highlight a different issue. For the HdC stars and the cool RCB U Aqr, the C_2 bands are very strong and the issues are somewhat different and related to the saturation of the lines.

For the (0,1) band, a ^{12}C abundance is found to fit well the entire illustrated region except that right at the bandhead the observed spectrum is shallower than that predicted. This mismatch is not peculiar to SU Tau and is insensitive to the choice of the C/He ratio. This best fit for SU Tau demands a C abundance of 8.1 or, equivalently, presents a C problem of 0.9 dex; the synthesis with a C abundance

Table 5.5. The derived carbon abundances for RCB stars from (0, 1) C_2 bands.

stars	logϵ(C) from (0, 1) C_2 band			logϵ(C) from C I lines
	C/He = 0.3% log ϵ(C) = 9.0	C/He = 1.0% log ϵ(C) = 9.5	C/He = 3.0% log ϵ(C) = 10.0	C/He = 1.0% log ϵ(C) = 9.5
VZ Sgr	9.0	8.9	8.8	8.9
UX Ant	8.4	8.3	8.2	8.7
RS Tel	···	···	···	8.7
R CrB	9.0	8.8	8.8	8.9
V2552 Oph	8.3	8.1	8.2	8.7
V854 Cen	8.4	8.3	8.3	8.8
V482 Cyg	8.4	8.3	8.3	8.9
SU Tau	8.1	8.0	8.0	8.6
V CrA	8.5	8.4	8.3	8.6
GU Sgr	8.2	8.1	8.1	8.9
FH Sct	7.8	7.7	7.7	8.9
V4334 Sgr[a]	9.8	9.7	9.7	9.8[b]

Note. — [a] Final Flash object.
[b] The carbon abundance from C I lines for V4334 Sgr is for C/He = 10% (log ϵ(C) = 10.5) from Asplund et al. (1997b).

Table 5.6. The derived carbon abundances for RCB stars from (0, 0) C_2 bands.

stars	logϵ(C) from (0, 0) C_2 band			logϵ(C) from C I lines
	C/He = 0.3% log ϵ(C) = 9.0	C/He = 1.0% log ϵ(C) = 9.5	C/He = 3.0% log ϵ(C) = 10.0	C/He = 1.0% log ϵ(C) = 9.5
VZ Sgr	9.0	8.8	8.7	8.9
UX Ant	8.2	8.1	8.0	8.7
RS Tel	8.4	8.3	8.3	8.7
R CrB	8.9	8.6	8.6	8.9
V2552 Oph	8.1	8.1	8.1	8.7
V854 Cen	8.4	8.3	8.2	8.8
V482 Cyg	8.2	8.1	8.1	8.9
SU Tau	7.8	7.8	7.8	8.6
V CrA	8.3	8.2	8.2	8.6
GU Sgr	8.1	8.1	8.1	8.9
FH Sct	7.8	7.8	7.7	8.9

Table 5.7. The derived carbon abundances for RCB stars from (1, 0) C_2 bands.

	logϵ(C) from (1, 0) C_2 band			logϵ(C) from C I lines
stars	C/He = 0.3% log ϵ(C) = 9.0	C/He = 1.0% log ϵ(C) = 9.5	C/He = 3.0% log ϵ(C) = 10.0	C/He = 1.0% log ϵ(C) = 9.5
VZ Sgr	9.0	8.8	8.6	8.9
UX Ant	8.4	8.1	8.0	8.7
RS Tel	8.7	8.5	8.4	8.7
R CrB	9.0	8.8	8.7	8.9
V2552 Oph	8.1	8.0	7.9	8.7
V854 Cen	···	8.5	8.2	8.8
V482 Cyg	8.2	8.2	8.1	8.9
SU Tau	7.8	7.7	7.7	8.6
V CrA	8.5	8.4	8.3	8.6
GU Sgr	8.2	8.1	8.0	8.9
FH Sct	7.7	7.7	7.6	8.9

Table 5.8. Summary of the derived carbon abundances for RCB stars from (0, 1), (0, 0) and (1, 0) C_2 bands.

	mean of the logϵ(C) from (0, 1), (0, 0)and (1, 0) C_2 bands			logϵ(C) from C I lines
stars	C/He = 0.3% log ϵ(C) = 9.0	C/He = 1.0% log ϵ(C) = 9.5	C/He = 3.0% log ϵ(C) = 10.0	C/He = 1.0% log ϵ(C) = 9.5
VZ Sgr	9.0	8.8	8.7	8.9
UX Ant	8.3	8.2	8.1	8.7
RS Tel	8.6	8.4	8.4	8.7
R CrB	9.0	8.7	8.7	8.9
V2552 Oph	8.2	8.1	8.1	8.7
V854 Cen	8.4	8.4	8.2	8.8
V482 Cyg	8.3	8.2	8.2	8.9
SU Tau	7.9	7.8	7.8	8.6
V CrA	8.4	8.3	8.3	8.6
GU Sgr	8.2	8.1	8.1	8.9
FH Sct	7.8	7.7	7.7	8.9
V4334 Sgr[a]	9.8	9.7	9.7	9.8[b]

Note. — [a] Final Flash object.
[b] The carbon abundance from C I lines for V4334 Sgr is for C/He = 10% (log ϵ(C) = 10.5) from Asplund et al. (1997b).

of 9.0 (i.e., zero C problem) is obviously a very poor representation of the observed spectrum.

Synthetic spectra for the (0,0) bands give results essentially identical to those for the (0,1) bands. The C abundance from the best-fitting synthesis as judged by the fit to the C_2 lines away from the bandhead is within 0.2 dex of the values from the (0,1) bands. The mismatch between synthesis and observation at the bandhead is greater than for the (0,1) band and extends over a greater wavelength interval than for the (0,1) band.

A special difficulty occurs at the (1,0) $^{12}C_2$ bandhead because there are strong atomic lines at and shortward of the bandhead. A line right at the head is a Fe I line and those shortward of the head are C I lines. These and weaker atomic lines make it difficult to distinguish the C_2 contribution to the spectrum from that of the atomic lines when the C_2 contribution is weak.

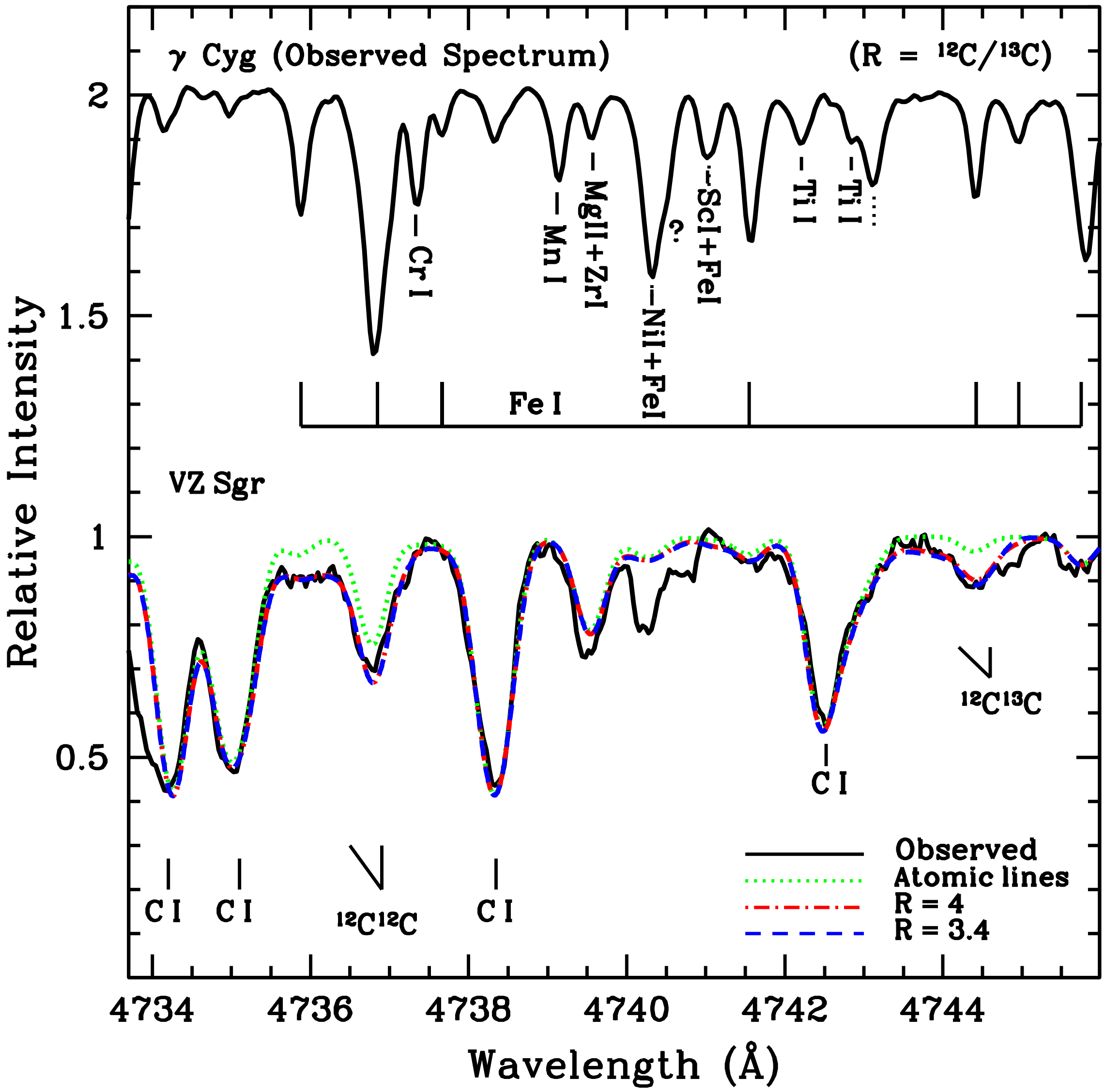

FIGURE 5.4: Observed and synthetic spectra of the (1,0) C_2 bands for VZ Sgr. Synthetic spectra are plotted for the values of the isotopic ratios (R) shown in the keys and for a spectrum with just the atomic lines. The spectrum of γ Cyg is also plotted – the positions of the key lines are also marked – the dotted line represents the blending of the one or more atomic lines.

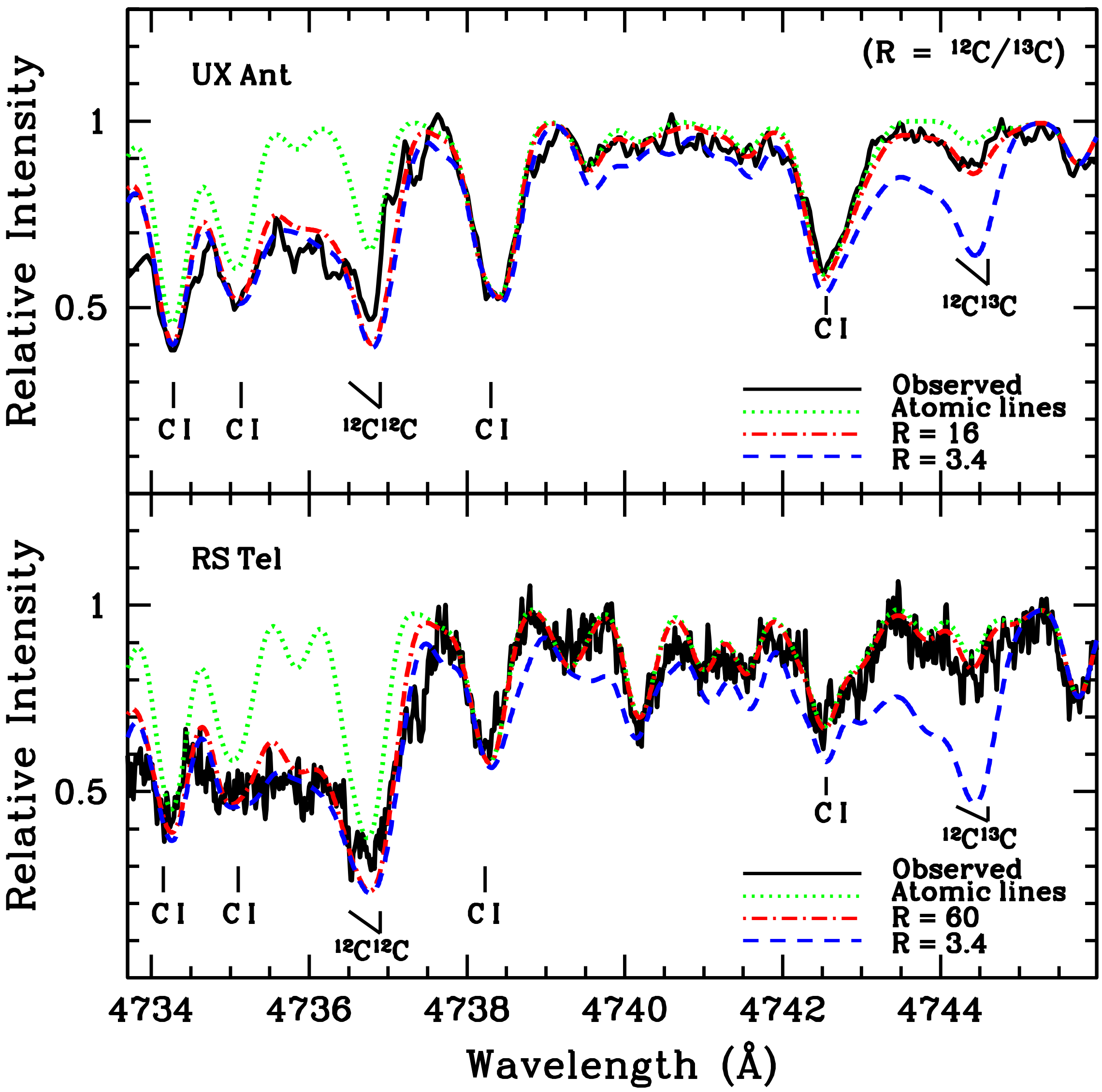

FIGURE 5.5: Observed and synthetic spectra of the (1,0) C_2 bands for UX Ant and RS Tel. Synthetic spectra are plotted for the values of the isotopic ratios (R) shown in the keys and for a spectrum with just the atomic lines. The positions of the key lines are also marked.

Table 5.9. The derived carbon abundances for HdC stars and RCB star U Aqr from (0, 1) and (1, 0) C_2 bands.

stars	logϵ(C) from (0, 1) C_2 band			logϵ(C) from (1, 0)			logϵ(C) from C I lines
	C/He = 0.1% log ϵ(C) = 8.5	C/He = 1.0% log ϵ(C) = 9.5	C/He = 10% log ϵ(C) = 10.5	C/He = 0.1% log ϵ(C) = 8.5	C/He = 1.0% log ϵ(C) = 9.5	C/He = 10% log ϵ(C) = 10.5	C/He = 1.0% log ϵ(C) = 9.5
HD 173409	...	8.7	...	...	8.7	...	8.6
HD 182040	8.8	9.0	8.9	8.8	9.0	8.9	9.0
HD 175893	8.9	9.0	8.9	8.8	8.9	8.8	8.5
HD 137613	8.8	9.0	8.9	8.8	9.0	8.9	8.5
U Aqr*	...	9.2	...	...	9.2	...	8.9

*Adopted ($T_{\rm eff}$, log g) = (5400, 0.5). If ($T_{\rm eff}$, log g) = (6000, 0.5) is adopted, the derived carbon abundance is about 10.4.

As long as the continuous opacity is provided by photoionization of neutral carbon, the carbon problem (see Tables 5.5, 5.6, 5.7, 5.8 and 5.9) raised by the C I lines cannot be erased by changes to the stellar parameters. The original carbon problem referred to the mismatch between the observed and predicted strengths of C I lines: the latter were stronger than the former by an amount equivalent to about a 0.6 dex reduction in a line's gf-value. The star-to-star variation in this reduction across the RCB sample was small: for example, the C I problem for the ten stars in Table 5.5, 5.6, 5.7 and 5.8, spanned the small interval of -0.3 to -0.9 with a mean value of -0.7 ± 0.1 (Asplund et al. 2000). This carbon problem's magnitude is almost independent of the assumed C/He ratio for which the model is constructed, i.e., the difference between the assumed and derived C abundance is maintained as C/He is adjusted. The C I lines included in present syntheses confirm the C problem. With gf-values from the NIST database, these lines demand a gf-value decrease of 0.5 to 0.8 dex for the eleven stars in Table 5.5, 5.6, 5.7 and 5.8 and the five stars in Table 5.9.

5.5 The $^{12}C/^{13}C$ ratio

The $^{12}C^{13}C$ molecule's contribution to the spectra is assessed from the (1,0) band. Unfortunately, there is an unidentified atomic line coincident with the $^{12}C^{13}C$ bandhead. Syntheses show that this atomic line is a major contributor to the stellar feature in most stars. There is also strong atomic blending of the $^{12}C_2$ bandhead but the ^{12}C abundance is provided securely from the (0,0) and (0,1) bands. Given these complications, our focus is on determining whether the $^{12}C/^{13}C$ ratio is close to the CN-cycle equilibrium ratio (= 3.4), as might be anticipated for a star produced by the FF scenario, or is a much higher value, as might be provided from the DD scenario. The intensity of a line from the heteronuclear $^{12}C^{13}C$ molecule and the corresponding line from the homonuclear $^{12}C_2$ molecule are related as $I(12-13) = 2I(12-12)/R$ where R is the $^{12}C/^{13}C$ ratio.

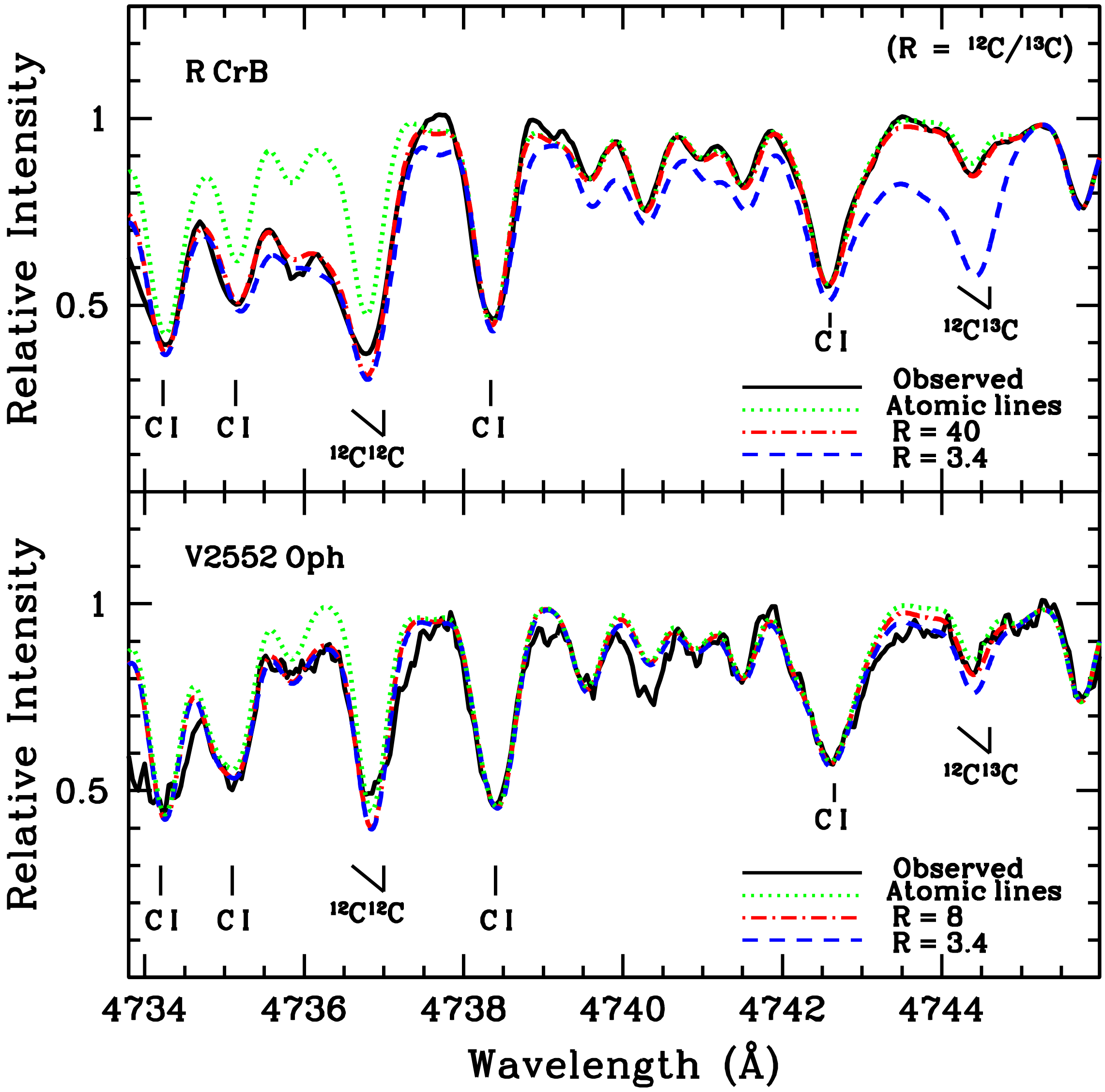

FIGURE 5.6: Observed and synthetic spectra of the (1,0) C_2 bands for R CrB and V2552 Oph. Synthetic spectra are plotted for the values of the isotopic ratios (R) shown in the keys and for a spectrum with just the atomic lines. The positions of the key lines are also marked.

Of particular concern to a determination of the $^{12}C/^{13}C$ ratio is the atomic line at 4744.39 Å which is coincident with the (1,0) $^{12}C^{13}C$ bandhead. This line is present in the spectrum of γ Cyg, also of the Sun and Arcturus. A line at this wavelength is present in spectra of the hotter RCB stars (V3795 Sgr and XX Cam) whose spectra show no sign of the stronger (0,0) C_2 band at 5165 Å. The interfering line is unidentified in Hinkle et al. (2000)'s Arcturus atlas. The line list given at the ccp7 website[5] identifies the line as arising from a lower level in Fe I at 4.50 eV but such a line and lower level is not listed by Nave et al. (1994) in their comprehensive study of the Fe I spectrum. The line list given in ccp7 is from Bell & Gustafsson (1989), an unpublished line list. Although this line is assigned in Table 5.3 to this (fictitious?) Fe I transition, the lack of a positive identification is not a serious issue except, as we note below, perhaps for the minority RCB stars. Given that the gf-value of the line is fixed from the line's strength in spectra of stars that span the temperature range of the RCBs (γ Cyg, Arcturus, and the Sun), alternative identifications have little effect on the predicted strength of the line in a RCB or a HdC star. We assume it is a Fe I line and predict its strength from the inferred gf-value (Table 5.3) and the Fe abundance derived from a sample of Fe I line in the same region (see above). Table 5.4 lists our derived Fe abundance, the Fe abundance from Asplund et al. (2000), and the Fe abundance obtained on the assumption that the entire $^{12}C^{13}C$ bandhead is attributable to the Fe I line. There is good agreement between our Fe abundance and that derived from different spectra by Asplund et al. (2000). Perfect agreement would not be expected for several reasons: for example, the stars are somewhat variable even out of decline and our spectra are not those analysed by Asplund et al. (2000). The difference between the mean Fe abundance and the abundance required to fit the feature at the $^{12}C^{13}C$ bandhead is a rough measure of the inferred molecular contribution to the feature.

Stars are discussed in the order of decreasing effective temperature. For all the stars synthetic spectra are computed for a model with the parameters given in Table 5.10 and with C/He= 1.0%. The $^{12}C_2$ bands are fitted and then several syntheses are computed for various values of the isotopic ratio R. The estimates of $^{12}C/^{13}C$ ratio are given in Table 5.10.

[5] http://ccp7.dur.ac.uk/ccp7/DATA/lines.bell.tar.Z

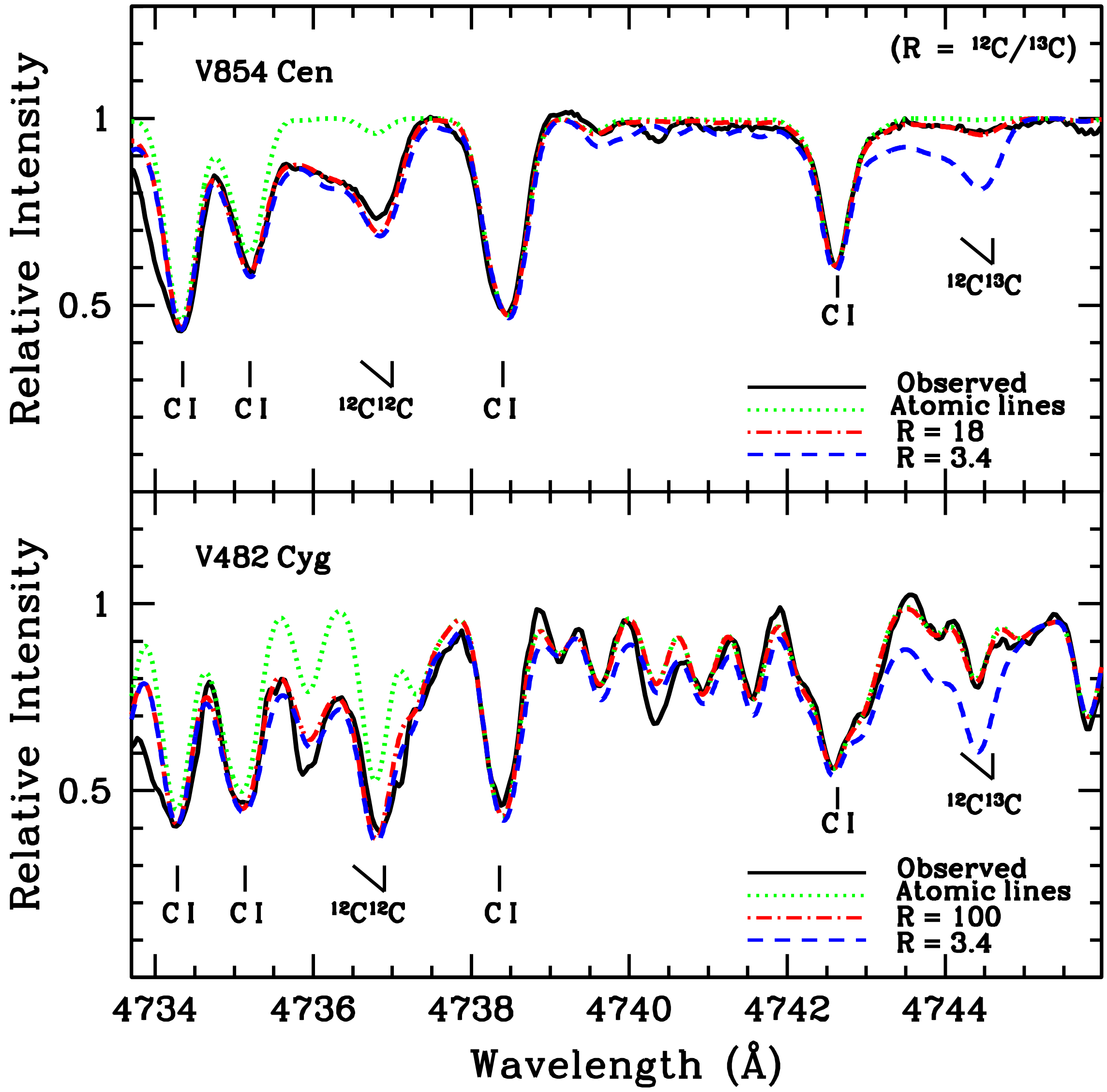

FIGURE 5.7: Observed and synthetic spectra of the (1,0) C_2 bands for V854 Cen and V482 Cyg. Synthetic spectra are plotted for the values of the isotopic ratios (R) shown in the keys and for a spectrum with just the atomic lines. The positions of the key lines are also marked.

VZ Sgr: Observed and synthetic spectra around the (1,0) band are shown in Figure 5.4 for this minority RCB star. At 4745 Å, the atomic line (here assumed to be the Fe I line from Table 5.3) is too weak to account for the observed feature; Table 5.4 shows that the Fe abundance must be increased by about 1 dex to remove

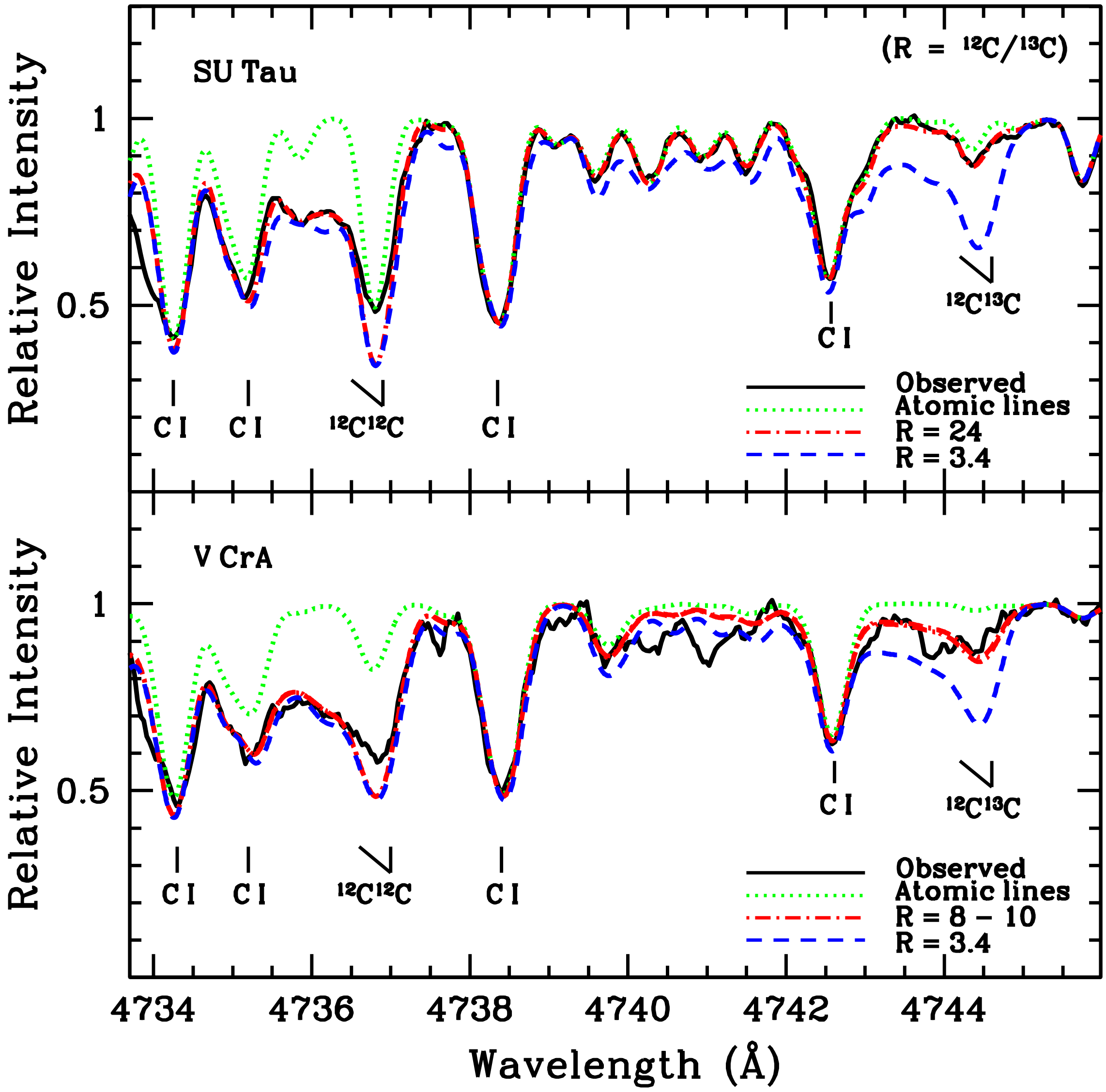

FIGURE 5.8: Observed and synthetic spectra of the (1,0) C_2 bands for SU Tau and V CrA. Synthetic spectra are plotted for the values of the isotopic ratios (R) shown in the keys and for a spectrum with just the atomic lines. The positions of the key lines are also marked.

the necessity for a contribution from $^{12}C^{13}C$. A contribution from $^{12}C^{13}C$ seems necessary with $R \simeq 3 - 6$, a value suggestive of CN-cycling.

Since the relative metal abundances for VZ Sgr, a minority RCB, are non-solar (Lambert & Rao 1994), the identity of the 4745 Å atomic line may affect the conclusion that this line is an unimportant contributor to the molecular bandhead. For example, VZ Sgr is a minority RCB especially rich in Si and S ([Si/Fe] $\sim$ [S/Fe] $\sim$ 2) and a blending line from these elements may reduce the need for a $^{12}C^{13}C$ contribution. However, a search of multiplet tables of Si I (Martin & Zalubas 1983) and S I (Kaufman & Martin 1993; Martin et al. 1990) did not uncover an unwanted blend. Thus, we suppose that VZ Sgr is rich in ^{13}C.

UX Ant: There is a strong (1,0) $^{12}C_2$ contribution to the spectrum. The predicted profile of the bandhead is broader than the observed head which is distorted by very strong cosmic ray hits on the raw frame. The Fe I line is predicted to be a weak contributor to the feature at the $^{12}C^{13}C$ wavelength. Values of R in the range 14 to 20 fit the observed feature quite clearly, a synthesis with $R = 3.4$ provides a bandhead that is incompatible with the observed head (Figure 5.5).

RS Tel: Observed and synthetic spectra shown in Figure 5.5 indicate that the Fe I line at the $^{12}C^{13}C$ band head accounts well for the observed feature and thus $R > 60$ is all that can be said for the carbon isotopic ratio from this spectrum of relatively low S/N ratio.

R CrB: Figure 5.6 shows observed and synthetic spectra. The Fe I line at the $^{12}C^{13}C$ bandhead accounts for the observed feature. Given that the identity of the line's carrier is uncertain, a conservative view must be that $^{12}C^{13}C$ contributes negligibly to the observed feature and $R > 40$ is estimated . It is clear, however, that $R = 3.4$ is excluded as a possible fit.

V2552 Oph: The spectrum of this recently discovered RCB is very similar to that of R CrB (Rao & Lambert 2003) but for its stronger N I lines and weaker C_2 bands (Figure 1 of Rao & Lambert 2003). The $^{12}C_2$ bandhead is very largely obscured by the overlying Fe I line. The apparent $^{12}C^{13}C$ bandhead is almost entirely reproduced by the atomic line. A high R value cannot be rejected but $R = 3.4$ may be excluded (Figure 5.6). $R > 8$ is our estimate.

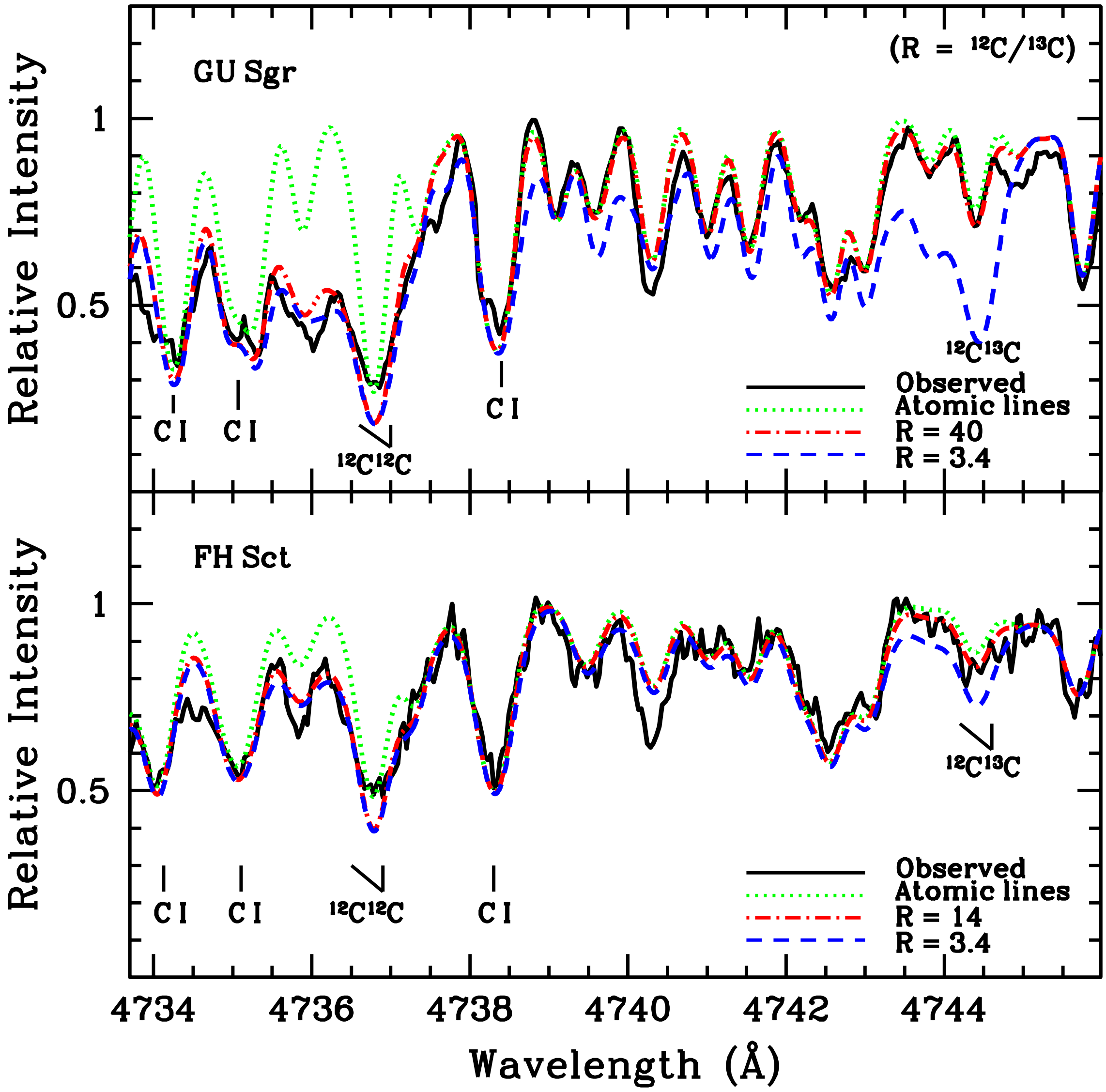

FIGURE 5.9: Observed and synthetic spectra of the (1,0) C_2 bands for GU Sgr and FH Sct. Synthetic spectra are plotted for the values of the isotopic ratios (R) shown in the keys and for a spectrum with just the atomic lines. The positions of the key lines are also marked.

V854 Cen: This RCB with low metal abundances provides a clean spectrum in the the region of the (1,0) Swan bands (Figure 5.7). The $^{12}C_2$ head is well fitted with a synthetic spectrum. Very high S/N ratio spectra are necessary to set strict limits on the $^{12}C^{13}C$ bandhead but it is clear that the blending Fe I line is a weak

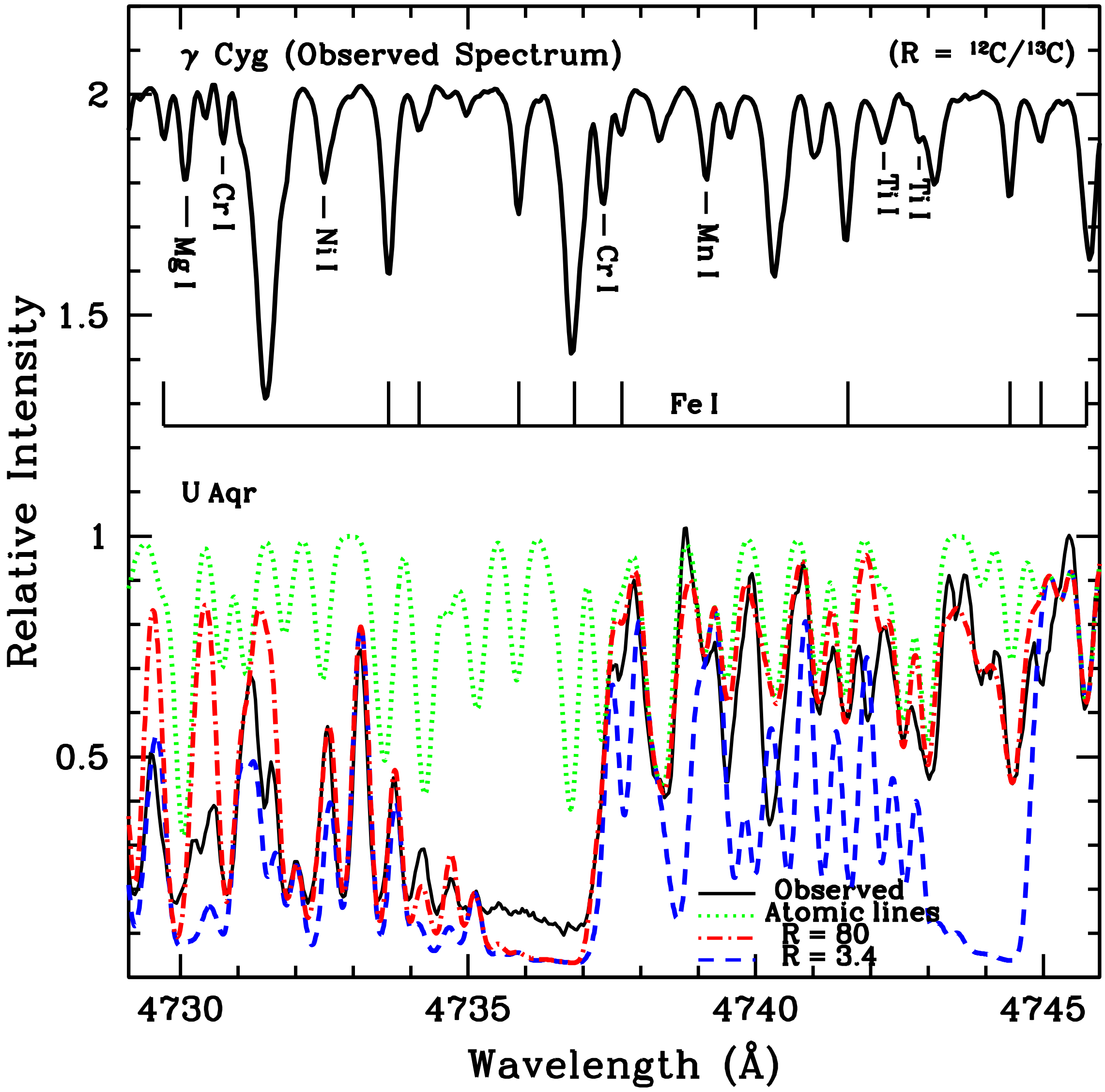

FIGURE 5.10: Observed and synthetic spectra of the (1,0) C_2 bands for U Aqr. Synthetic spectra are plotted for the values of the isotopic ratios (R) shown in the keys and for a spectrum with just the atomic lines. The spectrum of γ Cyg is also plotted – the positions of the key lines are also marked.

contributor; the Fe abundance must be increased by 1.5 dex to eliminate the need for a $^{12}C^{13}C$ contribution. A ratio $R = 3.4$ is firmly excluded. Values of R in the range 16 to 24 are suggested.

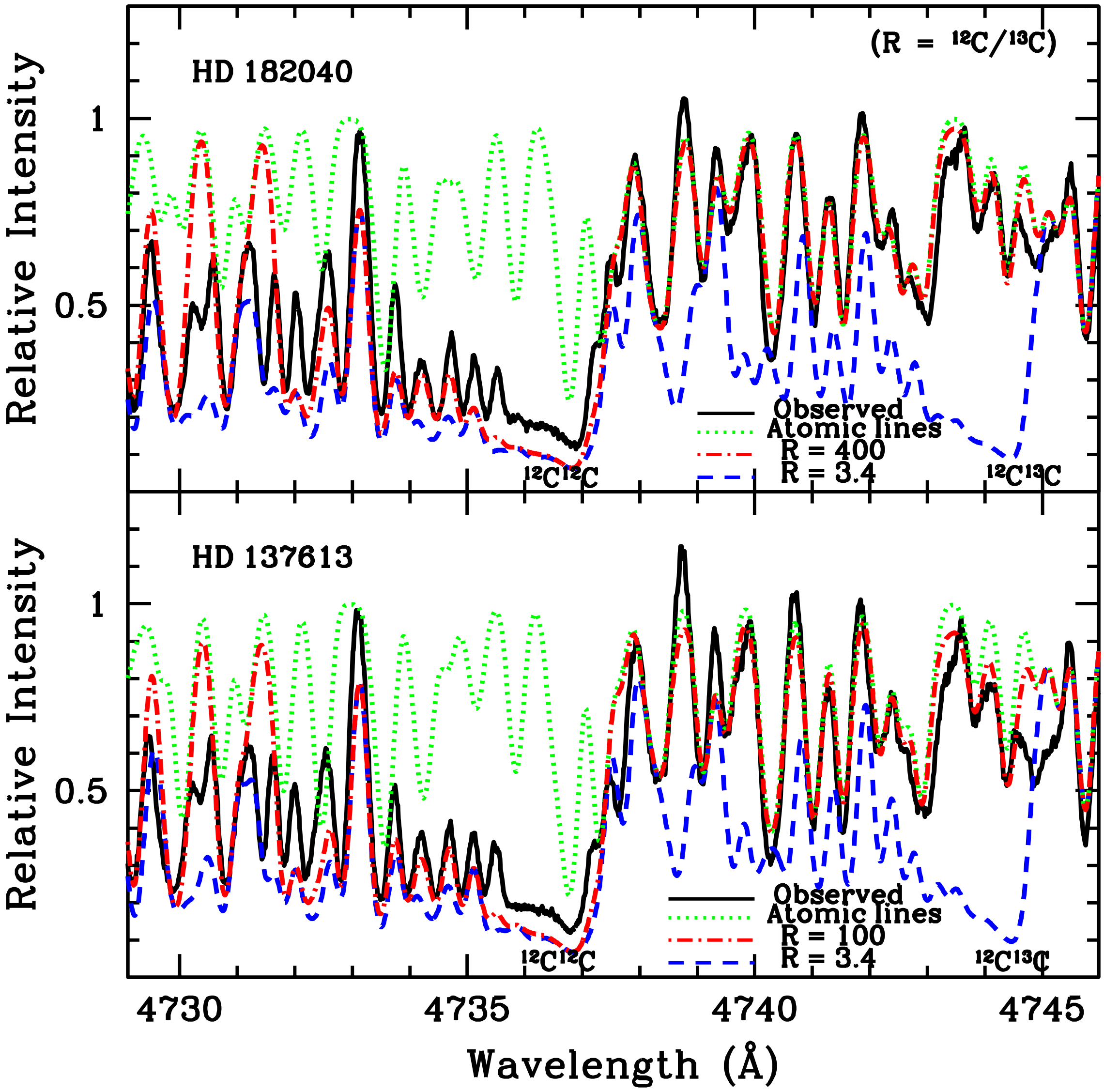

FIGURE 5.11: Observed and synthetic spectra of the (1,0) C_2 bands for HD 182040 and HD 137613. Synthetic spectra are plotted for the values of the isotopic ratios (R) shown in the keys and for a spectrum with just the atomic lines. The positions of the key lines are also marked.

V482 Cyg: The Fe I line accounts well for the observed feature (Figure 5.7) with a lower limit for the isotopic ratio $R > 100$.

SU Tau: At the $^{12}C^{13}C$ bandhead, the atomic line makes a dominant contribution but the profile of the observed feature suggests that the Swan band is contributing

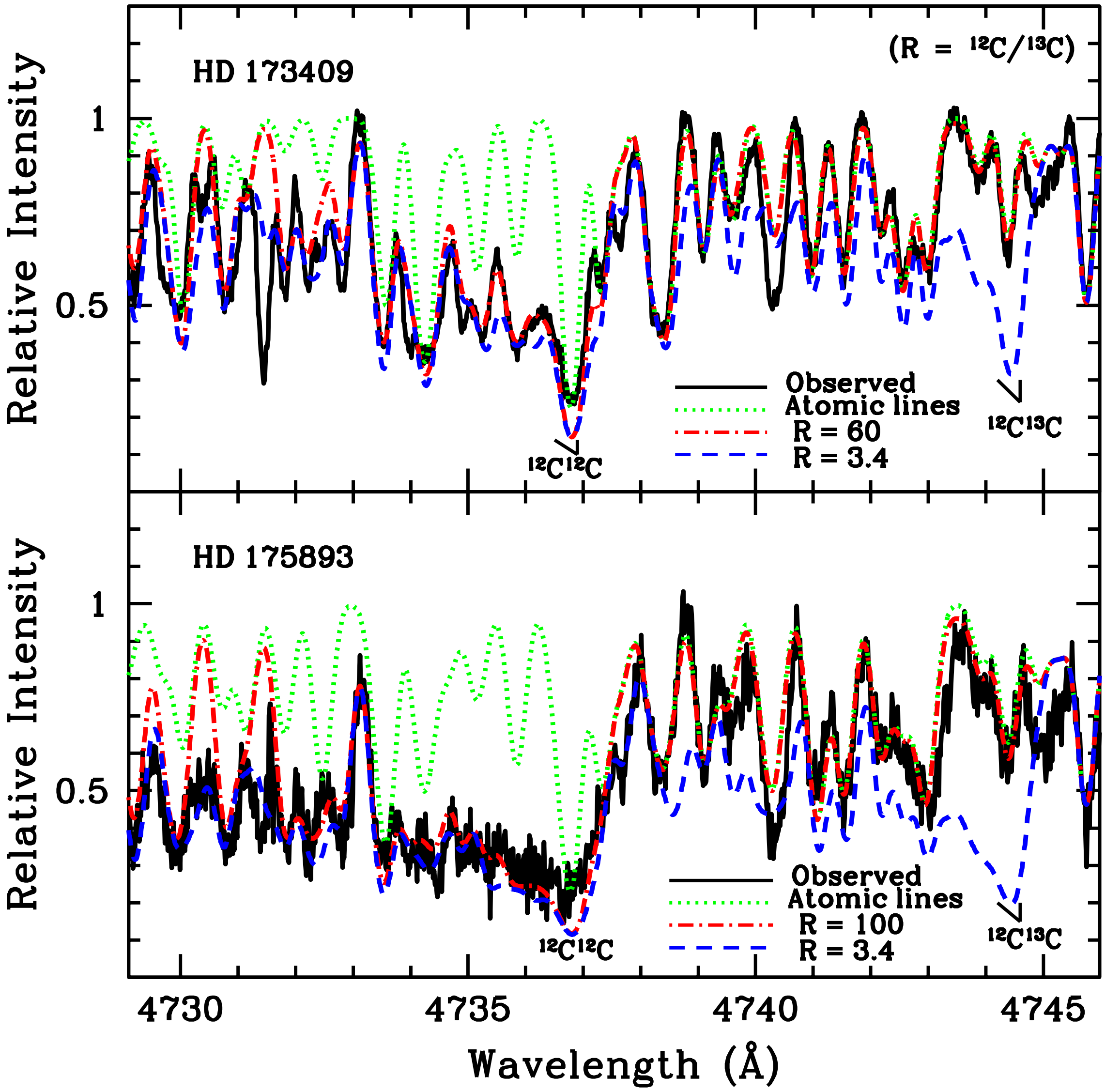

FIGURE 5.12: Observed and synthetic spectra of the (1,0) C_2 bands for HD 173409 and HD 175893. Synthetic spectra are plotted for the values of the isotopic ratios (R) shown in the keys and for a spectrum with just the atomic lines. The positions of the key lines are also marked.

to the blue of the atomic line (Figure 5.8): R seems to be >24. The R = 3.4 synthetic spectrum is clearly rejected as a fit to the observed spectrum.

V CrA: The Fe I line at the $^{12}C^{13}C$ bandhead is seemingly quite unimportant but V CrA is another minority RCB so that the identity of the line's carrier may be relevant here (see above notes on VZ Sgr). The $^{12}C_2$ band is quite strong (Figure 5.8). With the blending line assigned to Fe I, the observed $^{12}C^{13}C$ bandhead is well fit with $R \simeq 8$ to 10. Our derived $^{12}C/^{13}C$ ratio is in agreement with the upper limit of the range set by Rao & Lambert (2008) from the same spectrum. Note that an additional line about 0.6 Å to the blue of the $^{12}C^{13}C$ bandhead is seen in this spectrum.

GU Sgr: Presence of the $^{12}C^{13}C$ band is doubtful because atomic lines may account fully for the bandhead and the region just to the blue: R seems to be in the range >40 (Figure 5.9).

FH Sct: Spectrum synthesis shows that $^{12}C_2$ makes a minor contribution to the observed spectrum (Figure 5.9) but the ^{12}C abundance may be established from the (0,0) and (0,1) bands. The ratio $R > 14$ may be set and the CN-cycle's limit of R = 3.4 is excluded.

U Aqr: The (1,0) $^{12}C_2$ band is so strong (Figure 5.10) that the uncertainty over R is dominated by the derivation of the ^{12}C abundance from the very saturated (1,0) $^{12}C_2$ lines. The carbon abundance from (the also saturated) (0,1) C_2 band is used with the (1,0) $^{12}C^{13}C$ blend to derive the $^{12}C/^{13}C$ ratio. The Fe abundance is derived from several lines longward of the (1,0) $^{12}C^{13}C$ bandhead. A $^{12}C/^{13}C$ ratio in the range 110 to 120 is obtained.

HdC stars: Syntheses of the (1,0) band are shown in Figures 5.11 - 5.12 for the four HdC stars with the ^{12}C abundance set in each case by the fit to the (0,1) band (see Figure 5.13 for a typical fit). In contrast to U Aqr, the $^{12}C^{13}C$ bandhead is well fit by the blending atomic lines with the Fe abundance obtained from lines longward of the bandhead. The derived $^{12}C/^{13}C$ ratio is >100 for HD 137613, >400 for HD 182040, >100 for HD 175893, and >60 for HD 173409.

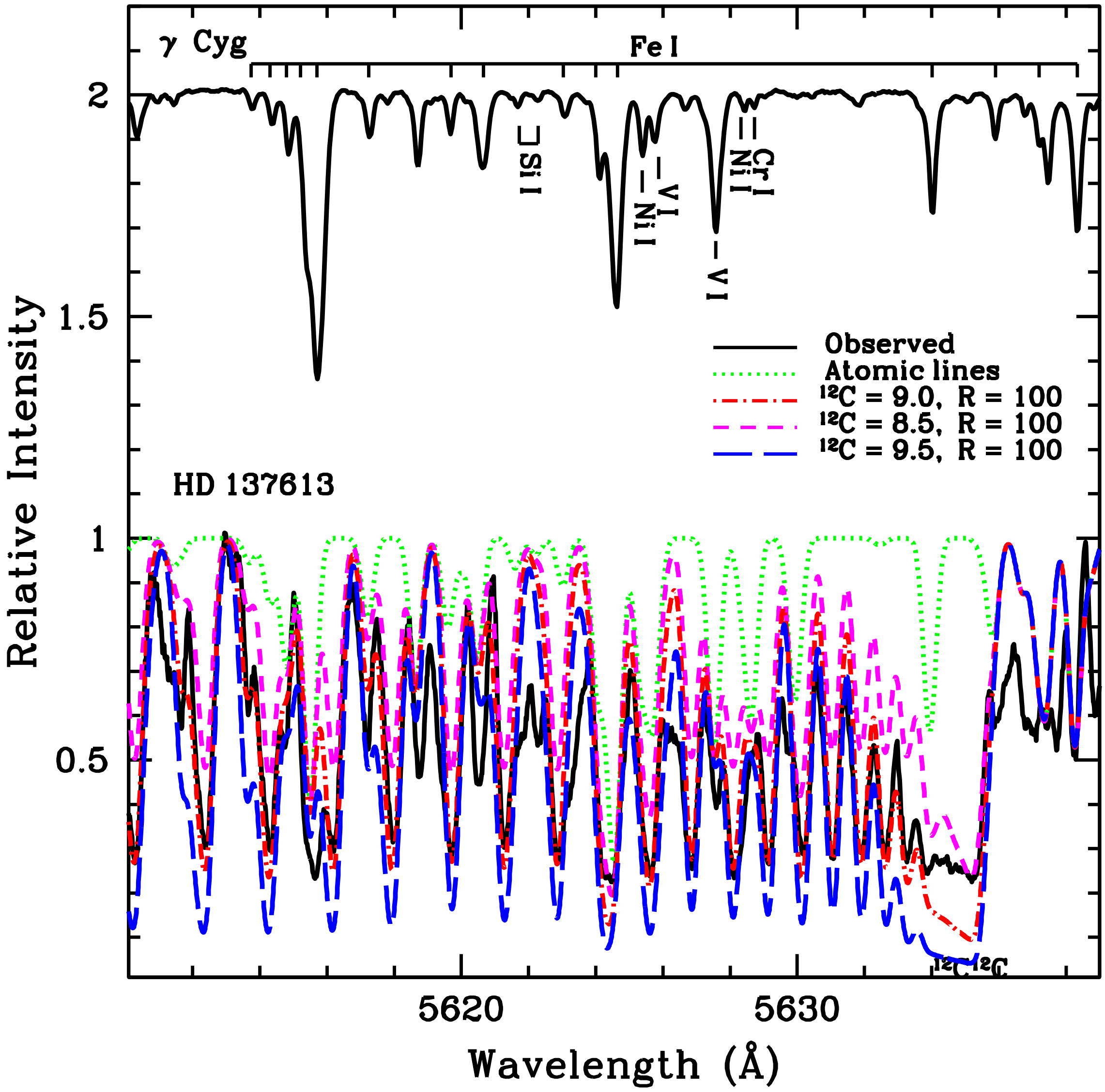

FIGURE 5.13: Observed and synthetic spectra of the (0, 1) C_2 band for HD 137613. Synthetic spectra are plotted for different values of the C abundance – see key on the figure. The spectrum of the γ Cyg is plotted with the positions of the key lines marked.

The final flash object V4334 Sgr

The carbon abundance and the ^{12}C/^{13}C ratio were also determined for the FF-object, V4334 Sgr (Sakurai's Object) to compare with those of the RCB and HdC stars. The spectrum of Sakurai's Object obtained from McDonald observatory on

Table 5.10. The adopted stellar parameters and the ^{12}C/^{13}C ratios for the analysed stars.

Star	($T_{\rm eff}$[K], log g[cgs], ξ_t[km s^{-1}])	^{12}C/^{13}C Ratio[a]	^{12}C/^{13}C Ratio
VZ Sgr	(7000, 0.5, 7.0)	3 - 6	···
UX Ant	(6750, 0.5, 5.0)	14 - 20	···
RS Tel	(6750, 1.0, 8.0)	>60	···
R CrB	(6750, 0.5, 7.0)	>40	>40[b]
V2552 Oph	(6750, 0.5, 7.0)	>8	···
V854 Cen	(6750, 0.0, 6.0)	16 - 24	···
V482 Cyg	(6500, 0.5, 4.0)	>100	···
SU Tau	(6500, 0.5, 7.0)	>24	···
V CrA	(6500, 0.5, 7.0)	8 - 10	4 - 10[c]
GU Sgr	(6250, 0.5, 7.0)	>40	···
FH Sct	(6250, 0.0, 6.0)	>14	···
U Aqr	(5400, 0.5, 5.0)	110 - 120	···
HD 173409	(6100, 0.5, 6.0)	>60	···
HD 182040	(5400, 0.5, 6.5)	>400	>100[d,e]
HD 175893	(5400, 0.5, 6.0)	>100	···
HD 137613	(5400, 0.5, 6.5)	>100	>500[e]
V4334 Sgr[f]	(6900, 0.5, 6.5)	3.4	3.4[g,h]

Note. — [a] Present work, [b] Cottrell & Lambert (1982), [c] Rao & Lambert (2008), [d] Climenhaga (1960), [e] Fujita & Tsuji (1997), [g] Asplund et al. (1997b), [h] Pavlenko et al. (2004)
[f] Final Flash object

7^{th} October 1996 was used for our analysis. The signal-to-noise ratio per pixel in the 4736Å region is about 140. For the same spectrum, the stellar parameters: ($T_{\rm eff}$, log g, $\xi_{\rm t}$) = (6900±300K, 0.5±0.3, 6.5±1 km s^{-1}) were determined by Asplund et al. (1997b). These stellar parameters were adopted for our analysis. The RCB star, VZ Sgr, and Sakurai's Object have similar stellar parameters (see Table 5.10). A relative analysis of these two stars was done to derive the carbon abundance in Sakurai's Object. The carbon abundance in Sakurai's Object is about 0.8 dex higher than in VZ Sgr. The carbon abundance of VZ Sgr is 8.9. As expected, the carbon abundance in the FF-product Sakurai's Object is higher than the carbon abundance in the RCB/HdC stars (see Table 5.5). As an example, the synthesis for Sakurai's Object for deriving the carbon abundance is shown in Figure 5.14.

The $^{12}C/^{13}C$ ratio for Sakurai's Object is derived using the (1,0) C_2 band. The $^{12}C/^{13}C$ ratio is about 3.4, the equilibrium value, as expected for the FF-product (see Figure 5.15).

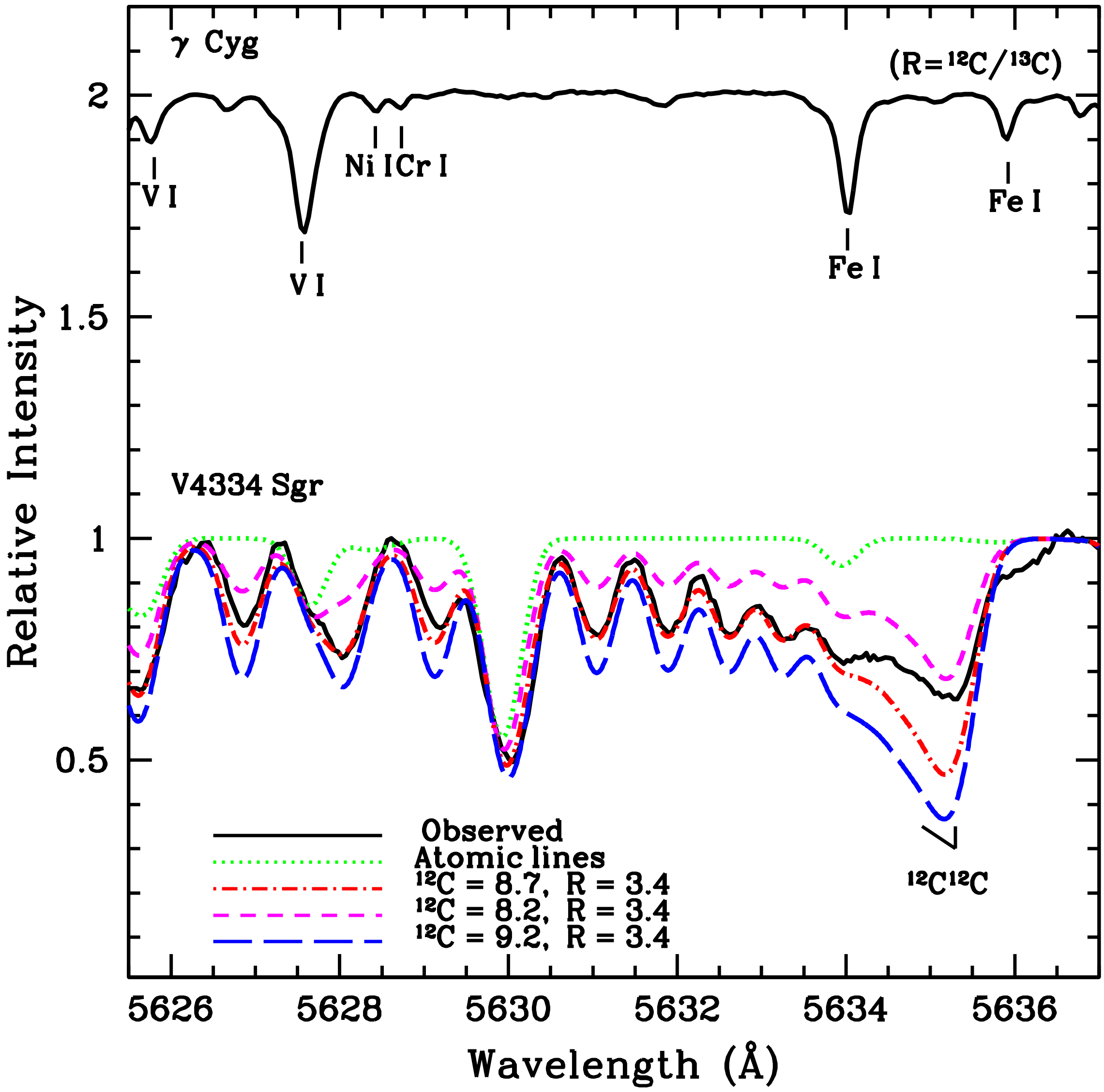

FIGURE 5.14: Observed and synthetic spectra of the (0, 1) C_2 band for Sakurai's Object. Synthetic spectra are plotted for different values of the C abundance – see key on the figure. The spectrum of the γ Cyg is plotted with the positions of the key lines marked.

5.6 Discussion - C_2 and the Carbon Problem

The carbon problem as it appears from the analysis of C I lines is discussed fully by Asplund et al. (2000). In brief, when analysed with state-of-the-art H-poor model atmospheres (Asplund et al. 1997a) constructed for a C/He ratio (= 1%) representative of EHe stars where direct determinations of C and He abundances are possible, the C I lines return a C abundance that is about 0.6 dex less than the input abundance of log ϵ(C) = 9.5. The derived abundance varies little from star-to-star: 13 of the 17 analysed RCBs have abundances between 8.8 and 9.0 and the mean from the set of 17 is 8.9±0.2. A similar result is apparent from Tables 5.5, 5.6, 5.7, 5.8 and 5.9 where the C abundance from C I lines from our spectrum syntheses is quoted. The discrepancy of 0.6 dex between assumed and derived C abundance is the (C I) carbon problem. As the C/He ratio of a model atmosphere is adjusted, the carbon problem (i.e., the 0.6 dex difference between assumed and derived C abundances) persists until a low C/He reached. This persistence arises because the continuous opacity arises from photoionization of neutral carbon from excited levels.

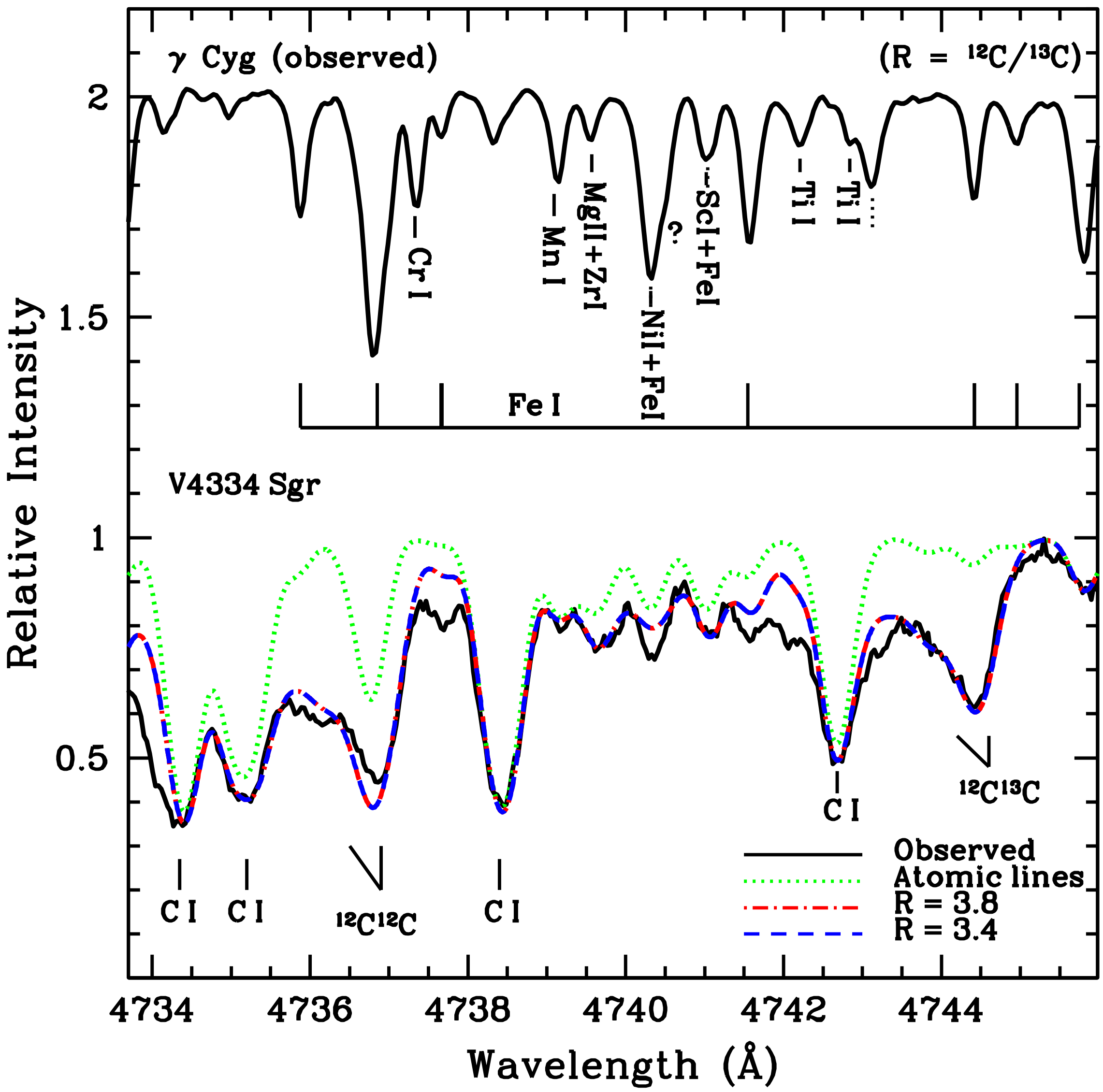

FIGURE 5.15: Figure show the observed and synthetic spectra of the (1,0) C_2 band for Sakurai's Object. Synthetic spectra are plotted for the values of the isotopic ratios (R) shown in the keys and for a spectrum with just the atomic lines. The spectrum of γ Cyg is also plotted – the positions of the key lines are also marked – the dotted line represents the blending of the one or more atomic lines.

Table 5.11. The log ϵ(C) from (0,0) and (0,1) C_2 bands, except for RS Tel which is only from (0, 0) C_2 band, with C/He ratio 1%.

Star	($T_{\rm eff}$, log g)	($T_{\rm eff}$-250, log g)	($T_{\rm eff}$, log g)	($T_{\rm eff}$+250, log g)	($T_{\rm eff}$, log g-0.5)	($T_{\rm eff}$, log g)	($T_{\rm eff}$, log g+0.5)	log ϵ (C I)
VZ Sgr	(7000, 0.5)	8.3	8.8	…	…	8.8	8.4	8.9
UX Ant	(6750, 0.5)	7.9	8.3	…	…	8.3	8.0	8.7
RS Tel	(6750, 1.0)	8.1	8.3	…	8.6	8.3	8.2	8.7
R CrB	(6750, 0.5)	8.3	8.8	…	…	8.8	8.4	8.9
V2552 Oph	(6750, 0.5)	7.9	8.1	…	8.5	8.1	8.0	8.7
V854 Cen	(6750, 0.0)	7.8	8.3	…	…	8.3	7.9	8.8
V482 Cyg	(6500, 0.5)	8.1	8.3	8.7	8.6	8.3	8.2	8.9
SU Tau	(6500, 0.5)	7.8	8.0	8.4	8.3	8.0	7.9	8.6
V CrA	(6500, 0.5)	8.2	8.4	8.8	8.7	8.4	8.3	8.6
GU Sgr	(6250, 0.5)	7.9	8.1	8.4	8.3	8.1	8.1	8.9
FH Sct	(6250, 0.0)	7.5	7.7	8.0	7.9	7.7	7.6	8.9
U Aqr	(5400, 0.5)	8.9	9.2	9.5	…	9.2	…	8.9
HD 173409	(6100, 0.5)	8.4	8.7	9.0	…	8.7	…	8.6
HD 182040	(5400, 0.5)	8.7	9.0	9.3	…	9.0	…	9.0
HD 175893	(5400, 0.5)	8.7	9.0	9.3	…	9.0	…	8.5
HD 137613	(5400, 0.5)	8.7	9.0	9.3	…	9.0	…	8.5

Tables 5.5, 5.6, 5.7, 5.8, and 5.9 also show that the C_2 bands exhibit a carbon problem but one that differs from that shown by the C I lines in several ways: (i) the C abundance from C_2 bands is almost independent of the assumed C/He ratio unlike the abundance from C I lines; (ii) the star-to-star spread in C abundances from C_2 bands is larger than found from the C I lines; (iii) the C abundance from C_2 bands is somewhat more sensitive than that from C I lines to changes in the adopted atmospheric parameters as reflected by Table 5.11, where models spanning the effective temperature and surface gravity uncertainties suggested by Asplund et al. (2000) are considered.

Taken in complete isolation, inspection of Table 5.5, 5.6, 5.7, and 5.8, suggests that a C/He ratio of less than 0.3% can be found for which the ratio adopted in the construction of the model atmosphere is equal to that derived from the C_2 bands. For the RCB stars, Table 5.5, 5.6, 5.7 and 5.8 suggests C/He ratios running from about 0.3% for VZ Sgr and R CrB down to 0.03% for GU Sgr and FH Sct. For the HdC stars (Table 5.9), a C/He of slightly larger than 0.1% is suggested. However, Asplund et al. (2000) remark that C/He $\leq$ 0.05% is required to eliminate the C I carbon problem by lowering the carbon abundance to the point that photoionization of neutral carbon no longer is the dominant opacity source.

Resolution of the carbon problems by invoking low C/He ratios deserves to be tested fully by constructing model atmospheres with lower C/He ratios and appropriate abundances for other elements and determining the C abundances from C I and C_2 lines. Asplund et al. (2000) recognized this possible way to address the C I carbon problem but discounted it on several grounds: (i) removal of carbon photoionization as the dominant continuous opacity makes it difficult to account for the near-uniformity of the C I equivalent widths across the RCB sample, especially as O abundance varies from star-to-star; (ii) an inverse carbon problem is created for the C II lines at 6578 Å and 6582 Å which are seen in the hottest RCBs; and (iii) these low C/He ratios for RCB stars are at odds with the higher ratios obtained directly from He and C lines for EHe stars which one assumes are intimate relatives of the RCB and HdC stars. Asplund et al. (2000) noted that published analyses of EHe stars gave the mean C/He = 0.8±0.3% over a range 0.3-1.0% with three unusual EHe stars providing much lower ratios (0.002% to 0.2%). Pandey et al. (2006) confirmed the C/He ratios for the leading group of EHe stars. From the following references (Drilling et al. 1998; Harrison & Jeffery 1997; Jeffery et al. 1998; Jeffery & Heber 1993; Jeffery et al. 1999; Pandey et al. 2001; Pandey & Lambert 2011; Pandey et al. 2006; Pandey & Reddy 2006), that also includes the recent analyses of these EHe stars, the mean value of C/He = 0.6±0.3% is noted.

The RCB-EHe mismatch of their C/He ratios invites two responses: (i) the carbon problems for the RCB stars should be resolved on the assumption that their C/He ratios and those of the EHe stars span similar ranges; or, (ii) as a result of different evolutionary paths, the C/He ratios of RCB and EHe stars span different ranges.

After considering a suite of possible explanations for their carbon problem, Asplund et al. (2000) proposed that the actual atmospheres of the RCB stars differed from the theoretical atmospheres in that the temperature gradient was flatter than predicted. Hand-crafted atmospheres were shown to solve the C I carbon problem. However, the issue of accounting for the additional heating and cooling of the hand-crafted atmospheres was left unresolved. In principle, the change in the temperature structure – a heating at modest optical depths – will require a higher C abundance to account for the C_2 bands so that the C I and C_2 carbon problems might be both eliminated.

Further exploration of the carbon problem was pursued by Pandey et al. (2004) who observed the 8727 Å and 9850 Å [C I] lines in a sample of RCB stars. The 8727 Å line gives a more severe carbon problem than the C I lines, say 1.2 dex versus 0.6 dex for C/He=1.0% model atmospheres. In part, this difference might be reduced by a revision of the effective temperature scale because the [C I] line being of low excitation potential has a temperature dependence relative to the continuous carbon opacity from highly excited levels. The 9850 Å line may give a similar carbon problem to the C I lines or the forbidden line may be blended with an unidentified line. To account for the 8727 Å carbon problem, Pandey et al. (2004) considered introducing a chromospheric temperature rise to the theoretical model photospheres. Such a chromosphere with LTE produces emission at the C_2 bandheads and offers a qualitative explanation for the fact that the best-fitting synthetic spectra from the theoretical photospheres (i.e., no chromospheric temperature rise) are deeper than the observed spectra at the bandheads.

Analysis of the C_2 bands suggests a novel clue to the C_2 carbon problem. As Figure 5.16 shows the C abundance from the C_2 bands is correlated with the O abundance derived by Asplund et al. (2000) from O I and/or [O I] lines. The points are distributed about the relation C/O $\sim$ 1. (The C abundance from the C I lines is not well correlated with the O abundance and most points fall below the C/O = 1 locus). In Figure 5.17, the EHe stars are plotted along with RCB stars. The RCBs may connect those EHes of very low C/He with the majority of higher C/He.

Perhaps a more powerful clue is the fact that the Fe abundance of the RCB and HdC stars is uniformly sub-solar. The mean Fe abundance excluding the minority RCBs is 6.5 or 1.0 dex less than the solar Fe abundance. EHe stars show a similar spread and mean Fe abundance of 6.7 (Jeffery et al. 2011).

5.7 Discussion - The $^{12}C/^{13}C$ ratio and the origin of the RCBs

Discussion of the determinations of the $^{12}C/^{13}C$ ratio may be focussed on three main points.

First, the ratio is low in the two minority RCBs VZ Sgr and V CrA. Unless there is an unidentified line from an element with an overabundance in a minority RCB star, VZ Sgr has a $^{12}C/^{13}C$ ratio equal within the measurement uncertainty to the equilibrium ratio for the H-burning CN-cycle. The ratio is higher ($\simeq$ 8) for V CrA but considerably lower than the upper limits set for majority RCBs. (Rao & Lambert (2008) gave the ratio as 3.4 for V CrA but apparently did not include the factor of two arising from the fact that $^{12}C^{13}C$ is not a homonuclear molecule, i.e., 3.4 should be 6.8.) In some respects, V854 Cen is a minority RCB star and its $^{12}C/^{13}C$ ratio of 18 is also generally lower than representative upper limits for majority RCB stars.

Second, the $^{12}C/^{13}C$ ratio for all majority RCBs is much larger than the equilibrium ratio for the CN-cycle. [6]

Third, there appears to be a range in the $^{12}C/^{13}C$ ratios among majority RCBs. The star with the lowest ratio appears to be UX Ant (Figure 5.5) for which the predicted blend of atomic lines at the (1,0) $^{12}C^{13}C$ bandhead accounts for less than half of the strength of the observed absorption feature. Similarly for U Aqr, the atomic lines at the bandhead account for about half of the observed feature but because the C_2 lines are strong the isotopic bandhead translates to the ratio $^{12}C/^{13}C \simeq 110$. For these cases at least, it seems likely that the $^{12}C^{13}C$ bandhead is present in our spectra. Within the uncertainties associated with the blend of atomic lines, other RCBs yield a lower limit to the isotopic ratio. This limit is highest for the HdCs where the C_2 bands are very strong. Note how the atomic lines account remarkably well for the observed spectrum between the $^{12}C_2$ and $^{12}C^{13}C$ (1,0) bandheads.

Our results are in good agreement with published results for the few stars previously analysed (Table 5.10). In the case of R CrB, Cottrell & Lambert (1982) determined a lower limit of 40 from the C_2 (0,1) band. Fujita & Tsuji (1977) from spectra of the CN Red system set lower limits of 500 for HD 137613 and >100 for HD 182040. The latter limit was also reported by Climenhaga (1960) from

[6] We note that Goswami et al. (2010)'s observation that the ratio is about 3.4 for U Aqr is incompatible with our spectra by simple inspection of Figure 5.10.

high-resolution photographic spectra of C_2 bands. Lower limits set by García-Hernández et al. (2009, 2010) are not competitive with those from CN or our limits from C_2.

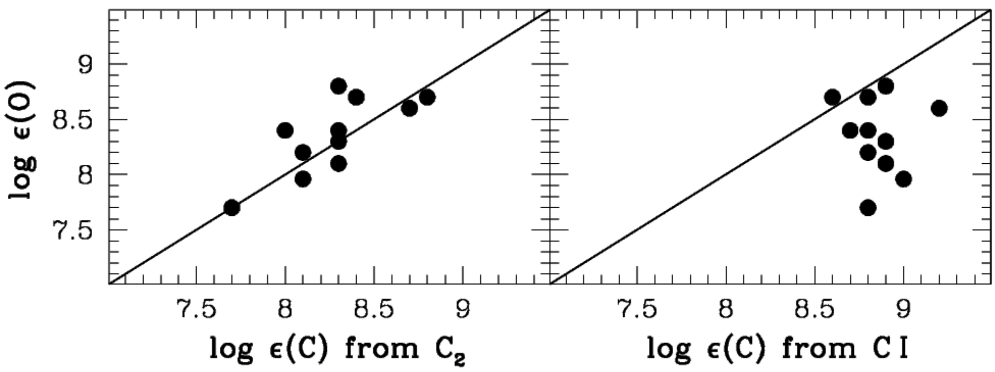

FIGURE 5.16: The plot of log ϵ(C), from C_2 bands and C I lines versus log ϵ(O) for RCB stars. The log ϵ(O) and the log ϵ(C), from C I lines, are from Asplund et al. (2000).

Prospects for a low $^{12}C/^{13}C$ ratio in the atmosphere of a product of the DD scenario are dim. In the scenario's cold version (i.e., no nucleosynthesis as a result of the merger), the C is provided by the He shell of the C-O white dwarf and quite likely also by layers of the C-O core immediately below the He shell. The latter contribution will be devoid of ^{13}C. In the He shell, ^{13}C may be present in the outermost layers as a result of penetration of protons from the H-rich envelope of the former AGB star into the He shell. Very slow penetration results in the build up of a $^{12}C/^{13}C$ ratio of about three and inhibits somewhat the conversion of the ^{13}C to ^{14}N, as usually occurs in the CN-cycle. This mechanism sustains the favored neutron source for the *s*-process in AGB stars; the $^{13}C(\alpha, n)^{16}O$ is the neutron source. The He is provided almost entirely by the He white dwarf which will have very little carbon but abundant nitrogen as a result of H-burning by the CNO-cycles.

A cold merger of the He white dwarf with the He shell of the C-O white dwarf results in a C/He ratio (see Pandey & Lambert (2011), eqn. 1)

$$\frac{\mathrm{C}}{\mathrm{He}} \simeq \frac{\mathrm{A(He)}}{\mathrm{A(C)}} \frac{\mu(\mathrm{C})_{\mathrm{C-O:He}} M(\mathrm{C-O:He})}{M(\mathrm{He})} \tag{5.1}$$

where $\mu(\mathrm{C})_{C-O:He}$ is the mass fraction of ^{12}C in the He shell, M(C-O:He) is the mass of the He shell and M(He) is the mass of the He white dwarf. With plausible values for the quantities on the right-hand side of the equation, i.e., $\mu(\mathrm{C})_{C-O:He}$ $\simeq 0.2$, M(C-O:He) $\simeq 0.02 M_{\odot}$, and M(He) $\simeq 0.3 M_{\odot}$, one obtains C/He $\simeq$ 0.4%, a value at the lower end of the C/He range found for EHe stars. Additional ^{12}C is likely provided by mixing with the layers of the C-O white dwarf immediately below the He shell.

The attendant ^{12}C/^{13}C ratio will be a maximum if these latter contributions are absent. Then, this ratio will depend on the fraction of the He shell over which ^{13}C is abundant (relative to ^{12}C), say ^{12}C/^{13}C $\sim 3/f_{13}$ where f_{13} is the fraction of the He shell which is rich in ^{13}C. For $f_{13} \sim 0.1$ and 0.01, the predicted isotopic ratio is 30 and 300, respectively. These estimates must be increased when the mixing at the merger includes the layers of the C-O white dwarf immediately below the He shell.

At present, there are no reliable *ab initio* calculations of the mass of the ^{13}C-rich layer in the He shell of an AGB star. Additionally, one is making a bold assumption that the He shell of the C-O white dwarf which accepts merger with the He white dwarf resembles the He shell of a AGB star. Mass estimates relevant to an AGB star may be obtained by the fit to observed s-process abundances. Gallino et al. (1998) suppose that the ^{13}C rich layer amounts to about 1/20 of the mass in a typical thermal pulse occurring in the He shell. With $f_{13} \simeq 0.05$, the isotopic ratio is 60. Interestingly, this is consistent with our inferred range. This will increase as the C-O white dwarf contributes to the mixing. Destruction of ^{13}C by α particles may occur in a 'hot' phase during the merger and thus also raise the isotopic ratio; the ^{13}C(α, n) destruction rate is roughly a factor of 100 faster than the ^{14}N(α, γ) rate providing ^{18}O. The low isotopic ratio for minority RCB

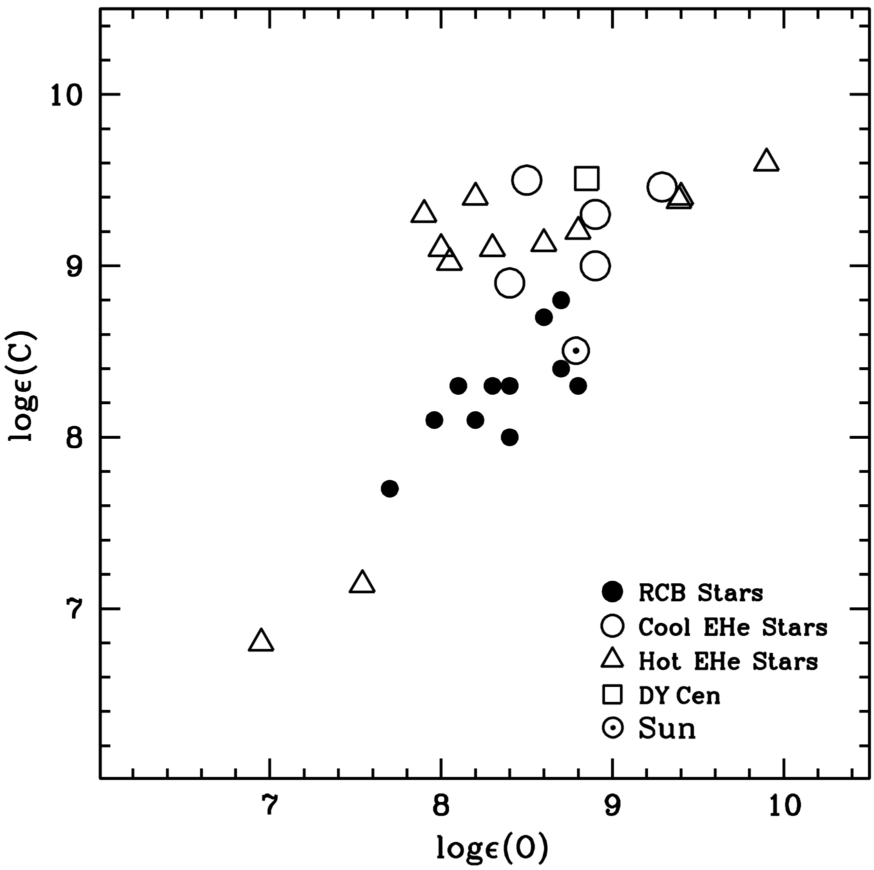

FIGURE 5.17: The plot of log ϵ(C) from C_2 bands versus log ϵ(O) (Asplund et al. 2000) for RCB and EHe stars. Our sample of eleven RCBs are represented by filled circles. Five cool EHes are represented by open circles (Pandey et al. 2001, 2006; Pandey & Reddy 2006). Twelve hot EHes are represented by open triangles (Drilling et al. 1998; Harrison & Jeffery 1997; Jeffery et al. 1998, 1999; Pandey & Lambert 2011). DY Cen, the hot minority RCB (Jeffery & Heber 1993) is represented by open square. $\odot$ represents the Sun.

stars – VZ Sgr, and V CrA – are unexplained as are their distinctive elemental abundances. Nevertheless, the high carbon abundance, and the low $^{12}C/^{13}C$ ratio of about 3.4 for the FF object V4334 Sgr are as expected.

5.8 Concluding remarks

The C_2 Swan bands are present in spectra of the HdC stars and in all but the hottest RCB stars. Analysis of these bands provides an alternative to the C I lines of providing estimates of the C abundance and in addition provide an opportunity to estimate the $^{12}C/^{13}C$ ratio. When analysed with Uppsala model atmospheres, the C_2 bands return a C abundance that is almost independent of the C/He ratio assumed in construction of the model atmosphere. If consistency between assumed and derived C abundances is demanded, the C_2 bands imply C/He ratios across the RCB and HdC sample run in the range 0.03% to 0.3%, a range that is notably lower than the range 0.3–1.0% found from a majority of EHes. This mismatch, if not a reflection of different modes of formation, implies that the C abundances for RCB and HdC stars are subject to a systematic error. Therefore, it appears that a version of the carbon problem affecting the C I lines (Asplund et al. 2000) applies to the C_2 lines. Although alternative explanations can not yet be totally eliminated, it appears that higher order methods of model atmosphere construction are needed in order to check that Asplund et al.'s suggestion of the real atmospheres have a flatter temperature gradient than predicted by present state-of-the-art model atmospheres. Nonetheless, that the carbon abundances derived from C_2 Swan bands are the real measure of the carbon abundances in these stars cannot be ruled out.

There is evidence for the presence of detectable amounts of ^{13}C in the spectra of a few RCB stars and especially for the minority RCB stars. For the other RCBs and the HdC stars, lower limits are set on the carbon isotopic ratio. Apart from the minority RCB stars, the estimates of the carbon isotopic ratio are consistent with simple predictions for a cold merger of a He white dwarf with a C-O white dwarf.

The minority RCB stars are an enigma. Their distinctive pattern of elemental abundances remains unaccounted for; for example, V CrA has a Fe deficiency of 2 dex but [Si/Fe] $\sim$ [S/Fe] $\sim$ [Sc/Fe] $\simeq$ 2 with [Na/Fe] $\sim$ [Mg/Fe] $\sim$ 1 (Rao & Lambert 2008). Add to these anomalies, the ^{12}C/^{13}C ratio is much lower than found for the majority RCB stars unless the (1,0) Swan ^{12}C^{13}C bandhead is blended with an as yet unidentified atomic line whose strength is unsuspected from examination of the spectra of majority RCB stars. The enigma calls for additional observational insights.

Chapter 6

Summary, Conclusions and Future Work

6.1 Summary and Conclusion

The aim of this thesis was to investigate the origin and evolution of H-deficient supergiants: RCB and HdC stars. We have investigated the origin of these stars: (a) by conducting a survey for identifying H-deficient stars in the globular cluster ω Centauri, and to locate these stars on the HR-diagram, and (b) by deriving the Galactic RCB/HdC stars', including the FF-object V4334 Sgr, C-abundances and the $^{12}C/^{13}C$ ratios that are potential clues to their origin.

A spectroscopic survey for identifying H-deficient stars in ω Cen

The survey is based on the Calamida et al. (2009)'s red giant sample of ω Cen. The existence of double main sequence and range in the metallicity of the red giants in ω Cen, which is not as expected for the globular clusters, was taken as a clue for the presence of H-deficient stars. By applying the photometric and the spectroscopic characteristics of the RCB/HdC stars, the program stars were selected. For these program stars, the low-resolution spectra were obtained from the Vainu Bappu Observatory (VBO), Kavalur, India.

The primary focus was to look for the weak or absent Hα-line in the observed spectra of the program stars. The strengths of the Hα-line in the observed spectra of the program stars are similar, and are as expected for their spectral class. Note that, none of the program stars' spectra showed a weak Hα-line or any of the carbon features typical to RCB/HdC stars. However, the program stars' spectra do exhibit the characteristics of the typical giants. There was a clear presence of the strong Mg *b* lines and the (0, 0) MgH band in the observed spectra of the metal rich giants of ω Cen. Hence, in our study, we have analyzed the (0, 0) MgH band in the observed spectra of the program stars. Based on the strengths of the Mg *b* lines and the (0, 0) MgH band, three groups were identified: (i) the metal rich giants with strong Mg *b* lines and the MgH band, (ii) the metal poor giants with weak Mg *b* lines and no MgH band, and (iii) the metal rich giants with strong Mg *b* lines, but no MgH band.

The spectra of program stars were analyzed by comparing the observed MgH band strengths of stars with similar stellar parameters, and by synthesizing the MgH bands for their adopted stellar parameters. The stellar parameters for the program stars, determined by Johnson & Pilachowski (2010) using high resolution spectra, were adopted for our analyses.

By comparing the observed MgH bands among the stars of (i) and (iii) group, with similar stellar parameters, four stars were identified having weaker or absent MgH band. Two stars: 178243 and 73170 are from the first group showing the strong Mg *b* lines, but weaker MgH band than expected for their stellar parameters. The other two stars: 262788 and 193804 are from the third group showing strong Mg *b* lines, but absent MgH band not as expected for their stellar parameters.

The MgH band strengths in the observed spectra of these four stars along with all the first and third group stars, were further analyzed by synthesis as discussed in

Chapter 3. The Mg abundances derived for these four stars are much lower than that expected for the red giants of ω Cen as given by Norris & Da Costa (1995) for their metallicities.

The weak/absent MgH band in the observed spectra of these four giants inspite of the presence of strong Mg *b* lines, may not be due to the stellar parameters or a lower Mg abundance. The only plausible reason is a relatively lower abundance of hydrogen in their atmosphere. Hence, we report the discovery of four giants with relatively lower abundance of hydrogen in their atmospheres. These giants may belong to the group of helium enriched ($n_{He}/n_H \sim 0.16-0.2$)[1] red giants of ω Cen similar to those found in the studies of Dupree & Avrett (2013); Dupree et al. (2011), for which the blue main sequence (bMS) stars may be the progenitors. The double main sequence, the red main sequence (rMS) and the blue main sequence (bMS), in ω Cen was discovered by Anderson (1997) and was confirmed by Bedin et al. (2004); Norris (2004); Piotto et al. (2005). The bMS stars differ from rMS stars by their helium enrichment upto Y $\sim$ 0.38 with the range: (0.35 $<$ Y $<$ 0.4) (Norris 2004; Piotto et al. 2005). The Y value for rMS stars is about 0.25 (Norris 2004; Piotto et al. 2005).

In this survey we have not found any H-deficient star of RCB-type. This result is in agreement with our prediction for the number of H-deficient stars formed by the DD and FF scenario in the globular cluster, ω Cen. From our predictions, we have estimated less than a couple of H-deficient stars in ω Cen (see Tables 4.1 and 4.2).

Determination of the C-abundance and the ^{12}C/^{13}C ratios for the Galactic RCB/HdC stars, and FF-object, V4334 Sgr

For RCB and HdC stars, the carbon abundances derived from C I lines are about a factor of four lower than the carbon abundance of the adopted model atmosphere.

[1]Note that, the expected n_{He}/n_H ratio and Y for the normal giants are about 0.1 and 0.25, respectively.

This has been dubbed as the 'carbon problem' by Asplund et al. (2000). This discrepancy persists with the change in the input carbon abundance of the adopted model atmosphere. Hence, the carbon abundances are not known for RCB and HdC stars. In this study, the C_2 Swan bands were analysed to examine the carbon problem by deriving the carbon abundances of these stars; $^{12}C/^{13}C$ ratios, which are potential clues to their origin, were also determined.

Using the high resolution spectra obtained from the McDonald Observatory and the VBO, the analyses were carried out. The carbon abundances were derived from (0, 0) and (0, 1) C_2 Swan bands, and the $^{12}C/^{13}C$ ratios were derived from (1,0) C_2 Swan band. The carbon abundances and the $^{12}C/^{13}C$ ratios were derived by synthesizing the spectra using the Uppsala spectrum synthesis code and the H-deficient line-blanketed model atmospheres (Asplund et al. 1997a) along with our newly constructed detailed C_2 molecular line list and the blending atomic lines. The stellar parameters and the elemental abundances were adopted from Asplund et al. (2000); Rao & Lambert (2003); Warner (1967) for RCB/HdC stars.

The carbon abundances derived from the different C_2 bands were essentially identical. The carbon abundances derived from the C_2 Swan bands is about the same for the adopted models constructed with different carbon abundances over the range: 8.5 (C/He = 0.1%) to 10.5 (C/He = 10%). For the RCB stars, C/He ratios varies from about 0.3% for VZ Sgr and R CrB down to 0.03% for GU Sgr and FH Sct. For the HdC stars, a C/He of slightly larger than 0.1% is suggested. The range of C/He ratio derived for the RCB and HdC stars is notably lower than the range 0.3% – 1.0% found from a majority of extreme helium (EHe) stars. This mismatch of C/He ratios of RCBs/HdCs and EHes, if not a reflection of different modes of formation, implies that the carbon abundances for the RCB and HdC stars are subject to a systematic error. Nonetheless, that the carbon abundances derived from C_2 Swan bands are the real measure of the carbon abundances in these stars cannot be ruled out. The carbon abundance derived for the FF-object, V4334 Sgr

(Sakurai's object) is about 10-100 times higher than the RCB/HdC stars and is as expected.

Similarly, the $^{12}C/^{13}C$ ratios were determined for RCB/HdC stars. Our focus was on determining whether the $^{12}C/^{13}C$ ratio is close to the CN-cycle equilibrium ratio ($^{12}C/^{13}C = 3.4$), as expected for a star produced by the FF scenario, or is a much larger value, as expected for the DD scenario. The derived $^{12}C/^{13}C$ ratios for all the majority RCBs and all the HdCs are much larger than the equilibrium ratio for the CN-cycle. The ratio is low in the two minority RCBs, VZ Sgr and V CrA that is 3–6 and 8–10, respectively.

Except for the minority RCB stars, VZ Sgr and V CrA, the estimates of the $^{12}C/^{13}C$ ratios for the majority RCBs and all the HdCs are consistent with simple predictions for a cold merger of a He white dwarf with a CO white dwarf. Due to their distinctive pattern of elemental abundances, the low $^{12}C/^{13}C$ ratios in minority RCB stars, VZ Sgr and V CrA remain unexplained. As expected, the $^{12}C/^{13}C$ ratio determined for the FF object, Sakurai's object is about 3–4.

6.2 Future work

We plan to carry out high resolution spectroscopy of the newly discovered H-deficient giants from our survey. For these giants, neither the Mg abundances nor the spectroscopic studies in the region of Mg *b* lines and the (0, 0) MgH band are available in the literature. Hence, the idea is to explore the degree of He-enhancement/H-deficiency in these stars by analyzing the (0, 0) MgH band using the model atmospheres constructed for different He/H ratios.

The recent spectroscopic studies of Dupree & Avrett (2013) and Marino et al. (2014) confirm the existence of the He-enhanced stars in ω Cen and NGC 2808, respectively. Hence, similar surveys for identifying the H-deficient giants in the other Galactic globular clusters are also planned.

One of the important clues from our studies of Galactic RCB and HdC stars is that the determined Fe abundances are subsolar. The same spread in the Fe abundances are also observed for the EHes. This clearly shows that RCBs, HdCs and EHes are related objects. An abundance analyses using the curve - of - growth (COG) technique was carried out by Warner (1967) for HdC stars using photographic plate spectra in the blue. Hence, an abundance analysis of the HdC stars with the modern model atmospheres using CCD spectra in the optical would provide better abundance estimates. These abundances are further clues to the origin and the evolutionary connection of HdC, RCB and EHe stars.

The carbon abundances are not known for the Galactic RCB and HdC stars due to the carbon problem of C I lines. From our studies, the carbon abundances for the Galactic RCB and HdC stars were determined from the C_2 Swan bands. The carbon abundances derived from the C_2 Swan bands are independent of the input carbon abundance of the adopted model atmosphere, unlike that for the observed C I lines. Hence, by adopting the carbon abundances derived from the C_2 Swan bands, new model atmospheres need to be computed for further analyses of RCB/HdC stars.

For the recently discovered RCB and HdC stars the abundance analyses are not yet conducted. We plan to carry out the abundance analyses for these stars by obtaining their high-resolution spectra.

Appendix A

The RCB, HdC and EHe stars in the Galaxy and in the Magellanic Clouds

Table A.1: The Galactic RCB stars

Sl No.	Stars	RA	Declination	m_v	References
1	XX Cam	04 08 38.7	+53 21 40.0	07.3	(1)
3	W Men	05 26 24.6	−71 11 12.0	13.8	(1)
4	HV 12842	05 45 02.5	−64 24 21.0	13.7	(1)
5	SU Tau	05 49 03.7	+19 04 22.0	09.7	(1)
6	UX Ant	10 57 09.1	−37 23 56.0	12.0	(1)
7	UW Cen	12 43 17.1	−54 31 41.0	09.1	(1)
8	Y Mus	13 05 48.3	−65 30 47.0	10.3	(1)
9	V854 Cen	14 34 49.3	−39 33 19.0	07.1	(1)
10	Z UMi	15 02 01.5	+83 03 50.0	11.0	(1)
11	S Aps	15 09 24.7	−72 03 46.0	09.7	(1)
12	ASAS-RCB-1	15 44 25.0	−50 45 01.2	11.9	(2)
13	R CrB	15 48 34.3	+28 09 25.0	05.8	(2)

Table A.1 – continued from previous page

Sl No.	Stars	RA	Declination	m_v	References
14	ASAS-RCB-9	16 22 28.8	−48 35 55.8	10.8	(3)
15	RT Nor	16 24 18.7	−59 20 39.0	10.2	(3)
16	RZ Nor	16 32 41.6	−53 15 34.0	11.0	(3)
17	ASAS-RCB-2	16 41 24.7	−51 47 43.4	11.8	(2)
18	ASAS-RCB-14	16 47 29.7	−15 25 22.9	12.5	(2)
19	ASAS-RCB-3	16 54 43.6	−49 25 55.0	11.8	(2)
20	ASAS-RCB-12	17 01 01.4	−50 15 34.9	11.7	(2)
21	ASAS-RCB-4	17 05 41.2	−26 50 03.4	11.9	(2)
22	ASAS-RCB-15	17 08 27.2	−32 26 49.5	14.2	(2)
23	ASAS-RCB-16	17 14 14.4	−21 26 13.7	12.8	(2)
24	V517 Oph	17 15 19.7	−29 05 39.0	12.0	(2)
25	ASAS-RCB-10	17 17 10.2	−20 43 15.8	11.4	(2)
26	V1773 Oph	17 17 22.3	−20 22 38.7	16.8	(2)
27	EROS2-CG-RCB-12	17 19 58.5	−30 04 21.3	18.04	(3)
28	ASAS-RCB-17	17 17 44.5	−29 38 00.1	13.1	(2)
29	V2552 Oph	17 23 14.5	−22 52 06.5	10.7	(4)
30	EROS2-CG-RCB-7	17 29 37.1	−30 39 36.7	18.63	(3)
31	EROS2-CG-RCB-6	17 30 23.8	−30 08 28.3	16.12	(3)
32	EROS2-CG-RCB-8	17 39 20.7	−27 57 22.4	16.92	(3)
33	V532 Oph	17 32 42.6	−21 51 40.8	11.7	(5)
34	EROS2-CG-RCB-10	17 45 31.4	−23 32 24.4	15.46	(3)
35	EROS2-CG-RCB-5	17 46 00.3	−33 47 56.6	17.24	(3)
36	EROS2-CG-RCB-4	17 46 16.2	−32 57 40.9	16.22	(3)
37	EROS2-CG-RCB-9	17 48 30.9	−24 22 56.5	19.88	(3)
38	EROS2-CG-RCB-11	17 48 41.5	−23 00 26.5	15.67	(3)
39	ASAS-RCB-7	17 49 15.7	−39 13 16.6	12.5	(2)
40	EROS2-CG-RCB-1	17 52 19.9	−29 03 30.8	15.71	(2)

Table A.1 – continued from previous page

Sl No.	Stars	RA	Declination	m_v	References
41	ASAS-RCB-5	17 52 25.5	−34 11 28.2	12.3	(2)
42	EROS2-CG-RCB-2	17 52 48.7	−28 45 18.9	18.85	(2)
43	EROS2-CG-RCB-3	17 58 28.3	−30 51 16.4	13.64	(2)
44	MACHO J175759.0-281813	17 57 59.0	−28 18 13.1	14.5	(6)
45	MACHO J175952.2-293950	17 59 52.2	−29 39 50.0	16.6	(6)
46	EROS2-CG-RCB-13	18 01 58.2	−27 36 48.3	14.54	(3)
47	V1783 Sgr	18 04 49.7	−32 43 13.0	10.5	(1)
48	ASAS-RCB-11	18 12 03.7	−28 08 36.2	11.8	(2)
49	ASAS-RCB-13	18 24 43.5	−45 24 43.8	9.9	(2)
50	GM Ser	18 08 35.8	−15 04 01.7	12.0	(2)
51	WX CrA	18 08 50.4	−37 19 44.0	10.4	(2)
52	V739 Sgr	18 13 10.5	−30 16 00.0	13.5	(2)
53	EROS2-CG-RCB-14	18 13 14.9	−27 49 40.9	15.43	(3)
54	V3795 Sgr	18 13 23.5	−25 46 41.0	11.0	(3)
55	VZ Sgr	18 15 08.6	−29 42 29.0	10.2	(3)
56	IRAS 1813.5-2419	18 16 39.2	−24 18 33.4	12.6	(2)
57	V4017 Sgr	18 18 02.2	−29 29 33.0	12.0	(7)
58	RS Tel	18 18 51.1	−46 32 54.0	09.9	(1)
59	MACHO 181927.4-212408	18 19 27.4	−21 24 08.2	17.3	(6)
60	MACHO J181933.9-283558	18 19 33.9	−28 35 57.8	14.3	(6)
61	GU Sgr	18 24 15.5	−24 15 26.0	10.1	(1)
62	V391 Sct	18 28 06.6	−15 54 44.1	13.25	(2)
63	MACHO J183218.6-131049	18 32 18.6	−13 10 48.9	16.3	(6)
64	FH Sct	18 45 14.9	−09 25 36.0	12.2	(1)
65	V CrA	18 47 32.2	−38 09 33.0	10.0	(1)
66	ASAS-RCB-21	18 58 41.8	−02 20 11.3	12.8	(2)
67	ASAS-RCB-18	19 00 09.4	−02 02 57.9	13.6	(2)

Table A.1 – continued from previous page

Sl No.	Stars	RA	Declination	m_v	References
68	ASAS-RCB-19	19 01 33.7	+14 56 09.6	13.5	(2)
69	ASAS-RCB-8	19 06 39.9	−16 23 59.2	10.9	(3)
70	SV Sge	19 08 11.7	+17 37 41.0	10.4	(3)
71	V1157 Sgr	19 10 12.1	−20 29 39.0	12.5	(3)
72	RY Sgr	19 16 32.7	−33 31 19.0	06.4	(3)
73	ES Aql	19 32 21.6	−00 11 31.0	11.5	(8)
74	ASAS-RCB-20	19 53 43.1	+14 41 09.3	12.7	(2)
75	V482 Cyg	19 59 42.6	+33 59 28.0	10.9	(2)
76	ASAS-RCB-6	20 30 04.9	−62 07 59.2	13.0	(2)
77	U Aqr	22 03 19.7	−16 37 35.0	11.2	(2)
78	UV Cas	23 02 14.7	+59 36 37.0	10.6	(2)

References – (1) Clayton (1996), (2) Tisserand et al. (2013), (3) Tisserand et al. (2008), (4) Hesselbach et al. (2003), (5) Clayton et al. (2009), (6) Zaniewski et al. (2005), (7) Jeffery et al. (1996), (8) Clayton et al. (2002)

Table A.2: The LMC RCB stars

Sl No.	Stars	RA	Declination	m_v	References
1	EROS2-LMC-RCB-3	04 59 35.8	−68 24 44.70	14.2	(1)
2	MACHO-18.3325.148	05 01 00.4	−69 03 43.20	14.5	(1)
3	EROS2-LMC-RCB-2	05 10 28.5	−69 47 04.50	14.3	(1)
4	HV 5637	05 11 31.0	−67 55 50.0	14.8	(2)
5	EROS2-LMC-RCB-1	05 14 40.2	−69 58 40.0	14.8	(1)
6	MACHO-16.5641.22	05 14 46.2	−67 55 47.4	14.9	(1)
7	MACHO-79.5743.15	05 15 51.8	−69 10 08.6	15.2	(1)
8	MACHO6.6575.13	05 20 48.2	−70 12 12.5	15.2	(3)
9	MACHO-6.6696.60	05 21 47.9	−70 09 56.90	15.0	(3)
10	MACHO-80.6956.207	05 22 57.4	−68 58 18.9	16.0	(3)
11	W Men	05 26 24.6	−71 11 12.0	13.8	(4)
12	MACHO-80.7559.28	05 26 33.9	−69 07 33.4	15.8	(4)
13	MACHO-81.8394.1358	05 32 13.4	−69 55 57.8	16.3	(3)
14	MACHO-11.8632.2507	05 33 48.9	−70 13 23.4	16.1	(3)
15	EROS2-LMC-RCB-4	05 39 36.9	−71 55 46.4	16.3	(1)
16	HV 12842	05 45 02.5	−64 24 21.0	13.7	(2)
17	MACHO-12.10803.56	05 46 47.7	−70 38 13.5	15.10	(2)
18	EROS2-LMC-RCB-5	06 04 05.4	−72 51 22.7	14.33	(1)
19	EROS2-LMC-RCB-6	06 12 10.5	−74 05 10.2	17.7	(1)

References – (1) Tisserand et al. (2009), (2) Jeffery et al. (1996), (3) Alcock et al. (2001), (4) Clayton (1996)

Table A.3: The SMC RCB stars

Sl No.	Stars	RA	Declination	m_v	References
1	RAW 21	00 37 47.07	−73 39 02.1	17.7	(1,2)
2	RAW 476	00 48 22.87	−73 41 04.7	14.7	(2)
3	MSX SMC 155	00 57 18.15	−72 42 35.2	...	(2, 3)
4	RAW 233	00 44 07.45	−72 44 16.3	18.7	(2)
5	[MH95] 431	00 40 14.65	−74 11 21.2	17.1	(2)
6	MSX SMC 014	00 46 16.33	−74 11 13.6	...	(3)

References – (1) Morgan et al. (2003), (2) Tisserand et al. (2004), (3) Kraemer et al. (2005)

Table A.4: The Galactic EHe stars from Jeffery et al. (1996)

Sl No.	Stars	RA	Declination	m_v
1	LSS 99	06 54 46.3	−10 48 41	12.3
2	BD+10 2179	10 38 55.2	+10 03 48	10.0
3	LSS 3184	14 01 36.6	−66 09 56	12.6
4	HD 124448	14 14 58.6	−46 17 19	10.0
5	CoD-48 10153	15 38 59.4	−48 35 57	11.5
6	HD 144941	16 09 24.6	−27 16 30	10.1
7	V2205 Oph	16 28 35.2	−09 19 34	10.5
8	V652 Her	16 48 04.7	+13 15 41	10.5
9	V2076 Oph	17 41 50.2	−17 54 08	09.8
10	CoD-46 11775	17 42 33.7	−46 58 46	11.2
11	LSS 4357	17 44 25.4	−19 38 03	12.6
12	LS IV-12	17 51 26.7	−01 43 15	11.0
13	BD-1 3438	18 03 55.3	+06 21 46	12.2
14	PV Tel	18 23 14.7	−56 37 43	09.3
15	LSS 5121	18 43 16.4	−18 31 47	13.3

Table A.4 – continued from previous page

Sl No.	Stars	RA	Declination	m_v
16	LS IV-14 109	18 59 39.4	−14 26 11	11.2
17	V1920 Cyg	19 45 17.0	+33 58 25	10.3
18	FQ Aqr	20 51 21.4	+02 18 47	09.6
'hot' RCB stars				
19	DY Cen	13 25 34.0	−54 14 47	12.5
20	V348 Sgr	18 40 19.9	−22 54 29.3	10.6
21	MV Sgr	18 44 32.1	−20 57 16	12.7

Table A.5: The Galactic HdC stars

Sl No.	Stars	RA	Declination	m_v	References
1	HE 1015-2050	10 17 34.2	−21 05 13.9	16.3	(1)
2	HD 137613	15 27 48.2	−25 10 10.0	07.5	(2)
3	HD 148839	16 35 45.7	−67 07 36.0	08.3	(3)
4	HD 173409	18 46 26.5	−31 20 33.0	09.5	(2)
5	HD 175893	18 58 47.2	−29 30 17.0	09.3	(2)
6	HD 182040	19 23 10.0	−10 42 11.0	07.0	(2)

References – (1) Goswami et al. (2010), (2) Bidelman (1953), (3) Warner (1967)

Appendix B

Line list for (1,0), (0,0) and (0,1) C_2 Swan Bands

Table B.1: The (1, 0) $^{12}C^{12}C$ linelist

Wavelength (Å)	**J″**	**χ(eV)**	**log gf**	**Wavelength (Å)**	**J″**	**χ(eV)**	**log gf**
4692.348	28.0	0.342	−0.270	4703.728	20.0	0.283	−0.413
4692.485	28.0	0.342	−0.270	4703.732	55.0	0.803	0.019
4692.548	27.0	0.342	−0.286	4703.744	56.0	0.803	0.027
4692.679	26.0	0.342	−0.302	4703.815	54.0	0.803	0.011
4692.794	61.0	0.940	0.064	4705.139	21.0	0.274	−0.393
4692.838	61.0	0.940	0.064	4705.240	55.0	0.781	0.019
4692.848	62.0	0.940	0.071	4705.250	20.0	0.275	−0.413
4692.931	60.0	0.940	0.057	4705.272	54.0	0.781	0.011
4693.077	60.0	0.940	0.057	4705.276	53.0	0.781	0.003
4694.391	27.0	0.331	−0.286	4705.339	53.0	0.781	0.003
4694.458	26.0	0.331	−0.302	4705.386	19.0	0.275	−0.435
4694.576	25.0	0.331	−0.319	4706.815	20.0	0.266	−0.413
4694.679	60.0	0.917	0.057	4706.926	19.0	0.267	−0.435
4694.687	61.0	0.917	0.064	4707.023	53.0	0.760	0.003
4694.810	60.0	0.917	0.057	4707.039	53.0	0.760	0.003
4696.325	26.0	0.321	−0.302	4707.044	54.0	0.760	0.011
4696.386	25.0	0.321	−0.319	4707.079	18.0	0.267	−0.458
4696.520	24.0	0.321	−0.336	4707.135	52.0	0.760	−0.005
4696.593	59.0	0.893	0.049	4708.383	19.0	0.259	−0.435
4696.637	59.0	0.893	0.049	4708.474	52.0	0.739	−0.005
4696.643	60.0	0.893	0.057	4708.483	53.0	0.739	0.003
4698.138	25.0	0.311	−0.319	4708.487	51.0	0.739	−0.013
4698.285	59.0	0.870	0.049	4708.510	18.0	0.259	−0.458
4698.292	57.0	0.870	0.034	4708.561	51.0	0.739	−0.013
4698.297	58.0	0.870	0.042	4708.659	17.0	0.259	−0.482
4698.339	23.0	0.311	−0.354	4709.972	18.0	0.251	−0.458
4698.406	57.0	0.870	0.034	4710.098	17.0	0.252	−0.482
4699.994	24.0	0.301	−0.336	4710.169	51.0	0.718	−0.013
4700.067	23.0	0.301	−0.354	4710.171	51.0	0.718	−0.013
4700.212	22.0	0.301	−0.373	4710.183	52.0	0.718	−0.005
4700.331	56.0	0.847	0.027	4710.267	16.0	0.252	−0.508
4701.729	23.0	0.292	−0.354	4710.270	50.0	0.719	−0.022
4701.817	22.0	0.292	−0.373	4711.456	17.0	0.245	−0.482
4701.841	56.0	0.825	0.027	4711.540	51.0	0.698	−0.013
4701.848	57.0	0.825	0.034	4711.545	50.0	0.699	−0.022
4701.942	21.0	0.292	−0.393	4711.567	49.0	0.699	−0.031
4701.962	55.0	0.825	0.019	4711.608	16.0	0.245	−0.508
4703.494	22.0	0.283	−0.373	4711.637	49.0	0.699	−0.031
4703.573	21.0	0.283	−0.393	4711.765	15.0	0.245	-0.535
4703.712	55.0	0.803	0.019	4712.950	16.0	0.238	-0.508

The (1, 0) $^{12}C^{12}C$ linelist–continued

Wavelength (Å)	**J″**	**χ(eV)**	**log gf**	**Wavelength (Å)**	**J″**	**χ(eV)**	**log gf**
4713.096	15.0	0.238	-0.535	4720.086	9.0	0.213	-0.747
4713.154	49.0	0.679	-0.031	4720.803	10.0	0.208	-0.704
4713.164	49.0	0.679	-0.031	4721.027	43.0	0.568	-0.087
4713.168	50.0	0.679	-0.022	4721.039	44.0	0.568	-0.077
4713.245	48.0	0.679	-0.039	4721.070	43.0	0.568	-0.087
4713.287	14.0	0.239	-0.564	4721.096	9.0	0.208	-0.747
4714.351	15.0	0.232	-0.535	4721.154	42.0	0.568	-0.097
4714.445	49.0	0.659	-0.031	4721.340	42.0	0.568	-0.097
4714.447	48.0	0.659	-0.039	4721.363	8.0	0.209	-0.796
4714.479	47.0	0.659	-0.049	4721.945	9.0	0.204	-0.747
4714.533	47.0	0.659	-0.049	4722.080	43.0	0.551	-0.087
4714.533	14.0	0.233	-0.564	4722.102	42.0	0.551	-0.097
4714.701	13.0	0.233	-0.595	4722.164	41.0	0.551	-0.107
4715.754	14.0	0.226	-0.564	4722.209	41.0	0.551	-0.107
4715.941	13.0	0.227	-0.595	4722.279	8.0	0.205	-0.796
4715.945	47.0	0.640	-0.049	4722.500	7.0	0.202	-0.850
4715.959	48.0	0.640	-0.039	4722.532	7.0	0.205	-0.850
4715.966	47.0	0.640	-0.049	4723.042	8.0	0.201	-0.796
4716.060	46.0	0.640	-0.058	4723.360	41.0	0.534	-0.107
4716.145	12.0	0.227	-0.628	4723.378	42.0	0.534	-0.097
4717.077	13.0	0.221	-0.595	4723.423	41.0	0.534	-0.107
4717.161	46.0	0.622	-0.058	4723.438	7.0	0.202	-0.850
4717.168	47.0	0.622	-0.049	4723.448	40.0	0.535	-0.118
4717.200	45.0	0.622	-0.067	4724.081	7.0	0.198	-0.850
4717.263	45.0	0.622	-0.067	4724.318	40.0	0.518	-0.118
4717.287	12.0	0.222	-0.628	4724.322	41.0	0.518	-0.107
4717.475	11.0	0.222	-0.665	4724.395	39.0	0.518	-0.129
4718.375	12.0	0.216	-0.628	4724.420	39.0	0.518	-0.129
4718.586	45.0	0.603	-0.067	4725.461	39.0	0.502	-0.129
4718.599	46.0	0.603	-0.058	4725.478	40.0	0.502	-0.118
4718.602	11.0	0.217	-0.665	4725.539	39.0	0.502	-0.129
4718.617	45.0	0.603	-0.067	4725.564	38.0	0.502	-0.140
4718.692	44.0	0.604	-0.077	4725.579	5.0	0.196	-0.985
4718.835	10.0	0.217	-0.704	4726.270	39.0	0.487	-0.129
4719.598	11.0	0.212	-0.665	4726.271	38.0	0.487	-0.140
4719.721	45.0	0.586	-0.067	4726.310	37.0	0.487	-0.151
4719.723	44.0	0.586	-0.077	4726.363	37.0	0.487	-0.151
4719.772	43.0	0.586	-0.087	4726.521	38.0	0.487	-0.140
4719.807	43.0	0.586	-0.087	4727.419	38.0	0.472	-0.140
4719.872	10.0	0.212	-0.704	4727.440	37.0	0.472	-0.151

The (1, 0) $^{12}C^{12}C$ linelist–continued

Wavelength (Å)	**J″**	**χ(eV)**	**log gf**	**Wavelength (Å)**	**J″**	**χ(eV)**	**log gf**
4727.488	36.0	0.472	-0.163	4735.289	26.0	0.321	-0.302
4727.498	37.0	0.472	-0.151	4735.320	25.0	0.321	-0.319
4728.183	37.0	0.457	-0.151	4735.335	8.0	0.205	-0.796
4728.228	36.0	0.457	-0.163	4735.435	24.0	0.321	-0.336
4728.296	35.0	0.457	-0.175	4735.437	7.0	0.205	-0.850
4728.333	35.0	0.457	-0.175	4735.624	25.0	0.311	-0.319
4729.189	36.0	0.442	-0.163	4735.624	10.0	0.208	-0.704
4729.198	35.0	0.443	-0.175	4735.669	24.0	0.311	-0.336
4729.257	34.0	0.443	-0.187	4735.708	9.0	0.208	-0.747
4729.817	35.0	0.429	-0.175	4735.762	23.0	0.311	-0.354
4729.875	34.0	0.429	-0.187	4735.801	8.0	0.209	-0.796
4729.997	33.0	0.429	-0.200	4735.937	11.0	0.212	-0.665
4730.758	34.0	0.415	-0.187	4735.970	24.0	0.301	-0.336
4730.767	33.0	0.415	-0.200	4735.999	23.0	0.301	-0.354
4730.871	32.0	0.415	-0.213	4736.025	10.0	0.212	-0.704
4731.795	33.0	0.402	-0.200	4736.119	22.0	0.301	-0.373
4731.817	32.0	0.402	-0.213	4736.130	9.0	0.213	-0.747
4731.895	31.0	0.402	-0.227	4736.210	23.0	0.292	-0.354
4732.158	32.0	0.389	-0.213	4736.216	12.0	0.216	-0.628
4732.170	31.0	0.389	-0.227	4736.269	22.0	0.292	-0.373
4732.277	30.0	0.389	-0.241	4736.283	11.0	0.217	-0.665
4732.783	31.0	0.377	-0.227	4736.367	21.0	0.292	-0.393
4732.809	30.0	0.377	-0.241	4736.421	10.0	0.217	-0.704
4732.809	30.0	0.377	-0.241	4736.431	13.0	0.221	-0.595
4732.902	29.0	0.377	-0.255	4736.463	22.0	0.283	-0.373
4733.375	30.0	0.365	-0.241	4736.511	21.0	0.283	-0.393
4733.407	29.0	0.365	-0.255	4736.527	12.0	0.222	-0.628
4733.515	28.0	0.365	-0.270	4736.621	21.0	0.274	-0.393
4733.897	29.0	0.353	-0.255	4736.622	20.0	0.283	-0.413
4733.933	28.0	0.353	-0.270	4736.630	14.0	0.226	-0.564
4733.939	5.0	0.196	-0.985	4736.634	11.0	0.222	-0.665
4734.029	27.0	0.353	-0.286	4736.680	20.0	0.275	-0.413
4734.426	28.0	0.342	-0.270	4736.699	13.0	0.227	-0.595
4734.447	27.0	0.342	-0.286	4736.760	15.0	0.232	-0.535
4734.556	26.0	0.342	-0.302	4736.781	20.0	0.266	-0.413
4734.848	27.0	0.331	-0.286	4736.784	19.0	0.275	-0.435
4734.894	26.0	0.331	-0.302	4736.829	19.0	0.267	-0.435
4734.912	7.0	0.202	-0.850	4736.830	12.0	0.227	-0.628
4734.913	8.0	0.201	-0.796	4736.840	14.0	0.233	-0.564
4734.983	25.0	0.331	-0.319	4736.846	19.0	0.259	-0.435
4735.255	9.0	0.204	-0.747	4736.862	16.0	0.238	-0.508

The (1, 0) $^{12}C^{12}C$ linelist–continued

Wavelength (Å)	**J$''$**	**χ(eV)**	**log gf**	**Wavelength (Å)**	**J$''$**	**χ(eV)**	**log gf**
4736.891	17.0	0.245	-0.482	4736.961	17.0	0.252	-0.482
4736.909	18.0	0.251	-0.458	4736.971	16.0	0.245	-0.508
4736.916	18.0	0.259	-0.458	4737.020	17.0	0.259	-0.482
4736.927	15.0	0.238	-0.535	4737.051	14.0	0.239	-0.564
4736.944	13.0	0.233	-0.595	4737.071	15.0	0.245	-0.535
4736.947	18.0	0.267	-0.458	4737.087	16.0	0.252	-0.508

Table B.2: The (1, 0) $^{12}C^{13}C$ linelist

Wavelength (Å)	**J″**	**χ(eV)**	**log gf**	**Wavelength (Å)**	**J″**	**χ(eV)**	**log gf**
4700.760	28.0	0.342	-0.270	4712.459	20.0	0.283	-0.413
4701.749	28.0	0.342	-0.270	4712.534	55.0	0.803	0.019
4701.736	27.0	0.342	-0.286	4712.607	56.0	0.803	0.027
4701.789	26.0	0.342	-0.302	4712.545	54.0	0.803	0.011
4703.775	61.0	0.940	0.064	4713.942	21.0	0.274	-0.393
4702.031	61.0	0.940	0.064	4714.047	55.0	0.781	0.019
4702.111	62.0	0.940	0.071	4713.987	20.0	0.275	-0.413
4702.041	60.0	0.940	0.057	4714.007	54.0	0.781	0.011
4703.961	60.0	0.940	0.057	4715.515	53.0	0.781	0.003
4703.586	27.0	0.331	-0.286	4714.016	53.0	0.781	0.003
4703.575	26.0	0.331	-0.302	4714.060	19.0	0.275	-0.435
4703.621	25.0	0.331	-0.319	4715.558	20.0	0.266	-0.413
4703.796	60.0	0.917	0.057	4715.605	19.0	0.267	-0.435
4703.887	61.0	0.917	0.064	4717.270	53.0	0.760	0.003
4705.702	60.0	0.917	0.057	4715.722	53.0	0.760	0.003
4705.450	26.0	0.321	-0.302	4715.786	54.0	0.760	0.011
4705.438	25.0	0.321	-0.319	4715.695	18.0	0.267	-0.458
4705.498	24.0	0.321	-0.336	4715.750	52.0	0.760	-0.005
4707.382	59.0	0.893	0.049	4717.068	19.0	0.259	-0.435
4705.694	59.0	0.893	0.049	4717.094	52.0	0.739	-0.005
4705.767	60.0	0.893	0.057	4717.172	53.0	0.739	0.003
4707.197	25.0	0.311	-0.319	4718.557	51.0	0.739	-0.013
4707.348	59.0	0.870	0.049	4717.132	18.0	0.259	-0.458
4708.886	57.0	0.870	0.034	4717.126	51.0	0.739	-0.013
4707.280	58.0	0.870	0.042	4717.221	17.0	0.259	-0.482
4707.254	23.0	0.311	-0.354	4718.599	18.0	0.251	-0.458
4707.325	57.0	0.870	0.034	4718.665	17.0	0.252	-0.482
4708.985	24.0	0.301	-0.336	4720.246	51.0	0.718	-0.013
4708.989	23.0	0.301	-0.354	4718.742	51.0	0.718	-0.013
4709.064	22.0	0.301	-0.373	4718.809	52.0	0.718	-0.005
4709.182	56.0	0.847	0.027	4718.775	16.0	0.252	-0.508
4710.657	23.0	0.292	-0.354	4718.777	50.0	0.719	-0.022
4710.675	22.0	0.292	-0.373	4720.028	17.0	0.245	-0.482
4710.697	56.0	0.825	0.027	4720.116	51.0	0.698	-0.013
4710.780	57.0	0.825	0.034	4720.056	50.0	0.699	-0.022
4710.733	21.0	0.292	-0.393	4721.474	49.0	0.699	-0.031
4710.757	55.0	0.825	0.019	4720.121	16.0	0.245	-0.508
4712.358	22.0	0.283	-0.373	4720.096	49.0	0.699	-0.031
4712.371	21.0	0.283	-0.393	4720.221	15.0	0.245	-0.535
4714.134	55.0	0.803	0.019	4721.468	16.0	0.238	-0.508

The (1, 0) $^{12}C^{13}C$ linelist–continued

Wavelength (Å)	**J$''$**	**χ(eV)**	**log gf**	**Wavelength (Å)**	**J$''$**	**χ(eV)**	**log gf**
4721.557	15.0	0.238	-0.535	4728.262	9.0	0.213	-0.747
4721.618	49.0	0.679	-0.031	4729.029	10.0	0.208	-0.704
4723.078	49.0	0.679	-0.031	4729.209	43.0	0.568	-0.087
4721.685	50.0	0.679	-0.022	4729.264	44.0	0.568	-0.077
4721.649	48.0	0.679	-0.039	4730.529	43.0	0.568	-0.087
4721.692	14.0	0.239	-0.564	4729.276	9.0	0.208	-0.747
4722.817	15.0	0.232	-0.535	4729.287	42.0	0.568	-0.097
4722.914	49.0	0.659	-0.031	4730.728	42.0	0.568	-0.097
4722.855	48.0	0.659	-0.039	4729.498	8.0	0.209	-0.796
4724.229	47.0	0.659	-0.049	4730.128	9.0	0.204	-0.747
4722.892	47.0	0.659	-0.049	4730.265	43.0	0.551	-0.087
4722.943	14.0	0.233	-0.564	4730.238	42.0	0.551	-0.097
4723.058	13.0	0.233	-0.595	4731.478	41.0	0.551	-0.107
4724.168	14.0	0.226	-0.564	4730.305	41.0	0.551	-0.107
4724.302	13.0	0.227	-0.595	4730.417	8.0	0.205	-0.796
4724.309	47.0	0.640	-0.049	4730.357	7.0	0.202	-0.850
4724.373	48.0	0.640	-0.039	4730.627	7.0	0.205	-0.850
4725.722	47.0	0.640	-0.049	4731.183	8.0	0.201	-0.796
4724.367	46.0	0.640	-0.058	4731.460	41.0	0.534	-0.107
4724.454	12.0	0.227	-0.628	4731.519	42.0	0.534	-0.097
4725.442	13.0	0.221	-0.595	4732.742	41.0	0.534	-0.107
4725.472	46.0	0.622	-0.058	4731.536	7.0	0.202	-0.850
4725.536	47.0	0.622	-0.049	4731.503	40.0	0.535	-0.118
4726.799	45.0	0.622	-0.067	4732.181	7.0	0.198	-0.850
4725.528	45.0	0.622	-0.067	4732.376	40.0	0.518	-0.118
4725.600	12.0	0.222	-0.628	4732.426	41.0	0.518	-0.107
4725.738	11.0	0.222	-0.665	4733.576	39.0	0.518	-0.129
4726.692	12.0	0.216	-0.628	4732.441	39.0	0.518	-0.129
4726.856	45.0	0.603	-0.067	4733.486	39.0	0.502	-0.129
4726.915	46.0	0.603	-0.058	4733.540	40.0	0.502	-0.118
4726.869	11.0	0.217	-0.665	4734.724	39.0	0.502	-0.129
4728.222	45.0	0.603	-0.067	4733.548	38.0	0.502	-0.140
4726.909	44.0	0.604	-0.077	4733.602	5.0	0.196	-0.985
4727.054	10.0	0.217	-0.704	4734.298	39.0	0.487	-0.129
4727.869	11.0	0.212	-0.665	4734.257	38.0	0.487	-0.140
4727.995	45.0	0.586	-0.067	4734.262	37.0	0.487	-0.151
4727.944	44.0	0.586	-0.077	4735.417	37.0	0.487	-0.151
4729.226	43.0	0.586	-0.087	4735.645	38.0	0.487	-0.140
4727.985	43.0	0.586	-0.087	4735.409	38.0	0.472	-0.140
4728.094	10.0	0.212	-0.704	4735.396	37.0	0.472	-0.151

The (1, 0) $^{12}C^{13}C$ linelist–continued

Wavelength (Å)	**J″**	χ**(eV)**	**log** gf	**Wavelength (Å)**	**J″**	χ**(eV)**	**log** gf
4735.406	36.0	0.472	-0.163	4742.978	26.0	0.321	-0.302
4736.556	37.0	0.472	-0.151	4742.995	25.0	0.321	-0.319
4736.141	37.0	0.457	-0.151	4743.009	8.0	0.205	-0.796
4736.149	36.0	0.457	-0.163	4743.095	24.0	0.321	-0.336
4736.186	35.0	0.457	-0.175	4743.127	7.0	0.205	-0.850
4737.266	35.0	0.457	-0.175	4743.300	25.0	0.311	-0.319
4737.113	36.0	0.442	-0.163	4743.272	10.0	0.208	-0.704
4737.091	35.0	0.443	-0.175	4743.330	24.0	0.311	-0.336
4737.116	34.0	0.443	-0.187	4743.369	9.0	0.208	-0.747
4737.712	35.0	0.429	-0.175	4743.412	23.0	0.311	-0.354
4737.736	34.0	0.429	-0.187	4743.476	8.0	0.209	-0.796
4738.815	33.0	0.429	-0.200	4743.576	11.0	0.212	-0.665
4738.622	34.0	0.415	-0.187	4743.632	24.0	0.301	-0.336
4738.603	33.0	0.415	-0.200	4743.649	23.0	0.301	-0.354
4738.678	32.0	0.415	-0.213	4743.675	10.0	0.212	-0.704
4739.635	33.0	0.402	-0.200	4743.758	22.0	0.301	-0.373
4739.627	32.0	0.402	-0.213	4743.793	9.0	0.213	-0.747
4739.681	31.0	0.402	-0.227	4743.861	23.0	0.292	-0.354
4739.969	32.0	0.389	-0.213	4743.847	12.0	0.216	-0.628
4739.956	31.0	0.389	-0.227	4743.909	22.0	0.292	-0.373
4740.037	30.0	0.389	-0.241	4743.923	11.0	0.217	-0.665
4740.571	31.0	0.377	-0.227	4743.999	21.0	0.292	-0.393
4740.571	30.0	0.377	-0.241	4744.072	10.0	0.217	-0.704
4740.643	29.0	0.377	-0.255	4744.056	13.0	0.221	-0.595
4741.139	30.0	0.365	-0.241	4744.103	22.0	0.283	-0.373
4741.150	29.0	0.365	-0.255	4744.144	21.0	0.283	-0.393
4741.235	28.0	0.365	-0.270	4744.159	12.0	0.222	-0.628
4741.641	29.0	0.353	-0.255	4744.254	21.0	0.274	-0.393
4741.655	28.0	0.353	-0.270	4744.247	20.0	0.283	-0.413
4741.661	5.0	0.196	-0.985	4744.250	14.0	0.226	-0.564
4741.733	27.0	0.353	-0.286	4744.275	11.0	0.222	-0.665
4742.149	28.0	0.342	-0.270	4744.305	20.0	0.275	-0.413
4742.153	27.0	0.342	-0.286	4744.325	13.0	0.227	-0.595
4742.243	26.0	0.342	-0.302	4744.377	15.0	0.232	-0.535
4742.555	27.0	0.331	-0.286	4744.407	20.0	0.266	-0.413
4742.582	26.0	0.331	-0.302	4744.405	19.0	0.275	-0.435
4742.600	7.0	0.202	-0.850	4744.450	19.0	0.267	-0.435
4742.586	8.0	0.201	-0.796	4744.463	12.0	0.227	-0.628
4742.657	25.0	0.331	-0.319	4744.461	14.0	0.233	-0.564
4742.915	9.0	0.204	-0.747	4744.467	19.0	0.259	-0.435

The (1, 0) $^{12}C^{13}C$ linelist–continued

Wavelength (Å)	**J$''$**	**χ(eV)**	**log gf**	**Wavelength (Å)**	**J$''$**	**χ(eV)**	**log gf**
4744.477	16.0	0.238	-0.508	4744.577	17.0	0.252	-0.482
4744.507	17.0	0.245	-0.482	4744.587	16.0	0.245	-0.508
4744.526	18.0	0.251	-0.458	4744.636	17.0	0.259	-0.482
4744.533	18.0	0.259	-0.458	4744.672	14.0	0.239	-0.564
4744.545	15.0	0.238	-0.535	4744.689	15.0	0.245	-0.535
4744.570	13.0	0.233	-0.595	4744.703	16.0	0.252	-0.508
4744.564	18.0	0.267	-0.458				

Table B.3: The (0, 0) $^{12}C^{12}C$ linelist

Wavelength (Å)	J$''$	χ(eV)	log gf	Wavelength (Å)	J$''$	χ(eV)	log gf
5129.601	47.0	0.640	0.465	5137.696	42.0	0.568	0.416
5129.601	48.0	0.640	0.474	5137.696	42.0	0.568	0.416
5129.601	47.0	0.640	0.465	5138.112	15.0	0.232	-0.022
5129.601	48.0	0.640	0.474	5138.316	14.0	0.233	-0.051
5129.694	46.0	0.640	0.455	5138.510	13.0	0.233	-0.082
5129.694	46.0	0.640	0.455	5139.323	43.0	0.551	0.427
5130.272	19.0	0.259	0.078	5139.323	42.0	0.551	0.416
5130.418	18.0	0.259	0.055	5139.323	43.0	0.551	0.427
5130.583	17.0	0.259	0.031	5139.323	42.0	0.551	0.416
5131.584	47.0	0.622	0.465	5139.448	41.0	0.551	0.406
5131.584	46.0	0.622	0.455	5139.448	41.0	0.551	0.406
5131.584	47.0	0.622	0.465	5139.933	14.0	0.226	-0.051
5131.584	46.0	0.622	0.455	5140.143	13.0	0.227	-0.082
5131.699	45.0	0.622	0.446	5140.381	12.0	0.227	-0.115
5131.699	45.0	0.622	0.446	5141.206	41.0	0.534	0.406
5132.360	18.0	0.251	0.055	5141.206	41.0	0.534	0.406
5132.497	17.0	0.252	0.031	5141.206	42.0	0.534	0.416
5132.699	16.0	0.252	0.006	5141.206	42.0	0.534	0.416
5133.719	46.0	0.603	0.455	5141.318	40.0	0.535	0.395
5133.719	45.0	0.603	0.446	5141.318	40.0	0.535	0.395
5133.719	46.0	0.603	0.455	5141.648	13.0	0.221	-0.082
5133.719	45.0	0.603	0.446	5141.896	12.0	0.222	-0.115
5133.825	44.0	0.604	0.436	5142.114	11.0	0.222	-0.151
5133.825	44.0	0.604	0.436	5142.843	40.0	0.518	0.395
5134.319	17.0	0.245	0.031	5142.843	41.0	0.518	0.406
5134.489	16.0	0.245	0.006	5142.843	41.0	0.518	0.406
5134.671	15.0	0.245	-0.022	5142.843	40.0	0.518	0.395
5135.586	44.0	0.586	0.436	5142.935	39.0	0.518	0.385
5135.586	45.0	0.586	0.446	5142.935	39.0	0.518	0.385
5135.586	45.0	0.586	0.446	5143.332	12.0	0.216	-0.115
5135.586	44.0	0.586	0.436	5143.599	11.0	0.217	-0.151
5135.693	43.0	0.586	0.427	5143.863	10.0	0.217	-0.191
5135.693	43.0	0.586	0.427	5144.575	40.0	0.502	0.395
5136.274	16.0	0.238	0.006	5144.575	39.0	0.502	0.385
5136.440	15.0	0.238	-0.022	5144.575	40.0	0.502	0.395
5136.660	14.0	0.239	-0.051	5144.575	39.0	0.502	0.385
5137.586	44.0	0.568	0.436	5144.694	38.0	0.502	0.373
5137.586	43.0	0.568	0.427	5144.694	38.0	0.502	0.373
5137.586	44.0	0.568	0.436	5144.924	11.0	0.212	-0.151
5137.586	43.0	0.568	0.427	5145.232	10.0	0.212	-0.191

The (0, 0) $^{12}C^{12}C$ linelist–continued

Wavelength (Å)	**J″**	**χ(eV)**	**log *gf***	**Wavelength (Å)**	**J″**	**χ(eV)**	**log *gf***
5145.476	9.0	0.213	-0.234	5152.515	5.0	0.196	-0.472
5146.082	38.0	0.487	0.373	5153.172	33.0	0.415	0.313
5146.082	39.0	0.487	0.385	5153.172	33.0	0.415	0.313
5146.082	38.0	0.487	0.373	5153.172	34.0	0.415	0.326
5146.082	39.0	0.487	0.385	5153.172	34.0	0.415	0.326
5146.207	37.0	0.487	0.362	5153.291	32.0	0.415	0.300
5146.207	37.0	0.487	0.362	5153.291	32.0	0.415	0.300
5146.465	10.0	0.208	-0.191	5154.337	32.0	0.402	0.300
5146.813	9.0	0.208	-0.234	5154.337	33.0	0.402	0.313
5147.115	8.0	0.209	-0.283	5154.337	33.0	0.402	0.313
5147.691	38.0	0.472	0.373	5154.337	32.0	0.402	0.300
5147.691	38.0	0.472	0.373	5154.452	31.0	0.402	0.286
5147.691	37.0	0.472	0.362	5154.452	31.0	0.402	0.286
5147.691	37.0	0.472	0.362	5155.516	32.0	0.389	0.300
5147.816	36.0	0.472	0.350	5155.516	32.0	0.389	0.300
5147.816	36.0	0.472	0.350	5155.524	31.0	0.389	0.286
5147.929	9.0	0.204	-0.234	5155.524	31.0	0.389	0.286
5148.325	8.0	0.205	-0.283	5155.649	30.0	0.389	0.272
5148.607	7.0	0.205	-0.337	5155.649	30.0	0.389	0.272
5149.088	36.0	0.457	0.350	5156.537	31.0	0.377	0.286
5149.088	36.0	0.457	0.350	5156.537	31.0	0.377	0.286
5149.088	37.0	0.457	0.362	5156.587	30.0	0.377	0.272
5149.088	37.0	0.457	0.362	5156.587	30.0	0.377	0.272
5149.210	35.0	0.457	0.338	5156.686	29.0	0.377	0.258
5149.210	35.0	0.457	0.338	5156.686	29.0	0.377	0.258
5149.330	8.0	0.201	-0.283	5157.605	30.0	0.365	0.272
5149.787	7.0	0.202	-0.337	5157.605	30.0	0.365	0.272
5150.558	35.0	0.443	0.338	5157.643	29.0	0.365	0.258
5150.558	36.0	0.442	0.350	5157.643	29.0	0.365	0.258
5150.558	35.0	0.443	0.338	5157.758	28.0	0.365	0.243
5150.558	36.0	0.442	0.350	5157.758	28.0	0.365	0.243
5150.667	7.0	0.198	-0.337	5158.490	29.0	0.353	0.258
5150.667	34.0	0.443	0.326	5158.490	29.0	0.353	0.258
5150.667	34.0	0.443	0.326	5158.562	28.0	0.353	0.243
5151.831	35.0	0.429	0.338	5158.562	28.0	0.353	0.243
5151.831	35.0	0.429	0.338	5158.654	27.0	0.353	0.227
5151.865	34.0	0.429	0.326	5158.654	27.0	0.353	0.227
5151.865	34.0	0.429	0.326	5159.453	28.0	0.342	0.243
5151.933	33.0	0.429	0.313	5159.453	28.0	0.342	0.243
5151.933	33.0	0.429	0.313	5159.470	27.0	0.342	0.227

The (0, 0) $^{12}C^{12}C$ linelist–continued

Wavelength (Å)	**J$''$**	**χ(eV)**	**log gf**	**Wavelength (Å)**	**J$''$**	**χ(eV)**	**log gf**
5159.470	27.0	0.342	0.227	5163.420	21.0	0.283	0.120
5159.600	26.0	0.342	0.211	5163.597	20.0	0.283	0.100
5159.600	26.0	0.342	0.211	5163.597	8.0	0.201	-0.283
5160.213	27.0	0.331	0.227	5163.597	20.0	0.283	0.100
5160.213	27.0	0.331	0.227	5163.597	7.0	0.202	-0.337
5160.283	26.0	0.331	0.211	5163.597	8.0	0.201	-0.283
5160.283	26.0	0.331	0.211	5163.597	7.0	0.202	-0.337
5160.385	25.0	0.331	0.195	5163.808	21.0	0.274	0.120
5160.385	25.0	0.331	0.195	5163.808	21.0	0.274	0.120
5161.037	26.0	0.321	0.211	5163.841	20.0	0.275	0.100
5161.037	26.0	0.321	0.211	5163.841	20.0	0.275	0.100
5161.054	25.0	0.321	0.195	5163.988	9.0	0.204	-0.234
5161.054	25.0	0.321	0.195	5163.988	19.0	0.275	0.078
5161.188	24.0	0.321	0.177	5163.988	9.0	0.204	-0.234
5161.188	24.0	0.321	0.177	5163.988	19.0	0.275	0.078
5161.680	25.0	0.311	0.195	5164.074	8.0	0.205	-0.283
5161.680	25.0	0.311	0.195	5164.074	7.0	0.205	-0.337
5161.741	24.0	0.311	0.177	5164.074	7.0	0.205	-0.337
5161.741	24.0	0.311	0.177	5164.074	8.0	0.205	-0.283
5161.854	23.0	0.311	0.159	5164.255	10.0	0.208	-0.191
5161.854	23.0	0.311	0.159	5164.255	20.0	0.266	0.100
5162.346	24.0	0.301	0.177	5164.255	19.0	0.267	0.078
5162.346	24.0	0.301	0.177	5164.255	10.0	0.208	-0.191
5162.378	23.0	0.301	0.159	5164.255	20.0	0.266	0.100
5162.378	23.0	0.301	0.159	5164.255	19.0	0.267	0.078
5162.527	22.0	0.301	0.140	5164.378	18.0	0.267	0.055
5162.527	22.0	0.301	0.140	5164.378	18.0	0.267	0.055
5162.578	5.0	0.196	-0.472	5164.406	9.0	0.208	-0.234
5162.578	5.0	0.196	-0.472	5164.406	9.0	0.208	-0.234
5162.864	23.0	0.292	0.159	5164.406	8.0	0.209	-0.283
5162.864	23.0	0.292	0.159	5164.406	8.0	0.209	-0.283
5162.942	22.0	0.292	0.140	5164.510	19.0	0.259	0.078
5162.942	22.0	0.292	0.140	5164.510	19.0	0.259	0.078
5163.049	21.0	0.292	0.120	5164.539	18.0	0.259	0.055
5163.049	21.0	0.292	0.120	5164.539	11.0	0.212	-0.151
5163.134	7.0	0.198	-0.337	5164.539	11.0	0.212	-0.151
5163.134	7.0	0.198	-0.337	5164.539	18.0	0.259	0.055
5163.420	21.0	0.283	0.120	5164.674	10.0	0.212	-0.191
5163.420	22.0	0.283	0.140	5164.674	17.0	0.259	0.031
5163.420	22.0	0.283	0.140	5164.674	17.0	0.259	0.031

The (0, 0) $^{12}C^{12}C$ linelist–continued

Wavelength (Å)	**J″**	**χ(eV)**	**log *gf***	**Wavelength (Å)**	**J″**	**χ(eV)**	**log *gf***
5164.674	10.0	0.212	-0.191	5165.242	14.0	0.239	-0.051
5164.753	12.0	0.216	-0.115	5165.242	14.0	0.239	-0.051
5164.753	18.0	0.251	0.055	5165.242	12.0	0.227	-0.115
5164.753	17.0	0.252	0.031	5165.242	13.0	0.233	-0.082
5164.753	9.0	0.213	-0.234	5165.242	13.0	0.233	-0.082
5164.753	12.0	0.216	-0.115				
5164.753	17.0	0.252	0.031				
5164.753	18.0	0.251	0.055				
5164.753	9.0	0.213	-0.234				
5164.900	17.0	0.245	0.031				
5164.900	13.0	0.221	-0.082				
5164.900	10.0	0.217	-0.191				
5164.900	17.0	0.245	0.031				
5164.900	16.0	0.245	0.006				
5164.900	16.0	0.252	0.006				
5164.900	16.0	0.252	0.006				
5164.900	11.0	0.217	-0.151				
5164.900	16.0	0.245	0.006				
5164.900	10.0	0.217	-0.191				
5164.900	13.0	0.221	-0.082				
5164.900	11.0	0.217	-0.151				
5165.026	12.0	0.222	-0.115				
5165.026	12.0	0.222	-0.115				
5165.026	15.0	0.238	-0.022				
5165.026	15.0	0.245	-0.022				
5165.026	15.0	0.245	-0.022				
5165.026	14.0	0.226	-0.051				
5165.026	14.0	0.226	-0.051				
5165.026	13.0	0.227	-0.082				
5165.026	13.0	0.227	-0.082				
5165.026	15.0	0.238	-0.022				
5165.026	14.0	0.233	-0.051				
5165.026	15.0	0.232	-0.022				
5165.026	15.0	0.232	-0.022				
5165.026	16.0	0.238	0.006				
5165.026	11.0	0.222	-0.151				
5165.026	14.0	0.233	-0.051				
5165.026	16.0	0.238	0.006				
5165.026	11.0	0.222	-0.151				
5165.242	12.0	0.227	-0.115				

TABLE B.4: The (0, 0) $^{12}C^{13}C$ linelist

Wavelength (Å)	J″	χ(eV)	log *gf*	Wavelength (Å)	J″	χ(eV)	log *gf*
5132.755	47.0	0.640	0.465	5140.304	42.0	0.568	0.416
5132.877	48.0	0.640	0.474	5138.808	42.0	0.568	0.416
5131.091	47.0	0.640	0.465	5139.345	15.0	0.232	-0.022
5131.171	48.0	0.640	0.474	5139.476	14.0	0.233	-0.051
5132.735	46.0	0.640	0.455	5139.600	13.0	0.233	-0.082
5131.101	46.0	0.640	0.455	5142.037	43.0	0.551	0.427
5131.816	19.0	0.259	0.078	5141.933	42.0	0.551	0.416
5131.879	18.0	0.259	0.055	5140.509	43.0	0.551	0.427
5131.965	17.0	0.259	0.031	5140.435	42.0	0.551	0.416
5134.741	47.0	0.622	0.465	5141.951	41.0	0.551	0.406
5134.627	46.0	0.622	0.455	5140.494	41.0	0.551	0.406
5133.075	47.0	0.622	0.465	5141.093	14.0	0.226	-0.051
5132.992	46.0	0.622	0.455	5141.233	13.0	0.227	-0.082
5133.031	45.0	0.622	0.446	5141.403	12.0	0.227	-0.115
5134.626	45.0	0.622	0.446	5143.711	41.0	0.534	0.406
5133.822	18.0	0.251	0.055	5142.253	41.0	0.534	0.406
5133.880	17.0	0.252	0.031	5143.818	42.0	0.534	0.416
5134.004	16.0	0.252	0.006	5142.319	42.0	0.534	0.416
5135.128	46.0	0.603	0.455	5143.723	40.0	0.535	0.395
5136.648	45.0	0.603	0.446	5142.296	40.0	0.535	0.395
5136.765	46.0	0.603	0.455	5142.739	13.0	0.221	-0.082
5135.052	45.0	0.603	0.446	5142.919	12.0	0.222	-0.115
5135.079	44.0	0.604	0.436	5143.072	11.0	0.222	-0.151
5136.645	44.0	0.604	0.436	5143.822	40.0	0.518	0.395
5135.703	17.0	0.245	0.031	5145.350	41.0	0.518	0.406
5135.795	16.0	0.245	0.006	5143.890	41.0	0.518	0.406
5135.902	15.0	0.245	-0.022	5145.250	40.0	0.518	0.395
5136.841	44.0	0.586	0.436	5143.852	39.0	0.518	0.385
5138.517	45.0	0.586	0.446	5145.240	39.0	0.518	0.385
5136.920	45.0	0.586	0.446	5144.355	12.0	0.216	-0.115
5138.408	44.0	0.586	0.436	5144.557	11.0	0.217	-0.151
5136.877	43.0	0.586	0.427	5144.758	10.0	0.217	-0.191
5138.403	43.0	0.586	0.427	5146.983	40.0	0.502	0.395
5137.581	16.0	0.238	0.006	5145.493	39.0	0.502	0.385
5137.672	15.0	0.238	-0.022	5145.554	40.0	0.502	0.395
5137.819	14.0	0.239	-0.051	5146.882	39.0	0.502	0.385
5140.410	44.0	0.568	0.436	5146.906	38.0	0.502	0.373
5140.298	43.0	0.568	0.427	5145.548	38.0	0.502	0.373
5138.842	44.0	0.568	0.436	5145.883	11.0	0.212	-0.151
5138.771	43.0	0.568	0.427	5146.128	10.0	0.212	-0.191

The (0, 0) $^{12}C^{13}C$ linelist–continued

Wavelength (Å)	**J$''$**	**χ(eV)**	**log gf**	**Wavelength (Å)**	**J$''$**	**χ(eV)**	**log gf**
5146.311	9.0	0.213	-0.234	5153.135	5.0	0.196	-0.472
5146.937	38.0	0.487	0.373	5154.940	33.0	0.415	0.313
5147.000	39.0	0.487	0.385	5153.760	33.0	0.415	0.313
5148.295	38.0	0.487	0.373	5155.026	34.0	0.415	0.326
5148.390	39.0	0.487	0.385	5153.808	34.0	0.415	0.326
5148.323	37.0	0.487	0.362	5153.831	32.0	0.415	0.300
5147.005	37.0	0.487	0.362	5154.978	32.0	0.415	0.300
5147.361	10.0	0.208	-0.191	5154.878	32.0	0.402	0.300
5147.649	9.0	0.208	-0.234	5154.926	33.0	0.402	0.313
5147.893	8.0	0.209	-0.283	5156.105	33.0	0.402	0.313
5149.905	38.0	0.472	0.373	5156.024	32.0	0.402	0.300
5148.546	38.0	0.472	0.373	5156.058	31.0	0.402	0.286
5148.489	37.0	0.472	0.362	5154.950	31.0	0.402	0.286
5149.809	37.0	0.472	0.362	5156.057	32.0	0.389	0.300
5149.843	36.0	0.472	0.350	5157.204	32.0	0.389	0.300
5148.556	36.0	0.472	0.350	5156.022	31.0	0.389	0.286
5148.765	9.0	0.204	-0.234	5157.131	31.0	0.389	0.286
5149.103	8.0	0.205	-0.283	5157.180	30.0	0.389	0.272
5149.330	7.0	0.205	-0.337	5156.104	30.0	0.389	0.272
5151.116	36.0	0.457	0.350	5158.145	31.0	0.377	0.286
5149.828	36.0	0.457	0.350	5157.035	31.0	0.377	0.286
5151.207	37.0	0.457	0.362	5157.042	30.0	0.377	0.272
5149.887	37.0	0.457	0.362	5158.118	30.0	0.377	0.272
5151.147	35.0	0.457	0.338	5158.141	29.0	0.377	0.258
5149.898	35.0	0.457	0.338	5157.103	29.0	0.377	0.258
5150.108	8.0	0.201	-0.283	5158.060	30.0	0.365	0.272
5150.510	7.0	0.202	-0.337	5159.137	30.0	0.365	0.272
5151.246	35.0	0.443	0.338	5158.060	29.0	0.365	0.258
5151.299	36.0	0.442	0.350	5159.099	29.0	0.365	0.258
5152.496	35.0	0.443	0.338	5159.142	28.0	0.365	0.243
5152.587	36.0	0.442	0.350	5158.138	28.0	0.365	0.243
5151.390	7.0	0.198	-0.337	5158.908	29.0	0.353	0.258
5151.302	34.0	0.443	0.326	5159.946	29.0	0.353	0.258
5152.519	34.0	0.443	0.326	5158.942	28.0	0.353	0.243
5153.770	35.0	0.429	0.338	5159.947	28.0	0.353	0.243
5152.520	35.0	0.429	0.338	5159.968	27.0	0.353	0.227
5152.501	34.0	0.429	0.326	5159.001	27.0	0.353	0.227
5153.718	34.0	0.429	0.326	5160.838	28.0	0.342	0.243
5153.700	33.0	0.429	0.313	5159.833	28.0	0.342	0.243
5152.521	33.0	0.429	0.313	5160.784	27.0	0.342	0.227

The (0, 0) $^{12}C^{13}C$ linelist–continued

Wavelength (Å)	J″	χ(eV)	log gf	Wavelength (Å)	J″	χ(eV)	log gf
5159.817	27.0	0.342	0.227	5164.368	21.0	0.283	0.120
5159.914	26.0	0.342	0.211	5164.493	20.0	0.283	0.100
5160.848	26.0	0.342	0.211	5164.056	8.0	0.201	-0.283
5160.560	27.0	0.331	0.227	5163.774	20.0	0.283	0.100
5161.527	27.0	0.331	0.227	5164.036	7.0	0.202	-0.337
5160.597	26.0	0.331	0.211	5163.769	8.0	0.201	-0.283
5161.531	26.0	0.331	0.211	5163.785	7.0	0.202	-0.337
5160.671	25.0	0.331	0.195	5164.002	21.0	0.274	0.120
5161.567	25.0	0.331	0.195	5164.756	21.0	0.274	0.120
5162.285	26.0	0.321	0.211	5164.018	20.0	0.275	0.100
5161.351	26.0	0.321	0.211	5164.737	20.0	0.275	0.100
5161.340	25.0	0.321	0.195	5164.470	9.0	0.204	-0.234
5162.236	25.0	0.321	0.195	5164.833	19.0	0.275	0.078
5161.446	24.0	0.321	0.177	5164.147	9.0	0.204	-0.234
5162.309	24.0	0.321	0.177	5164.151	19.0	0.275	0.078
5162.863	25.0	0.311	0.195	5164.534	8.0	0.205	-0.283
5161.966	25.0	0.311	0.195	5164.513	7.0	0.205	-0.337
5162.862	24.0	0.311	0.177	5164.262	7.0	0.205	-0.337
5162.000	24.0	0.311	0.177	5164.246	8.0	0.205	-0.283
5162.089	23.0	0.311	0.159	5164.762	10.0	0.208	-0.191
5162.914	23.0	0.311	0.159	5165.151	20.0	0.266	0.100
5163.467	24.0	0.301	0.177	5165.100	19.0	0.267	0.078
5162.605	24.0	0.301	0.177	5164.403	10.0	0.208	-0.191
5163.438	23.0	0.301	0.159	5164.432	20.0	0.266	0.100
5162.613	23.0	0.301	0.159	5164.418	19.0	0.267	0.078
5162.740	22.0	0.301	0.140	5165.176	18.0	0.267	0.055
5163.530	22.0	0.301	0.140	5164.529	18.0	0.267	0.055
5162.805	5.0	0.196	-0.472	5164.888	9.0	0.208	-0.234
5162.985	5.0	0.196	-0.472	5164.565	9.0	0.208	-0.234
5163.099	23.0	0.292	0.159	5164.866	8.0	0.209	-0.283
5163.924	23.0	0.292	0.159	5164.578	8.0	0.209	-0.283
5163.945	22.0	0.292	0.140	5164.673	19.0	0.259	0.078
5163.155	22.0	0.292	0.140	5165.355	19.0	0.259	0.078
5163.243	21.0	0.292	0.120	5165.337	18.0	0.259	0.055
5163.997	21.0	0.292	0.120	5165.074	11.0	0.212	-0.151
5163.322	7.0	0.198	-0.337	5164.679	11.0	0.212	-0.151
5163.573	7.0	0.198	-0.337	5164.690	18.0	0.259	0.055
5163.614	21.0	0.283	0.120	5165.181	10.0	0.212	-0.191
5163.633	22.0	0.283	0.140	5165.427	17.0	0.259	0.031
5164.424	22.0	0.283	0.140	5164.816	17.0	0.259	0.031

The (0, 0) $^{12}C^{13}C$ linelist–continued

Wavelength (Å)	**J″**	**χ(eV)**	**log gf**	**Wavelength (Å)**	**J″**	**χ(eV)**	**log gf**
5164.822	10.0	0.212	-0.191	5165.875	14.0	0.239	-0.051
5165.318	12.0	0.216	-0.115	5165.371	14.0	0.239	-0.051
5165.551	18.0	0.251	0.055	5165.376	12.0	0.227	-0.115
5164.895	17.0	0.252	0.031	5165.840	13.0	0.233	-0.082
5164.912	9.0	0.213	-0.234	5165.373	13.0	0.233	-0.082
5164.887	12.0	0.216	-0.115				
5165.506	17.0	0.252	0.031				
5164.904	18.0	0.251	0.055				
5165.235	9.0	0.213	-0.234				
5165.653	17.0	0.245	0.031				
5165.497	13.0	0.221	-0.082				
5165.407	10.0	0.217	-0.191				
5165.042	17.0	0.245	0.031				
5165.611	16.0	0.245	0.006				
5165.611	16.0	0.252	0.006				
5165.035	16.0	0.252	0.006				
5165.040	11.0	0.217	-0.151				
5165.035	16.0	0.245	0.006				
5165.048	10.0	0.217	-0.191				
5165.031	13.0	0.221	-0.082				
5165.435	11.0	0.217	-0.151				
5165.591	12.0	0.222	-0.115				
5165.160	12.0	0.222	-0.115				
5165.696	15.0	0.238	-0.022				
5165.157	15.0	0.245	-0.022				
5165.696	15.0	0.245	-0.022				
5165.659	14.0	0.226	-0.051				
5165.155	14.0	0.226	-0.051				
5165.623	13.0	0.227	-0.082				
5165.157	13.0	0.227	-0.082				
5165.157	15.0	0.238	-0.022				
5165.155	14.0	0.233	-0.051				
5165.157	15.0	0.232	-0.022				
5165.696	15.0	0.232	-0.022				
5165.161	16.0	0.238	0.006				
5165.166	11.0	0.222	-0.151				
5165.659	14.0	0.233	-0.051				
5165.737	16.0	0.238	0.006				
5165.561	11.0	0.222	-0.151				
5165.807	12.0	0.227	-0.115				

Table B.5: The (0, 1) $^{12}C^{12}C$ linelist

Wavelength (Å)	J$''$	χ(eV)	log gf	Wavelength (Å)	J$''$	χ(eV)	log gf
5587.533	21.0	0.474	-0.360	5598.817	41.0	0.732	-0.074
5587.684	20.0	0.474	-0.381	5598.817	41.0	0.732	-0.074
5587.876	19.0	0.475	-0.403	5598.817	42.0	0.731	-0.064
5588.125	45.0	0.800	-0.035	5598.958	40.0	0.732	-0.085
5588.125	45.0	0.800	-0.035	5598.958	40.0	0.732	-0.085
5588.125	46.0	0.800	-0.025	5600.697	16.0	0.438	-0.475
5588.125	46.0	0.800	-0.025	5600.909	15.0	0.439	-0.502
5588.263	44.0	0.800	-0.044	5601.175	14.0	0.439	-0.531
5588.263	44.0	0.800	-0.044	5601.203	41.0	0.715	-0.074
5590.368	20.0	0.466	-0.381	5601.203	41.0	0.715	-0.074
5590.512	19.0	0.466	-0.403	5601.203	40.0	0.716	-0.085
5590.746	18.0	0.467	-0.425	5601.203	40.0	0.716	-0.085
5590.831	44.0	0.782	-0.044	5601.348	39.0	0.716	-0.096
5590.831	45.0	0.782	-0.035	5601.348	39.0	0.716	-0.096
5590.831	45.0	0.782	-0.035	5603.043	15.0	0.432	-0.502
5590.831	44.0	0.782	-0.044	5603.293	14.0	0.433	-0.531
5590.953	43.0	0.782	-0.054	5603.534	13.0	0.433	-0.562
5590.953	43.0	0.782	-0.054	5603.663	39.0	0.700	-0.096
5593.040	19.0	0.459	-0.403	5603.663	40.0	0.700	-0.085
5593.220	18.0	0.459	-0.425	5603.663	40.0	0.700	-0.085
5593.423	17.0	0.459	-0.450	5603.663	39.0	0.700	-0.096
5593.640	43.0	0.765	-0.054	5603.803	38.0	0.700	-0.107
5593.640	43.0	0.765	-0.054	5603.803	38.0	0.700	-0.107
5593.640	44.0	0.765	-0.044	5605.349	14.0	0.427	-0.531
5593.640	44.0	0.765	-0.044	5605.610	13.0	0.427	-0.562
5593.771	42.0	0.765	-0.064	5605.900	39.0	0.684	-0.096
5593.771	42.0	0.765	-0.064	5605.900	38.0	0.684	-0.107
5595.700	18.0	0.451	-0.425	5605.900	39.0	0.684	-0.096
5595.872	17.0	0.452	-0.450	5605.900	38.0	0.684	-0.107
5596.122	16.0	0.452	-0.475	5605.900	12.0	0.427	-0.596
5596.160	43.0	0.748	-0.054	5606.037	37.0	0.685	-0.119
5596.160	42.0	0.748	-0.064	5606.037	37.0	0.685	-0.119
5596.160	42.0	0.748	-0.064	5606.037	37.0	0.685	-0.119
5596.160	43.0	0.748	-0.054	5607.834	12.0	0.422	-0.596
5596.321	41.0	0.748	-0.074	5608.108	11.0	0.422	-0.632
5596.321	41.0	0.748	-0.074	5608.173	37.0	0.669	-0.119
5598.212	17.0	0.445	-0.450	5608.173	38.0	0.669	-0.107
5598.420	16.0	0.445	-0.475	5608.173	37.0	0.669	-0.119
5598.640	15.0	0.445	-0.502	5608.173	38.0	0.669	-0.107
5598.817	42.0	0.731	-0.064	5608.317	36.0	0.670	-0.130

The (0, 1) $^{12}C^{12}C$ linelist–continued

Wavelength (Å)	J$''$	χ(eV)	log gf	Wavelength (Å)	J$''$	χ(eV)	log gf
5608.317	36.0	0.670	-0.130	5617.912	32.0	0.600	-0.181
5609.657	12.0	0.417	-0.596	5617.912	32.0	0.600	-0.181
5609.988	11.0	0.417	-0.632	5618.053	31.0	0.601	-0.194
5610.239	37.0	0.655	-0.119	5618.053	31.0	0.601	-0.194
5610.239	37.0	0.655	-0.119	5619.644	32.0	0.588	-0.181
5610.300	36.0	0.655	-0.130	5619.644	31.0	0.588	-0.194
5610.300	36.0	0.655	-0.130	5619.644	32.0	0.588	-0.181
5610.365	35.0	0.655	-0.142	5619.644	31.0	0.588	-0.194
5610.365	35.0	0.655	-0.142	5619.811	30.0	0.588	-0.208
5611.667	11.0	0.412	-0.632	5619.811	30.0	0.588	-0.208
5612.044	10.0	0.413	-0.671	5621.158	5.0	0.397	-0.952
5612.339	36.0	0.640	-0.130	5621.177	31.0	0.575	-0.194
5612.339	35.0	0.641	-0.142	5621.177	31.0	0.575	-0.194
5612.339	35.0	0.641	-0.142	5621.236	30.0	0.576	-0.208
5612.339	9.0	0.413	-0.715	5621.236	30.0	0.576	-0.208
5612.339	36.0	0.640	-0.130	5621.369	29.0	0.576	-0.223
5612.489	34.0	0.641	-0.155	5621.369	29.0	0.576	-0.223
5612.489	34.0	0.641	-0.155	5622.780	30.0	0.563	-0.208
5613.609	10.0	0.408	-0.671	5622.780	29.0	0.564	-0.223
5614.031	9.0	0.409	-0.715	5622.780	30.0	0.563	-0.208
5614.228	35.0	0.627	-0.142	5622.780	29.0	0.564	-0.223
5614.228	35.0	0.627	-0.142	5622.945	28.0	0.564	-0.238
5614.252	34.0	0.627	-0.155	5622.945	28.0	0.564	-0.238
5614.252	34.0	0.627	-0.155	5624.162	29.0	0.552	-0.223
5614.391	33.0	0.627	-0.167	5624.162	29.0	0.552	-0.223
5614.391	8.0	0.409	-0.763	5624.204	28.0	0.552	-0.238
5614.391	33.0	0.627	-0.167	5624.204	28.0	0.552	-0.238
5615.436	9.0	0.405	-0.715	5624.345	27.0	0.552	-0.253
5615.917	8.0	0.405	-0.763	5624.345	27.0	0.552	-0.253
5616.162	34.0	0.613	-0.155	5625.565	27.0	0.541	-0.253
5616.162	34.0	0.613	-0.155	5625.565	28.0	0.541	-0.238
5616.162	33.0	0.613	-0.167	5625.565	27.0	0.541	-0.253
5616.162	33.0	0.613	-0.167	5625.565	28.0	0.541	-0.238
5616.285	7.0	0.406	-0.818	5625.735	26.0	0.541	-0.269
5616.305	32.0	0.614	-0.181	5625.735	26.0	0.541	-0.269
5616.305	32.0	0.614	-0.181	5626.765	27.0	0.530	-0.253
5617.190	8.0	0.401	-0.763	5626.765	27.0	0.530	-0.253
5617.745	7.0	0.402	-0.818	5626.825	26.0	0.530	-0.269
5617.888	33.0	0.600	-0.167	5626.825	26.0	0.530	-0.269
5617.888	33.0	0.600	-0.167	5626.962	25.0	0.530	-0.286

The (0, 1) $^{12}C^{12}C$ linelist–continued

Wavelength (Å)	J″	χ(eV)	log *gf*	Wavelength (Å)	J″	χ(eV)	log *gf*
5626.962	25.0	0.530	-0.286	5633.180	20.0	0.466	-0.381
5628.002	26.0	0.520	-0.269	5633.236	19.0	0.466	-0.403
5628.002	26.0	0.520	-0.269	5633.236	19.0	0.466	-0.403
5628.002	25.0	0.520	-0.286	5633.423	18.0	0.467	-0.425
5628.002	25.0	0.520	-0.286	5633.423	18.0	0.467	-0.425
5628.192	24.0	0.520	-0.303	5633.732	19.0	0.459	-0.403
5628.192	24.0	0.520	-0.303	5633.732	19.0	0.459	-0.403
5629.038	25.0	0.510	-0.286	5633.814	18.0	0.459	-0.425
5629.038	25.0	0.510	-0.286	5633.814	18.0	0.459	-0.425
5629.107	24.0	0.510	-0.303	5633.965	17.0	0.459	-0.450
5629.107	24.0	0.510	-0.303	5633.965	17.0	0.459	-0.450
5629.243	23.0	0.510	-0.321	5634.114	8.0	0.401	-0.763
5629.243	23.0	0.510	-0.321	5634.114	8.0	0.401	-0.763
5630.072	24.0	0.500	-0.303	5634.217	18.0	0.451	-0.425
5630.072	24.0	0.500	-0.303	5634.217	18.0	0.451	-0.425
5630.118	23.0	0.501	-0.321	5634.217	7.0	0.402	-0.818
5630.118	23.0	0.501	-0.321	5634.217	7.0	0.402	-0.818
5630.280	22.0	0.501	-0.340	5634.305	17.0	0.452	-0.450
5630.280	22.0	0.501	-0.340	5634.305	17.0	0.452	-0.450
5630.956	23.0	0.491	-0.321	5634.484	9.0	0.405	-0.715
5630.956	23.0	0.491	-0.321	5634.484	9.0	0.405	-0.715
5631.025	22.0	0.491	-0.340	5634.484	16.0	0.452	-0.475
5631.025	22.0	0.491	-0.340	5634.484	16.0	0.452	-0.475
5631.166	21.0	0.492	-0.360	5634.598	8.0	0.405	-0.763
5631.166	21.0	0.492	-0.360	5634.598	17.0	0.445	-0.450
5631.795	22.0	0.482	-0.340	5634.598	8.0	0.405	-0.763
5631.795	22.0	0.482	-0.340	5634.598	17.0	0.445	-0.450
5631.858	21.0	0.483	-0.360	5634.705	7.0	0.406	-0.818
5631.858	21.0	0.483	-0.360	5634.705	7.0	0.406	-0.818
5632.028	20.0	0.483	-0.381	5634.705	16.0	0.445	-0.475
5632.028	20.0	0.483	-0.381	5634.705	16.0	0.445	-0.475
5632.514	21.0	0.474	-0.360	5634.835	15.0	0.445	-0.502
5632.514	21.0	0.474	-0.360	5634.835	10.0	0.408	-0.671
5632.598	20.0	0.474	-0.381	5634.835	10.0	0.408	-0.671
5632.598	20.0	0.474	-0.381	5634.835	15.0	0.445	-0.502
5632.742	19.0	0.475	-0.403	5634.913	9.0	0.409	-0.715
5632.742	19.0	0.475	-0.403	5634.913	16.0	0.438	-0.475
5633.090	5.0	0.397	-0.952	5634.913	16.0	0.438	-0.475
5633.090	5.0	0.397	-0.952	5634.913	9.0	0.409	-0.715
5633.180	20.0	0.466	-0.381	5634.964	15.0	0.439	-0.502

The (0, 1) $^{12}C^{12}C$ linelist–continued

Wavelength (Å)	**J″**	χ**(eV)**	**log** gf	**Wavelength (Å)**	**J″**	χ**(eV)**	**log** gf
5634.964	15.0	0.439	-0.502	5635.202	12.0	0.417	-0.596
5635.079	15.0	0.432	-0.502	5635.324	9.0	0.413	-0.715
5635.079	11.0	0.412	-0.632	5635.324	9.0	0.413	-0.715
5635.079	15.0	0.432	-0.502	5635.324	11.0	0.417	-0.632
5635.079	8.0	0.409	-0.763	5635.324	11.0	0.417	-0.632
5635.079	11.0	0.412	-0.632	5635.333	12.0	0.422	-0.596
5635.079	8.0	0.409	-0.763	5635.333	13.0	0.433	-0.562
5635.195	10.0	0.413	-0.671	5635.333	12.0	0.422	-0.596
5635.195	10.0	0.413	-0.671	5635.333	13.0	0.433	-0.562
5635.195	14.0	0.433	-0.531	5635.333	13.0	0.427	-0.562
5635.195	14.0	0.439	-0.531	5635.333	13.0	0.427	-0.562
5635.195	14.0	0.439	-0.531	5635.490	10.0	0.418	-0.671
5635.195	14.0	0.433	-0.531	5635.490	10.0	0.418	-0.671
5635.202	13.0	0.421	-0.562	5635.499	12.0	0.427	-0.596
5635.202	13.0	0.421	-0.562	5635.499	11.0	0.422	-0.632
5635.202	14.0	0.427	-0.531	5635.499	11.0	0.422	-0.632
5635.202	12.0	0.417	-0.596	5635.499	12.0	0.427	-0.596
5635.202	14.0	0.427	-0.531				

Table B.6: The (0, 1) $^{12}C^{13}C$ linelist

Wavelength (Å)	J″	χ(eV)	log *gf*	Wavelength (Å)	J″	χ(eV)	log *gf*
5579.970	21.0	0.474	-0.360	5590.674	41.0	0.732	-0.074
5580.008	20.0	0.474	-0.381	5592.398	41.0	0.732	-0.074
5580.092	19.0	0.475	-0.403	5590.769	42.0	0.731	-0.064
5582.309	45.0	0.800	-0.035	5590.717	40.0	0.732	-0.085
5580.424	45.0	0.800	-0.035	5592.404	40.0	0.732	-0.085
5582.465	46.0	0.800	-0.025	5592.570	16.0	0.438	-0.475
5580.532	46.0	0.800	-0.025	5592.686	15.0	0.439	-0.502
5582.300	44.0	0.800	-0.044	5592.858	14.0	0.439	-0.531
5580.451	44.0	0.800	-0.044	5594.778	41.0	0.715	-0.074
5582.684	20.0	0.466	-0.381	5593.053	41.0	0.715	-0.074
5582.720	19.0	0.466	-0.403	5592.956	40.0	0.716	-0.085
5582.848	18.0	0.467	-0.425	5594.644	40.0	0.716	-0.085
5584.863	44.0	0.782	-0.044	5594.653	39.0	0.716	-0.096
5583.123	45.0	0.782	-0.035	5593.011	39.0	0.716	-0.096
5585.009	45.0	0.782	-0.035	5594.814	15.0	0.432	-0.502
5583.012	44.0	0.782	-0.044	5594.970	14.0	0.433	-0.531
5583.032	43.0	0.782	-0.054	5595.122	13.0	0.433	-0.562
5584.835	43.0	0.782	-0.054	5595.319	39.0	0.700	-0.096
5585.241	19.0	0.459	-0.403	5595.409	40.0	0.700	-0.085
5585.315	18.0	0.459	-0.425	5597.098	40.0	0.700	-0.085
5585.416	17.0	0.459	-0.450	5596.962	39.0	0.700	-0.096
5587.516	43.0	0.765	-0.054	5596.974	38.0	0.700	-0.107
5585.711	43.0	0.765	-0.054	5595.369	38.0	0.700	-0.107
5585.813	44.0	0.765	-0.044	5597.020	14.0	0.427	-0.531
5587.666	44.0	0.765	-0.044	5597.192	13.0	0.427	-0.562
5587.506	42.0	0.765	-0.064	5599.194	39.0	0.684	-0.09
5585.738	42.0	0.765	-0.064	5599.066	38.0	0.684	-0.107
5587.788	18.0	0.451	-0.425	5597.550	39.0	0.684	-0.096
5587.858	17.0	0.452	-0.450	5597.459	38.0	0.684	-0.107
5588.008	16.0	0.452	-0.475	5597.395	12.0	0.427	-0.596
5588.224	43.0	0.748	-0.054	5599.073	37.0	0.685	-0.119
5588.120	42.0	0.748	-0.064	5599.073	37.0	0.685	-0.119
5589.890	42.0	0.748	-0.064	5597.513	37.0	0.685	-0.119
5590.030	43.0	0.748	-0.054	5599.323	12.0	0.422	-0.596
5589.908	41.0	0.748	-0.074	5599.514	11.0	0.422	-0.632
5588.185	41.0	0.748	-0.074	5599.643	37.0	0.669	-0.119
5590.191	17.0	0.445	-0.450	5599.725	38.0	0.669	-0.107
5590.299	16.0	0.445	-0.475	5601.203	37.0	0.669	-0.119
5590.424	15.0	0.445	-0.502	5601.333	38.0	0.669	-0.107
5592.541	42.0	0.731	-0.064	5599.703	36.0	0.670	-0.130

The (0, 1) $^{12}C^{13}C$ linelist–continued

Wavelength (Å)	**J″**	**χ(eV)**	**log gf**	**Wavelength (Å)**	**J″**	**χ(eV)**	**log gf**
5601.225	36.0	0.670	-0.130	5610.332	32.0	0.600	-0.181
5601.140	12.0	0.417	-0.596	5608.974	32.0	0.600	-0.181
5601.388	11.0	0.417	-0.632	5610.364	31.0	0.601	-0.194
5601.702	37.0	0.655	-0.119	5609.051	31.0	0.601	-0.194
5603.264	37.0	0.655	-0.119	5612.059	32.0	0.588	-0.181
5603.203	36.0	0.655	-0.130	5610.637	31.0	0.588	-0.194
5601.679	36.0	0.655	-0.130	5610.701	32.0	0.588	-0.181
5601.668	35.0	0.655	-0.142	5611.950	31.0	0.588	-0.194
5603.145	35.0	0.655	-0.142	5610.740	30.0	0.588	-0.208
5603.062	11.0	0.412	-0.632	5612.014	30.0	0.588	-0.208
5603.358	10.0	0.413	-0.671	5612.098	5.0	0.397	-0.952
5605.237	36.0	0.640	-0.130	5613.479	31.0	0.575	-0.194
5603.636	35.0	0.641	-0.142	5612.165	31.0	0.575	-0.194
5605.114	35.0	0.641	-0.142	5612.161	30.0	0.576	-0.208
5603.577	9.0	0.413	-0.715	5613.435	30.0	0.576	-0.208
5603.712	36.0	0.640	-0.130	5612.236	29.0	0.576	-0.223
5603.708	34.0	0.641	-0.155	5613.465	29.0	0.576	-0.223
5605.149	34.0	0.641	-0.155	5613.700	30.0	0.563	-0.208
5604.919	10.0	0.408	-0.671	5614.872	29.0	0.564	-0.223
5605.264	9.0	0.409	-0.715	5614.975	30.0	0.563	-0.208
5606.999	35.0	0.627	-0.142	5613.643	29.0	0.564	-0.223
5605.519	35.0	0.627	-0.142	5613.751	28.0	0.564	-0.238
5606.907	34.0	0.627	-0.155	5614.941	28.0	0.564	-0.238
5605.466	34.0	0.627	-0.155	5615.020	29.0	0.552	-0.223
5605.534	33.0	0.627	-0.167	5616.251	29.0	0.552	-0.223
5605.550	8.0	0.409	-0.763	5616.196	28.0	0.552	-0.238
5606.930	33.0	0.627	-0.167	5615.006	28.0	0.552	-0.238
5606.664	9.0	0.405	-0.715	5615.096	27.0	0.552	-0.253
5607.071	8.0	0.405	-0.763	5616.241	27.0	0.552	-0.253
5608.812	34.0	0.613	-0.155	5616.312	27.0	0.541	-0.253
5607.370	34.0	0.613	-0.155	5617.553	28.0	0.541	-0.238
5608.696	33.0	0.613	-0.167	5617.458	27.0	0.541	-0.253
5607.300	33.0	0.613	-0.167	5616.362	28.0	0.541	-0.238
5607.369	7.0	0.406	-0.818	5616.431	26.0	0.541	-0.269
5608.729	32.0	0.614	-0.181	5617.537	26.0	0.541	-0.269
5607.372	32.0	0.614	-0.181	5617.508	27.0	0.530	-0.253
5608.340	8.0	0.401	-0.763	5618.654	27.0	0.530	-0.253
5608.824	7.0	0.402	-0.818	5618.624	26.0	0.530	-0.269
5610.417	33.0	0.600	-0.167	5617.518	26.0	0.530	-0.269
5609.020	33.0	0.600	-0.167	5617.610	25.0	0.530	-0.286

The (0, 1) $^{12}C^{13}C$ linelist–continued

Wavelength (Å)	**J″**	**χ(eV)**	**log *gf***	**Wavelength (Å)**	**J″**	**χ(eV)**	**log *gf***
5618.672	25.0	0.530	-0.286	5623.632	20.0	0.466	-0.381
5619.798	26.0	0.520	-0.269	5623.663	19.0	0.466	-0.403
5618.691	26.0	0.520	-0.269	5624.472	19.0	0.466	-0.403
5619.709	25.0	0.520	-0.286	5623.827	18.0	0.467	-0.425
5618.647	25.0	0.520	-0.286	5624.595	18.0	0.467	-0.425
5618.794	24.0	0.520	-0.303	5624.157	19.0	0.459	-0.403
5619.815	24.0	0.520	-0.303	5624.966	19.0	0.459	-0.403
5620.742	25.0	0.510	-0.286	5624.217	18.0	0.459	-0.425
5619.679	25.0	0.510	-0.286	5624.984	18.0	0.459	-0.425
5620.727	24.0	0.510	-0.303	5625.074	17.0	0.459	-0.450
5619.706	24.0	0.510	-0.303	5624.350	17.0	0.459	-0.450
5620.781	23.0	0.510	-0.321	5624.827	8.0	0.401	-0.763
5619.804	23.0	0.510	-0.321	5624.486	8.0	0.401	-0.763
5621.690	24.0	0.500	-0.303	5624.619	18.0	0.451	-0.425
5620.667	24.0	0.500	-0.303	5625.386	18.0	0.451	-0.425
5621.654	23.0	0.501	-0.321	5624.903	7.0	0.402	-0.818
5620.676	23.0	0.501	-0.321	5624.605	7.0	0.402	-0.818
5621.738	22.0	0.501	-0.340	5624.689	17.0	0.452	-0.450
5620.801	22.0	0.501	-0.340	5625.413	17.0	0.452	-0.450
5622.489	23.0	0.491	-0.321	5625.226	9.0	0.405	-0.715
5621.511	23.0	0.491	-0.321	5624.843	9.0	0.405	-0.715
5621.544	22.0	0.491	-0.340	5624.852	16.0	0.452	-0.475
5622.481	22.0	0.491	-0.340	5625.534	16.0	0.452	-0.475
5621.653	21.0	0.492	-0.360	5624.969	8.0	0.405	-0.763
5622.547	21.0	0.492	-0.360	5624.981	17.0	0.445	-0.450
5622.311	22.0	0.482	-0.340	5625.310	8.0	0.405	-0.763
5623.249	22.0	0.482	-0.340	5625.705	17.0	0.445	-0.450
5623.236	21.0	0.483	-0.360	5625.091	7.0	0.406	-0.818
5622.343	21.0	0.483	-0.360	5625.389	7.0	0.406	-0.818
5623.336	20.0	0.483	-0.381	5625.754	16.0	0.445	-0.475
5622.483	20.0	0.483	-0.381	5625.072	16.0	0.445	-0.475
5622.997	21.0	0.474	-0.360	5625.829	15.0	0.445	-0.502
5623.890	21.0	0.474	-0.360	5625.610	10.0	0.408	-0.671
5623.052	20.0	0.474	-0.381	5625.184	10.0	0.408	-0.671
5623.904	20.0	0.474	-0.381	5625.190	15.0	0.445	-0.502
5623.979	19.0	0.475	-0.403	5625.270	9.0	0.409	-0.715
5623.171	19.0	0.475	-0.403	5625.962	16.0	0.438	-0.475
5623.523	5.0	0.397	-0.952	5625.279	16.0	0.438	-0.475
5623.736	5.0	0.397	-0.952	5625.654	9.0	0.409	-0.715
5624.484	20.0	0.466	-0.381	5625.958	15.0	0.439	-0.502

The (0, 1) $^{12}C^{13}C$ linelist–continued

Wavelength (Å)	**J''**	χ**(eV)**	**log** gf	**Wavelength (Å)**	**J''**	χ**(eV)**	**log** gf
5634.964	15.0	0.439	-0.502	5635.202	12.0	0.417	-0.596
5635.079	15.0	0.432	-0.502	5635.324	9.0	0.413	-0.715
5635.079	11.0	0.412	-0.632	5635.324	9.0	0.413	-0.715
5635.079	15.0	0.432	-0.502	5635.324	11.0	0.417	-0.632
5635.079	8.0	0.409	-0.763	5635.324	11.0	0.417	-0.632
5635.079	11.0	0.412	-0.632	5635.333	12.0	0.422	-0.596
5635.079	8.0	0.409	-0.763	5635.333	13.0	0.433	-0.562
5635.195	10.0	0.413	-0.671	5635.333	12.0	0.422	-0.596
5635.195	10.0	0.413	-0.671	5635.333	13.0	0.433	-0.562
5635.195	14.0	0.433	-0.531	5635.333	13.0	0.427	-0.562
5635.195	14.0	0.439	-0.531	5635.333	13.0	0.427	-0.562
5635.195	14.0	0.439	-0.531	5635.490	10.0	0.418	-0.671
5635.195	14.0	0.433	-0.531	5635.490	10.0	0.418	-0.671
5635.202	13.0	0.421	-0.562	5635.499	12.0	0.427	-0.596
5635.202	13.0	0.421	-0.562	5635.499	11.0	0.422	-0.632
5635.202	14.0	0.427	-0.531	5635.499	11.0	0.422	-0.632
5635.202	12.0	0.417	-0.596	5635.499	12.0	0.427	-0.596
5635.202	14.0	0.427	-0.531				

Bibliography

Alcock, C., et al. 2001, *Astrophys. J.*, 554, 298

Alonso, A., Arribas, S., & Martínez-Roger, C. 1999, *Astron. Astrophys. Suppl.*, 140, 261

Anderson, A. J. 1997, PhD thesis, UNIVERSITY OF CALIFORNIA, BERKELEY

Asplund, M., Grevesse, N., Sauval, A. J., Allende Prieto, C., & Blomme, R. 2005, *Astron. Astrophys.*, 431, 693

Asplund, M., Grevesse, N., Sauval, A. J., & Scott, P. 2009, *Annurev.aa.* , 47, 481

Asplund, M., Gustafsson, B., Kiselman, D., & Eriksson, K. 1997a, *Astron. Astrophys.*, 318, 521

Asplund, M., Gustafsson, B., Lambert, D. L., & Kameswara Rao, N. 1997b, *Astron. Astrophys.*, 321, L17

Asplund, M., Gustafsson, B., Lambert, D. L., & Rao, N. K. 2000, *Astron. Astrophys.*, 353, 287

Bedin, L. R., Piotto, G., Anderson, J., Cassisi, S., King, I. R., Momany, Y., & Carraro, G. 2004, *Astrophys. J. Lett.*, 605, L125

Bell, R. A., & Gustafsson, B. 1989, *Mon. Not. Roy. Astron. Soc.*, 236, 653

Berman, L. 1935, *Astrophys. J.*, 81, 369

Bessell, M. S., & Brett, J. M. 1988, *Pub. Astron. Soc. Pac.*, 100, 1134

Bidelman, W. P. 1953, *Astrophys. J.*, 117, 25

Blöcker, T. 2003, in IAU Symposium, Vol. 209, Planetary Nebulae: Their Evolution and Role in the Universe, ed. S. Kwok, M. Dopita, & R. Sutherland, 101

Bloecker, T. 1995, *Astron. Astrophys.*, 299, 755

Böhm-Vitense, E. 1992, Introduction to Stellar Astrophysics

Bonnarel, F., et al. 2000, *Astron. Astrophys. Suppl.*, 143, 33

Calamida, A., et al. 2009, *Astrophys. J.*, 706, 1277

Cannon, A. J., & Pickering, E. C. 1912, Annals of Harvard College Observatory, 56, 65

Catchpole, R. M., & Glass, I. S. 1974, *Mon. Not. Roy. Astron. Soc.*, 169, 69P

Clayton, G. C. 1996, *Pub. Astron. Soc. Pac.*, 108, 225

Clayton, G. C., & De Marco, O. 1997, *Astron. J.*, 114, 2679

Clayton, G. C., Geballe, T. R., Herwig, F., Fryer, C., & Asplund, M. 2007, *Astrophys. J.*, 662, 1220

Clayton, G. C., Hammond, D., Lawless, J., Kilkenny, D., Evans, T. L., Mattei, J., & Landolt, A. U. 2002, *Pub. Astron. Soc. Pac.*, 114, 846

Clayton, G. C., Herwig, F., Geballe, T. R., Asplund, M., Tenenbaum, E. D., Engelbracht, C. W., & Gordon, K. D. 2005, *Astrophys. J. Lett.*, 623, L141

Clayton, G. C., Kilkenny, D., Wils, P., & Welch, D. L. 2009, *Pub. Astron. Soc. Pac.*, 121, 461

Climenhaga, J. L. 1960, *Astron. J.*, 65, 50

Cottrell, P. L., & Lambert, D. L. 1982, *Astrophys. J.*, 261, 595

Dickens, R. J., & Woolley, R. v. d. R. 1967, Royal Greenwich Observatory Bulletins, 128, 255

Dixon, W. V. D., Brown, T. M., & Landsman, W. B. 2004, *Astrophys. J. Lett.*, 600, L43

Drilling, J. S. 1996, in Astronomical Society of the Pacific Conference Series, Vol. 96, Hydrogen Deficient Stars, ed. C. S. Jeffery & U. Heber, 461

Drilling, J. S., Jeffery, C. S., & Heber, U. 1998, *Astron. Astrophys.*, 329, 1019

Dupree, A. K., & Avrett, E. H. 2013, *Astrophys. J. Lett.*, 773, L28

Dupree, A. K., Strader, J., & Smith, G. H. 2011, *Astrophys. J.*, 728, 155

Feast, M. W. 1975, in IAU Symposium, Vol. 67, Variable Stars and Stellar Evolution, ed. V. E. Sherwood & L. Plaut, 129–141

Feast, M. W. 1997, *Mon. Not. Roy. Astron. Soc.*, 285, 339

Forbes, D. A., & Bridges, T. 2010, *Mon. Not. Roy. Astron. Soc.*, 404, 1203

Freeman, K. C. 1993, in Astronomical Society of the Pacific Conference Series, Vol. 48, The Globular Cluster-Galaxy Connection, ed. G. H. Smith & J. P. Brodie, 608

Freeman, K. C., & Rodgers, A. W. 1975, *Astrophys. J. Lett.*, 201, L71

Fujita, Y., & Tsuji, T. 1977, *Pub. Astron. Soc. Japan*, 29, 711

Gallino, R., Arlandini, C., Busso, M., Lugaro, M., Travaglio, C., Straniero, O., Chieffi, A., & Limongi, M. 1998, *Astrophys. J.*, 497, 388

García-Hernández, D. A., Hinkle, K. H., Lambert, D. L., & Eriksson, K. 2009, *Astrophys. J.*, 696, 1733

García-Hernández, D. A., Lambert, D. L., Kameswara Rao, N., Hinkle, K. H., & Eriksson, K. 2010, *Astrophys. J.*, 714, 144

Gonzalez, G., Lambert, D. L., Wallerstein, G., Rao, N. K., Smith, V. V., & McCarthy, J. K. 1998, *Astrophys. J.S*, 114, 133

Goswami, A., Karinkuzhi, D., & Shantikumar, N. S. 2010, *Astrophys. J. Lett.*, 723, L238

Gustafsson, B., Edvardsson, B., Eriksson, K., Jørgensen, U. G., Nordlund, Å., & Plez, B. 2008, *Astron. Astrophys.*, 486, 951

Han, Z. 1998, *Mon. Not. Roy. Astron. Soc.*, 296, 1019

Harris, W. E. 1996, *Astron. J.*, 112, 1487

Harrison, P. M., & Jeffery, C. S. 1997, *Astron. Astrophys.*, 323, 177

Heber, U. 1986, in Astrophysics and Space Science Library, Vol. 128, IAU Colloq. 87: Hydrogen Deficient Stars and Related Objects, ed. K. Hunger, D. Schoenberner, & N. Kameswara Rao, 33–48

Hema, B. P., Pandey, G., & Lambert, D. L. 2012, *Astrophys. J.*, 747, 102

Herwig, F. 2001, *Astrophys. J. Lett.*, 554, L71

—. 2005, *Annurev.aa.* , 43, 435

Herwig, F., Blöcker, T., Langer, N., & Driebe, T. 1999, *Astron. Astrophys.*, 349, L5

Herzberg, G., & Phillips, J. G. 1948, *Astrophys. J.*, 108, 163

Hesselbach, E., Clayton, G. C., & Smith, P. S. 2003, *Pub. Astron. Soc. Pac.*, 115, 1301

Hilker, M., Kayser, A., Richtler, T., & Willemsen, P. 2004, *Astron. Astrophys.*, 422, L9

Hinkle, K., Wallace, L., Valenti, J., & Harmer, D. 2000, Visible and Near Infrared Atlas of the Arcturus Spectrum 3727-9300 A

Hinkle, K. H., Wallace, L., Ram, R. S., Bernath, P. F., Sneden, C., & Lucatello, S. 2013, *Astrophys. J.S*, 207, 26

Hurley, J. R., & Shara, M. M. 2003, *Astrophys. J.*, 589, 179

Iben, Jr., I. 1967, *Annurev.aa.* , 5, 571

—. 1974, *Annurev.aa.* , 12, 215

—. 1984, *Astrophys. J.*, 277, 333

Iben, Jr., I., & Renzini, A. 1983, *Annurev.aa.* , 21, 271

Iben, Jr., I., & Tutukov, A. V. 1985, *Astrophys. J.S*, 58, 661

Iben, Jr., I., Tutukov, A. V., & Yungelson, L. R. 1996, *Astrophys. J.*, 456, 750

—. 1997, *Astrophys. J.*, 475, 291

Ideta, M., & Makino, J. 2004, *Astrophys. J. Lett.*, 616, L107

Ivanova, N., Belczynski, K., Fregeau, J. M., & Rasio, F. A. 2005, *Mon. Not. Roy. Astron. Soc.*, 358, 572

Jackson, T., Ivezić, Ž., & Knapp, G. R. 2002, *Mon. Not. Roy. Astron. Soc.*, 337, 749

Jeffery, C. S. 1996, in Astronomical Society of the Pacific Conference Series, Vol. 96, Hydrogen Deficient Stars, ed. C. S. Jeffery & U. Heber, 152

Jeffery, C. S., Hamill, P. J., Harrison, P. M., & Jeffers, S. V. 1998, *Astron. Astrophys.*, 340, 476

Jeffery, C. S., & Heber, U. 1993, *Astron. Astrophys.*, 270, 167

Jeffery, C. S., Heber, U., Hill, P. W., Dreizler, S., Drilling, J. S., Lawson, W. A., Leuenhagen, U., & Werner, K. 1996, in Astronomical Society of the Pacific Conference Series, Vol. 96, Hydrogen Deficient Stars, ed. C. S. Jeffery & U. Heber, 471–+

Jeffery, C. S., Hill, P. W., & Heber, U. 1999, *Astron. Astrophys.*, 346, 491

Jeffery, C. S., Karakas, A. I., & Saio, H. 2011, *Mon. Not. Roy. Astron. Soc.*, 414, 3599

Jeffery, C. S., & Saio, H. 2002, in Astronomical Society of the Pacific Conference Series, Vol. 263, Stellar Collisions, Mergers and their Consequences, ed. M. M. Shara, 239

Ji, J., & Bregman, J. N. 2013, *Astrophys. J.*, 768, 158

Johnson, C. I., & Pilachowski, C. A. 2010, *Astrophys. J.*, 722, 1373

Johnson, C. I., Pilachowski, C. A., Michael Rich, R., & Fulbright, J. P. 2009, *Astrophys. J.*, 698, 2048

Kaufman, U., & Martin, W. C. 1993, Journal of Physics Conference Series, 22, 279

Kraemer, K. E., Sloan, G. C., Wood, P. R., Price, S. D., & Egan, M. P. 2005, *Astrophys. J. Lett.*, 631, L147

Kurucz, R. L. 1998, http://kurucz.harvard.edu/

Lambert, D. L., & Rao, N. K. 1994, Journal of Astrophysics and Astronomy, 15, 47

Lee, Y.-W., Joo, J.-M., Sohn, Y.-J., Rey, S.-C., Lee, H.-C., & Walker, A. R. 1999, *Nature*, 402, 55

Luck, R. E., & Lambert, D. L. 1981, *Astrophys. J.*, 245, 1018

Lundmark, K. 1921, *Pub. Astron. Soc. Pac.*, 33, 314

Marino, A. F., et al. 2014, *Mon. Not. Roy. Astron. Soc.*, 437, 1609

Martin, W. C., & Zalubas, R. 1983, Journal of Physical and Chemical Reference Data, 12, 323

Martin, W. C., Zalubas, R., & Musgrove, A. 1990, Journal of Physical and Chemical Reference Data, 19, 821

McWilliam, A., & Lambert, D. L. 1988, *Mon. Not. Roy. Astron. Soc.*, 230, 573

Menon, A., Herwig, F., Denissenkov, P. A., Clayton, G. C., Staff, J., Pignatari, M., & Paxton, B. 2013, *Astrophys. J.*, 772, 59

Miller, A. A., Richards, J. W., Bloom, J. S., Cenko, S. B., Silverman, J. M., Starr, D. L., & Stassun, K. G. 2012, *Astrophys. J.*, 755, 98

Milone, A. P., et al. 2012, *Astron. Astrophys.*, 540, A16

Morgan, D. H., Hatzidimitriou, D., Cannon, R. D., & Croke, B. F. W. 2003, *Mon. Not. Roy. Astron. Soc.*, 344, 325

Naulin, C., Costes, M., & Dorthe, G. 1988, Chemical Physics Letters, 143, 496

Nave, G., Johansson, S., Learner, R. C. M., Thorne, A. P., & Brault, J. W. 1994, *Astrophys. J.S*, 94, 221

Nelemans, G., Yungelson, L. R., Portegies Zwart, S. F., & Verbunt, F. 2001, *Astron. Astrophys.*, 365, 491

Norris, J. E. 2004, *Astrophys. J. Lett.*, 612, L25

Norris, J. E., & Da Costa, G. S. 1995, *Astrophys. J.*, 447, 680

Norris, J. E., Freeman, K. C., & Mighell, K. J. 1996, *Astrophys. J.*, 462, 241

Pancino, E., Ferraro, F. R., Bellazzini, M., Piotto, G., & Zoccali, M. 2000, *Astrophys. J. Lett.*, 534, L83

Pandey, G. 2006, *Astrophys. J. Lett.*, 648, L143

Pandey, G., Kameswara Rao, N., Lambert, D. L., Jeffery, C. S., & Asplund, M. 2001, *Mon. Not. Roy. Astron. Soc.*, 324, 937

Pandey, G., & Lambert, D. L. 2011, *Astrophys. J.*, 727, 122

Pandey, G., Lambert, D. L., Jeffery, C. S., & Rao, N. K. 2006, *Astrophys. J.*, 638, 454

Pandey, G., Lambert, D. L., & Rao, N. K. 2008, *Astrophys. J.*, 674, 1068

Pandey, G., Lambert, D. L., Rao, N. K., Gustafsson, B., Ryde, N., & Yong, D. 2004, *Mon. Not. Roy. Astron. Soc.*, 353, 143

Pandey, G., & Reddy, B. E. 2006, *Mon. Not. Roy. Astron. Soc.*, 369, 1677

Pavlenko, Y. V., Geballe, T. R., Evans, A., Smalley, B., Eyres, S. P. S., Tyne, V. H., & Yakovina, L. A. 2004, *Astron. Astrophys.*, 417, L39

Pesic, D. S., Vujisic, B. R., Rakotoarijimy, D., & Weniger, S. 1983, Journal of Molecular Spectroscopy, 100, 245

Peterson, R. C., Dalle Ore, C. M., & Kurucz, R. L. 1993, *Astrophys. J.*, 404, 333

Phillips, J. G., & Davis, S. P. 1968, The Swan system of the C2 molecule. The spectrum of the HgH molecule, ed. Phillips, J. G. & Davis, S. P.

Pigott, E., & Englefield, H. C. 1797, Royal Society of London Philosophical Transactions Series I, 87, 133

Piotto, G., et al. 2005, *Astrophys. J.*, 621, 777

Prabhu, T. P., Anupama, G. C., & Surendiranath, R. 1998, Bulletin of the Astronomical Society of India, 26, 383

Ramírez, I., & Allende Prieto, C. 2011, *Astrophys. J.*, 743, 135

Rao, N. K., & Lambert, D. L. 1996, in Astronomical Society of the Pacific Conference Series, Vol. 96, Hydrogen Deficient Stars, ed. C. S. Jeffery & U. Heber, 43

Rao, N. K., & Lambert, D. L. 2003, *Pub. Astron. Soc. Pac.*, 115, 1304

—. 2008, *Mon. Not. Roy. Astron. Soc.*, 384, 477

Rao, N. K., Sriram, S., Jayakumar, K., & Gabriel, F. 2005, Journal of Astrophysics and Astronomy, 26, 331

Reddy, B. E., & Lambert, D. L. 2005, *Astron. J.*, 129, 2831

Renzini, A. 1979, in Astrophysics and Space Science Library, Vol. 75, Stars and star systems, ed. B. E. Westerlund, 155–171

Renzini, A. 1990, in Astronomical Society of the Pacific Conference Series, Vol. 11, Confrontation Between Stellar Pulsation and Evolution, ed. C. Cacciari & G. Clementini, 549–556

Renzini, A. 1998, *Astron. J.*, 115, 2459

Renzini, A., & Buzzoni, A. 1986, in Astrophysics and Space Science Library, Vol. 122, Spectral Evolution of Galaxies, ed. C. Chiosi & A. Renzini, 195–231

Renzini, A., & Fusi Pecci, F. 1988, *Annurev.aa.* , 26, 199

Rey, S.-C., Lee, Y.-W., Ree, C. H., Joo, J.-M., Sohn, Y.-J., & Walker, A. R. 2004, *Astron. J.*, 127, 958

Russo, R. E., Bol'Shakov, A. A., Mao, X., McKay, C. P., Perry, D. L., & Sorkhabi, O. 2011, Spectrochimica Acta, 66, 99

Saio, H., & Jeffery, C. S. 2002, *Mon. Not. Roy. Astron. Soc.*, 333, 121

Schmidt, T. W., & Bacskay, G. B. 2007, , 127, 234310

Schoenberner, D. 1975, *Astron. Astrophys.*, 44, 383

—. 1979, *Astron. Astrophys.*, 79, 108

Schönberner, D. 2008, in Astronomical Society of the Pacific Conference Series, Vol. 391, Hydrogen-Deficient Stars, ed. A. Werner & T. Rauch, 139

Scott, P. C., Asplund, M., Grevesse, N., & Sauval, A. J. 2006, *Astron. Astrophys.*, 456, 675

Smith, V. V., Cunha, K., & Lambert, D. L. 1995, *Astron. J.*, 110, 2827

Smith, V. V., Suntzeff, N. B., Cunha, K., Gallino, R., Busso, M., Lambert, D. L., & Straniero, O. 2000, *Astron. J.*, 119, 1239

Sneden, C. A. 1973, PhD thesis, THE UNIVERSITY OF TEXAS AT AUSTIN.

Sollima, A., Ferraro, F. R., Pancino, E., & Bellazzini, M. 2005, *Mon. Not. Roy. Astron. Soc.*, 357, 265

Spinrad, H., & Wood, D. B. 1965, *Astrophys. J.*, 141, 109

Stanford, L. M., Da Costa, G. S., Norris, J. E., & Cannon, R. D. 2006, *Astrophys. J.*, 647, 1075

—. 2007, *Astrophys. J.*, 667, 911

Stawikowski, A., & Greenstein, J. L. 1964, *Astrophys. J.*, 140, 1280

Strömgren, B. 1966, *Annurev.aa.* , 4, 433

Suntzeff, N. B., & Kraft, R. P. 1996, *Astron. J.*, 111, 1913

Tisserand, P., Clayton, G. C., Welch, D. L., Pilecki, B., Wyrzykowski, L., & Kilkenny, D. 2013, *Astron. Astrophys.*, 551, A77

Tisserand, P., et al. 2004, *Astron. Astrophys.*, 424, 245

—. 2008, *Astron. Astrophys.*, 481, 673

—. 2009, *Astron. Astrophys.*, 501, 985

Toonen, S., Claeys, J. S. W., Mennekens, N., & Ruiter, A. J. 2013, ArXiv e-prints

Tull, R. G., MacQueen, P. J., Sneden, C., & Lambert, D. L. 1995, *Pub. Astron. Soc. Pac.*, 107, 251

Urdahl, R. S., Bao, Y., & Jackson, W. M. 1991, Chemical Physics Letters, 178, 425

van de Ven, G., van den Bosch, R. C. E., Verolme, E. K., & de Zeeuw, P. T. 2006, *Astron. Astrophys.*, 445, 513

Warner, B. 1967, *Mon. Not. Roy. Astron. Soc.*, 137, 119

Webbink, R. F. 1984, *Astrophys. J.*, 277, 355

Whitford, A. E. 1958, *Astron. J.*, 63, 201

Whitford, A. E., & Rich, R. M. 1983, *Astrophys. J.*, 274, 723

Zaniewski, A., Clayton, G. C., Welch, D. L., Gordon, K. D., Minniti, D., & Cook, K. H. 2005, *Astron. J.*, 130, 2293

Zhang, X., & Jeffery, C. S. 2012, *Mon. Not. Roy. Astron. Soc.*, 426, L81

Zinnecker, H., Keable, C. J., Dunlop, J. S., Cannon, R. D., & Griffiths, W. K. 1988, in IAU Symposium, Vol. 126, The Harlow-Shapley Symposium on Globular Cluster Systems in Galaxies, ed. J. E. Grindlay & A. G. D. Philip, 603